ATMOSPHERES OF ROCKY EXOPLANETS

Oliver Herbort

A Thesis Submitted for the Degree of PhD
at the
University of St Andrews

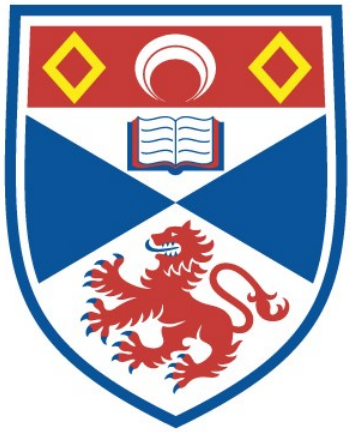

2022

ATMOSPHERES OF ROCKY EXOPLANETS

Oliver Herbort

University of
St Andrews

This thesis is submitted in partial fulfilment for the degree of

Doctor of Philosophy (PhD)

at the University of St Andrews

25.03.2022

Declaration

Candidate's declaration

I, Oliver Herbort, do hereby certify that this thesis, submitted for the degree of PhD, which is approximately 40,000 words in length, has been written by me, and that it is the record of work carried out by me, or principally by myself in collaboration with others as acknowledged, and that it has not been submitted in any previous application for any degree. I confirm that any appendices included in my thesis contain only material permitted by the 'Assessment of Postgraduate Research Students' policy.

I was admitted as a research student at the University of St Andrews in September 2018.

I received funding from an organisation or institution and have acknowledged the funder(s) in the full text of my thesis.

Date Signature of candidate

Supervisor's declaration

I hereby certify that the candidate has fulfilled the conditions of the Resolution and Regulations appropriate for the degree of PhD in the University of St Andrews and that the candidate is qualified to submit this thesis in application for that degree. I confirm that any appendices included in the thesis contain only material permitted by the 'Assessment of Postgraduate Research Students' policy.

Date Signature of supervisor

Permission for publication

In submitting this thesis to the University of St Andrews we understand that we are giving permission for it to be made available for use in accordance with the regulations of the University Library for the time being in force, subject to any copyright vested in the work not being affected thereby. We also understand, unless exempt by an award of an embargo as requested below, that the title and the abstract will be published, and that a copy of the work may be made and supplied to any bona fide library or research worker, that this thesis will be electronically accessible for personal or research use and that the library has the right to migrate this thesis into new electronic forms as required to ensure continued access to the thesis.

I, Oliver Herbort, confirm that my thesis does not contain any third-party material that requires copyright clearance.

The following is an agreed request by candidate and supervisor regarding the publication of this thesis:

Printed copy

Embargo on part (Chapter 5 - Chemical state of CHNOPS elements and implications on habitability) of print copy for a period of 1 year on the following ground(s):

- Publication would preclude future publication

Supporting statement for printed embargo request

The work presented in Chapter 5 is currently unpublished. The embargo is requested until the chapter is published as a paper.

Electronic copy

Embargo on part (Chapter 5 - Chemical state of CHNOPS elements and implications on habitability) of electronic copy for a period of 1 year on the following ground(s):

- Publication would preclude future publication

Supporting statement for printed embargo request

The work presented in Chapter 5 is currently unpublished. The embargo is requested until the chapter is published as a paper.

I agree to the title and abstract being published.

Date Signature of candidate

Date Signature of supervisor

Underpinning Research Data or Digital Outputs

Candidate's declaration

I, Oliver Herbort, hereby certify that no requirements to deposit original research data or digital outputs apply to this thesis and that, where appropriate, secondary data used have been referenced in the full text of my thesis.

Date Signature of candidate

Collaboration Statement

This thesis is the result of my own work, which was carried out at the University of St Andrews between September 2018 and March 2022. For the last six month I joined the Intitut für Weltraumforschung of the Österreichische Akademie der Wissenschaften in Graz as a visiting PhD student. The work in this thesis is based on the equilibrium chemistry solver GGchem by Woitke et al. (2018), which is publicly available[1].

The Chapters 2, 3, and 4 are based on published papers, while Chapter 5 will be submitted for publication after submission of this thesis.
Chapter 2 is published as 'The atmospheres of rocky exoplanets I. Outgassing of common rock and the stability of liquid water' by O. Herbort, P. Woitke, Ch. Helling, and A. Zerkle in Astronomy & Astrophysics 636, A71 (2020).
Chapter 4 is published as 'The atmospheres of rocky exoplanets II. Influence of surface composition on the diversity of cloud condensates' by O. Herbort, P. Woitke, Ch. Helling, and A. L. Zerkle in Astronomy & Astrophysics 658, A180 (2022).
All co-authors have given comments on the final manuscript of these papers.

Chapter 3 is based on work published as 'Coexistence of CH_4, CO_2, and H_2O in exoplanet atmospheres' by P. Woitke, O. Herbort, Ch. Helling, E. Stüeken, M. Dominik, P. Barth, D. Samra and published in Astronomy & Astrophysics 646, A43 (2021). As the second author of this paper I contributed substantially to the evolution of the idea as well as the discussion and implications of our results. Furthermore I provided the temperature sequences for different element abundances presented in the work.

[1] https://github.com/pw31/GGchem

Abstract

The increasing number of known rocky exoplanets motivates investigations of the diversity of atmospheric and surface composition of these planets. We investigate the link between the composition of the surface, near-crust atmosphere and the lower atmosphere, including the presence of different cloud condensates. This allows working towards inferring the surface composition from clouds and gas species present in the atmosphere. Understanding the diversity of the atmospheric composition provides a further step towards the characterisation of rocky exoplanets.

In this thesis, a fast and simple atmospheric model for the lower atmospheres of rocky exoplanets is presented. A range of different sets of total element abundances is used to investigate the surface composition in contact with the near-crust atmosphere in chemical and phase equilibrium. The atmosphere based on this crust-atmosphere interaction layer is build from bottom-to-top. At every point in the atmosphere, chemical equilibrium is solved and all thermally stable condensates are removed, depleting the atmospheric layers above in the affected elements.

In order to characterise the general atmospheric composition, atmospheric types based on the chemical state of carbon, hydrogen, oxygen, and nitrogen are introduced. In order to further constrain the potential of an atmospheric environment for habitability, different habitability levels are introduced. These take the stability of liquid water as well as the chemical states of carbon, nitrogen, and sulphur into account.

The investigation of the atmosphere-crust interaction layer shows, that the thermal stability of liquid water is only given, if all phyllosilicates (minerals which incorporate OH groups into their lattice structure) have completely formed. The composition of the resulting atmosphere can be categorised into three different atmospheric types. Of special interest is the possibility of the coexistence of CO_2 and CH_4 in chemical equilibrium. The atmospheric type is intrinsic to an atmosphere, as it does not change with the removal of thermally stable condensates in one given atmospheric model.

The atmospheric models reveal a large diversity in thermally stable cloud condensates, which constrain the surface conditions of rocky exoplanets. The presence of water clouds is an integral part of many planetary atmospheres and is independent of the stability of water condensates at the surface. At the water cloud base, we show that reduced gaseous forms of carbon, nitrogen, and sulphur are present, while phosphorus is absent.

Acknowledgements

General acknowledgements

After the 3.5 years of studies for this PhD, the time has come to thank the people without whom the writing of this thesis and the work that needed to be undertaken in order to arrive where this body of work stands at the time being would not have been possible.

First of all I want thank my supervisors Peter Woitke and Aubrey Zerkle for their very kind and helpful academic support over the years. Further, I want to thank Peter for the introduction to Golf and the lessons in Tennis. Great support has also been given by Christiane Helling and Mark Claire, which I am very grateful for.

As I had the great opportunity to be supervised in astronomy and geosciences, I want to thank both working groups for the comforting and knowledgeable environments they provided. Especially I want to thank the exoplanet atmosphere group for their endless time spent looking at plots with far too many lines. Being part of the geobiochemistry group provided a special opportunity to learn many things I would otherwise have never have heard of. The friendly and keen researchers at StA-CES and SEBD allowed for great environments for scientific discussions, and great opportunities for presentations.

Special thanks have to go to Dom and Patrick. Not only for great time in spend in the office, but also great evenings, tastings, hikes, and rounds of golf and Skat, which made the time in St Andrews very special. Furthermore the Astro-Suite has to be mentioned and thanked for great chats and the ritual Friday lunches. Especially I want to thank Tatiana, Elliot, Sam, and Till.

Life is nothing without the ‘occasional’ dram of whisky. For this very special part of life in St Andrews, I want to especially thank Aedan and Andrew and in extend the St Andrews Quaich Society for bringing joy to the many evenings involving whisky - Sláinte.

Special thanks have to go out to Duda and Leo for their mental support during the PhD in general, but especially the difficult times put upon us.

I want to congratulate Christiane Helling again for her position at the IWF, which allowed me to also join in Austria for the last part of the PhD. Although starting during a pandemic at a

different institute is not the best of all ideas, I want to thank the members of the IWF in Graz for the warm welcome. Especially I want to thank Helmut Lammer for incorporating me quickly into his research.

The Graz Grimms Quidditch team has to be mentioned and thanked for making me feel at home in Graz and part of the team since training one! Especially I want to thank Traudi and Dominik.

Last, but by no means at all least, I want to express my gratitude to my family for the support during the entire time. Especially for enabling me to follow my dream of researching exoplanets - thank you very much.

Funding

This work was supported by the St Andrews Centre for Exoplanet Science Doctoral Fellowship with shared funding by the St Leonard's College, School of Physics and Astronomy, and School of Earth and Environmental Science.

During the last half year of the PhD, I have been a visiting PhD student the Institut für Weltraumforschung of the Österreichische Akademie der Wissenschaften in Graz, which provided further support during this period.

Contents

List of Figures

List of Tables

"What a wonderful and amazing Scheme have we here of the magnificent Vastness of the Universe! So many Suns, so many Earths, and every one of them stock'd with so many Herbs, Trees and Animals, and adorn'd with so many Seas and Mountains! And how must our wonder and admiration be encreased when we consider the prodigious distance and multitude of the Stars?"

- Christiaan Huygens

1 Introduction

One of the fundamental questions for planetary science is how surfaces of other planets similar to the rocky bodies in our solar system look. What is the rock structure like? Will there be water? Are there any active atmospheric cycles? How can the surface conditions be inferred from the information made available by future observations? Is it possible to characterize different planetary environments based on these observations? On which planets is the formation of life possible?

The thesis at hand is presenting work, which is working towards understanding the links between the surface conditions, the atmospheric composition and the potential cloud condensates in the atmosphere. In the following, the background necessary for the understanding of this thesis is provided by an introduction to exoplanets and their detection in more general terms (Sect. 1.1) before focussing on the atmospheres of rocky exoplanets (Sect. 1.2). This is followed up by a brief introduction of planetary habitability (Sect. 1.3) and a description of the most important modelling background used in this thesis (Sect. 1.4). The introduction is concluded with the formulation of the research question (Sect. 1.5) and a description of the structure of the thesis as a

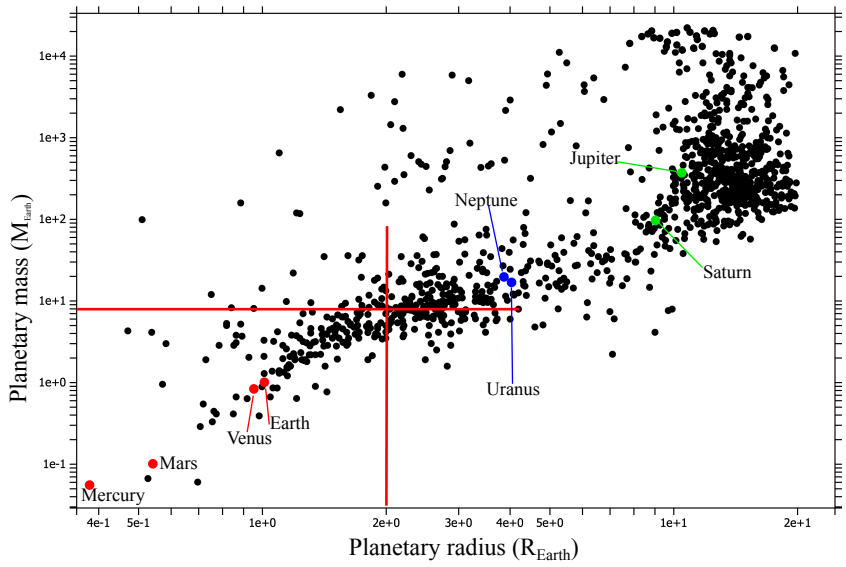

Figure 1.1: Shown are 1139 exoplanets for which the radius and mass are known. The solar system planets are also displayed for comparison. The red lines indicate the approximate boundaries for rocky exoplanets (image adapted from: exoplanet.eu).

whole (Sect. 1.6).

1.1 Exoplanets

The field of exoplanets is a relatively young field of research, with the first actual detections of planets around other stars than our sun dating back to the the 1990s. Wolszczan & Frail (1992) detected not only the first planetary body around the pulsar PSR B1257+12, but also a multi planet system with a third planetary body detected two years later Wolszczan (1994). This planet has a mass of only 0.020 M_{Earth} (Konacki & Wolszczan, 2003), which corresponds to 1.6 M_{moon} and remains among the planets with the lowest mass of the known planets to date[1]. Shortly after, Mayor & Queloz (1995) detected 51 Peg b, a 0.5 M_{J} planet orbiting the host star in 4.2 days. This discovery marks the first known exoplanet around a main-sequence star.

Besides ground-based observations with various telescopes, the use of space telescopes like CoRoT (Baglin et al., 2006) and Kepler (Borucki et al., 2010) allowed for the steady increase in the numbers of known exoplanets to almost 5000 exoplanets to date. Whereas Kepler was used to find exoplanets in a particular part of the sky, current space telescopes such as TESS (Ricker et al., 2015) survey the entire sky in order to find exoplanets, while CHEOPS (Benz et al., 2021) investigates known exoplanets to precisely measure their mass and radius.

[1] `http://exoplanet.eu`

Most of the exoplanets found so far do not have analogues in our solar system. While some planets are populating the mass parameter space not present in our solar system, others are orbiting much closer to their host star than is the case for the planets in our solar system. Struve (1952) wrote that there 'seems to be no compelling reason why the hypothetical stellar planets should not [...] be much closer to their parent stars than is the case in the solar system', predicting the presence of planets in very short orbits. Examples for these include hot Jupiters like 51 Peg b, highly-irradiated super-Earths like 55 Cnc e (McArthur et al., 2004), or tightly-packed planetary systems like Trappist 1 with its 7 rocky planets (Gillon et al., 2017). Figure 1.1 visualises the diversity of known exoplanets to date by showing the variation in planetary mass and radius. The comparison to the solar system planets underlines the diversity of known exoplanets. Especially the abundance of planets smaller and lighter than Neptune, but larger and more massive than Earth should be noted (e.g. Benneke & Seager, 2013). In this parameter range, the planets are expected to range from large rocky bodies to those with an substantial gaseous envelope. These classes of planets are known as super-Earths and mini-Neptunes, respectively. The nature of these planets can be very diverse and includes planets which are rocky nature with a small atmosphere, planets with a substantial gas envelope, and planets with a substantial water fraction.

In this thesis, we focus on rocky exoplanets, which are all planetary bodies which are consistent with an overall rocky composition. This correlates to an average density of $\rho \lesssim 5\,\mathrm{g/cm^3}$. Within the detection errors this correlates roughly to planets with a mass of less than 8 Earth masses ($M_\oplus$) and radius of less than 2 Earth radii ($R_\oplus$).

1.1.1 Detecting exoplanets and their atmospheres

Although this thesis is working towards a theoretical understanding of the links between the rocky exoplanet surfaces and atmospheres, a background of how exoplanets can be detected is provided, as it further motivates the importance of the understanding of the link of atmospheres and planetary surfaces. Most exoplanets to date have been detected with the transit and radial velocity methods, which are briefly described in the following.

According to Kepler's laws, the planet in a stellar system is orbiting around the centre of mass of the star-planet system. As the stellar mass is much greater than the planetary mass, the orbital velocity of the planet on its orbit is also much faster than the movement of the star. However, this periodic movement with a period P of the star relative to an observer is Doppler-shifting the light from the star along the line of sight of the observer (see Fig. 1.2). The resulting observable half

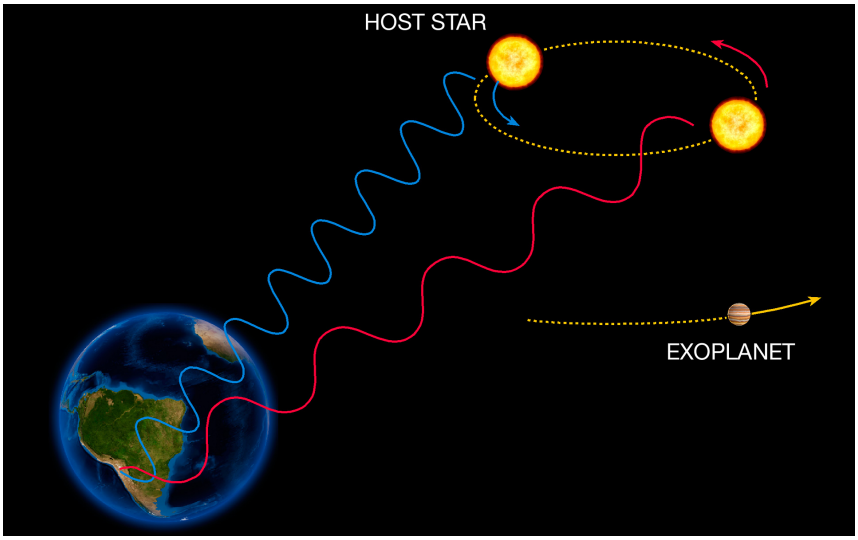

Figure 1.2: Schematic description of the radial velocity method for exoplanet detection (image credits: ESO).

amplitude of the stellar velocity K can be expressed by

$$K = \left(\frac{2\pi G}{P}\right)^{1/3} \frac{M_\mathrm{P} \sin i}{(M_\mathrm{S} + M_\mathrm{P})^{2/3}}. \tag{1.1}$$

Here, G is the gravitational constant, and M_P and M_S are the planetary and stellar mass, respectively. i is the inclination of the system towards the line of sight towards the observer. By tracking the observed frequency of spectral features, this movement can be observed and a minimum mass of the planet can be given. The exact mass can only be calculated, if the inclination of the system is known ($M_\mathrm{P} \cdot \sin(i)$). This shows that this detection method is biased towards more massive planets. Furthermore planets on shorter orbits are easier to be detected, as the star has to be observed for shorter times.

In our solar system for example the Sun's movement due to Jupiter and Earth is 12.4 m/s and 0.089 m/s, respectively, at periods of 11.86 years and 1 year, respectively.The development of high-resolution spectrographs with high thermal stability increased the precision of the measurements from 13 km/s for the early detections (Mayor & Queloz, 1995) to about 10 cm/s (e.g. ESPRESSO Pepe et al., 2021).

The second detection method is based on transits, that is if the planet is moving in between the observer and the host star and blocking some of the star's light (see Fig.1.3). The fraction of the

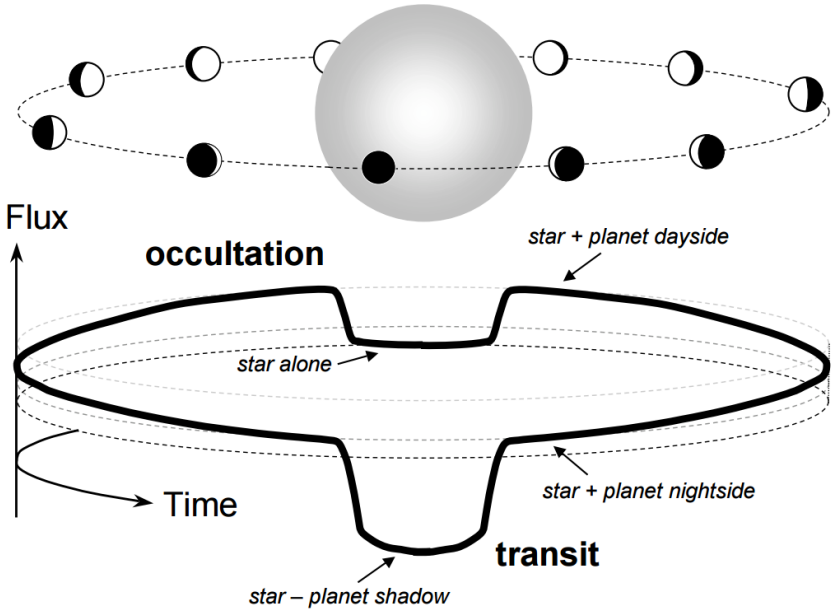

Figure 1.3: Schematic description of planetary transits and their influence on the observed flux over the course of a full planetary orbit (adopted from Winn, 2010).

light that is blocked during the primary transit is described by

$$\frac{\Delta F_S}{F_S} = \frac{R_P^2}{R_S^2}, \tag{1.2}$$

where F_S is the observed out-of-transit flux of the star , ΔF_S the flux difference of in and out-of-transit, and R_P and R_S are the planetary and stellar radii, respectively (Winn, 2010; Seager, 2010). From the periodic observation of such transits, the orbital period and planetary radius can be directly observed. As these transits only occur for inclinations with $\sin(i) \approx 1$, the combination of transit observations with radial velocity measurements can be used to precisely measure the mass and radius of the planets. Therefore the planetary bulk density can be derived, which allows the first characterisation of the nature of the planet by distinguishing the overall composition of the planet.

As the thesis at hand is working towards the theoretical understanding of the potential composition of atmospheres of rocky exoplanets, it is important to briefly introduce how these can be observed. As it is not possible to directly probe the atmospheric composition of exoplanetary atmospheres, the detection has to be done remotely, especially by investigating the transmission and emission spectra of the planet.

For the transmission spectra of the planet, the transit method is utilized. While the planet is moving in front of the host star, parts of the stellar light is in fact travelling through the atmo-

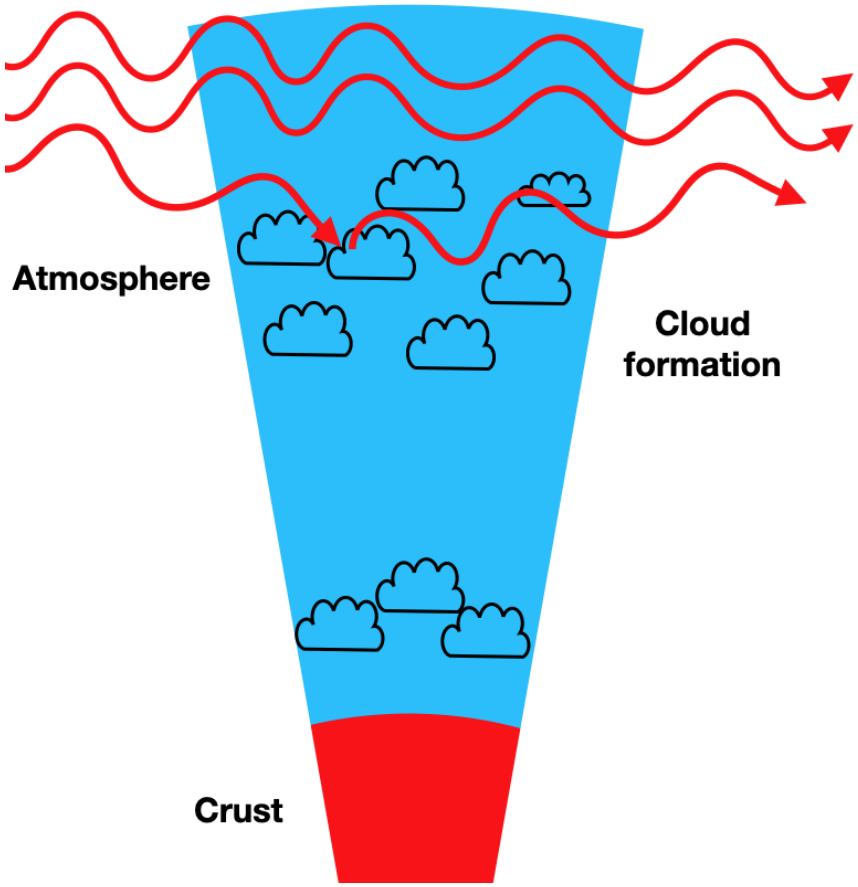

Figure 1.4: Sketch of the effect of an atmosphere during transmission spectroscopy.

sphere of the planet, where different atmospheric gases and aerosols absorb and scatter the light. Figure 1.4 shows a sketch of the influence of molecules and cloud condensates on the transmission spectrum. The observation of specific absorption features provides constraints on the composition of the atmosphere. However, the transmission spectroscopy is limited to the high atmosphere and cannot directly probe the atmosphere directly above the surface. Additional effects such as clouds and hazes can further limit the observability of gas phase features with transmission spectroscopy due to scattering of light. If the cloud layer is above the potentially observable parts of the atmosphere, the transmission spectrum will appear flat due to scattering by the cloud condensates (e.g. Kreidberg et al., 2014). Furthermore it should be noted, that with transmission spectroscopy the terminator region of the planet is investigated, which can have significantly different characteristics for the morning and evening terminator (e.g. Helling et al., 2019).

Besides the observations during the primary transit, the secondary transit, also called occultation, that is the planet moving behind the star (see Fig. 1.3), can be used to investigate the reflected and emitted light of the planet. The observed flux before and after the secondary transit consists

of the stellar and the planetary flux combined, while during the secondary transit only the stellar flux is visible. This allows to determine the reflected and emitted light of the planet itself. In the optical, this is dominated by reflected light and can provide information on the planetary albedo. The use of polarisation can in principle distinguish the reflection from molecules, clouds, rock, or ocean (Rossi & Stam, 2017, 2018). In the infrared the emission of the planet can be detected and provide the insights on the planetary temperature.

Monitoring the planetary system for the entirety of the orbit allows the investigation of the planetary phase curve. Based on this, the day-nightside difference can be directly observed. Especially for close in exoplanets, which are tidally locked, that is showing the same planetary side to the host star at all times, the information on the difference of the day- and nightside constrains the heat distribution in a potential atmosphere. For example Demory et al. (2016a) show that the day-night temperature difference of the super-Earth 55 Cnc e is $\approx$ 1300 K. In the example of the tidally locked LHS 3844 b (Kreidberg et al., 2019), the strong difference of day and nightside temperature together with the nightside temperature being at one sigma consistent with 0 K suggest the absence of an atmosphere, leaving the planet to be a bare rock - comparable to Mercury. However, Mercury does not have such a cold nightside temperature, as it is not tidally locked, but instead in a 3:2 spin-orbit resonance.

1.1.2 Future observations of atmospheres of rocky exoplanets

While the current space missions and ground based instruments allow the detection of specific gas species and some cloud compositions in atmospheres of giant exoplanets, these detections for rocky exoplanets are very limited due to the small size of the planets. With the launch of JWST (Gardner et al., 2006) in December 2021, investigations of the atmospheres of rocky exoplanets become more feasible. However, for detailed observations, in order to characterise the atmospheric composition of planets, a large number of transits need to be observed. For example, while JWST could observe CO_2 on a cloud free Trappist 1 e with only 5 transits, the observation of H_2O could need 100 transits (Wunderlich et al., 2020). If clouds are present, these numbers will increase or make the detections impossible. With future instruments this limit of detectability can be drawn to less observations of smaller planets. Here, the planned missions such as ARIEL (Tinetti et al., 2018), HabEx (Stahl et al., 2020), and LUVOIR (Bolcar et al., 2016) become of interest, as they are designed to be capable of studying the composition of atmospheres of rocky exoplanets. Ito et al. (2021) show that 10 transit observations with ARIEL of 55 Cnc e can be sufficient to distinguish

the presence of a rock vapour atmospheres from cloud free atmospheres dominated by H_2 or H_2O.

In addition to the space-based missions, also the observation possibilities with ground based instruments increase. Especially the new generation of extremely large telescopes will allow the detection of atmospheric features of rocky exoplanets from the ground (Lopez-Morales et al., 2019). Especially the high resolution spectrograph HIRES (Marconi et al., 2016) at the ELT (Gilmozzi & Spyromilio, 2007) will provide the possibility for these investigations. Furthermore, instruments like the METIS instrument at the ELT (Brandl et al., 2014) or the proposed LIFE mission (Quanz et al., 2021), should allow the direct imaging of exoplanets around nearby stars (Bowens et al., 2021) and the spectroscopic investigation of their atmospheres.

1.2 Atmospheres of rocky exoplanets

In the previous section, it has been discussed in how far atmospheres of rocky exoplanets can be detected, but in order to understand and correctly interpret these observations it is important to understand the fundamental properties of these atmospheres. Especially important are the questions of what compositions of atmospheres are to be expected and how do these form (e.g. Leconte et al., 2015; Grenfell et al., 2020; Wordsworth & Kreidberg, 2021).

During the planet formation, planets can accrete a hydrogen-dominated atmosphere from the gas in the protoplanetary disk. This so-called primary atmosphere will be subject to severe atmospheric loss for most rocky exoplanets, as they are not massive enough to keep this envelope of a low mean molecular weight atmosphere (see e.g. Sekiya et al., 1980; Stökl et al., 2015). Especially for magnetically-active stars, this atmospheric loss can be severe and remove such atmospheres very efficiently (e.g. Owen & Wu, 2016; Johnstone et al., 2019). While planets similar in size to Earth or smaller lose their primary atmosphere within ≈ 100 Myr after the protoplanetary disk has dissipated, it is possible for more massive planets to hold on to their primary atmosphere (e.g. Lammer et al., 2014).

The remaining planet can over time form a secondary atmosphere, formed by the outgassing of volatile gas species (Lammer et al., 2018; Kite & Barnett, 2020). The atmospheric composition can be diverse and is highly dependent on the planetary temperature and the evolution of the planet. During the early stages of the planetary lifetime, the planet cools down from the formation and can release steam atmospheres doinated by e.g. H_2O or CO_2 (Bower et al., 2019; Katyal et al., 2019; Nikolaou et al., 2019). The composition of the outgassed atmosphere is determined

by the composition of planet as a whole, but more specifically the magma ocean and after the formation of a planetary curst, the mantle composition (see e.g. Elkins-Tanton, 2012; Katyal et al., 2019, 2020; Spaargaren et al., 2020). After the formation of the crust, different tectonic regimes can evolve, ranging from Earth-like plate tectonics, hemispheric tectonics to stagnant lids (Greber et al., 2017; Stern et al., 2018; Schaefer & Elkins-Tanton, 2018; Dorn et al., 2018; Ortenzi et al., 2020; Meier et al., 2021; Kruijver et al., 2021; Höning et al., 2021). Especially the more active tectonic regimes can yield to large volcanic activity providing sources for atmospheric material (Gaillard & Scaillet, 2014). Especially for planets close to the host star or another planet with a large magnetic field, the planet can be heated by tidal forces or induction heating, which both can cause active volcanism on these worlds (e.g. Greber et al., 2017; Kislyakova et al., 2017). The atmosphere building from volcanism can have various different compositions including secondary atmospheres rich in H_2 (Liggins et al., 2020). Wogan et al. (2020) argue that CH_4-rich atmospheric outgassing from volcanism are expected to be accompanied by CO.

For the highly-irradiated and young planets, large parts of the planetary surface are covered with magma oceans which define the early planetary atmosphere (Hirschmann, 2012; Elkins-Tanton, 2012; Kite et al., 2016) The atmospheres of these high-temperature worlds are expected to include various metals and metal oxides (e.g. Schaefer & Fegley, 2007; Miguel et al., 2011; Schaefer et al., 2012). As at these temperatures the rock is molten and partially vaporised, this atmospheric composition is refereed to as a rock vapour atmosphere.

Such atmospheres themselves are not steady objects over time, but rather influenced by many different processes. The incoming radiation of the host star of a planet is not only driving the atmospheric loss, but also it causes photochemical reactions which can alter the atmospheric composition. This has not only influences on the gas phase composition, but also triggers the formation of hazes (photolysis-induced aerosols in the high atmosphere) especially consisting of hydrocarbons (Trainer et al., 2006; Haqq-Misra et al., 2008; Zahnle et al., 2016). Similarly, in Titan's atmosphere, hydrocarbon haze is present (Trainer et al., 2006).

Planets are inherently three-dimensional objects. Not only does the temperature of the planetary surface change depending on the latitudinal position on the planet, but also height in the atmosphere. This can have significant effects on the atmospheric composition, if the temperature differences are high enough, especially for strong day and night side differences. Furthermore, the formation of clouds is a universal concept for most planetary atmospheres (see Helling, 2019). As

a result of the condensation of clouds, the affected elements are depleted in the atmosphere with respect to the element abundances below the cloud layer. The presence of clouds has a strong influence on the observability of atmospheres of exoplanets, as a complete cloud layer provides an optical surface for the planet, whereas the real rock surface lies deeper in the atmosphere. While the cloud structure could be constrained with polarimetry (Rossi & Stam, 2017), even the presence of a partial cloud cover can provide difficulties for the detection of the planetary surface in reflected light (Teinturier et al., 2022).

1.3 Habitability of exoplanets

With the possibility of investigating a large number of diverse exoplanets, it becomes possible to attempt to answer the question of whether or not Earth is the only planet with a biosphere. For answering this question, it is necessary to ask, what life is and to investigate under which conditions such life forms (Bains, 2014). In principle, instead of being a carbon-based life form, which uses water as a solvent, life could be silicon-based and use other liquids such as ammonia as solvents (Ballesteros et al., 2019). However, as we only know of the existence of water-based life, such other forms of life are not discussed in this thesis. Therefore finding the existence of liquid water and understanding under which conditions liquid water can form on an exoplanet is a fundamental question for the search for life.

With liquid water as the most fundamental precondition for the evolution of life, the habitable zone of stars was postulated as the range of orbital distances, where the equilibrium temperature of a planet can allow the stability of liquid water (e.g. Huang, 1959; Kasting et al., 1993). However, even if a planet resides in the habitable zone of a host star, it does not mean that this planet will have liquid water present and also planets outside of the traditional habitable zone can show the presence of liquid water, especially if other mechanisms of planetary heating than stellar irradiation are present. This liquid water however, may not be present at the planetary surface, but rather in the atmosphere as clouds or underneath an icy mantle. This is reflected in our solar system, as for example Mars is believed to have had liquid water on its surface in the past, while some icy moons such as Europa and Enceladus show evidence for liquid water under their ice sheets.

While Way et al. (2016) argue that Venus could have been the first habitable planet in the solar system, models by Turbet et al. (2021) show that the evolution of Venus did not allow for the condensation of water in the planetary lifetime. This underlines the importance of understanding

the planetary cooling in order to distinguish whether a planet evolves to become habitable (Seales & Lenardic, 2021). Here, the influence of the host star is a major factor Chen et al. (2020); Locci et al. (2022); Teal et al. (2022). The stellar-activity history, especially whether the star was a fast or slow rotator, has a significant effect on the existence of a planetary atmosphere (Ribas et al., 2005; Johnstone, 2020; Bonfanti et al., 2021). An additional effect that gains importance for the long term habitability is the tectonic regime present on the planet itself (e.g. Tosi et al., 2017; Spaargaren et al., 2020).

In the following the search for different regimes of habitability in our solar system and beyond are discussed before signatures for the detection of life are summarised.

1.3.1 Search for life in our solar system and beyond

Observations of Mars with early telescopes resulted in discussions on potential structures built by a Martian form of life (Schiaparelli, 1882; Lowell, 1908). Although past investigations of the Martian surface by various landers have not revealed the existence of life forms, future missions will further investigate whether microbial life evolved on Mars, while it still had liquid water on the surface (e.g. Vago et al., 2017). On Earth, Mars analogue studies have investigated environments similar to those of past Mars in order to understand the extreme conditions in which life can thrive and whether life on past-Mars would have been possible when liquid water was present (e.g. Moreras-Marti et al., 2021; Shen et al., 2021).

It has also been discussed whether the formation of life was ever possible on Venus. While Krissansen-Totton et al. (2021) suggest that Venus might have been the first planet in our solar system, where habitable conditions evolved on the surface, other studies focussed on the potential of existing life forms in Venus' clouds (e.g. Morowitz & Sagan, 1967). This possibility has been more recently discussed after the controversial tentative discovery of PH_3 in the clouds of Venus (Greaves et al., 2021), which sparked many discussions on its existence (e.g. Snellen et al., 2020; Lincowski et al., 2021), and its origin under the assumption of its actual presence. (Bains et al., 2021) discussed that there is no process known capable of abiotically producing a sufficient amount of PH_3 to give a feature of the observed strength. Omran et al. (2021) further discuss the phosphine production on rocky exoplanets in broader terms. Assuming the production by some kind of life forms, this would introduce a biosphere which is only present in the cloud layer. Individual organisms in this 'aerial biosphere' would need to remain afloat for long enough to metabolize and reproduce, before eventually falling towards the surface of Venus (Seager et al., 2021a,b;

Patel et al., 2022). One hurdle for the existence of such an aerial biosphere is the formation of life without a surface. However, such an origin of life in water droplets in the atmosphere has been discussed previously (e.g. Woese, 1979).

Besides the rocky planets in our solar system, there is also a discussion on life forming on icy moons in our solar system (e.g. Reynolds et al., 1983; Vance et al., 2007; Taubner et al., 2020). Especially the ice-covered Jupiter moon Europa will be investigated in depth with ESA's JUICE (Grasset et al., 2013) and NASA's Europa Clipper (Phillips & Pappalardo, 2014) missions in the future. Additionally, Enceladus and Titan are interesting moons for the understanding of the formation of life (Tjoa et al., 2020; Vance & Melwani Daswani, 2020; Marusiak et al., 2021). It has been proposed, that the presence of CH_4 in the plumes of Enceladus could be cause by methanogenic processes (Affholder et al., 2021). Methanogenesis describes the CH_4 production by microbes.

Besides these worlds in our solar system, an increasing amount of environments unlike anything in our solar system have been detected. These worlds show large differences in planetary mass, but also the extent of the atmosphere. These also raise the question whether life could evolve in any of these scenarios. Especially the increased surface area of planets larger than Earth could provide more scenarios for the formation of life and therefore make such a planet more likely to be habitable than an Earth-like planet (Heller & Armstrong, 2014; Del Genio et al., 2019; Schulze-Makuch et al., 2020). However, while some of these planets can be expected to be partially covered with water and show exposed land, others will potentially show an overabundance of water, which results in an ocean covering the entire surface of the planet. Especially if this global ocean is deep, it can have significant implications for life (Noack et al., 2016; Kite & Ford, 2018), similar to those for the icy moons.

A further assumption for habitability is the presence of an atmosphere on the planet, which becomes easier for a more massive planet to retain. Therefore super-Earths (planets with significantly more mass than Earth, but still a rock-like surface) could provide abundant possibilities for planets with atmospheres and liquid water on the surface. However, for larger planets, this atmosphere may be of primordial composition, as the atmosphere could not be lost (Lammer et al., 2014).

Besides these planets directly, also some exoplanets should have moons orbiting them (Kipping et al., 2012). These so called exomoons could, similar to the icy moons in our solar system,

provide potentially-habitable environments (e.g. Heller & Barnes, 2013; Zollinger et al., 2017; Martínez-Rodríguez et al., 2019). However, these candidates for habitability are even harder to investigate remotely than exoplanets themselves.

As mentioned above for the case of Venus, life in an aerial biosphere could in principle be possible. This allows the principle chance for habitability on any planet which has thermally stable clouds of liquid water. Here, especially the planetary class of sub-Neptunes are of interest, as their atmospheres could host such environments (see Seager et al., 2021b). The presence of liquid water clouds in the atmosphere of the planet K2-18 b is discussed (Benneke et al., 2019; Charnay et al., 2021).

1.3.2 Biosignatures

The search for existing or extinct life in our solar system can be carried out in situ, whereas life on other planets can only be observed indirectly (Fujii et al., 2018; Schwieterman et al., 2018). Here, we focus on the influence of life forms on the atmospheric composition. These signatures of biology are generally referred to as biosignatures. On Earth, the N_2-O_2 dominated atmosphere with the presence of CH_4 is a result of the presence of biology and therefore a biosignature in our atmosphere. However, Earth's atmospheric composition has changed significantly over time, especially with the emergence of methanogenesis (methane production of microbes) and the great oxidation event (GOE), which caused the appearance of oxygen as a major atmospheric species on Earth (e.g. Holland, 2002; Catling & Claire, 2005; Ueno et al., 2006; Claire et al., 2006; Stüeken et al., 2016; Zahnle et al., 2019; Gregory et al., 2021).

In order to understand the presence of any atmospheric molecule, the abiotic production of it has to be ruled out. For example Meadows (2017) and Meadows et al. (2018) have worked on understanding the pathways to abiotic production of O_2 in order to understand under which conditions the detection of O_2 can be a biosignature. Similar approaches have been made to understand the presence of N_2 (Lammer et al., 2019), NH_3 (Huang et al., 2021), or CH_4 (Wogan et al., 2020) as biosignatures, while other studies focussed on understanding the abiotic production processes of for example CH_4 (Guzmán-Marmolejo et al., 2013) or O_3 Domagal-Goldman et al. (2014). However, these molecules are investigated as biosignatures, as they are dominant in Earth's atmosphere and therefore biased by our own environment. In order to understand which molecules are potential biosignatures in different environments, an extended list of molecules has to be investigated by understanding their production processes (Seager et al., 2016; Catling et al.,

2018). Especially atmospheric compositions, which are possible in chemical equilibrium should be excluded as biosignatures (Seager et al., 2013b). Based on this approach phosphine has been diagnosed to be a potential biosignature for anoxic life forms on rocky planets (Sousa-Silva et al., 2020).

Besides the investigation of individual molecules, some research focusses on the coexistence of multiple molecules as biosignatures. Discussed examples are the presence of N_2+O_2 (Sproß et al., 2021) or CO_2+CH_4 with a lack of CO (Krissansen-Totton et al., 2019; Mikal-Evans, 2021). However, also these atmospheric gas mixtures have to be understood in their surrounding to avoid false positives (see Chapter 3 and Woitke et al. (2021) for a discussion of the possibilities of the coexistence of CH_4 and CO_2 in chemical equilibrium). This underlines again the importance of the context of the planetary surrounding for the understanding of biosignatures (Krissansen-Totton et al., 2022). For example in hydrogen dominated atmospheres, the potential signatures of life can be expected to differ from signatures by Earth-like biospheres (Seager et al., 2013a,b).

In addition to the understanding of which atmospheric gas species could be produced by life, the investigation and understanding of the principles of the formation of life can be used to determine which planetary environments are suitable for the formation of simple life forms. Therefore we briefly discuss potential pathways that can lead to the formation of pre-biotic molecules from which simple life forms could evolve.

In the literature different pathways to the formation of pre-biotic molecules have been discussed. Experiments dating back to Miller (1953) and Miller & Urey (1959) have shown that, especially under reducing conditions, it is possible to form amino acids from electrical discharges. These reactions triggered by for example lightning can also be made possible by high-energy photons from the stellar irradiation or cosmic radiation (Ranjan et al., 2021; Barth et al., 2021). The most important elements which need to be present for the formation of pre-biotic molecules, are carbon, hydrogen, nitrogen, oxygen, phosphorus, and sulphur (in the following called CHNOPS elements) (Horneck et al., 2016). One example for the production processes which leads to pre biotic molecules is HCN, which can be a result of lightning if N_2 and CH_4 are present (Hodosan et al., 2017; Pearce et al., 2022). The presence of this molecule is necessary for the further precursor of amino acids (Ferris et al., 1978) and nucleobases (Ferus et al., 2017). Additionally, ribonucleic acid (RNA) precursors can be produced with UV radiation if HCN and H_2S are present (Patel et al., 2015). While the original works by Miller and Urey did not include any sulphur source, it

has been shown that the presence of H_2S to reactions in the Miller-Urey-like experiments enhance the production of amino acids (Parker et al., 2011). Another example of the formation of pre-biotic molecules is the production of HC_3N on super-Earths rich in nitrogen and an overall reduced atmospheric composition (Rimmer et al., 2021b). While phosphorus is the limiting factor for the extent of the biosphere on Earth (Syverson et al., 2021), phosphates are necessary for the formation of some life precursors (Cafferty et al., 2016).

Another possibility to form life could potentially be in the atmosphere itself in form of an aerial biosphere. This concept enlarges the possibilities for 'habitable' environments from water surfaces to planets with liquid water clouds in the planets. As this does not necessarily have to have a surface in the traditional sense, this could also be providing habitable environments on temperate sub-Neptunes. See Seager et al. (2021b) for an in depth discussion on such worlds. It should be noted, that in such atmospheric environments heavier elements are lacking, which could be crucial for many aspects of the metabolism of life or the formation of life itself.

Besides the detection of certain molecules in the atmosphere, also broader features have been discussed as detection possibilities of life on exoplanets. The presence of large-scale vegetation on the surface of Earth results in a distinct feature in emission spectra of Earth, known as the 'vegetation red edge' (Sagan et al., 1993). The detection of such a feature could be a direct detection of life although the presence of extended cloud cover on the planet in question could be challenging for the detection itself (Seager et al., 2005; Sterzik et al., 2012). The wavelength at which this feature of exovegetation is to be expected is a function of the stellar spectrum, as life is expected to evolve to be optimized for the given host star (Tinetti et al., 2006). While this detection would indicate plant based life, other potentially possible detection methods for highly-evolved life forms are potentially including the detection of artificial light emission from the nightside (Beatty, 2022) and technosignatures (Pinchuk et al., 2019).

1.4 Modelling planetary atmospheres in chemical equilibrium

In order to allow for the investigation of the large parameter space necessary to understand the compositional diversity of exoplanets, all investigated atmospheres are considered to be in chemical equilibrium. The chemical phase equilibrium allows the study of the condensate phase of the planetary crust as well as thermally stable cloud condensates. The models presented in this thesis are based on the equilibrium chemistry solver GGchem (Woitke et al., 2018) and the principal

concepts used for the calculation of these chemical phase equilibria are described in this section.

The chemical equilibrium of a gas phase describes the system of gas phase particles (molecules, atoms, and ions) at a given pressure p and temperature T which is most stable. Such a system has reached the minimum of Gibbs free energy of formation ΔG_f, which is given by

$$\Delta G_f = \Delta H_f - T\Delta S, \tag{1.3}$$

where ΔH_f is the enthalpy of formation, T the temperature of the system, and ΔS the entropy. The enthalpy of formation of a given gas-phase molecule is described by the atomisation energy E_a, that is the energy that is required for transforming the molecule in the individual atoms. For example for H_2O[g], this leads to

$$E_a(H_2O) = 2\Delta H_f(H) + \Delta H_f(O) - \Delta H_f(H_2O). \tag{1.4}$$

For cold temperatures, the enthalpy term of the Gibbs free energy dominates over the entropy and minimising the Gibbs free energy is essentially minimising the enthalpy of formation. As a result, the energetically-favourable composition for colder temperatures becomes purer, meaning that fewer components are present. Similarly for higher temperatures, where the entropy is of higher importance, trace gases become increasingly important. The minimisation of the total Gibbs free energy of the system is used in numerical models by for example Ackerman & Marley (2001), Miller-Ricci et al. (2009), or Blecic et al. (2016). Equivalently to directly minimising the Gibbs free energy of the system, the law of mass action can be used. Examples, where this approach has been used are Tsuji (1973), Stock (2008), Bilger et al. (2013), and Woitke et al. (2018). The system of equations resulting from the second approach can be solved more efficiently than the minimisation of the Gibbs free energy of the system.

In order to describe the functionality of the approach used in GGchem, we consider an arbitrary molecule ($A_aB_bC_c$) made of the different elements A, B, and C with stoichiometric factors a, b, and c. For example, for a molecule such as H_2SO_4 this translates to A, B, and C representing the elements H, S, and O. The stoichiometric factors a, b, and c therefore are equal to 2, 1, and 4, respectively. Following Berline & Bricker (1969), Guldberg's law of mass action for such a

molecule can be written as

$$\frac{p_{\mathrm{A}_a\mathrm{B}_b\mathrm{C}_c}}{p^\circ} = \left(\frac{p_\mathrm{A}}{p^\circ}\right)^a \left(\frac{p_\mathrm{B}}{p^\circ}\right)^b \left(\frac{p_\mathrm{C}}{p^\circ}\right)^c \exp\left(-\frac{\Delta G_f^\circ}{RT}\right). \tag{1.5}$$

Here, p° is the reference pressure, while p_i are the atomic pressures, and R is the ideal gas constant. ΔG_f° is the Gibbs free energy of formation of the molecule $\mathrm{A}_a\mathrm{B}_b\mathrm{C}_c$ at standard pressure. It can be expressed by the Gibbs free energies of the neutral atoms

$$\Delta G_f^\circ = G^\circ\left(\mathrm{A}_a\mathrm{B}_b\mathrm{C}_c, T\right) - aG^\circ(A,T) - bG^\circ(B,T) - cG^\circ(C,T). \tag{1.6}$$

where $G^\circ(k,T)$ is the Gibbs free energy of the elements k in the gas phase. The rearrangement of Eq. 1.5 to

$$p_{\mathrm{A}_a\mathrm{B}_b\mathrm{C}_c} = k_p\left(\mathrm{A}_a\mathrm{B}_b\mathrm{C}_c, T\right) p_\mathrm{A}^a p_\mathrm{B}^b p_\mathrm{C}^c, \tag{1.7}$$

allows the introduction of equilibrium constants k_p as

$$k_p\left(\mathrm{A}_a\mathrm{B}_b\mathrm{C}_c, T\right) = \left(p^\circ\right)^{1-a-b-c} \exp\left(-\frac{\Delta G_f^\circ}{RT}\right). \tag{1.8}$$

In cgs-units, these equilibrium constants have the unit of $[\mathrm{dyn/cm^2}]^{1-a-b-c}$. The element conservation of the gas phase can be given as

$$\epsilon_k n_{\langle H\rangle} = \sum_i s_{i,k} n_i, \tag{1.9}$$

where ϵ_k is the hydrogen normalised abundance of the element k, $n_{\langle H\rangle}$ the total hydrogen nuclei density, $s_{i,k}$ the stoichiometric factor of element k for the gas particle i. With the gas-particle density n_i and gas-particle mass m_i, the gas density ρ is defined by

$$\rho = \sum_i m_i n_i. \tag{1.10}$$

Using Eq. 1.9, allows the elimination of the gas-particle densities from the gas density, in favour of element abundances. It follows that

$$\rho = n_{\langle H\rangle} \sum_k m_k \epsilon_k, \tag{1.11}$$

with the elemental mass m_k for the element k. The total gas pressure p is

$$p = \sum_i p_i = \sum_i n_i k_\mathrm{B} T, \tag{1.12}$$

where k_B is the Boltzmann constant. As the total particle density $n = \sum_i n_i$ and mean molecular weight $\mu = \sum_i m_i n_i / n$ are dependent on density and temperature, the pressure can also be written as

$$p = n(\rho, T) k_\mathrm{B} T = \frac{\rho k_\mathrm{B} T}{\mu(\rho, T)}. \tag{1.13}$$

This allows the elimination of all particle densities from the element conservation equations given in Eq. 1.9, resulting in a set of K equations, where K is the number of elements k. These results only depend on the T, $n_{\langle H \rangle}$, and the set of ϵ_k.

In order to describe the interaction of the atmosphere with the planetary crust and cloud condensates, we use the chemical phase equilibrium. The thermal stability of a condensate j[cond] with a directly corresponding gas phase particle j[gas] is defined by the supersaturation ratio S_j, which is given by the temperature-dependent vapour pressure p_j^vap and the partial pressure of the gas phase of the condensible p_j by

$$S_j = \frac{p_j}{p_j^\mathrm{vap}(T)}. \tag{1.14}$$

The vapour pressure itself is given by the Gibbs free energies as

$$p_j^\mathrm{vap}(T) = p^\circ \exp\left(\frac{G^\circ(j[\mathrm{cond}], T) - G^\circ(j[\mathrm{gas}], T)}{RT}\right). \tag{1.15}$$

For the investigation of the crustal composition of rocky exoplanets, the thermal stability of minerals is of fundamental importance. As most minerals have no corresponding molecule in the gas phase, Eq. 1.14 is not defined. Therefore a fictive gas phase molecule j[gas], with the same stoichiometric composition as the condensate, is assumed, which has the unknown G° (j[gas], T). Using Eqs. 1.7, 1.14, and 1.15 the unknown Gibbs free energy can be cancelled out and the generalised supersaturation ratio of

$$S_j = \prod_k \left[\left(\frac{p_k}{p^\circ}\right)^{s_{j,k}}\right] \exp\left(-\frac{\Delta G_f^\circ(j[\mathrm{cond}], \mathrm{T})}{RT}\right) \tag{1.16}$$

can be derived. Analogue to Eq. 1.6, the Gibbs free energy of formation is given as

$$\Delta G_f^\circ = G^\circ\left(j[\text{cond}], T\right) - \sum_k s_{j,k} G^\circ(k, T). \tag{1.17}$$

The calculation of the supersaturation ratio can result in three different regimes:

1) $S_j < 1$: condensate is not stable;

2) $S_j = 1$: condensate is stable and present;

3) $S_j > 1$: not possible in phase equilibrium, as condensation should occur.

As a result of this limit in supersaturation and Eq. 1.14, the partial pressure of every gas phase particle which has a directly corresponding condensate, is limited by the vapour pressure at any temperature.

Further details on the numerical calculation of the gas phase equation are described in Woitke et al. (2018). For a detailed description on the numerical processes of the condensation see appendix B in Helling et al. (2008).

The models for planetary atmospheres presented throughout this thesis assume chemical and phase equilibrium between the near-crust atmosphere and the crust. By the construction of these models, processes driving the atmosphere away from equilibrium are not included. In particular this includes material delivery by impactors and geological processes like volcanic outgassing and crustal recycling. Furthermore, solubility of gas species in liquid species are not included. Especially for the magma ocean stage, significant amounts of gaseous species can be stored in the liquid magma ocean (e.g. Nikolaou et al., 2019; Lichtenberg et al., 2021). Another aspect beyond the scope of this thesis is the effect of stellar irradiation on the atmospheres of the planetary atmospheres. This will not only change the atmospheric composition by photochemical reactions, but also drive atmospheric loss. However, the investigation of planetary atmospheres in chemical equilibrium does allow investigations of the influence of different element abundances on the atmospheric composition.

1.5 Research Question

The motivation for the research undertaken during this thesis is given by the curiosity of the compositional diversity of rocky exoplanets, how surface compositions can be confined by observables and what characterises planets suitable for the formation of life.

The overarching question of planetary diversity can be split into questions of what surface compositions can be present on different planets and which gases and cloud condensates are to be expected in the atmospheres of these planets with different surfaces. This further leads to the question in how far it is possible to characterise the different planetary atmospheres.

A good theoretical background of the fundamental characterisation possibilities of the diversity of rocky exoplanets can allow for the finding of specific observable features, which can constrain the surface and atmospheric conditions. At this point, 'observable features' are defined broadly by gas species present in the higher parts of the atmosphere and the highest cloud condensates in a given atmosphere. The further investigation of which of these features can be observed with a current or future instrument on a given planet is another step to be investigated and undertaken in the future. However, in order to prepare for such observations, it is necessary to understand the diversity of planets which is to be expected based on theoretical models.

As many models show the presence of liquid water somewhere in their atmosphere, it provides the question what the surrounding composition of the atmosphere is. Is it common to have conditions favourable for the formation of life? If not, what are the limiting factors for the formation of life?

1.6 Structure of this thesis

The work in this thesis is working towards understanding the diversity of atmospheres of rocky exoplanets and the possibility of constraining the surface conditions of a rocky exoplanet by investigating the observable higher atmosphere. In Chapter 2, the variation of the crust and near-atmosphere composition based on different element compositions is discussed. In Chapter 3 atmospheric types based on atmospheres composed of CHNO are described. Based on the bottom-to-top atmospheric models presented in Chapter 4 the chemical environment of water condensates is investigated with respect to implications on habitability (Chapter 5). This thesis is summarised in Chapter 6 and an outlook is given in the final Chapter 7.

”Ec man iotna, ár um borna,
þá er forðom mic fædda hofðo;
nío man ec heima, nío íviði,
miotvið mæran fyr mold neðan.”
I remember yet the giants of yore,
Who gave me bread in the days gone by;
Nine worlds I knew, the nine in the tree
With mighty roots beneath the mold.

- Voluspá

2

Outgassing of common rock and the stability of liquid water

The work presented in this chapter investigates the composition of the outgassed atmospheres in chemical and phase equilibrium with the planetary crust. Total element abundances of various different compositions inspired by common rocks are investigated over a large temperature and pressure range. The results are compared to previous studies and especially analysed with respect to the stability of liquid water as a condensate.

The work has been published as ‘The atmospheres of rocky exoplanets I. Outgassing of common rock and the stability of liquid water’ by O. Herbort, P. Woitke, Ch. Helling, and A. Zerkle in Astronomy & Astrophysics 636, A71 (2020).

2.1 Introduction

After the first detections of exoplanets around the pulsar PSR B1257+12 by Wolszczan & Frail (1992), and the main sequence star 51Peg by Mayor & Queloz (1995), more than 5000 exoplanet detections have been confirmed to date[1]. Until recently, the overwhelming majority of the exoplanets found were gaseous giant planets in close orbits to their host stars.

In recent years, it became possible to detect exoplanets of rocky composition in the habitable zones of their host stars, mostly M dwarfs. Notable detections are the planets around our closest star Proxima Centauri (Anglada-Escudé et al., 2016), Barnard's star (Ribas et al., 2018) and the seven-planet system around Trappist 1 (Gillon et al., 2017). Even though these planets are in close orbits to their host stars, their equilibrium temperatures are lower than 500 K due to the low effective temperatures of their host star. Turbet et al. (2016) showed for Proxima Centauri b that liquid water can be present and might be detectable in the future. On the other hand, rocky exoplanets with short orbital periods around solar-type stars such as 55 Cnc e (McArthur et al., 2004) or CoRoT-7b (Léger et al., 2009) have temperatures on the day side of $T_{\rm eq} \approx 2400$ K (Léger et al., 2011; Demory et al., 2016b). This temperature is high enough to melt the surface of the planet on the dayside, while the nightside remains solid (magma pond; Kite et al., 2016). During the formation of terrestrial planets the surface can melt and cause a global magma ocean with a mass-dependent depth (Elkins-Tanton, 2012). For short orbital periods and host stars with extensive magnetic fields, this magma ocean can prevail due to inductive heating (Kislyakova et al., 2017).

To date, it is impossible to determine whether the surface material has been processed by plate tectonics or by radiation and stellar winds on an exposed surface only. For planets with enough heat from e.g. stellar irradiation, inductive heating or tidal forces, an active mantle can prevail that causes active surface processing like volcanism or plate tectonics. Planetary structure modelling suggests that hot Super-Earths like 55 Cnc e have high atmospheric abundances of refractory elements such as Ca and Al (Dorn et al., 2019). These atmospheres are shown to allow the formation of mineral clouds (Mahapatra et al., 2017).

The number of rocky exoplanets whose atmospheres have already been spectroscopically analysed is very small. However, in the near future the number of exoplanet atmospheres in reach for detailed analysis will increase because of spectrographs with high spectral resolution in the near

[1] http://exoplanet.eu/catalog/

infrared (e.g. CARMENES (Quirrenbach et al., 2012), CRIRES+ (Follert et al., 2014)), the 30 m telescopes and space missions like JWST and ARIEL. These instruments will allow the analysis of the atmospheric composition of nearest rocky exoplanets with unprecedented precision.

Current studies have revealed a large diversity in the composition of rocky exoplanets, see `http://exoplanet.eu` and Fig. 1 in Kaltenegger (2017). It seems reasonable to expect a comparably large diversity with respect to their atmospheres (Leconte et al., 2015). The study of exoplanet atmospheres has so far been focused on gas giants (Désert et al. 2008; Snellen et al. 2010; Nikolov et al. 2018; Arcangeli et al. 2018; Salz et al. 2018) due to observational limitations. Kreidberg et al. (2014) observed the super-Earth GJ 1214 b and showed that the analysis of the atmosphere's chemical composition is frustrated by clouds. Atmospheres of exoplanets have been observed to be generally affected by cloud formation (for a recent review see Helling, 2019).

In what follows, we investigate the atmospheric gas ('near-crust atmosphere') that forms above a surface made of a mixture of solid and liquid materials under certain thermodynamic conditions and for different sets of element abundances. We assume thermo-chemical equilibrium for the molecules in the gas phase and phase equilibrium for the condensates in contact with that gas. Our approach is to study the atmospheric gas in contact with the rocky planet's crust and derive the gas composition immediately above the crust. Schaefer et al. (2012) have presented a similar approach, and Miguel (2018) used the thermo-chemical equilibrium code TEA (Blecic et al. 2016) to discuss the atmospheric gas composition of the potential magma-ocean dayside of 55 Cnc e. All studies assume that the near-crust atmospheric gas had enough time to reach local thermodynamic equilibrium (LTE) with the planetary crust.

We apply the equilibrium code GGchem (Woitke et al., 2018) which enables us to calculate the thermo-chemical equilibrium chemistry for gases and condensates in phase equilibrium to temperatures as low as 100 K. GGchem has been benchmarked against TEA by Woitke et al. (2018). GGchem also allows us to investigate the stability of liquid and solid water at low temperatures. Woitke et al. (2018) have shown that phyllosilicates (sheet minerals which incorporate OH groups into their lattice structure) become stable below about $500 - 700$ K in a solar composition gas in phase equilibrium at $p = 1$ bar, which then in fact interferes with the stability of liquid water. Such clay materials can form on the timescales of days on Earth (e.g. Velde, 1995, and references therein). We note that such phyllosilicate materials form already in planet-forming disks (Thi et al., 2020) and may contribute substantially to the water delivery to Earth.

We benchmark our code against earlier work by Sharp & Huebner (1990) and compare our results with Schaefer et al. (2012). Different planets in different stellar environments and in different evolutionary states will also differ in their elemental composition which is crucial for the composition of the atmosphere. We study the effect of different sets of total element abundances.

We utilize total element abundances informed by geological studies on Earth, Continental Crust (CC), Bulk Silicate Earth (BSE), and Mid Oceanic Ridge Basalt (MORB), and those informed by astronomical studies, solar abundances, carbonaceous chondrites of the CI group (CI) and abundances deduced from Polluted White Dwarf observations (PWD). A wide range of pressures (0.001 bar to 100 bar) and temperatures (100 K to 5000 K) is considered. Kinetic effects and geological processes such as plate tectonics and volcanism are not included in our model, and we assume that our system had always enough time to reach the thermo-chemical equilibrium after it may have been affected by momentary disequilibrium events like volcanism etc.

In Sect. 2.2 we briefly describe the GGchem code that is used in this work. A detailed comparison to previously published results is provided in Sect. 2.3 for element abundances of CC and BSE. Sect. 2.4 presents additional results for MORB, CI chondrite and PWD abundances. In Sect. 2.5, the stability of liquid water is studied by modifying the BSE composition to see by how much the content of gaseous atmospheric water needs to increase for liquid water to be present eventually. The effect of the atmospheric pressure on the thermo-chemical equilibrium is discussed in Sect. 2.6. Sect. 2.7 focuses on the estimation of timescales at which the chemical equilibrium is reached. In Sect. 2.8 we conclude with a discussion. At the end of this chapter a glossary of structural formulae for some condensed species is provided (Tab. 2.1).

2.2 Method: Phase equilibrium with GGchem

We use the thermo-chemical equilibrium code GGchem (Woitke et al., 2018). Based on the principle of minimisation of the total Gibbs free energy the chemical equilibrium for the molecules in the gas phase and phase equilibrium for the condensates is solved. A short summary is provided here. For more details see (Woitke et al., 2018).

Figure 2.1 shows the basic procedure: A set of elements $k = 1, ..., K$ is selected, their abundances with respect to hydrogen, ϵ_k^0, are henceforth called the *total element abundances*. Based on gas pressure p, gas temperature T and ϵ_k^0, GGchem determines the stable condensates, calculates their abundances (which results in the abundance of condensed elements $\epsilon_k^{\rm cond}$) and calculates the

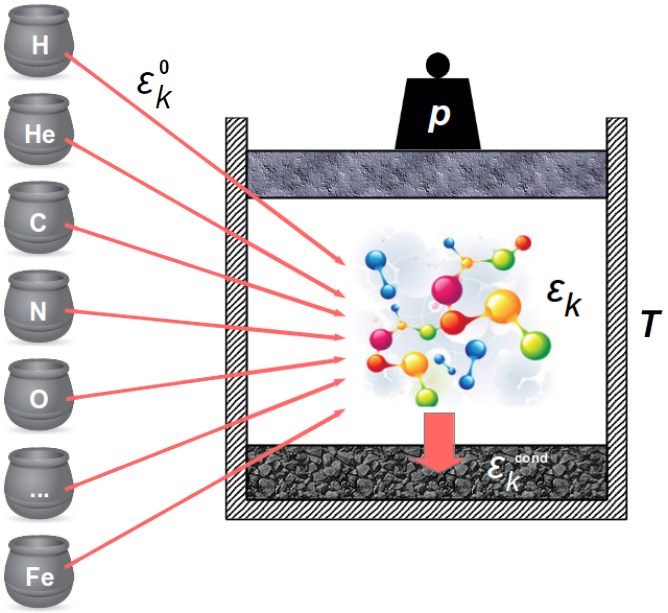

Figure 2.1: The principle modelling procedure of GGchem: Elements are selected and included with given total abundances ϵ_k^0. GGchem calculates the equilibrium gas phase and condensate abundances at given gas pressure p and temperature T, providing the element abundances contained in the condensates ($\epsilon_k^{\rm cond}$) and the remaining gas phase (ϵ_k).

ion, atom and molecular concentrations in the gas (which results in the element abundances left in the gas phase ϵ_k). Condensates $j = 1, ..., J$ are considered stable and present in their condensate form if their supersaturation ratios are unity $S_j = 1$, whereas all other condensates are unstable and not present, i.e. $S_j < 1$. The conservation of elements $\epsilon_k^0 = \epsilon_k + \epsilon_k^{\rm cond}$ is obeyed for all elements k. The resulting abundances of all gas and condensed phase species obey the conditions of chemical and phase equilibrium.

In many astrophysical objects, such as AGB star winds, brown dwarf atmospheres or protoplanetary discs, the majority of elements remains in the gas phase, i.e. $\sum \epsilon_k^0 \approx \sum \epsilon_k \gg \sum \epsilon_k$. However, for most applications considered in this chapter, such as a gas in contact with a hot planetary crust, only a small fraction of the elements ($10^{-1}...10^{-5}$) will actually remain in the gas phase, depending on the temperature, i.e. $\sum \epsilon_k^0 \approx \sum \epsilon_k^{\rm cond} \gg \sum \epsilon_k^{\rm cond}$. Therefore, the vapour pressure of stable condensates is a major component for the composition of the gas.

GGchem combines different thermo-chemical data sources. For the molecular equilibrium constants, $k_p(T)$, we use Stock (2008) and Barklem & Collet (2016), complemented by some new fits to the NIST/JANAF database (Chase et al., 1982; Chase, 1986, 1998). The condensed phase data $\Delta G_{\rm f}^0(T)$ is taken from SUPCRTBL (Zimmer et al., 2016) and NIST/JANAF. These datasets allow us to calculate the concentrations of all atoms, ions, molecules and condensed phases in

chemical equilibrium for a mixture of up to 41 elements (hydrogen to zirconium, and tungsten). The actual number of gas-phase species and condensates depends on the selection of elements and will be stated in the corresponding sections for the different calculations.

Phase-equilibrium models can generally provide only a very simplified and limited approach to describe the occurrence of condensates in gases, and the nature of gases above solid surfaces, especially when low temperatures are considered, where both the outgassing and the deposition rates are small. No kinetic rates are considered, and the relaxation timescale toward chemical and phase equilibrium cannot easily be discussed. For example, the atmosphere of a rocky planet is in contact with the crust partly on the hot dayside and partly on the cold nightside. Other processes are not considered, such as cloud formation, photo-dissociation and cosmic ray induced processes, volcanism, etc. Still, equilibrium models can provide a first understanding and can be used to inform more ambitious kinetic condensation models, for example, about the choice of condensates.

2.3 Comparison to previous phase equilibrium models

We compare the phase-equilibrium results obtained with GGchem to previous equilibrium condensation models published by Sharp & Huebner (1990) and Schaefer et al. (2012) in the following Sects. 2.3.1 and 2.3.2, respectively. The paper by Sharp & Huebner (1990) includes sufficiently detailed information about the selection of molecules and condensates, and their thermo-chemical data, that allow us to benchmark our results. For Schaefer et al. (2012), we do not exactly know their choice of molecules and condensates, nor their thermo-chemical data applied, so we broadly compare our results, and identify the differences between the two models.

2.3.1 Sharp & Huebner

Sharp & Huebner (1990) used a numerical method that directly minimises the total Gibbs free energy of gas phase and condensed phase species. GGchem uses a different numerical method, for details see Woitke et al. (2018) and Sect. 1.4, so the aim of this section is mainly to verify our numerical approach. Therefore the chosen elements, element abundances (Tab. 2.2) and the thermo-chemical data for the gas and condensate species are exactly as described in Sharp & Huebner (1990). Thus both codes use the same 18 elements (H, C, N, O, F, Na, Mg, Al, Si, P, S, Cl, K, Ca, Sc, Ti, V, Cr, Mn, Fe, Ni, Cu and Zr) with 165 gas species and 62 solid condensed species. As in Sharp & Huebner (1990), the pressure is set to 0.5 mbar and the temperature ranges

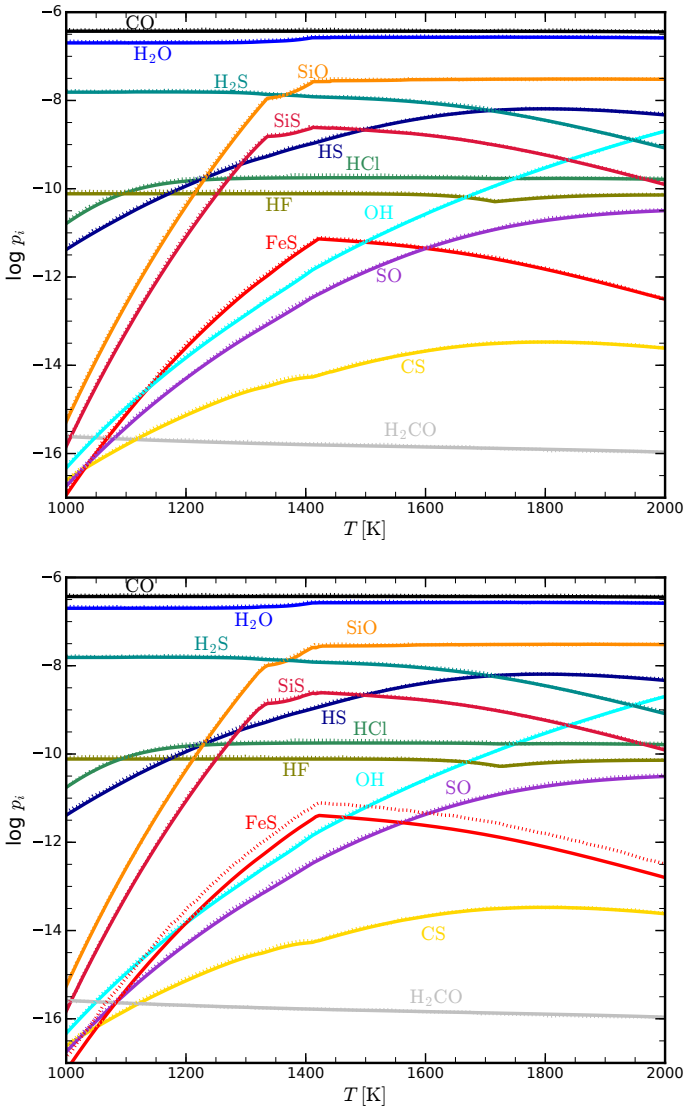

Figure 2.2: Comparison of molecular partial pressures computed by GGchem (solid lines) to the results by Sharp & Huebner (1990, dotted lines). Calculations are based on the solar element abundances listed in Sharp & Huebner (1990) for a constant pressure of $p = 0.5$ mbar. The shown elements are chosen to match Fig. 1 in Sharp & Huebner (1990). **Upper panel:** GGchem only uses the molecules and condensates selected by Sharp & Huebner (1990) and applies their thermo-chemical data, **Lower panel:** GGchem uses all molecules and condensates found in its own database and uses its own thermo-chemical data. The agreement is very good. The only visible difference is in FeS, which is slightly depleted in the lower panel.

from 1000 K to 2000 K.

In Fig. 2.2, the resulting GGchem molecular partial pressures are shown, with the Sharp & Huebner results over plotted as dashed lines. The graphs from Sharp & Huebner's Fig. 1 have been digitised from an electronic version of their paper. Within the precision of that digitising process, our results are identical. In addition, the 'appearance and disappearance temperatures' of the condensates listed in Table 3 of Sharp & Huebner (1990) agree within ±1 K with our results. This demonstrates that our numerical method produces equivalent results for both, condensates

and molecules.

In the lower panel of Fig. 2.2, we have applied the full GGchem dataset for molecules and condensed species to the same selection of elements and their abundances, resulting in 388 gas-phase and 204 condensed species, 35 of them being liquids. The results are still very close, with FeS being the only molecule with relevant concentrations that shows a lower concentration compared to the results by Sharp & Huebner (1990). This is caused by the additional occurrence of FeH as a gas phase species, which was not included in Sharp & Huebner (1990). Additional differences in the selection of molecules and condensates are as follows: All gas species and condensates in Sharp & Huebner (1990) are also considered in the full GGchem model. We find that SiO[s], $ZrSiO_4$[s], $CaTiSiO_5$[s] and $MgCr_2O_4$[s] become stable condensates, while $MgTi_2O_5$[s] and Cr_2O_3[s] are not becoming stable. In the gas phase of these two models, the major difference is that our CrH and CuH concentrations differ by more than one order of magnitude. This is caused by the stability of the additional gas phase species NiCl, TiF_3, $TiOF_2$, $TiOCl_2$, TiOCl, AlF_2O, MnF, MnCl, ZrF_3, ZrF_4, CaCl, P_4O_6, PO_2, PCH, FeH, CrS and TiH, which are all not included in Sharp & Huebner (1990).

2.3.2 Schaefer et al.

Two sets of total element abundances were considered by Schaefer et al. (2012) for the calculation of the atmospheric composition above a rocky planet: Continental Crust (CC) and Bulk Silicate Earth (BSE), based on Wedepohl (1995) and Kargel & Lewis (1993), respectively. The corresponding element abundances are listed in Table 2.2. The following 18 elements are selected: H, C, N, O, F, Na, Mg, Al, Si, P, S, Cl, K, Ca, Ti, Cr, Mn and Fe, together with their respective single ions. The pressure is kept constant at 100 bar.

The model used in Schaefer et al. (2012) is based on IVTANTHERMO (Belov et al., 1999) with a database including data from Robie & Hemingway (1995) and Holland & Powell (2011). The phyllosilicates present in their dataset were excluded as their focus was on higher temperatures. In order to better compare our model to Schaefer et al. (2012), we computed two models with GGchem, one with and one without phyllosilicates. For the selected elements, GGchem finds 471 gas species in its database and 188 condensates, where 30 of those are liquids and 39 are phyllosilicates.

Phyllosilicates should be an integral part of equilibrium condensation models as they are

known in geology to form effectively in a wide temperature range on relatively short timescales as condensates directly from the gas phase, and as alterations in silicate rocks exposed to water vapour (e.g. Velde, 1995, and references therein). The effective formation of phyllosilicates is underlined by spectrometric evidence of phyllosilicates on Mars' surface (Poulet et al., 2005). Based on laboratory analysis of different chondrite materials, using backscattered electron micrography, Bischoff (1998) concluded for many carbonaceous chondrites that the aqueous alteration of parent bodies is a fundamental process in their evolution and even argued for pre-accretionary aqueous alteration of distinct components in carbonaceous chondrites. In the cold midplanes of protoplanetary discs, D'Angelo et al. (2019) showed that the hydration of forsterite surfaces by water vapour adsorption should occur within the lifetime of the solar nebula at densities $\sim 10^8\,\mathrm{cm}^{-3}$ and temperatures lower than 500 K, providing between 0.5 and 10 times the amount of water in Earth's oceans to the bulk composition of Earth, depending on grain size. Thi et al. (2020) argued that the chemisorption sites for OH and H_2O molecules in the silicate cores become occupied at temperatures between 250 K and 700 K on timescales shorter than 10^5 yrs for 1 mm grains at gas densities of $10^8\,\mathrm{cm}^{-3}$.

a) Continental Crust is a proxy of an SiO_2-rich (felsic) elemental composition which on Earth results from plate tectonics, see e.g. Taylor & McLennan (1995) for a review. The crust of Earth differentiated into two different parts, continental and oceanic crust. The oceanic crust is geologically younger and consists mainly of basalt (SiO_2-poor igneous rock) whereas the continental crust is much older, less dense, and consists mainly of *granite*, which is a composite material mostly made of SiO_2 (*quartz*) and *feldspar*. Plate tectonics on Earth strongly affected the differentiation into the different crust types. Whether other planets have a similar bulk crust composition remains unclear, but planets with Earth-like plate tectonics can be expected to also have a felsic composition, at least in parts of their crusts. Furthermore bulk compositions with high SiO_2 abundances can result in overall felsic compositions. On Venus, spectrometer measurements from the Galileo mission suggest that the highlands are felsic in composition (e.g. Hashimoto et al., 2008), while for Mars, the buried rock underneath the dominant basaltic surface might be of felsic composition (e.g. Cousin et al., 2017). The overall composition of the CC is controversial and leads to different proposed compositions. For further reading, see e.g. Taylor & McLennan (1995), Rudnick & Gao (2003) and Greber et al. (2017). In order to allow a comparison to Schaefer et al. (2012) we use their composition taken from Wedepohl (1995).

Overall, the results of the model by Schaefer et al. (2012) and our GGchem model without

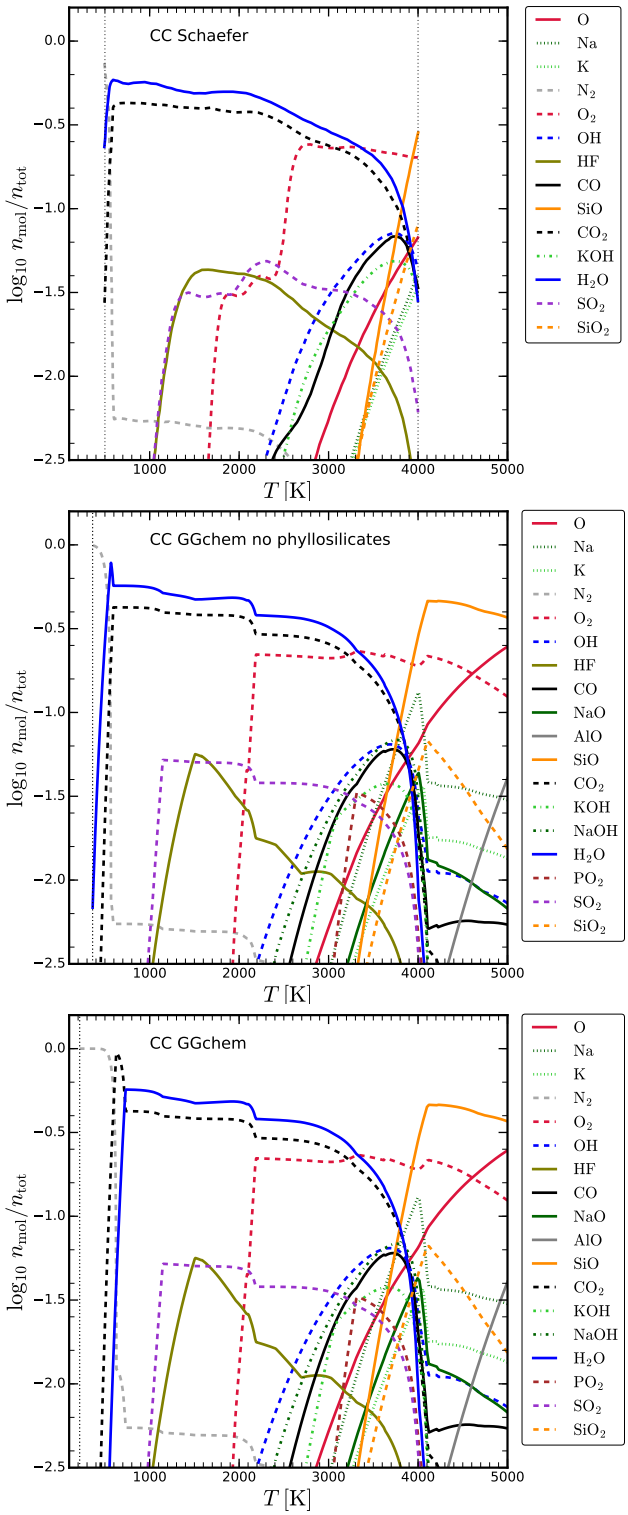

Figure 2.3: Comparing the molecular concentrations ($n_{\rm mol}/n_{\rm tot}$) over Continental Crust (CC) at $P = 100$ bar predicted by GGchem with the results obtained by Schaefer et al. (2012). **Top panel:** results by Schaefer et al. (2012) scanned from their Fig. 1. **Middle panel:** results from GGchem disregarding phyllosilicates. **Bottom panel:** results from GGchem for the full dataset. All species with $\log n_{\rm mol}/n_{\rm tot} > 1.5$ are shown. The thin, vertical dotted lines indicate the upper and lower limits of the models. For the GGchem models this means that all elements are condensed below the corresponding temperature.

phyllosilicates are similar for CC abundances, both showing H_2O and CO_2 as the major gas species between about 570 K and 3500 K, with constant particle ratio H_2O:CO_2=1.35:1, which is a direct consequence of the assumed total element abundances, since neither hydrogen nor carbon can condense at these temperatures.

At higher temperatures $\gtrsim$3500 K, O_2 and SiO become the most abundant species, followed by CO, OH, metal oxides such as SiO, SiO_2, NaO, and AlO, and hydroxides such as NaOH and KOH, and by the atoms K and Na. Liquid Al_2O_3[l] is found to be stable for temperatures up to 5150 K at 100 bar in our model, where it is the first stable condensate. Other liquid metal oxides are stable at high temperatures as well, in particular $MgAl_2O_4$[l], CaO[l], FeO[l], SiO_2[l], K_2SiO_3[l], Na_2SiO_3[l], with the last liquid solidifying at 1696 K, the melting point of SiO_2.

At lower temperatures, GGchem identifies the following solid compounds as abundant stable condensates (with $\max\{\log_{10}(n_{\rm solid}/n_{\langle {\rm Si}\rangle})\}>-2$): SiO_2[s] (*quartz*, by far the most abundant), the three major components of *feldspar*: $CaAl_2Si_2O_8$[s] (*anorthite*), $NaAlSi_3O_8$[s] (*albite*) and $KAlSi_3O_8$[s] (*microcline*), $MgSiO_3$[s] (*enstatite*), Mg_2SiO_4[s] (*fosterite*), $CaMgSi_2O_6$[s] (*diopside*), $KAlSi_2O_6$[s] (*leucite*), Fe_2O_3[s] (*hematite*), Fe_3O_4[s] (*magnetite*), $CaSiO_3$[s] (*wollastonite*), and Ca_2SiO_4[s] (*larnite*).

At temperatures $\lesssim$ 570 K, H_2O gas becomes liquid, and carbon becomes thermally stable as $CaMgC_2O_6$[s] (*dolomite*), and so N_2 remains the only abundant gas species. Eventually, at 360 K, nitrogen is found to be stable in form of NH_4Cl (*ammonium chloride*) and there is no physical solution anymore to produce a $p = 100$ bar gas as all selected elements condense. Such atmospheres would mainly consist of noble gases, which are not included here.

Some deviations between the two models are found for O_2, SO_2 and HF. The results by Schaefer et al. (2012) show two major steps in the O_2 concentration at $\sim$ 2600 K and at $\sim$ 1800 K. These changes in O_2 abundances in the gas phase are caused by the chemical stability of different Fe species in the corresponding temperature regimes: Fe_2SiO_4[l] ($T > 2500$ K), Fe_3O_4[l] (1900 K $< T <$ 2500 K) and Fe_2O_3[l]($T <$ 1900 K). In contrast, in the GGchem-model, there is only one transition, at about 2150 K, where one of the major liquids FeO[l] solidifies to form Fe_3O_4[s] (*magnetite*), which consumes large amounts of molecular oxygen as

$$6\ {\rm FeO[l]}\ +\ {\rm O_2}\ \longleftrightarrow\ 2\ {\rm Fe_3O_4[s]}\ .$$

The liquid phases Fe_2SiO_4[l], Fe_3O_4[l] and Fe_2O_3[l] are currently not included in our model. The thermodynamic data for liquids originates mostly from NIST/JANAF, which does not include liquid phases of Fe_2SiO_4[l], Fe_3O_4[l] and Fe_2O_3[l]. Towards higher temperatures, the O_2 abundance increases further according to its increasing vapour pressure over the mostly liquid condensates, such as SiO_2[l], $MgSiO_3$[l] and FeO[l].

Towards lower temperatures, fluorine becomes stable in form of CaF_2[s] (*fluorite*) around 1500 K, reducing HF in the gas phase. At about 1150 K, sulphur becomes thermally stable in form of $CaSO_4$[s] (*anhydrite*) at the expense of $CaMgSi_2O_6$[s] (*diopside*). This transition removes sulphur from the gas phase, leading to a fast decrease of the SO_2 concentration below 1150 K. Eventually, in our model without phyllosilicates, H_2O[l] (*liquid water*) is thermally stable for $T \lesssim 570$ K and leaves behind an N_2-rich atmosphere.

When we do include phyllosilicates in our model (lower panel of Fig. 2.3), the atmospheric composition does not change at higher temperatures, however, at $T < 720$ K, phyllosilicates become stable and have a profound influence on both the molecular and solid composition. We find two phyllosilicates in our CC model, $Mg_3Si_4O_{12}H_2$[s] (*talc*) at $T < 720$ K, and $Ca_2FeAl_2Si_3O_{13}H$[s] (*epidote*) at $T < 410$ K. These are very effective in removing water from the gas phase, for example

$$SiO_2[s] \; + \; 3\; MgSiO_3[s] \; + \; H_2O \; \longleftrightarrow \; Mg_3Si_4O_{12}H_2[s]\,,$$

thereby inhibiting the stability of liquid water on the surface. Since hydrogen disappears sooner than carbon from the gas phase in the model including phyllosilicates, there is in fact a narrow temperature interval 600 K − 720 K where CO_2 is the most abundant molecule.

b) Bulk Silicate Earth is an approximation for the composition of the Earth excluding its core. This leads to a composition that is rich in MgO and FeO-bearing silicates (mafic), but relatively poor in C, N, F, P, S, Cl and K. For the model comparison we use the same total element abundance as Schaefer et al. (2012) taken from Kargel & Lewis (1993).

Relevant liquids at high temperatures in our GGchem-model are SiO_2[l], FeO[l], $MgSiO_3$[l], Mg_2SiO_4[l], $MgAl_2O_4$[l], MgO[l] and CaO[l], with the first stable condensate being $MgAl_2O_4$[l] at 4900 K. The relevant solid composition at lower temperatures includes Mg_2SiO_4[s] (*fosterite*), $MgSiO_3$[s] (*enstatite*), FeO[s] (*ferropericlase*), $CaMgSi_2O_6$[s] (*diopside*), $MgAl_2O_4$[s] (*spinel*), $NaAlSiO_4$[s] (*nepheline*), Fe_2SiO_4[s] (*fayalite*), Fe_3O_4[s] (*magnetite*), $FeAl_2O_4$[s] (*hercynite*),

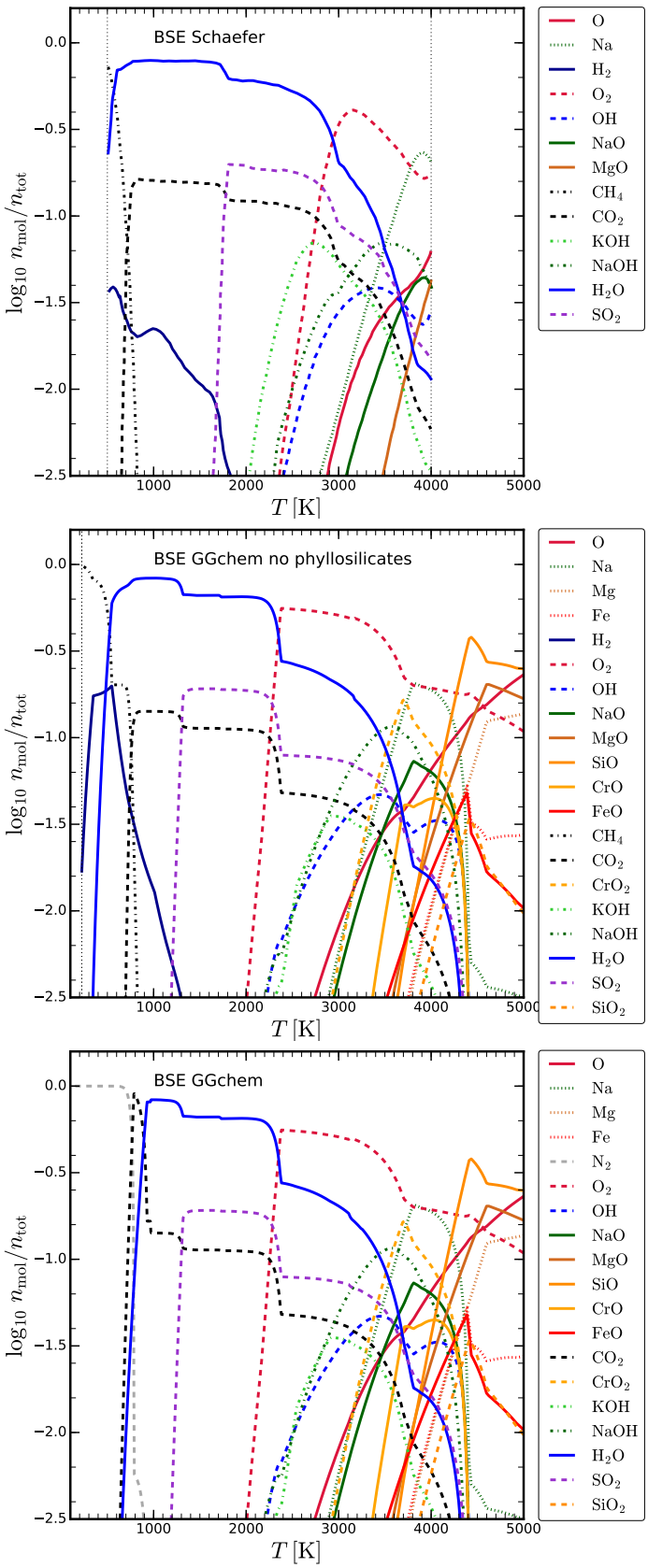

Figure 2.4: Similar to Fig. 2.3 but for Bulk Silicate Earth (BSE) total element abundances.

$CaAl_2Si_2O_8$[s] (*anorthite*), $NaAlSi_3O_8$[s] (*albite*), $NaAlSi_2O_6$[s] (*jadeite*), $MgFe_2O_4$[s] (*magnetoferrite*), $Ca_3Al_2Si_3O_{12}$[s] (*grossular*), $Ca_2MgSi_2O_7$[s] (*åkermanite*) and Ca_2SiO_4[s] (*larnite*).

Concerning the gas phase abundances, both the Schaefer et al. (2012) model and our GGchem-model show that H_2O and O_2 are the most abundant gas species in a wide temperature range, but the deviations between the models are more pronounced for BSE abundances.

For high temperatures $\gtrsim 4200$ K, both models find the gas phase to be mostly composed of O, Na, Mg, Fe, SiO and MgO, in addition to O_2. The most obvious deviation is the concentration of O_2, which dominates the gas phase in our GGchem-model between about 2300 K and 4200 K, whereas it drops already at 3100 K in the model by Schaefer et al. (2012). Similar to the model for CC abundances, the disappearance of O_2 in our model for BSE abundances is caused by the solidification of FeO[l] around 2300 K, which consumes oxygen as

$$Mg_2SiO_4[l] \; + \; 2\;FeO[l] \; + \; \tfrac{1}{2}\,O_2 \; \longleftrightarrow \; MgSiO_3[l] \; + \; MgFe_2O_4[s]\;.$$

Once O_2 has disappeared, H_2O becomes the most abundant and SO_2 the second most abundant species. At $T \approx 1300$ K, sulphur condenses in form of FeS[s] (*troilite*), for example as

$$2\;FeO[s] \; + \; 2\;SO_2 \; \longleftrightarrow \; 2\;FeS[s] \; + \; 3\;O_2\;.$$

This removes SO_2 and hence sulphur from the gas phase, making CO_2 the second most abundant gas species after H_2O.

For $T \lesssim 550$ K, H_2O is thermally stable as liquid water H_2O[l]. Both our GGchem model and the Schaefer et al. (2012) model suggest that, after water is stable as a liquid, the atmosphere becomes rich in CH_4, with some traces of H_2. At even lower temperatures, the GGchem model predicts that NH_4Cl (*ammonium chloride*) becomes stable at 330 K and CH_4[s] (*methane ice*) at 220 K, below which there is no solution anymore for a 100 bar atmosphere.

At temperatures below about 1000 K, the inclusion of phyllosilicates (lower panel in Fig. 2.4) again leads to substantial differences between our model and Schaefer et al. (2012). As the phyllosilicates $KMg_3AlSi_3O_{12}H_2$[s] (*phlogopite*) and $NaMg_3AlSi_3O_{12}H_2$[s] (*sodaphlogopite*) become stable at temperatures of 970 K and 930 K, respectively, the water in the atmosphere is removed. This removal leads to an earlier domination of CO_2 and subsequently to the formation of solid C[s] (*graphite*) at about 800 K, and the development of an N_2-rich atmosphere, in contrast to the

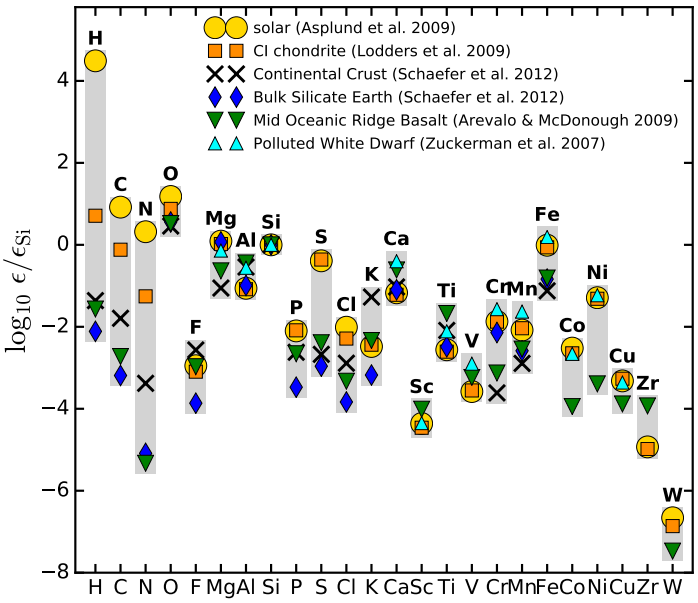

Figure 2.5: Element abundances relative to silicon (nuclei particle ratios) for different materials and astronomical sources.

model without phyllosilicates. In fact, nitrogen stays in the atmosphere down to 100 K and does not condense in form of NH_4Cl as in our CC model.

Our models without phyllosilicates match those of Schaefer et al. (2012), which do not include phyllosilicates. The inclusion of phyllosilicates as condensed species causes strong deviations in the gas phases for temperatures below $\sim$ 1000 K. This underlines the importance of phyllosilicates for the investigation of atmospheres of rocky exoplanets.

2.4 Other total element abundances

One of the major aims and challenges of exoplanet research is to determine the element composition of surfaces and atmospheres, for the purpose of characterisation. After having studied the theoretical predictions for Continental Crust (CC) and Bulk Silicate Earth (BSE) element abundances in the previous section, where we also have checked our results against previously published results, we will now explore three additional sets of total element abundances for our phase equilibrium models: (1) Mid Oceanic Ridge Basalt (MORB) elemental abundances, (2) measured elemental abundances of carbonaceous chondrites (CI), and (3) exoplanet elemental abundances deduced from spectral analyses of polluted white dwarfs. In Fig. 2.5, we plot these element abundances in units of the silicon abundance, the dominant rock-forming element, and compare them to the element abundances discussed earlier in this chapter.

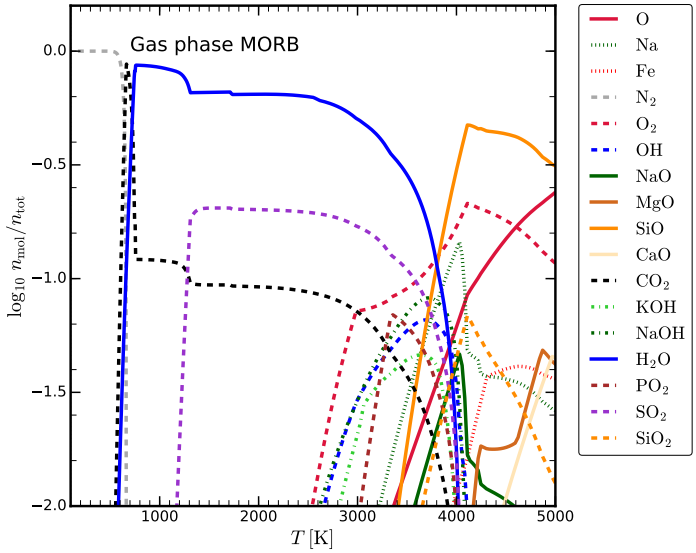

Figure 2.6: Molecular concentrations $n_{\rm mol}/n_{\rm tot}$ for Mid Oceanic Ridge Basalt (MORB) element abundances as function of temperature for a constant pressure of $p = 100$ bar. Phyllosilicates are included in this model. All species with maximum log concentration > -1.4 are shown.

2.4.1 Mid Oceanic Ridge Basalt

Measurements by probes and orbiter missions infer that rocks of basaltic composition are very common in the solar system as they can also be found on Mars, Venus, Mercury and on our Moon (e.g. Grotzinger, 2013; Gilmore et al., 2017; Wang et al., 2019b). The major difference of these rock compositions is the Fe content, which is related to the planetary mass, causing a different degree of differentiation (Elkins-Tanton, 2012). Another factor is the accretion history of the planet as well as the interior chemistry, causing different interior redox states. On Earth, basalt is most common in the oceanic crust. Therefore, we used the mean composition of the Mid Oceanic Ridge Basalt (MORB) from Arevalo & McDonough (2010) for our analysis.

Figure 2.5 and Table 2.2 show that MORB, in general, has element abundances similar to CC and BSE, but is enriched in S, Ca and Ti, and poor in N. The abundance of Mg in MORB is significantly larger than in CC, but less than in BSE. We restrict our model to the same elements as in the previous section (H, C, N, O, F, Na, Mg, Al, Si, P, S, Cl, K, Ca, Ti, Cr, Mn, Fe and their corresponding ions).

The results of this model are shown in Fig. 2.6. Important liquids at high temperatures are found to be SiO_2[l], FeO[l], $MgSiO_3$[l], Al_2O_3[l], Na_2SiO_3[l], $MgTi_2O_5$[l], CaO[l] and $MgAl_2O_4$[l], with the first condensate being Al_2O_3[l] at 5150 K in this model. At lower temperatures, MORB shows a particularity rich solid composition in our model, including SiO_2[s] (*quartz*), $MgSiO_3$[s]

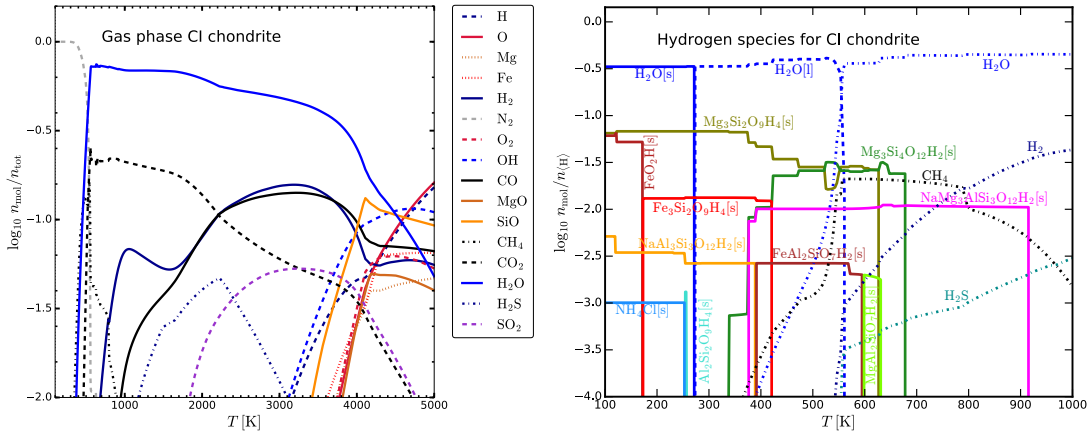

Figure 2.7: Results for carbonaceous chondrite (CI) total element abundances at constant pressure $p = 100$ bar. Phyllosilicates are included in the model. **Left panel:** gas phase concentrations ($n_{\rm mol}/n_{\rm tot}$) between 100 K and 5000 K. All species with maximum log concentration > -1.4 are shown. **right panel:** gaseous and condensed species that contain hydrogen per H-nucleus ($n/n_{\langle H\rangle}$) between 100 K and 1000 K, note the different scaling. The linestyles correspond to the different categories of condensates: silicates (solid), liquids (dotted), phyllosilicates (short dashed), other H-bearing species (long dashed), and other condensates (dash dotted).

(*enstatite*), $FeTiO_3$[s] (*ilmenite*), Fe_2SiO_4[s] (*fayalite*), $NaAlSi_3O_8$[s] (*albite*), $CaTiSiO_5$[s] (*sphene*), $CaMgSi_2O_6$[s] (*diopside*), Fe_3O_4[s] (*magnetite*), $CaAl_2Si_2O_8$[s] (*anorthite*), Al_2SiO_5[s] (*kyanite*), FeO[s] (*ferropericlase*), Mg_2SiO_4[s] (*fosterite*), $NaAlSi_2O_6$[s] (*jadeite*), $Ca_3Al_2Si_3O_{12}$[s] (*grossular*), $CaSiO_3$[s] (*wollastonite*) Fe_2TiO_4[s] (*ulvospinel*), Ca_2SiO_4[s] (*larnite*), FeS[s] (*troilite*), and C[s] (*graphite*).

The atmosphere over MORB is predicted to be more reducing than over CC and BSE, with O_2 only playing a minor role. Between temperatures of about 1300 K and 3500 K, the atmosphere consists mainly of H_2O and SO_2 with a particle ratio of about 6:1, according to the assumed element abundances of H and S. At higher temperatures, the gas mainly consists of SiO molecules and O atoms. At lower temperatures, FeS[s] condenses at $T < 1300$ K, removing SO_2 from the gas phase. The following phyllosilicates become stable below about 750 K: $Mg_3Si_4O_{12}H_2$[s] (*talc*), $FeAl_2SiO_7H_2$[s] (*Fe-chloritoid*) and $KMg_3AlSi_3O_{12}H_2$[s] (*phlogopite*). These phyllosilicates remove the water from the atmosphere and lead to a narrow temperature interval within which CO_2 becomes the most abundant gas species. They also prevent the formation of liquid water at lower temperatures. At $T < 650$ K, C[s] (*graphite*) condenses, leaving behind an N_2-rich atmosphere.

2.4.2 CI chondrite abundances

Chondrites are believed to be remainders of the formation period of the planets and thus can provide insights into the composition of the planets at very early stages. It remains a matter of

debate whether it is still possible today to find meteorites that resemble the building blocks of Earth, since their isotope ratios do not match those on Earth (see e.g. Drake & Righter, 2002; Yoshizaki et al., 2018). However, the isotope ratios of the planets can be explained by a mixture of different types of chondrites.

In order to investigate potential atmospheres based on these primitive remainders of the planet formation, Fig. 2.7 shows the results for CI chondrite element abundances, based on the *Orgueil* meteorite (see Lodders et al., 2009, and Table 2.2). This meteorite has an extraordinarily primitive composition, which is rich in Fe, Mg and S, but has only little Si, Ca and Al. The volatile elements H, C and N are significantly more abundant than for CC, BSE and MORB (see Fig. 2.5).

Due to these differences, the liquid and solid composition is very different from all other cases studied so far. The first condensate $MgAl_2O_4$[l] appears at $T \approx 4500$ K at 100 bar, while other abundant liquids are SiO_2[l], FeO[l], FeS[l], $MgSiO_3$[l], Mg_2SiO_4[l] and MgO[l]. The most important solid condensates are SiO_2[s] (*quartz*), FeS[s] (*troilite*), $MgSiO_3$[s] (*enstatite*), $NaAlSi_3O_8$[s] (*albite*), C[s] (*graphite*), FeS_2[s] (*pyrite*), Fe_3O_4[s] (*magnetite*), FeO[s] (*ferropericlase*), Fe_2SiO_4[s] (*fayalite*), and $NaAlSiO_4$[s] (*nepheline*). A number of carbonates becomes stable below about 500 K, among them $FeCO_3$[s] (*siderite*), $MgCO_3$[s] (*magnesite*), and $MnCO_3$[s] (*rhodochrosite*). At temperatures below 400 K to 900 K, hydration is very common, leading to the formation as phyllosilicates as $Mg_3Si_4O_{12}H_2$[s] (*talc*) $NaMg_3AlSi_3O_{12}H_2$[s] (*sodaphlogopite*), $Mg_3Si_2O_9H_4$[s] (*lizardite*), and $Fe_3Si_2O_9H_4$[s] (*greenalite*). Despite the formation of those phyllosilicates, there is still enough hydrogen available for liquid and solid water to become thermally stable in this model, H_2O[l] at 560 K and H_2O[s] at 271 K. Interestingly, FeO_2H[s] (*goethite*) becomes stable at about 170 K.

The gas phase mainly consists of H_2O for almost all temperatures considered, followed by CO_2, CO and H_2, and the sulphur molecules H_2S and SO_2. At very high temperatures, $T >$ 4500 K, O, H, OH, SiO, and CO become more abundant. Once the phyllosilicates, graphite and the carbonates have formed around 500 K, the gas phase is dominated by N_2. Although NH_4Cl (*ammonium chloride*) becomes stable around 250 K in this model, the chlorine abundance is not large enough here to exhaustively consume N_2.

In the bottom panel of Fig. 2.7 we show the hydrogen bearing species between 100 K and 1000 K. The different phases of H_2O incorporate most of the H atoms. The first H bearing condensate is $NaMg_3AlSi_3O_{12}H_2$[s] *(sodaphlogopite)* at about 910 K, followed by $Mg_3Si_4O_{12}H_2$[s]

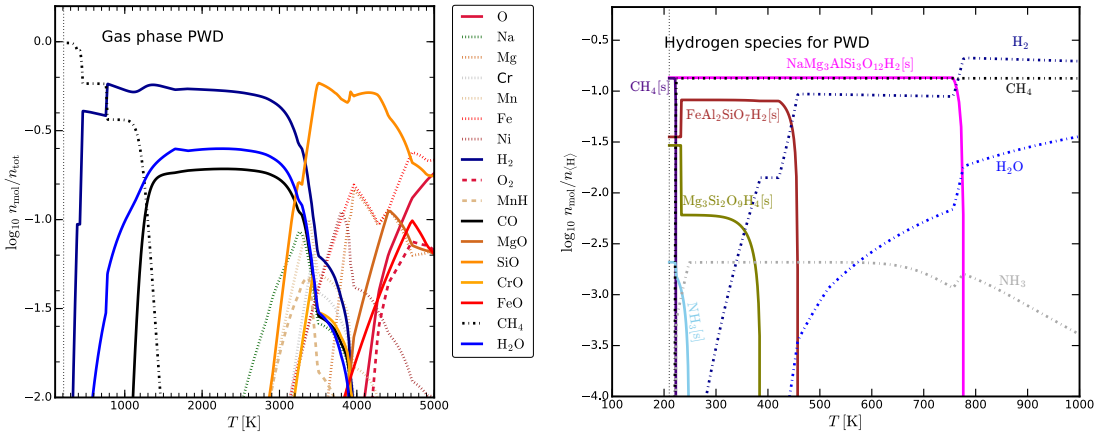

Figure 2.8: Results for Polluted White Dwarf (PWD) total element abundances at constant pressure $p = 100$ bar. Phyllosilicates are included as possible condensates. **Top panel:** gas phase concentrations ($n_{\rm mol}/n_{\rm tot}$) between 100 K and 5000 K. All species with maximum $\log n_{\rm mol}/n_{\rm tot} > -1.4$ are shown. **Bottom panel:** gaseous and condensed species that contain hydrogen are plotted with their concentration per H-nucleus $n/n_{\langle H\rangle}$ between 100 K and 1000 K (note the different scalings).

(talc), $MgAl_2SiO_7H_2$[s] *(Mg-chloritoid)*, $Mg_3Si_2O_9H_4$[s] *(lizardite)*, and $FeAl_2SiO_7H_2$[s] *(Fe-chloritoid)*, before H_2O[l] condenses at about 550 K. The amount of H kept in phyllosilicates increases steadily to lower temperatures, but is insufficient to suppress the thermal stability of liquid water.

The CI chondrite composition is the only rocky element composition considered in this chapter that produces liquid and solid water without the need for additional hydrogen and oxygen. Although other rock compositions produce large amounts of gaseous water as well, phyllosilicates are thermodynamically more favourable than the liquid water, and hence inhibits the stability of liquid water for those other element abundances in phase equilibrium. However, the CI chondrites are hydrated so much that even after the formation of the phyllosilicates, there is still some water left to condense.

2.4.3 Polluted white dwarf abundances

The bulk composition of an exoplanet can be studied in terms of its mean density, which is determined by the planet's mass and diameter. These quantities can be measured by a combination of radial velocity and transit observations (e.g. Weiss & Marcy, 2014; Rice et al., 2019). A new, powerful and potentially more direct approach to measure the bulk composition of exoplanets is to determine the element composition in the atmospheres of polluted white dwarfs.

White dwarfs (WDs), the burnt-out cores of low-mass stars which become visible only after the terminal ejection of a planetary nebulae, usually have pure hydrogen/helium atmospheres, because

all elements heavier then He settle down quickly ($\sim 10^5$ yrs) in the extremely strong gravitational field of the object (see e.g. Paquette et al., 1986; Koester, 2009). Nevertheless, some WDs show an enrichment in elements like O, Mg, Al, Si, Ca, Fe, Si, and C (e.g. Wilson et al., 2016; Farihi et al., 2016). These white dwarfs with metal absorption line features are hence called *Polluted White Dwarfes* (PWDs). The observed relative metal abundances in these PWDs are comparable to the Earth's composition with some deviations, see references in Wilson et al. (2019) and Fig. 2.5. The most plausible reason for such enrichment with heavy elements in a white dwarf's atmosphere is the accretion of planetesimals or planets from the white dwarf's planetary system. The challenge is, however, that the datasets from PWDs are lacking some important elements as their detection is presently very challenging.

In Table 2.2 we have listed the measurements for the WD GD 362 by Zuckerman et al. (2007), which shows a composition that is particularly Fe-rich, see Fig. 2.5. Unfortunately, the abundances of H and He as pollutant are impossible to derive this way, since these elements originate from the WD atmosphere itself. Thus, we excluded He from our calculations. Furthermore the values for C, N and O are only provided as upper limits. In our model, we have therefore used averaged abundances for elements H, C, N and O, computed from mean values of the logarithmic abundances from the columns denoted by 'CC Schaefer', 'BSE Schaefer', 'MORB' and 'CI meteorite' in Table 2.2. This results in $\epsilon_{\mathrm{H}} = 6.218$, $\epsilon_{\mathrm{C}} = 5.344$, $\epsilon_{\mathrm{N}} = 3.5365$ and $\epsilon_{\mathrm{O}} = 7.903$. In this work, we only investigate element abundances from a single PWD which has inferred abundances for a large number of elements allowing a more diverse atmosphere and condensate composition. An in-depth analysis of multiple elemental abundances inferred from PWD is beyond the scope of this chapter. The origins of the pollutant material range from complete planets, stripped planetary cores, comets to gas giants (see e.g. Harrison et al., 2018; Bonsor et al., 2020).

We have included 17 elements in our model (H, C, N, O, Na, Mg, Al, Si, Ca, Ti, V, Cr, Mn, Fe, Ni, Cu). Some important elements have been disregarded, because their element abundances are not available, in particular F, P, S, Cl and K. We also excluded Sc and Co because the condensate data in our model is not reliable for these elements. GGchem finds 194 gas species and 142 condensed species in its database, 23 of them being liquids, for the included 17 elements.

The results of our phase-equilibrium model are shown in Fig. 2.8. At $T \gtrsim 3700\,\mathrm{K}$, Fe is the most abundant gas species, followed by SiO and O. Additionally, O_2, FeO, Mg and MgO are abundant in the gas, but oxygen never becomes the dominant gas species as it is kept in large

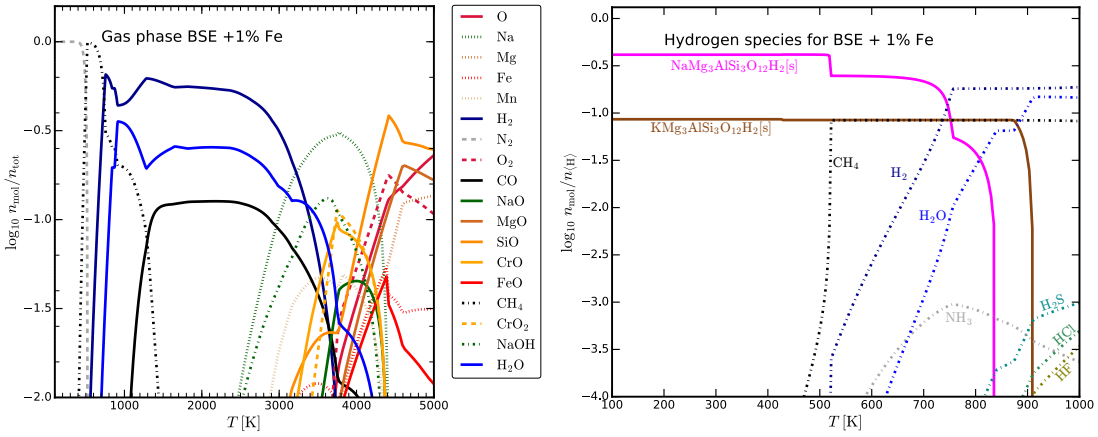

Figure 2.9: Results for BSE total element abundances at constant pressure $p = 100$ bar. Phyllosilicates are included as possible condensates. **Left panel:** gas phase concentrations ($n_{\rm mol}/n_{\rm tot}$) between 100 K and 5000 K. All species with maximum $\log n_{\rm mol}/n_{\rm tot} > -1.4$ are shown. **Right panel:** gaseous and condensed species that contain hydrogen are plotted with their concentration per H-nucleus $n/n_{\langle H\rangle}$ between 100 K and 1000 K (note the different scalings).

quantities in FeO[l].

At $T \approx 4900$ K, CaO[l] and $MgAl_2O_4$[l] are the first condensates. Other relevant liquids are FeO[l], MgO[l], $MgSiO_3$[l], $MgTiO_3$[l], and Fe[l], before CaO[l] solidifies as Ca_2SiO_4[s] at $T \approx 3900$ K. Further condensates are Ni[l] and Ti_4O_7[s], before the condensation of SiO_2[l], $CaSiO_3$[s], Ca_2SiO_4[s], Mn_2SiO_4[s], Na_2SiO_3[l], and $Ca_2MgSi_2O_7$[s] in the temperature range 2900 K $< T <$ 3400 K causes the atmospheric composition to change from an SiO dominated atmosphere to an H_2 dominated atmosphere with H_2O and CO being further abundant gas species.

At $T \lesssim 1300$ K, CO transforms into CH_4, which causes the H_2O concentration to decrease, which leaves an atmosphere rich in H_2, CH_4 and H_2O. The thermal stability of the phyllosilicates $NaMg_3AlSi_3O_{12}H_2$[s] *(sodaphlogopite)* at $T \lesssim 770$ K, $FeAl_2SiO_7H_2$[s] *(iron-chloritoid)* at $T \lesssim 460$ K, and $Mg_3Si_2O_9H_4$[s] *(lizardite)* at $T \lesssim 380$ K removes H_2 and H_2O from the gas phase, eventually leading to a pure CH_4 atmosphere. The trace gas NH_3 condenses at $T \lesssim 250$ K. The last gas species to become stable as a condensate is CH_4 at $T \lesssim 220$ K. For even lower temperatures, no species remain stable in the gas, and therefore no physical solution is possible for a $p = 100$ bar atmosphere. The formation of phyllosilicates inhibits once again the formation of water as a condensate.

The PWD element abundances are particularly rich in Fe, which binds oxygen from the atmosphere to form additional Fe-bearing solid compounds. Hence, increasing the total Fe abundance causes a more reducing atmosphere. The same effect can be achieved by increasing the Fe content in other element mixtures. For example, considering BSE abundances, an increase for the

Fe abundance by 1 wt % causes the atmosphere to change from a mixture of H_2O, CO_2 and SO_2 to a mixture of H_2, H_2O and CH_4 (see Fig. 2.9). The results for Fe-enriched BSE abundances and PWD abundances are indeed very similar. Thus, a reducing atmosphere is expected for planets with increased total iron abundance in the crust, or could be caused by the late delivery of iron-rich bodies to the planet surface.

2.5 Stability of condensed water

The occurrence of surface water is believed to be one of the necessary conditions for the emergence of life as we know it (e.g. Westall & Brack, 2018). Therefore, we investigate the potential stability of water in an equilibrium crust-atmosphere model.

The results of our models, as discussed in the previous sections, show that the formation of phyllosilicates can inhibit the formation of liquid and solid water for most rock compositions, except for the CI chondrite abundances. This raises the question by how much we need to change the total element abundances in order to allow for water to condense. We therefore have carried out additional simulations with altered element abundances based on the Bulk Silicate Earth (BSE) dataset.

Crucial for the water formation is the presence of hydrogen. We have therefore tested two approaches: (i) increasing the H abundance, and (ii) increasing the H and O abundances with particle ratio 2:1. The respective elements are added to the BSE abundances before normalising them to 1. Fig. 2.10 shows our results for temperatures between 100 K and 1000 K for these models.

The two top panels once again demonstrate the effect of the phyllosilicates. Only if the phyllosilicates are artificially removed from our list of condensates, we find liquid water to be thermally stable between about 350 K and 550 K. If the phyllosilicates are included, however, in particular $NaMg_3AlSi_3O_{12}H_2$[s] (*sodaphlogopite*) and $KMg_3AlSi_3O_{12}H_2$[s] (*phlogopite*), hydrogen is very efficiently removed from the gas phase, and liquid water cannot become thermally stable (upper right panel of Fig. 2.10).

With additional H only, we have been unable to find models where liquid water would be thermally stable. We depict the concentrations of the hydrogen species in the middle panels of Fig. 2.10 after increasing the hydrogen abundance by 1% and 10%, respectively. The dominant H bearing species in both cases is found to be H_2. In comparison to the unaltered BSE model,

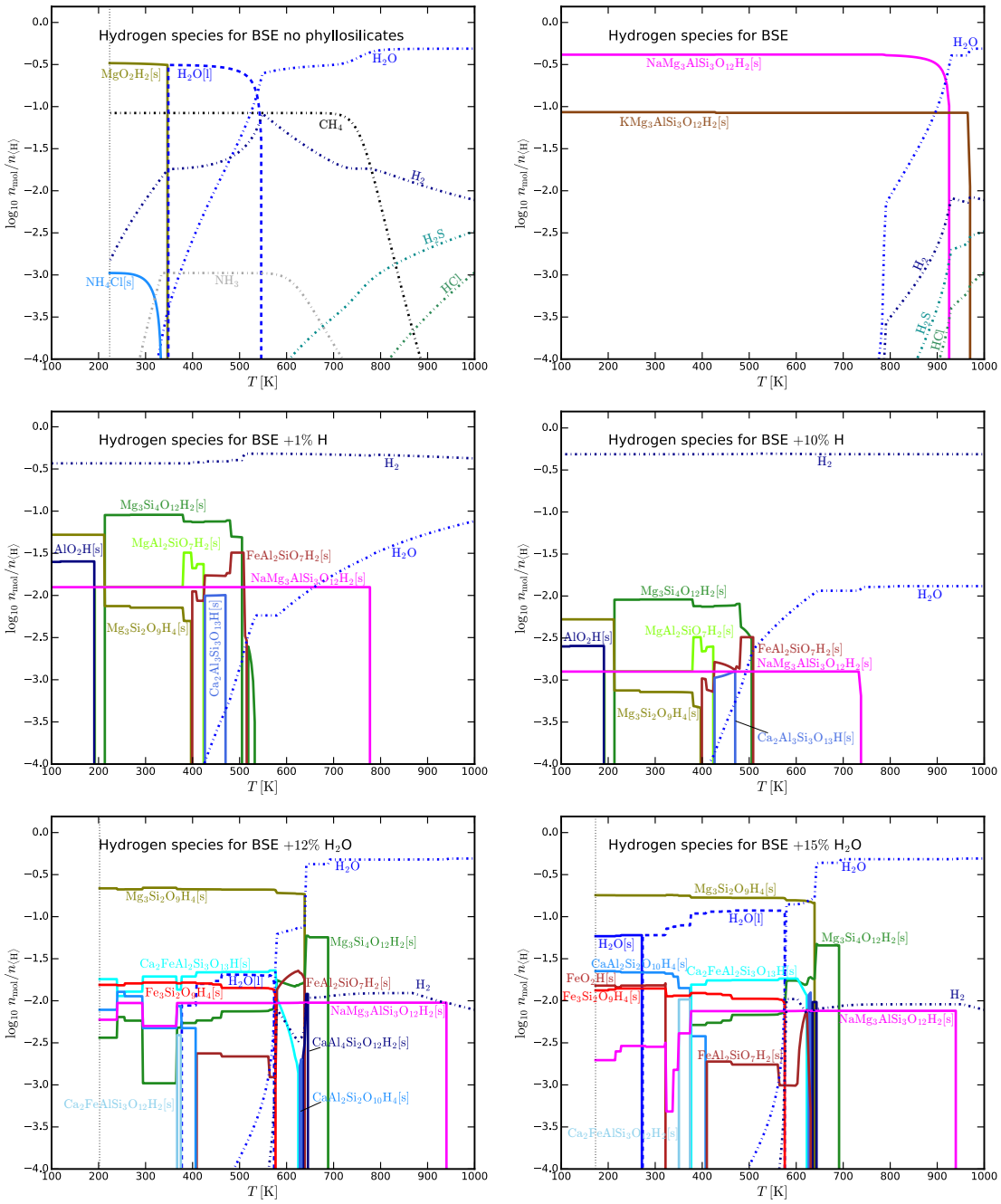

Figure 2.10: Distribution of hydrogen among the different gas and condensed species. All models are run at 100 bar and for the following abundances: **Top left panel:** BSE without phyllosilicates; **Top right panel:** BSE; **middle left panel:** BSE + 1 wt % H; **middle right panel:** BSE + 10 wt % H; **bottom left panel:** BSE + 12 wt % H_2O; **bottom right panel:** BSE + 15 wt % H_2O. The threshold concentration for species to be shown is set to 10^{-3} for all abundances except for BSE + 10% H ($10^{-3.5}$).

however, a larger variety of phyllosilicates is found to form: $NaMg_3AlSi_3O_{12}H_2$[s] (*sodaphlogopite*), $FeAl_2SiO_7H_2$[s] *(iron-chloritoid)*, $Ca_2Al_3Si_3O_{13}H$[s] *(clinozoisite)*, $Mg_3Si_4O_{12}H_2$[s] *(talc)*, $MgAl_2SiO_7H_2$[s] *(Mg-chloritoid)*, $Mg_3Si_2O_9H_4$[s] *(lizardite)*, and AlO_2H *(diaspore)*.

With additional H and O, the formation of liquid and solid water succeeds in our models, see

lower panels of Fig. 2.10. Since the mass ratio O:H is 16:1, the inclusion of 1 wt % water results in an increase of 1/9 wt % for H and 8/9 wt % for O. We found that liquid water becomes stable after adding about 12 wt % of H_2O to the total BSE element abundances, whereas 15 wt % are required for the stability of solid water. The diversity of phyllosilicates increases again. In addition we find $Ca_2FeAl_2Si_3O_{13}H$[s] (*epidote*), $CaAl_2Si_2O_{10}H_4$[s] (*lawsonite*), $Ca_2FeAlSi_3O_{12}H_2$[s] (*ferri-prehnite*), $CaAl_4Si_2O_{12}H_2$[s] (*margarite*), and $Fe_3Si_2O_9H_4$[s] (*greenalite*). For $T < 200$ K, no atmosphere is found to be stable, since all included elements are thermally stable in condensates.

This analysis shows that phyllosilicates can act as a reservoir for capturing a certain amount of water. By adding sufficient hydrogen *and* oxygen, it is possible to saturate the phyllosilicates and to have liquid and solid water as stable condensates. The added water in our model could be an indicative of an additional delivery of water to the planet, for example via the incorporation of icy comets. However, there are other possible explanations. For example, the existence of phyllosilicates is thermodynamically impossible in the hot core and the overwhelming part of the mantle. The large amount of water that had once been present in this matter is likely to have been driven out into the crust and atmosphere during planet evolution. This way, there is plenty of water available to saturate the phyllosilicates in the crust *and* to have excess water to form an ocean.

2.6 Pressure variation

In the previous sections only a particular, fixed pressure of 100 bar was considered. However, the atmospheric pressures at the surfaces of rocky planets can vary by orders magnitude, from several mbars to about 100 bars, comparable to our Solar System planets Mars and Venus, respectively. The hot atmospheres of very young rocky exoplanets might even have atmospheric pressures of multiple 100 bars (e.g. Dhaliwal et al., 2018; Olson & Sharp, 2018), following the general trend of increased vapour pressures for higher temperatures. Therefore, we investigate the influence of the atmospheric pressure on the atmospheric and crust composition in this section. This analysis is based on the BSE total element abundances.

In Fig. 2.11 we show the most abundant gas species in the $(p-T)$ plane between 0.001 bar and 100 bar, and between 100 K and 5000 K. The middle and lower panels show the atmospheric compositions at selected, constant pressures of 10 bar, 1 bar, 0.1 bar, and at 0.001 bar, respectively. The plot for $p = 100$ bar was already shown in Fig. 2.4, lower panel.

Generally speaking, the phase changes occurring in the atmosphere are the same, but shift

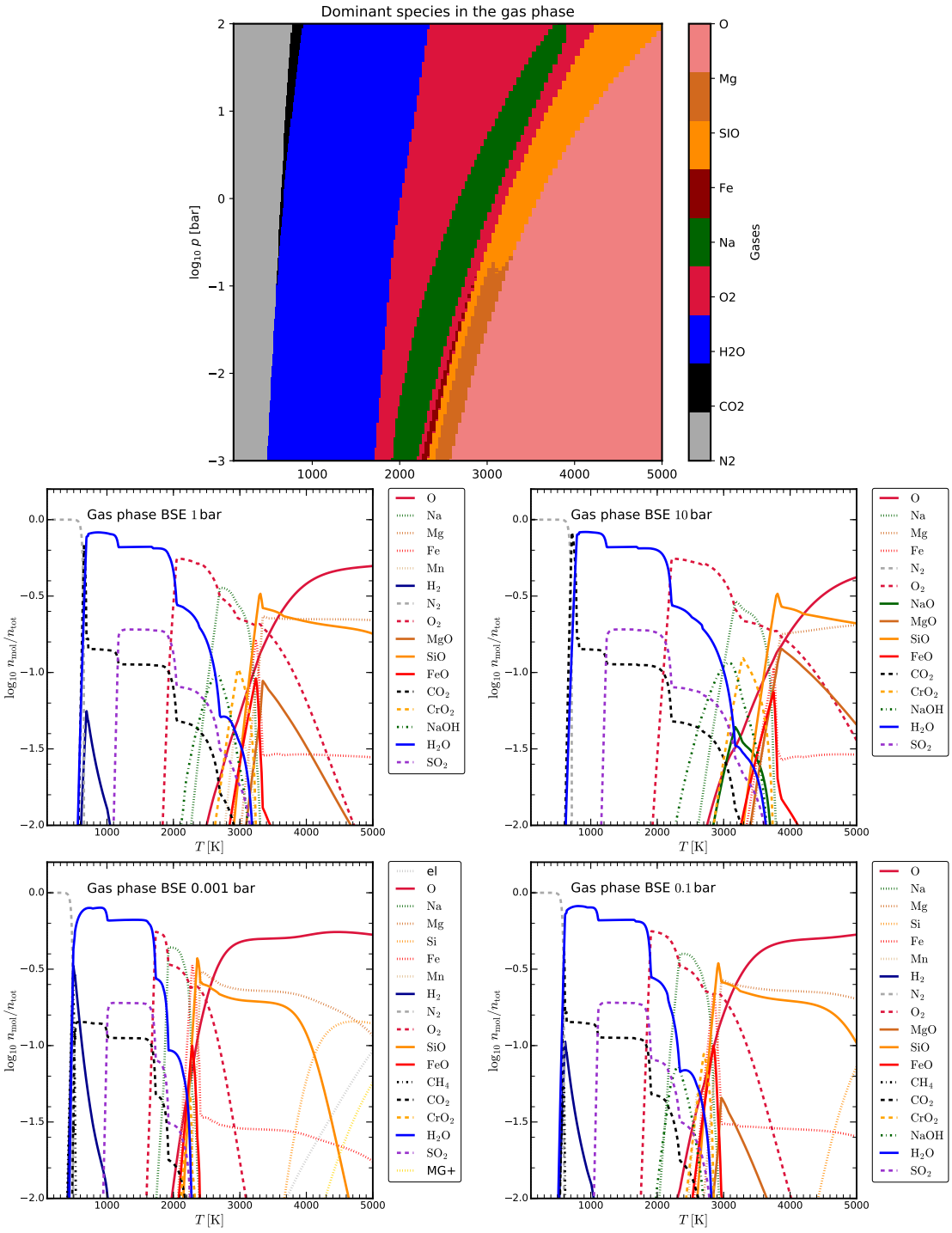

Figure 2.11: Results for BSE total abundances at different pressures. **Upper panel:** dominant gas species with respect to the highest concentration in the $p-T$ plane. **Middle panels:** gas concentrations ($n_{\mathrm{mol}}/n_{\mathrm{tot}}$) at $p = 1$ bar and $p = 10$ bar. **Lower panels:** gas concentrations ($n_{\mathrm{mol}}/n_{\mathrm{tot}}$) at $p = 0.001$ bar and $p = 0.1$ bar. The transitions in composition are caused by phase changes as listed in Tab. 2.3.

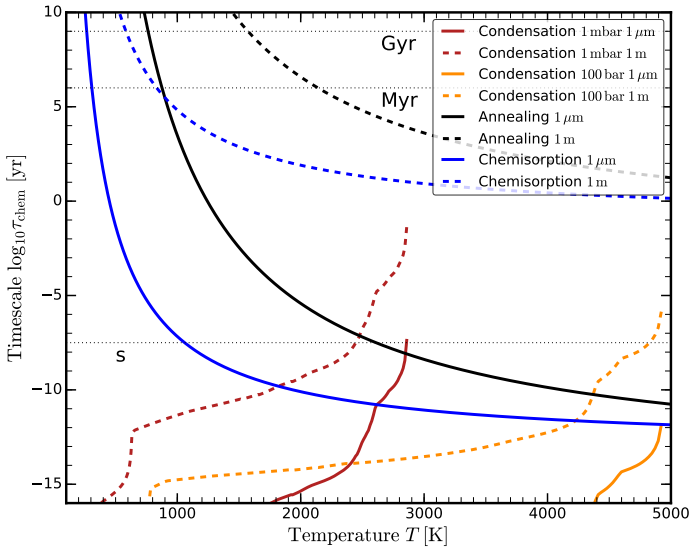

Figure 2.12: Timescale estimates for the BSE total element abundances. The condensation timescale is shown for different pressures and length scales of 1 μm and 1 m. The timescales for annealing and chemisorption are shown for scales of 1 μm and 1 m each. The horizontal dotted lines illustrate times of 1 s, 1 Myr and 1 Gyr, respectively.

to lower temperatures for lower pressures. In particular, the temperature window in which O_2 is the dominant gas species becomes narrower for lower pressures. At 100 bar this range is roughly 2000 K to 4000 K, whereas at 0.001 bar it narrows down to about 1600 K to 1900 K. The temperatures where the various condensates appear and disappear are shifted likewise, see Table 2.3.

2.7 Timescales

All calculations presented assumed that our systems have reached chemical equilibrium. We address this assumption by investigating three timescales. First, we calculate the timescale for the condensation from the gas phase to form the different condensates. Second, an annealing timescale that rearranges the condensate phase towards the thermodynamically favoured phase is considered. Last, we investigate the chemisorption timescale, describing the formation of phyllosilicates.

We consider the relaxation of a state $y(t)$ towards equilibrium y_0 via the first-order ordinary differential equation $\mathrm{d}y/\mathrm{d}t = f(y)$, where f is the given time derivative. The relaxation timescale is found by considering small deviations from the equilibrium state as

$$\frac{\mathrm{d}y}{\mathrm{d}t} \approx f(y_0) + \frac{\mathrm{d}f}{\mathrm{d}y}(y - y_0), \tag{2.1}$$

where $f(y_0) = 0$. The relaxation timescale is $(y - y_0)/(\mathrm{d}y/\mathrm{d}t)$, hence

$$\tau_{\mathrm{relax}} = \left(\left. \frac{\partial f}{\partial y} \right|_{y_0} \right)^{-1}. \tag{2.2}$$

Close to the equilibrium state, the system relaxes as

$$y(t) = y_0 + (y(0) - y_0) \exp(-t/\tau_{\mathrm{relax}}). \tag{2.3}$$

For the gas-condensed phase transition we have $y = V_s$ and

$$f(V_s) = (n - n_0) v_{\mathrm{th}} A_{\mathrm{tot}} V_1 \alpha \tag{2.4}$$

$$= (V_{s0} - V_s) v_{\mathrm{th}} A_{\mathrm{tot}} \alpha. \tag{2.5}$$

where V_s is the volume of a condensate s per cm^3, V_{s0} its value in phase equilibrium, n the number of key molecules in the gas phase forming the condensate, and n_0 its value in phase equilibrium. n and V are connected as

$$V_1(n - n_0) = -(V_s - V_{s0}), \tag{2.6}$$

i.e. an excess of key molecules in the gas phase means that the condensation is momentarily not complete. V_1 is the monomer volume. A_{tot} is the total surface of all condensates and α the sticking coefficient, assumed to be unity. v_{th} is the thermal velocity calculated by

$$v_{\mathrm{th}} = \sqrt{\frac{8 k_{\mathrm{B}} T_{\mathrm{g}}}{\pi m}}. \tag{2.7}$$

with the mass m of the gas species containing most of the limiting element. The limiting element is the least abundant element in the gas phase that is included in the considered condensate. When computing Eq. 2.8, we consider the longest timescale of all active condensates. The identifications of the slowest condensate, its limiting element and key species have little effect on the results as they only enter via the thermal velocity which requires a species mass. k_{B} is the Boltzmann constant and T_{g} the gas temperature. Inserting Eq. 2.5 in Eq. 2.2 the condensation timescale τ_{cond} follows as

$$\tau_{\mathrm{cond}} = (v_{\mathrm{th}} A_{\mathrm{tot}} \alpha)^{-1} = \left(v_{\mathrm{th}} \frac{A_{\mathrm{tot}}}{V_{\mathrm{tot}}} V_{\mathrm{tot}} \alpha \right)^{-1}. \tag{2.8}$$

$V_{\rm tot}$ is the total volume of all condensates. Equation 2.8 expresses the time it takes for the key molecule of the slowest condensate to collide with an existing surface. We approximate the surface-volume fraction $A_{\rm tot}/V_{\rm tot}$ by the dimension ratio

$$\frac{A_{\rm tot}}{V_{\rm tot}} \propto \frac{a^2}{a^3} = \frac{1}{a}, \tag{2.9}$$

with a length scale of a. The inclusion of different scales will introduce factors of the order of 10^0. E.g. spherical symmetric grains with a radius of a will have a surface-volume ratio of

$$\frac{A_{\rm tot}}{V_{\rm tot}} = \frac{4\pi a^2}{\frac{4}{3}\pi a^3} = \frac{3}{a}. \tag{2.10}$$

In Fig. 2.12, the condensation timescale for BSE abundances is shown for pressures of 100 bar and 1 mbar as well as for different length scales of 1 μm and 1 m. For the 1 mbar calculation, no condensates are stable for $T \gtrsim 2900$ K, thus the condensation timescale cannot be calculated. In case of the 100 bar atmosphere, this threshold is at $T \approx 4900$ K.

The timescale based on reorganisation of condensates in the lattice structure itself is based on the transfer of sub groups of molecules from one point in the lattice to another by solid diffusion. This annealing process is described by Duschl et al. (1996) and Gail & Sedlmayr (1999) and the timescale can be calculated by

$$\tau_{\rm annealing} = \frac{(\Delta a)^2}{\frac{1}{3}\lambda^2 \nu \exp\left(\frac{-E_{\rm a}}{k_{\rm B}T}\right)}. \tag{2.11}$$

λ is the step length, ν the oscillation frequency, $E_{\rm a}$ the activation energy that needs to be overcome in order to move from one to an adjacent lattice place, $k_{\rm B}$ the Boltzmann constant and T the temperature. Δa is the total distance that the particle needs to travel in the lattice structures by random walk.

The black lines in Fig. 2.12 show the annealing timescales for different annealing distances Δa of 1 μm and 1 m. As Gail & Sedlmayr (1999), we use the typical SiO_4 vibration frequency $\nu = 2 \cdot 10^{13}\,{\rm s}^{-1}$ for the annealing process. SiO nucleation experiments from Nuth & Donn (1982) resulted in a characteristic activation energies for silicates of $E_{\rm a}/k_{\rm B} = 41000$ K. We assume a step size of $\lambda = 1$ nm, based on the order of magnitude of the monomer size calculated by $\lambda = \sqrt[3]{V_1}$ for monomer volumes V_1.

For the formation of phyllosilicates, the chemisorption of H_2O in silicates is of importance (Thi et al., 2020). The formula to calculate these timescales is also given by Eq. 2.11. Thi et al. (2020) calculate the oscillation frequency for H_2O at a surface sight as $\nu = 10^{12}\,\mathrm{s}^{-1}$. The activation energy for a chemisorbed H_2O at the surface to occupy a free silicate core chemisorption site is $E_\mathrm{a}/k_\mathrm{B} = 13470\,\mathrm{K}$ (Okumura & Nakashima, 2004). The chemisorption timescales for different thicknesses of 1 m and 1 μm are shown in Fig. 2.12 as blue lines.

The timescales in Fig. 2.12 show that the formation of new condensates from the gas phase is quicker than 1 yr for all temperatures and pressures considered. However, the formation of the thermodynamically most favourable lattice structure by rearrangement via solid diffusion may take a long time. For μm-sized particles, the silicate rearrangement (annealing) timescale exceeds 1 Myr at about 900 K. In comparison, the chemisorption timescale for the diffusion of water into the rock structure is faster, exceeding 1 Myr at about 300 K for μm-sized particles.

The comparison of condensation timescales and annealing timescales provides a first order insight to the structure of the condensates. The condensate will be crystalline if $\tau_\mathrm{cond} > \tau_\mathrm{annealing}$, because the condensates can rearrange quick enough to form the crystalline structure. For $\tau_\mathrm{cond} \ll \tau_\mathrm{annealing}$ the condensation occurs much faster and the formed condensate is amorphous (Gail & Sedlmayr, 1999).

Especially the timescales for the phyllosilicate formation are very interesting as small rocks can be hydrated on timescales of planetary evolution which is in agreement to the conclusions of Thi et al. (2020). This underlines the importance of the inclusion of phyllosilicates to atmosphere-crust models.

2.8 Summary and Discussion

The composition of the near-crust atmosphere of a rocky planet depends on the composition of the crust, and vice versa, as the atmosphere and the crust form a coupled thermo-chemical system. The gas in such near-crust atmospheres will diffuse (or be transported) into the higher, low-pressure atmospheric regions where it may become, for example, subject to cloud-formation and/or mass loss. In our model we investigate the composition of the atmospheric gas directly in contact with the crust based on chemical phase equilibrium. The assumed total element abundances, and the thermo-chemical data of the condensed species included, are crucial factors for the determination of the composition of crust and atmosphere. All temperature values correspond to an atmospheric pressure of 100 bar.

Near-crust gas composition regimes: The near-crust atmospheres of the investigated rocky compositions (CC, BSE, MORB and CI chondrite) fall roughly into three regimes:

(i) near-crust atmospheres with $T \lesssim 600\,\mathrm{K}$ are dominated by N_2 or CH_4,

(ii) near-crust atmospheres with $600\,\mathrm{K} \lesssim \mathrm{T} \lesssim 3000\,\mathrm{K}$ are dominated by H_2O, CO_2 and SO_2, but O_2 dominates for a BSE-crust for $T \gtrsim 2000\,\mathrm{K}$,

(iii) near-crust atmospheres with $T \gtrsim 3000\,\mathrm{K}$ consist of a combination of O_2, metal atoms, oxides and hydroxides.

The resulting near-crust atmospheric composition at lower temperatures ($T \lesssim 700\,\mathrm{K}$) depends on whether or not phyllosilicates are included. This can result in a shift from CH_4 as a dominant gas species to N_2, as the hydrogen is consumed by condensates in the form of phyllosilicates. The model results for the CI chondrite abundances are the only ones that produces CO in gas concentrations higher than 10%, due to the relatively high C abundance.

The near-crust atmosphere for a rocky surface according to the polluted white dwarfs metal abundance remains inconclusive with respect to P, S and K species as they are not measured in the PWD spectra. Nevertheless, our results for PWD abundances provide insight into the atmospheric composition of a potential iron rich planet. The major species of the corresponding near-crust gas phase would be CH_4 ($T \lesssim 750\,\mathrm{K}$), H_2 ($750\,\mathrm{K} \lesssim \mathrm{T} \lesssim 3300\,\mathrm{K}$), SiO ($330\,\mathrm{K} \lesssim \mathrm{T} \lesssim 4700\,\mathrm{K}$) and Fe ($4700\,\mathrm{K} \lesssim \mathrm{T}$).

Implications on magma oceans: We observe in our models that liquids start to play a role at temperatures $T \gtrsim 1700\,\mathrm{K}$, where parts of the crust are molten for all total element abundances considered. For hot super earth planets like 55 Cnc e or CoRoT-7b with dayside temperatures in the range from about 2500 K to 3000 K the crust is mainly liquid, but also contains some solids. The crust composition can be grouped into two regimes correlating with the difference in the Mg/Si ratio

(i) BSE/CI: melt consisting of mainly $MgSiO_3$[l], FeO[l], and $MgSiO_4$[l] while the main solids are $Ca_2MgSi_2O_7$[s] (*åkermanite*), $MgCr_2O_4$[s] (*picrochomite*), and MnO[s] (*manganosite*).

(ii) CC/MORB: melt consisting of mainly SiO_2[l], $MgTi_2O_5$[l], and FeO[l] while the solids contain $MnSiO_4$[s] (*tephroite*), Cr_2O_3[s] (*eskolaite*), and $CaSiO_3$[s] (*wollastonite*).

The near-crust atmosphere above a magma ocean consists, in all cases, mainly of H_2O, O_2, CO_2 and SO_2. The major differences are the dominance of O_2 over H_2O for the BSE abundances and the occurrence of H_2 and CO as the second and third most abundant gases in case of the CI chondrite element abundances.

Water stability: Phyllosilicates inhibit the thermal stability of liquid and solid water. The CI chondrite total element abundance is the only case for which the thermal stability of water as a condensate is not inhibited by phyllosilicates. In fact, water is abundant enough to overcome the stability of phyllosilicates in the CI case. Similarly, we are able to force the BSE composition to have liquid water as a thermally stable condensate by adding 12 wt% H_2O to the total element abundance. An additional 3 wt% H_2O allow solid water to be thermally stable. This shows the importance of phyllosilicates for the search for planets with potential liquid water. The role of phyllosilicates for the water content of exoplanets is further emphasised by their continuous formation on Earth's surface on short timescales. On the other hand, it is hypothesised, that most of the Earth's water is trapped in phyllosilicates in the wet mantle transition zone (Wang et al., 2019a). But this zone is not saturated with water and is believed to take up all of Earth's water.

Timescale investigations show that hydration of small rocks occurs on evolutionary timescales also for temperatures as low as 300 K underlining the importance of phyllosilicates to the system. The rearrangement in refractory condensates towards the thermodynamically most favourable state is only valid for small scales and temperatures above 900 K. However, the major changes of the atmospheric composition at temperatures below 1000 K are caused by the formation of phyllosilicates and ices.

Implication for habitability: The search for habitable and inhabited planets is one of the ultimate goals of astrophysics. The occurrence of life will alter the atmosphere and produce some gas species that can be used as biotracers. Earlier studies suggest that O_2 and O_3 would be a good biosignature, but more recent studies show that also abiotic sources can produce sufficient levels of O_2 in atmospheres (Domagal-Goldman et al., 2014; Harman et al., 2015; Luger & Barnes, 2015; Harman et al., 2018). This underlines the necessity of understanding the difference between biosignatures and false positives. Previous studies show that various gas species can be used as biotracers (O_2, O_3, N_2O, CH_4, CH_3Cl, NH_3, C_2H_6 and sulphur hazes (Domagal-Goldman et al., 2011; Lammer et al., 2019, and references therein)). In this study we find that some of these species are consistent with equilibrium models, but the occurrence of multiple of these species can be a sign for non equilibrium chemistry. While O_2 is a major constituent of the atmosphere at

$T < 2000$ K, we are unable to produce stable O_2 at lower temperatures ($T \lesssim 1500$ K). Some further gas species that might be linked to life, especially N_2 and CH_4, only occur at low temperatures. According to our model and the element abundances analysed in this work, we conclude that the following gas compositions as possible signs for non-equilibrium and potential signature of life, ordered by the strength of argument

(i) O_2 as abundant gas species for $T \lesssim 1500$ K,

(ii) N_2 and O_2 at the same time for $T \lesssim 1500$ K (see also Stüeken et al., 2016),

(iii) NO or NO_2 for $T \lesssim 1500$ K,

(iv) CH_4 and O_2 at the same time.

The simultaneous occurrence of N_2 and O_2 with high concentrations is also possible for sufficiently high N abundances. N_2 is usually outgassing as a volatile whereas O_2 is produced from molten rock at high temperatures, but if we simply assume a much higher N-abundance, both O_2 and N_2 can coexist also at high temperatures in equilibrium. We note, however, that the detection of N_2 can be affected by lightning in cloudy atmospheres Ardaseva et al. (2017).

One of the crucial aspects in the formation of life as we know it is the occurrence of liquid water. From the results of this work, the upper crust of a (cooling) planet needs to be saturated in phyllosilicates in order to allow for the stability of liquid water on the surface. The detection of gaseous water in the atmosphere is not conclusive for the existence of liquid water, as the phyllosilicates are able to incorporate all potential liquid water in phase equilibrium.

Other conclusions about the crust composition on the basis of observations of the atmospheric composition can be ambiguous as well, but can still provide the first steps to characterise the conditions on the surface of terrestrial exoplanets.

2.9 Additional Tables

Table 2.1: Glossary for different condensed species.

Name	Sum formula	Structural formula
Dolomite	$CaMgC_2O_6$	$CaMg(CO_3)_2$
Grossular	$Ca_3Al_2Si_3O_{12}$	$Ca_3Al_2(SiO_4)_3$
Phlogopite	$KMg_3AlSi_3O_{12}H_2$	$KMg_3(AlSi_3O_{10})(F,OH)_2$
Flourophlogopite	$KMg_3AlSi_3O_{10}F_2$	
Sodaphlogopite	$NaMg_3AlSi_3O_{12}H_2$	$NaMg_3(AlSi_3O_{10})(OH)_2$
Talc	$Mg_3Si_4O_{12}H_2$	$Mg_3Si_4O_{10}(OH)_2$
Fe-Chloritoid	$FeAl_2SiO_7H_2$	$(Fe,Mg,Mn)_2Al_4Si_2O_{10}(OH)_4$
Mg-Chloritoid	$MgAl_2SiO_7H_2$	
Mn-Chloritoid	$MnAl_2SiO_7H_2$	
Lizardite	$Mg_3Si_2O_9H_4$	$Mg_3Si_2O_5(OH)_4$
Greenalite	$Fe_3Si_2O_9H_4$	$Fe_3Si_2O_5(OH)_4$
Goethite	FeO_2H	$FeO(OH)$
Epidote	$Ca_2FeAl_2Si_3O_{13}H$	$Ca_2(FeAl_2)(Si_2O_7)(SiO_4)O(OH)$
Lawsonite	$CaAl_2Si_2O_{10}H_4$	$CaAl_2(Si_2O_7)(OH)_2(H_2O)$
Prehnite	$Ca_2Al_2Si_3O_{12}H_2$	$Ca_2Al_2Si_3O_{10}(OH)_2$
Ferri-Prehnite	$Ca_2FeAlSi_3O_{12}H_2$	$Ca_2FeAlSi_3O_{10}(OH)_2$
Margarite	$CaAl_4Si_2O_{12}H_2$	$CaAl_2Al_2Si_2O_{10}(OH)_2$

Table 2.2: Element abundances from different astronomical and geological sources. 'H normalised' means $\log_{10}$ of nuclei particle ratio with respect to hydrogen, where H is normalised to 12, and 'mfrac [%]' means mass fraction in the condensate.

Element	Solar	CC Schaefer	BSE Schaefer	MORB	CI meteorite	Polluted White dwarf
References	1	2	2	3	4	5
	H normalised	mfrac [%]	mfrac [%]	mfrac [%]	mfrac[%]	H normalised
H	12	0.045	0.006	0.045	1.97	12
He				0.000006	0.000000917	13.14
Li				0.00065	0.000147	
Be				0.000076	0.0000021	
B				0.00016	0.0000775	
C	8.5695	0.199	0.006	1.5	3.48	¡ 7.5
N	8.0704	0.006	8.8E-05	0.14	0.295	¡ 9
O	8.83	47.2	44.42	43.94564	45.9	¡ 8
F	4.8867	0.053	0.002	0.0087	0.00582	
Ne					0.000000018	
Na	6.2757	2.36	0.29	2.06978	0.499	5.35 ± 0.20
Mg	7.5233	2.2	22.01	4.57101	9.68	7.16 ± 0.25
Al	6.427	7.96	2.12	7.77999	0.85	6.74 ± 0.20
Si	7.4976	28.8	21.61	23.59144	10.7	7.3 ± 0.30
P	5.4798	0.076	0.008	0.08030	0.0967	
S	7.1965	0.07	0.027	4	5.35	
Cl	5.2534	0.047	0.004	0.037	0.0698	
Ar					0.000000133	
K	5.1208	2.14	0.02	0.13282	0.0544	
Ca	6.3555	3.85	2.46	8.14033	0.922	6.9 ± 0.10
Sc	3.0416			0.00398	0.00059	2.95 ± 0.30
Ti	4.9408	0.401	0.12	1.00690	0.0451	5.19 ± 0.10
V	3.9159			0.0309	0.00543	4.4 ± 0.30
Cr	5.6014	0.013	0.29	0.0249	0.265	5.73 ± 0.10
Mn	5.4661	0.072	0.11	0.14250	0.193	5.67 ± 0.10
Fe	7.4167	4.32	6.27	8.10729	18.5	7.49 ± 0.10
Co	6.1788			0.0043	0.0506	4.64 ± 0.40
Ni				0.0092	1.08	6.07 ± 0.15
Cu	4.23			0.0074	0.0131	3.94 ± 0.40
Zn				0.00913	0.0323	
Ga				0.00175	0.000971	
Ge				0.0021	0.00326	
As				0.00018	0.000174	
Se				0.0013	0.00203	
Br	2.6279			0.00012	0.000326	
Kr					0.00000000522	
Rb				0.000288	0.000231	
Sr	2.9273			0.0129	0.000781	2.72 ± 0.30
Y	2.1788			0.00368	0.000253	
Zr	2.9447			0.01169	0.000362	
W				0.000012	0.0000096	
Sum		99.812	99.773	105.423	100.066	

References: (1) Sharp & Huebner (1990); (2) Schaefer et al. (2012); (3) Gale et al. (2013); (4) Lodders et al. (2009); (5) Zuckerman et al. (2007)

Table 2.3: Temperatures where different condensed species appear ($T_{\rm high}$) and disappear ($T_{\rm low}$) in phase equilibrium for BSE abundances. Three different pressure levels are considered as indicated. The condensates are ordered by the temperature of their first appearance at $p = 100$ bar.

Condensates	Name	$T_{\rm high}$ [K]	$T_{\rm low}$ [K]	$T_{\rm high}$ [K]	$T_{\rm low}$ [K]	$T_{\rm high}$ [K]	$T_{\rm low}$ [K]
		$p = 100$ bar		$p = 1$ bar		$p = 1$ mbar	
$MgAl_2O_4$ [l]		4871	2403	3653	2403	2532	2403
MgO[l]		4562	3849				
CaO [l]		4562	3799				
$MgSiO_3$ [l]		4387	1850	3290	1850	2341	1850
FeO [l]		4387	1644	3247	1644	2281	1644
$MgTiO_3$ [l]		4330	2499	3205	2499		
Mg_2SiO_4 [l]		3849	2164	3333	2164	2403	2164
MnO	Manganosite	3849	2341	2924	2341		
Na_2SiO_3 [l]		3799	2193	2703	2193		
Ca_2SiO_4	Larnite	3799	3205	3421	3205		
Cr_2O_3	Eskolaite	3701	3701				
$Mg_3P_2O_8$		3512	3247				
$MgCr_2O_4$	Picrochomite	3377	320	2963	320	2251	320
$Ca_5P_3O_{13}H$	Hydroxyaoatite	3247	3081	2532	2372		
$Ca_2MgSi_2O_7$	Åkermanite	3205	1975	3205	1975	2403	1975
P_2O_{10}		3122	1688	2372	1666	1850	1581
K_2SiO_3 [l]		2886	2532				
Al_2O_3 [l]						2668	2532
$Ca_2Al_2SiO_7$	Gehlenite					2532	2435
$KAlSiO_4$	Kalsilite	2532	2081	2341	2081		
$MgTi_2O_5$ [l]		2499	2001	2499	2001	2311	2001
$Ca_3MgSi_2O_8$	Merwinite					2435	2403
$MgAl_2O_4$	Spinel	2403	2136	2403	2136	2403	2136
$MgFe_2O_4$	Magnesioferrite	2372	1924	2027	1924		
$MnTiO_3$	Pyrophanite	2341	1850	2341	1850	2136	1850
$NaAlSiO_4$	Nepheline	2193	1949	2193	1949	380	277
Mg_2SiO_4	Forsterite	2164		2164		2164	
$CaAl_2Si_2O_8$	Anorthite	2136	570	2136	570	2136	570
$KAlSi_2O_6$	Leucite	2081	1155	2081	1155	1874	1155
Fe_2TiO_4	Ulvöspinel	2001	1233	2001	1233	2001	1233
$CaMgSi_2O_6$	Diopside	1975	347	1975	347	1975	347
$NaAlSi_3O_8$	Albite	1949	380	1949	380	1924	380
Fe_3O_4	Magnetite	1924		1924		1733	
SiO_2 [l]		1850	1826	1850	1826	1850	1826
$MnSiO_3$	Pyroxmangite	1850	1581	1850	1581	1850	1581
$MgSiO_3$	Enstatite	1826		1826		1826	
$Ca_5P_3O_{12}F$	Flourapatite	1710				1623	
FeO	Ferropericlase	1644	1000	1644	1000	1644	1000
Mn_2SiO_4	Tephroite	1581	1560	1581	1560	1581	1560
$MnTiO_3$ *	Pyrophanite	1560	1170	1560	1170	1560	1170
NaCl [l]		1462	1068				
FeS	Troilite	1316		1170		1000	
$FeTiO_3$	Ilmenite	1233		1233		1233	
$Mn_3Al_2Si_3O_{12}$	Spessartine	1170		1170		1170	
$KAlSi_3O_8$	Microcline	1155	962	1155	712	1155	513
$KMg_3AlSi_3O_{10}F_2$	Flourophlogopite	1140	427	925	427	731	427
NaCl	Halite	1068		1054		780	
Fe_2SiO_4	Fayalite	1000	150	1000	150	1000	150
$KMg_3AlSi_3O_{12}H_2$	Phlogopite	962		712		513	
$NaMg_3AlSi_3O_{12}H_2$	Sodaphlogopite	925		684		493	
C	Graphite	780		649		487	
$FeAl_2O_4$	Hercynite	570		570		570	
MgF_2		427	187	427	187	427	187
$NaAlSiO_4$ *	Nepheline	380	277	380	277	380	277
$Ca_3Al_2Si_3O_{12}$	Grossular	347		347		347	
Cr_2O_3 *	Eskolaite	320		320		320	
$NaAlSi_2O_6$	Jadeite	277		277		277	
CaF_2		187	100	187	100	187	100
Fe	Iron	150		150		150	
MgF_2 *		100		100		100	

Notes: The * indicates species, that are stable at a second temperature range.

" Wir müssen wissen - wir werden wissen"
We have to know - we will know

- David Hilbert

3

Atmospheric types based on CHNO elements

In this chapter the composition of atmospheres, which only consist of carbon, hydrogen, nitrogen, and oxygen (in the following CHNO), is characterised. The investigation focusses on the element abundances and chemical state of these elements. The aim is to allow a characterisation of atmospheres of the most abundant elements in planetary atmospheres. Equilibrium chemistry calculations allow the differentiation into three different atmospheric types with characteristic atmospheric compositions and condensates.

The work presented in this chapter is based on 'Coexistence of CH_4, CO_2, and H_2O in exoplanet atmospheres' by P. Woitke, O. Herbort, Ch. Helling, E. Stüeken, M. Dominik, P. Barth, D. Samra and published in Astronomy & Astrophysics 646, A43 (2021). As the second author of this paper I contributed substantially to the evolution of the idea as well as the discussion and implications of our results. The framework of the equilibrium composition of CHNO atmospheres based on the activation energies was led by P. Woitke, but is included in this thesis in my own words as a necessary background for the subsequent work. Particularly, I contributed to this work by investigations of the analysis of full chemical models of the limited and extended sets of elements.

This especially includes the the temperature sequences for different element abundances presented here in Fig. 3.4.

3.1 Motivation

With the future space-based telescopes and instrumentation for the 30 m-class telescopes, it becomes increasingly important to be able to characterise the atmospheric composition of rocky exoplanets and planets in general. The question of atmospheric characterisation based on models gains importance, as not all possible atmospheric compositions are represented in our solar system. The potential atmospheric diversity is large and needs to be understood in order to not misunderstand future observations (e.g. Leconte et al., 2015; Grenfell et al., 2020)

One of the targets of interest in exoplanet science is the question of habitability. This question can be divided into the questions of 'what planets could sustain life as we know it?', 'on what planets can life evolve?', and 'how to distinguish a planet with a biosphere from an uninhabited planet?'. For the latter question it is important to understand what atmospheric compositions are possible without the influence of a biosphere (Seager et al., 2013b). The atmospheric signatures that distinguish an atmosphere influenced by biology from an abiotic atmosphere are called biosignatures (Seager et al., 2016; Catling et al., 2018). However, it is of vital importance to understand the surrounding of the planet itself in order to understand whether a molecule is a biosignature. For example O_2 can be a biosignature in itself, if potential abiotic sources are ruled out (Meadows et al., 2018). Abundant N_2 could be a result of tectonic regimes or biology itself (Lammer et al., 2019). However, if N_2 and O_2 are both abundant in an atmosphere, this could be a sign of a biosphere (Sproß et al., 2021). For different observations, molecules with no dipole moment like N_2 or O_2 are relatively hard to detect. However, for example the presence of the easier-to-detect molecule O_3 could suggest the presence of abundant O_2 (see the discussion in Gaudi et al., 2018). While some individual molecules like PH_3 (Sousa-Silva et al., 2020) have been discussed as direct biosignatures further pairs of molecules have been proposed as well. One example is the coexistence of CH_4 and CO_2 if CO is not present in the atmosphere (Krissansen-Totton et al., 2019, 2022). The coexistence of these molecules is very interesting, as they represent different ends of the redox-spectrum of carbon, ranging from fully reduced (CH_4) to fully oxidised (CO_2). In fact, in Earth's atmosphere any present CH_4 has a short lifetime, as it is not thermally stable in a oxygen-rich atmosphere at Earth-like temperatures and will be destroyed photochemically (Zerkle et al., 2012). The presence of CH_4 in our atmosphere is a direct result of biology (Sandora & Silk,

2020).

Although the coexistence of CH_4 and CO_2 with a low CO abundance can be a biosignature for certain planetary systems, it is of interest, whether it is possible to create this chemical coexistence under certain conditions. One example that shows that these conditions are possible in chemical equilibrium with the crust can be seen in Fig. 2.7, where the atmosphere in chemical phase equilibrium with the crust for a CI chondrite element abundances are shown. For $T \approx 500\,\mathrm{K}$ and $p = 100\,\mathrm{bar}$ CH_4 and CO_2 are both more abundant than 10%. As discussed by Seager et al. (2013b) it is important to exclude biosignatures which are possible to form in chemical equilibrium, motivating a further investigation of the possibility of the presence of the coexistence of CH_4 and CO_2 in planetary atmospheres.

In the following Sect. 3.2 we describe and characterise the gas phase composition in chemical equilibrium, based on minimised Gibbs free energy (see also Woitke et al., 2021). Based on this characterisation, we investigate different gas phase abundances from atmosphere crust phase equilibrium models in Chapter 2 with respect to their atmospheric type (Sect. 3.3).

3.2 Chemical equilibrium of CHNO atmospheres

As described in Sect. 1.4 the chemical composition in chemical equilibrium can be calculated by the minimisation of Gibbs free energy ΔG_f, given by

$$\Delta G_f = \Delta H_f - T\Delta S, \tag{3.1}$$

where ΔH_f is the enthalpy of formation, T the temperature of the system, and ΔS the entropy. Especially, for colder temperatures ($T \lesssim 600\,\mathrm{K}$), the entropy term becomes negligible and the minimisation of the Gibbs free energy becomes a minimisation of enthalpy of formation ΔH_f. The enthalpy of formation of a given gas-phase molecule can be described by the atomisation energy E_a, that is the energy that is required for transforming the molecule in the individual atoms. For example for H_2O, this leads to

$$E_a(\mathrm{H_2O}) = 2\Delta H_f(\mathrm{H}) + \Delta H_f(\mathrm{O}) - \Delta H_f(\mathrm{H_2O}). \tag{3.2}$$

Note that the ΔH_f are in general dependent on T. However, here we are using the ΔH_f for 0 K from NIST/JANAF (Chase et al., 1982; Chase, 1986, 1998).

Table 3.1: Atomisation energies E_a of some important gas phase molecules.

Molecule	E_a [eV]	Molecule	E_a [eV]	Molecule	E_a [eV]
N_2	9.76	NH_3	12.00	HCN	13.09
H_2O	9.51	H_2	4.48	O_2	5.12
CO_2	16.56	CO	11.11		
CH_4	17.02	C_2H_2	16.86		

For a system only consisting of CHNO, GGchem (Woitke et al., 2018) includes 52 gas phase molecules (H_2, C_2, C_3, C_4, C_5, N_2, N_3, O_2, O_3, CH, CH_2, CH_3, CH_4, C_2H, C_2H_2, C_2H_4, C_3H, NH, NH_2, NH_3, N_2H_2, N_2H_4, OH, HO_2, H_2O, CN, C_2N, C_2N_2, C_4N_2, CNN, NCN, CO, CO_2, C_2O, C_3O_2, NO, NO_2, NO_3, N_2O, N_2O_3, N_2O_4, N_2O_5, HCN, HCO, H_2CO, C_2H_4O, CNO, HNO, HONO, HNO_2, HNO_3, and CHNO). The atomisation energies for a selection of these molecules is listed in Table 3.1. Based on these, the set of most stable molecules of a gas mixture of CHNO can be found by exothermic reactions of CHNO molecules with members of the set which produce only molecules, which are part of the set of the most stable molecules again. Examples of such reactions are

$$
\begin{aligned}
H_2 &+ \tfrac{1}{4}CO_2 &&\rightarrow \tfrac{1}{2}\,H_2O &&+ \tfrac{1}{4}\,CH_4 && && \text{(-0.39 eV)},\\
CO &+ \tfrac{1}{2}H_2O &&\rightarrow \tfrac{3}{4}\,CO_2 &&+ \tfrac{1}{4}\,CH_4 && && \text{(-0.81 eV)},\\
HCN &+ \tfrac{3}{4}H_2O &&\rightarrow \tfrac{3}{8}\,CO_2 &&+ \tfrac{5}{8}\,CH_4 &&+ \tfrac{1}{2}\,N_2 && \text{(-1.51 eV)},\\
C_2H_2 &+ \tfrac{3}{2}H_2 &&\rightarrow \tfrac{3}{4}\,CO_2 &&+ \tfrac{5}{4}\,CH_4 && && \text{(-2.56 eV)},\\
NH_3 &+ \tfrac{3}{8}CO_2 &&\rightarrow \tfrac{3}{4}\,H_2O &&+ \tfrac{3}{8}\,CH_4 &&+ \tfrac{1}{2}\,N_2 && \text{(-2.83 eV)},\\
O_2 &+ \tfrac{1}{2}CH_4 &&\rightarrow \quad H_2O &&+ \tfrac{1}{2}\,CO_2 && && \text{(-4.17 eV)}.
\end{aligned}
$$

This shows that the most stable forms of CHNO is the set of CH_4, CO_2, H_2O, and N_2. As long as all four of these molecules are present, the further addition of any other CHNO bearing molecule will eventually exothermically react to form only molecules that are parts of this set. With increasing temperatures, the entropy term gains importance and H_2 and CO are the first additional molecules which become present.

For such an atmosphere with only these four molecules, the total gas pressure $p_{\rm gas}$ can be expressed by the partial pressures p_m of the molecules m as

$$p_{\rm gas} = p_{H_2O} + p_{CH_4} + p_{CO_2} + p_{N_2}. \tag{3.3}$$

Furthermore the hypothetical atomic pressure $\tilde{p}_{\mathrm{atom}}$ after full atomisation can be expressed as

$$\tilde{p}_{\mathrm{atom}} = 3 \cdot p_{\mathrm{H_2O}} + 5 \cdot p_{\mathrm{CH_4}} + 3 \cdot p_{\mathrm{CO_2}} + 2 \cdot p_{\mathrm{N_2}}. \tag{3.4}$$

The hypothetical partial atomic pressure $\tilde{p}_k$ of element k is given by the partial pressures of the molecules i and the stoichiometric factors $s_{i,k}$ with

$$\tilde{p}_k = \sum_i p_i s_{i,k}. \tag{3.5}$$

For the set of most stable molecules, this results in

$$\tilde{p}_{\mathrm{H}} = H \cdot p_{\mathrm{atom}} = 2 \cdot p_{\mathrm{H_2O}} + 4 \cdot p_{\mathrm{CH_4}}, \tag{3.6}$$

$$\tilde{p}_{\mathrm{C}} = C \cdot p_{\mathrm{atom}} = p_{\mathrm{CO_2}} + 4 \cdot p_{\mathrm{CH_4}}, \tag{3.7}$$

$$\tilde{p}_{\mathrm{O}} = O \cdot p_{\mathrm{atom}} = p_{\mathrm{H_2O}} + 2 \cdot p_{\mathrm{CO_2}}, \tag{3.8}$$

$$\tilde{p}_{\mathrm{N}} = N \cdot p_{\mathrm{atom}} = 2 \cdot p_{\mathrm{N_2}}. \tag{3.9}$$

Here H, C, O, and N represent the element abundances normalised by $H + C + O + N = 1$.

Based on Eqs. 3.3 and 3.6 to 3.9 we can formulate the molecular partial pressures of the set of most stable molecules as

$$\frac{p_{\mathrm{H_2O}}}{p_{\mathrm{gas}}} = \frac{H + 2O - 4C}{H + 2O + 2N}, \tag{3.10}$$

$$\frac{p_{\mathrm{CH_4}}}{p_{\mathrm{gas}}} = \frac{H - 2O + 4C}{2H + 4O + 4N}, \tag{3.11}$$

$$\frac{p_{\mathrm{CO_2}}}{p_{\mathrm{gas}}} = \frac{2O + 4C - H}{2H + 4O + 4N}, \tag{3.12}$$

$$\frac{p_{\mathrm{N_2}}}{p_{\mathrm{gas}}} = \frac{2N}{H + 2O + 2N}. \tag{3.13}$$

As long as the element abundances satisfy that all four partial pressures are not negative, this set of molecules is the favourable one in chemical equilibrium. The only pressure, which cannot become negative, is $p_{\mathrm{N_2}}$, underlining that the N abundance does not interfere with the CHO system. The

other molecular partial pressures can become negative for

$$C > \frac{1}{4}H + \frac{1}{2}O, \tag{3.14}$$

$$O > \frac{1}{2}H + 2C, \tag{3.15}$$

$$H > 2O + 4C. \tag{3.16}$$

For these constraints, the respective molecule is replaced by condensed graphite (C[s]), O_2, and H_2, respectively. Based on these atmospheric compositions, we define the three different atmospheric types of hydrogen-rich type A, oxygen-rich type B, and the coexistence of H_2O, CH_4, CO_2, and N_2.

By pairwise equating Eqs. 3.10, 3.11, and 3.12, we can find the parameter values, where two molecules are equally abundant. This results in

$$p_{H_2O} = p_{CH_4} \Leftrightarrow 12C = 6O + H, \tag{3.17}$$

$$p_{H_2O} = p_{CO_2} \Leftrightarrow 12C = 2O + 3H, \tag{3.18}$$

$$p_{CO_2} = p_{CH_4} \Leftrightarrow H = 2O. \tag{3.19}$$

In Fig. 3.1 the atmospheric type in the plane of CHO are shown. In order to show this three dimensional space in two dimensions, we choose axes to represent the oxygen to hydrogen ratio and the carbon abundance. For the oxygen to hydrogen ratio, we $(O-H)/(O+H)$, where +1 equates to only oxygen and no hydrogen ($O/H \rightarrow \infty$) and -1 to a pure hydrogen mix ($O/H \rightarrow 0$). As the results are mostly independent of the nitrogen abundance, the carbon abundance is calculated relative to the CHO system.

3.2.1 Chemical equilibrium with GGchem

Following up on the simplified estimations based on $\Delta H_f(0\,\mathrm{K})$, we compare this to calculations of the equilibrium chemistry with GGchem (Woitke et al., 2018) based on the minimisation of the total Gibbs free energy. The inclusion of the four CHNO elements results in the above mentioned 52 gas phase molecules. The result of the full chemical equilibrium for $T_{\mathrm{gas}} = 400\,\mathrm{K}$, $p_{\mathrm{gas}} = 1\,\mathrm{bar}$, and $N = 10^{-4}$ can be seen in Fig. 3.2. As shown in Eq. 3.13, the theoretical partial pressure of N_2 cannot become negative and is decoupled from the CHO phase. Therefore the presented calculations for the chemical equilibrium are calculated for constant N abundances, chosen to be

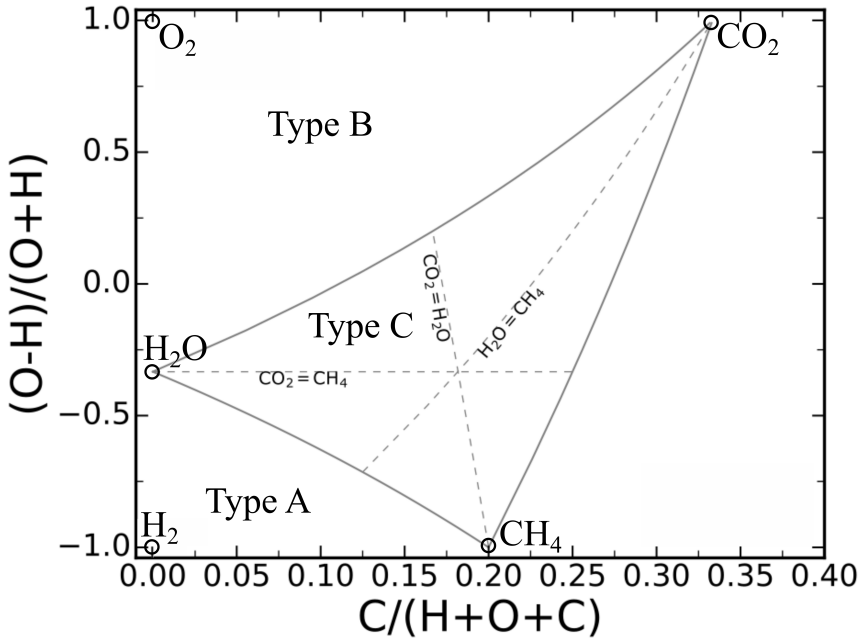

Figure 3.1: Atmospheric types in the CHO plane. The solid lines indicate the boundary between the atmospheric types as defined by Eq. 3.10 and 3.13. The dashed lines are showing the parameters, where two molecules show equal abundances of two molecules (see Eqs.3.17, 3.18, and 3.19). Indicated are also the positions of pure H_2, CH_4, CO_2, H_2O, and O_2 atmospheres.

$N = 10^{-4}$. It can be seen, that the theoretical assumptions above are matched very well and the atmospheric types can be clearly distinguished. The only molecule that is contaminating the type C atmosphere is H_2. For higher temperatures, CO gains importance and reaches abundances of a few %. Further models with different $T_{\rm gas}$ and N can be found in the Appendix B of Woitke et al. (2021).

In order to quantify the level of impurities, we investigate the atmospheric composition, with equal abundances of H_2O, CH_4, CO_2, and N_2. Based on Eqs. 3.10 - 3.13 this is given by $H = 6/13$, $C = 2/13$, $O = 3/13$, and $N = 2/13$. The amount of impurities by H_2, CO, and NH_3 for different temperatures can be seen in Table 3.2. It can be seen that the simplified chemical equilibrium is a good approximation for colder temperatures of $T \lesssim 600\,\mathrm{K}$.

These results of the major gas phase molecules are independent of the chosen nitrogen abundance, pressure, and temperature (see Appendix B of Woitke et al., 2021). The largest difference from the element mixing ratios can occur for type A atmospheres. For all abundances in type A atmospheres, CH_4, H_2O, and NH_3 are present. The set of these three fixed molecules is completed by one of N_2 or H_2. In order to distinguish which atmospheric subtype is present, can be expressed by the ratio between the hydrogen, that is not bound to carbon and oxygen ($H_{\rm eff} = H - 2O - 4C$) and the N. If $(N - H_{\rm eff})/(N + H_{\rm eff}) < -0.5$, H_2 is present, otherwise, the two nitrogen bearing

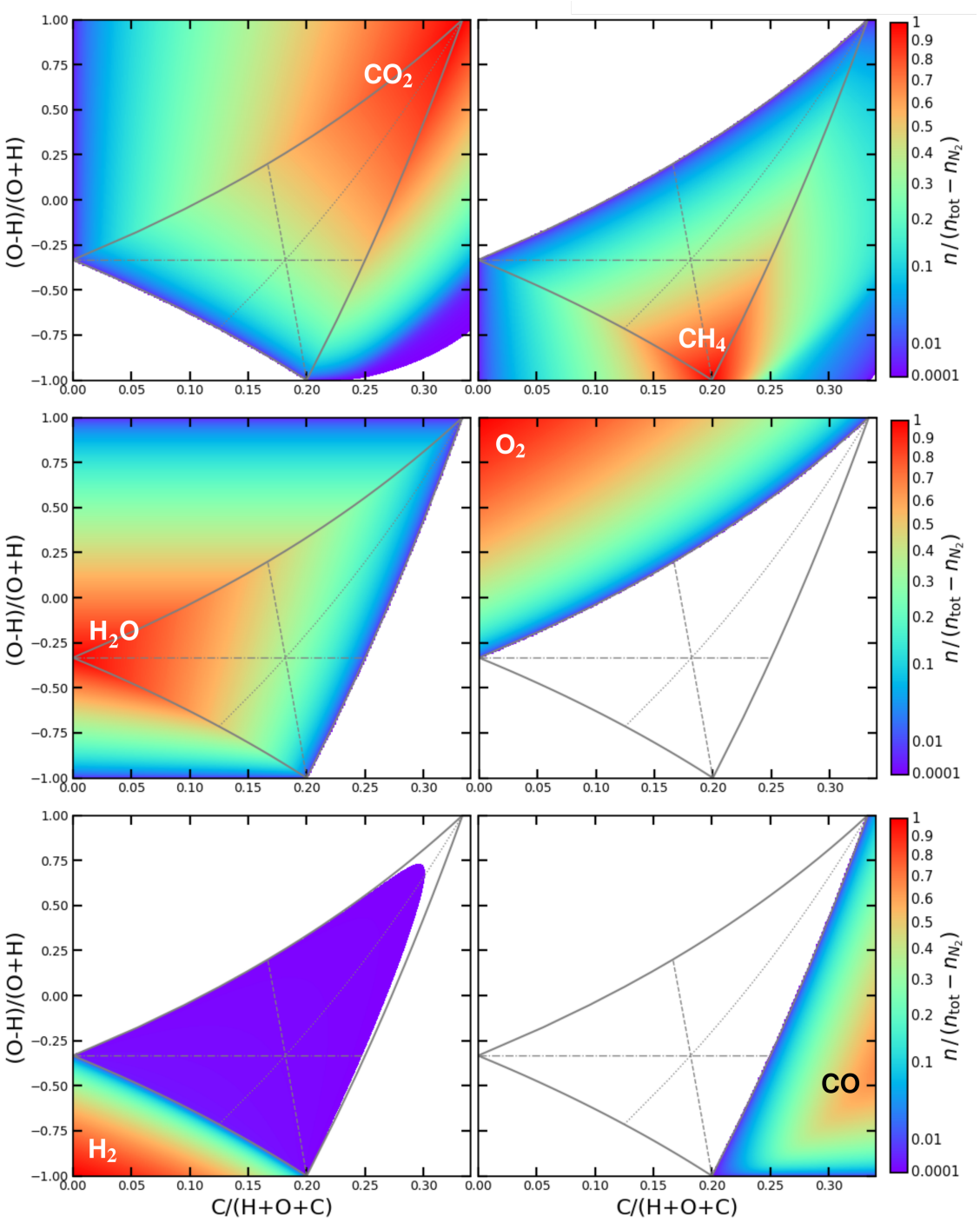

Figure 3.2: Chemical equilibrium calculations with GGchem for atmospheres with varying CHNO abundances at $T = 400$ K and $p = 1$ bar. The grey lines are indicating the theoretical model based on the enthalpy of formation discussion above. See also Fig. 3.1 for the grey background lines of the equilibrium model.

Table 3.2: Abundances of trace gases in a gas mixture of H_2O, CH_4, CO_2, and N_2 at equal abundances.

	200 K	300 K	400 K	500 K	600 K	700 K
H_2	2 ppb	5.8 ppm	390 ppm	0.52 %	2.9 %	9.5 %
CO	< 1 ppb	< 1 ppb	260 ppb	39 ppm	0.11 %	1.2 %
NH_3	205 ppb	4.7 ppm	23 ppm	101 ppm	130 ppm	130 ppm

species N_2 and NH_3. These subtypes are a result of the exothermic reaction of H_2 and N_2 by

$$N_2 + 3H_2 \rightarrow 2NH_3 \quad : -0.81\,\mathrm{eV}.$$

Based on this, the two subcategories of type A1 and type A2 are defined by the presence of N_2 and H_2, respectively.

3.2.2 Condensation of water and graphite

In the models so far, the potential supersaturation and resulting condensation of different molecules in the gas phase has been ignored. In principle various different condensates could be thermally stable, where the thermal stability of a condensate c is defined by supersaturation, that is $S(c) > 1$. In GGchem a total of seven condensates are included, which only incorporate CHNO elements. These condensates are H_2O[s], H_2O[l], NH_3[s], C[s], CH_4[s], CO[s], and CO_2[s]. However, for $T_{\mathrm{gas}} > 300\,\mathrm{K}$ only H_2O[l] and C[s] are thermally stable. In Fig. 3.3 the $S(\mathrm{C[s]}) = 1$ and $S(H_2O[l]) = 1$ saturation curves in the CHO abundance plane are shown for different temperatures. It can be seen, that H_2O[l] can be a thermally stable condensate for all three atmospheric types, whereas C[s] can only be saturated for type C atmospheric compositions. For colder temperatures an increasing part of the CHO parameter space is not achievable in chemical phase equilibrium as the condensation of the supersaturated molecule causes condensation and therefore changes in the elemental composition of the gas phase.

The maximum partial pressures $p(H_2O)$ is limited by the vapour pressure of water at the given pressure and temperature. Similarly, the partial pressures of the carbon containing gas particles are constrained by the vapour pressure of graphite. The only atmospheric compositions, which are unaffected by supersaturation are tending towards $(O-H)/(O+H) = \pm 1$ for smaller temperatures. The remaining atmospheric compositions are dominated by O_2 and CO_2 (for $(O-H)/(O+H) \rightarrow +1$) or H_2, NH_3, and CH_4 (for $(O-H)/(O+H) \rightarrow -1$). The parameter space of potential type C atmospheres becomes increasingly small. The atmospheric composition tends to either CO_2 or CH_4 dominance, while the other carbon bearing molecule looses significance.

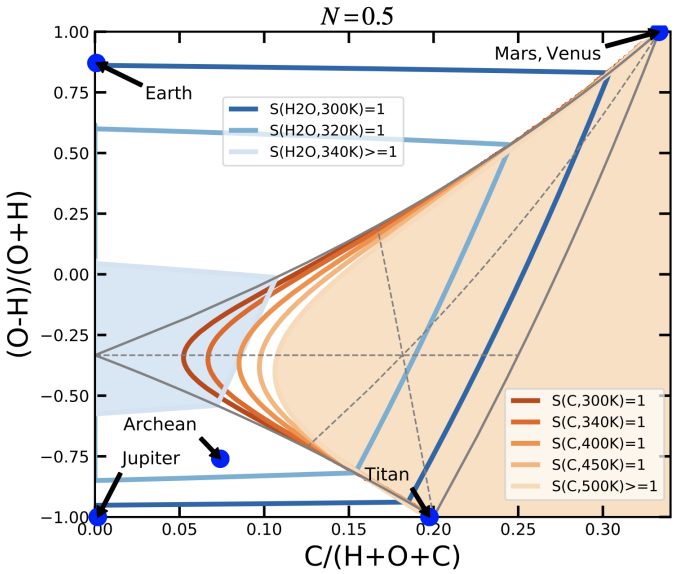

Figure 3.3: Supersaturation levels of H_2O[l,s] and C[s] for different temperatures. For this model, $N = 0.5$ is chosen. The atmospheric compositions of the present day Earth, Mars, Venus, Titan, and Jupiter as well as the atmospheric composition of Earth during the Archean (Miller, 1953). For the current day Earth composition, a 1.5% water content is assumed.

While the atmospheric composition is not dependent on N and p, the supersaturation of the different condensates is, as it is dependent on the partial pressure of the condensates. A lower N or a higher p_{gas} both result in a higher partial pressure of the present molecules for a given set of element abundances and therefore a higher supersaturation ratio. Thus the parameter space covered, where a condensate is supersaturated, is increasing.

3.3 Atmospheric type of near-crust atmospheric compositions

In the section before, the atmospheric composition was calculated by including only CHNO elements. However, the atmospheric composition of real planets have many more elements included. Especially further volatile elements like S can play significant roles in atmospheres of rocky exoplanets. As shown in Chapter 2 (Herbort et al., 2020), for higher temperatures it can be expected to also have further elements in the gas phase, including various different metals.

In this section, we want to investigate in how far the atmospheric compositions from Chapter 2 and Herbort et al. (2020) are behaving with respect to the atmospheric types introduced in this chapter. In Fig. 3.4, we show the atmospheric composition of different phase equilibrium models as described in Chapter 2 (Herbort et al., 2020), but for $p = 1$ bar. The different elemental abundances are described in Tab. 2.2 at the end of Chapter 2. For the visualisation we restrict the temperature range from 600 K to 200 K. In addition to the these rock inspired compositions for

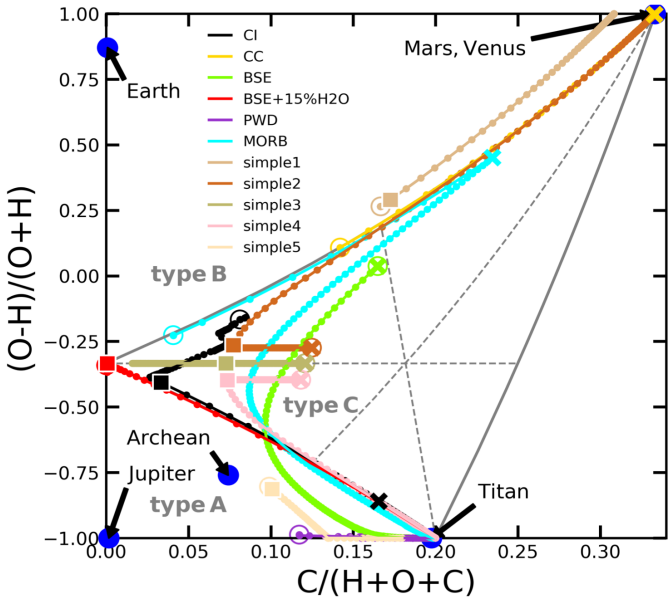

Figure 3.4: Visualisation of various different atmospheric compositions based on equilibrium chemistry models with equilibrium condensation as in Chapter 2.

the full model including 18 elements, further simple models with only four elements are include models starting at $T = 600\,\mathrm{K}$ in type A and type B atmospheres as well as three models for type C atmospheres.

The visualisation of the simple models shows that the location of an atmospheric compositions in the CHO parameter space can change in three different ways. 1) The condensation and removal of C[s] only reduces the Carbon content and therefore atmospheric compositions move leftward, where $(O-H)/(O+H)$ stays unaffected. 2) The condensation and removal of H_2O[l,s] is reducing H and O simultaneously, which in effect changes $(O-H)/(O+H)$ and carbon abundance. As a result, the atmosphere moves radially away from $(O-H)/(O+H) = -0.33$. 3) The simultaneous condensation and removal of H_2O[l,s] and C[s] results in a movement along the type C boundary towards atmospheric dominance of either CO_2 or CH_4. It should be noted, that noted, that none of the simple models changes the atmospheric type with condensation of either H_2O[l,s] or C[s].

The models from Chapter 2 follow this trend in general as well. However, the thermal stability of other condensates is also changing the gas phase composition. Especially the formation of phyllosilicates has a major influence on the availability of hydrogen in the gas phase (see. Sect. 2.5). The atmospheric type of these gas compositions can change for different temperatures.

Table 3.3: Summary of the atmospheric types introduced in this chapter.

	H_2O	CH_4	CO_2	N_2	NH_3	H_2	O_2	H_2O[l,s]	C[s]
Type A1	✔	✔	✘	✔	✔	✘	✘	✔	✘
Type A2	✔	✔	✘	✘	✔	✔	✘	✔	✘
Type B	✔	✘	✔	✔	✘	✘	✔	✔	✘
Type C	✔	✔	✔	✔	✘	✘	✘	✔	✔

3.4 Conclusion

In this chapter, we presented a definition of atmospheric types based on the thermally most stable atmospheric composition of atmospheres containing only the four elements CHNO. We find that the coexistence of CH_4, CO_2, H_2O, and N_2 is the most stable combination of molecules for low temperatures, where the entropy term of the Gibbs free energy becomes small with respect to the enthalpy. If due to stoichiometric constraints, the formation of only these four molecules is not possible, further atmospheric types are formed. For H-rich atmospheres, the atmospheric composition contains H_2O, CH_4, NH_3, and one of either N_2 or H_2 defining type A1 and A2 atmospheres. For these CO_2 and O_2 are not present. Atmospheres rich in O are type B atmospheres which are formed by H_2O, CO_2, O_2, and N_2, while CH_4 and H_2 are absent. In Table 3.3 these atmospheric types are summarised.

The investigation of our Solar System shows, that both type A (Jupiter, Titan) and type B (Earth, Mars) atmospheres are present. The second most important molecule in Titan's N_2 dominated atmosphere is CH_4, with an abundance of about 5 %. Due to its cold temperature the atmosphere is almost free of water, which has frozen out. However, the about 0.15% of H_2 present (Niemann et al., 2005) show that this atmosphere can be categorised as a type A atmosphere. The CO_2 dominated atmosphere of Mars on the other hand is a type B atmosphere, as there are about 0.1% O_2 present (Barker, 1972). Venus' atmosphere is also CO_2 dominated with trace abundances of O_2, but no sign of CH_4 or NH_3 (see Rimmer et al., 2021a, and citations therein). Thus the Venus atmosphere is classified as a type B atmosphere as well. Type C atmospheres are not present in our solar system. However, for slightly warmer planets there are less constraints by the condensation of water and graphite, that this atmospheric composition is more feasible. The diversity of detected planets with various different equilibrium temperatures provides no reasoning that these worlds should not exist. Especially the equilibrium chemistry calculations for a larger set of elements and element abundances inspired by rock compositions show that type C atmospheres

should form for $T \gtrsim 400\,\mathrm{K}$. This underlines the importance of understanding the planetary surrounding before the detection of an atmospheric composition is claimed to be a biosignature. For example, the coexistence of CO_2 and CH_4 in Earth's atmosphere is a result of biology producing CH_4. However, these molecules can be in equilibrium at high abundances in type C atmospheres. Our atmospheric types suggest that exclusive pairs of molecules such as CH_4 and O_2 or NH_3 and CO_2 potential gas phase pairs for the search for biosignatures. For example Krissansen-Totton et al. (2019) proposed that the detection of CH_4 and CO_2 without substantial amounts of CO can only be sustained, if large fluxes of CH_4 are present to replenish the CH_4 depletion caused by photochemistry. It is argued that fluxes large enough to do so can only be sustained by biological processes. Therefore it is important to re-evaluate, whether naturally occurring atmospheric compositions can exist, where the photochemical destruction of CH_4 can be naturally replenished by exothermic reactions.

"He knew as soon as those clouds hit, his world would go dark, the wind tossing up the soot on the ground and stirring it up into a frenzy until wind and cloud and graphite rain scratched out whatever remained."

- Kilae Palpant, *After Colour* in *Around Distant Suns*

4

Influence of surface composition on the diversity of cloud condensates

In this chapter a bottom-to-top atmospheric model based on an atmosphere-crust interaction layer in chemical equilibrium is introduced. The atmospheres are investigated with respect to the thermal stability of different condensates in the resulting atmospheres. This allows the investigation of what cloud condensates could be present in atmospheres of various different planets. The results from this work provide a first step towards characterising the surface conditions of rocky exoplanets based on the atmospheric composition of the higher atmosphere and the presence of different cloud condensates.

This chapter is published as 'The atmospheres of rocky exoplanets II. Influence of surface composition on the diversity of cloud condensates' by O. Herbort, P. Woitke, Ch. Helling, and A. L. Zerkle in Astronomy & Astrophysics 658, A180 (2022).

4.1 Introduction

The surfaces of rocky planets, moons, and exoplanets show a remarkable diversity of physical and chemical conditions. Surfaces range from bare rocks (e.g. Mercury or LHS 3844 b (Kreidberg et al., 2019)), frozen or liquid water (e.g. Europa or Earth), and magma oceans, covering the entire planet during their formation (Nikolaou et al., 2019; Elkins-Tanton, 2012) or covering only the dayside of highly irradiated, tidally locked planets (magma ponds; Kite et al., 2016). Examples would be exoplanets such as 55 Cnc e or CoRoT 7b (Léger et al., 2009, 2011). Although there is no rocky planet larger than Earth in our Solar System, such planets, referred to as super Earths, have been detected in multiple stellar systems at various distances from the host star (e.g. Dittmann et al., 2017; Ribas et al., 2018; Bluhm et al., 2020; Stock et al., 2020). In addition to these super Earths, planets with a mass, radius, and stellar irradiation more similar to Earth, such as Proxima Centauri b (Anglada-Escudé et al., 2016) or the seven rocky planets in the Trappist 1 system (Gillon et al., 2017), have been detected. Some of these (e.g. Trappist 1 d, e, f, and g) might allow for liquid water on their surface.

The composition of the surface rocks on Earth alone varies substantially from mafic (magnesium and iron rich, e.g. basalts) to felsic (rich in lighter elements, such as Si, e.g. granite), depending on location. This elemental composition is not only dependent on the planet itself, but also on the stellar system. Elemental ratios in the nearby stars vary by orders of magnitude with respect to the solar values (Hinkel et al., 2014). Therefore, a substantial variation in the composition of the surface rocks for exoplanets can be expected. However, through outgassing and deposition, the surface conditions of rocky planets are coupled to the gas composition and cloud formation in the atmosphere, which can be observed (see Grenfell et al., 2020).

Present-day observational techniques do not allow observations of the surfaces of rocky exoplanets in more detail than a large-scale temperature map (see e.g. Demory et al., 2016a; Hammond & T. Pierrehumbert, 2017). Furthermore, global aspects of planets, such as the presence of a cloud cover on GJ 1214 b (Kreidberg et al., 2014) or ruling out a hydrogen-dominated extended atmosphere for the two innermost planets of the Trappist 1 system (De Wit et al., 2016), are possible. Transmission spectroscopy can provide insights into the optically thin part of the atmosphere. This allows the detection of gas phase abundances as well as some cloud properties from absorption or scattering features (Samra et al., 2020). This is, however, currently only possible for a very limited number of rocky planets, due to their small size. Tentative detections of the gas phase molecules

HCN (55 Cnc e Tsiaras et al., 2016) and H_2O (LHS 1140 b Edwards et al., 2020) have also been suggested. For gas giants, the situation is different and various atoms and molecules have been detected: He (Nortmann et al., 2018), Na (Seidel et al., 2019), K and Li (Chen et al., 2018), CO (Barman et al., 2015; Sheppard et al., 2017), CH_4 (Barman et al., 2015), H_2O (Barman et al., 2015; Alonso-Floriano et al., 2019), HCN, NH_3, C_2H_2 (Giacobbe et al., 2021) Fe and Ti (Hoeijmakers et al., 2018), TiO (Chen et al., 2021).

The James Webb Space Telescope (JWST) (Gardner et al., 2006) will enable the detection of a handful of atmospheric molecules by a sequence of repeated transit observations for rocky exoplanets (see e.g. Komacek et al., 2020; Wunderlich et al., 2020). Planned space telescopes such as ARIEL (Tinetti et al., 2018), LUVOIR (Bolcar et al., 2016), and HabEx (Stahl et al., 2020) are designed to characterise atmospheres of rocky exoplanets in the habitable zone. The 30 m class telescopes, for example the E-ELT (Gilmozzi & Spyromilio, 2007), will also provide the opportunity to observe some atmospheric molecules (see Lopez-Morales et al., 2019). These instruments may allow the combined detection of atmospheric composition, and strict limits on surface temperature and surface pressure, which could result in the detection of liquid water on exoplanets and potentially a planet that could be habitable to life as we know it.

Emission spectra can in principle provide direct clues about the surface composition (Hu et al., 2012; Mansfield et al., 2019), in particular if polarimetry is used. However, this will be strongly affected by clouds being present (Rossi & Stam, 2017, 2018). In case of full cloud coverage, similar to Venus, the view on the surface will be obstructed, and hence information can only be deduced from the top of the cloud layer, rather than the planet surface. Therefore it is not only important to better understand the fundamental physics of cloud formation (see Helling, 2019), but also in how far the chemical composition of clouds can be linked to the surface composition and conditions ($p_{\rm surf}, T_{\rm surf}$).

Atmospheres of hot rocky planets have been modelled as vaporised rock compositions (e.g. Miguel et al., 2011; Schaefer et al., 2012; Kite et al., 2016). Thompson et al. (2021) present experimental compositions of gas outgassed from heated chondritic material. For hot rocky planets, the chemical composition of the clouds can drastically differ from the clouds known in our solar system, with models suggesting a composition of condensed minerals (e.g. Mahapatra et al., 2017). These minerals are also found to contribute to the cloud composition of highly irradiated gas giants (e.g. Ackerman & Marley, 2001; Wakeford & Sing, 2015; Helling et al., 2020; Woitke et al., 2020;

Samra et al., 2020). The interaction between the interior of a rocky planet and its atmosphere is a matter of recent research, especially focusing on the atmospheres of young rocky exoplanets in contact with magma oceans and volcanic outgassing (e.g. Gaillard & Scaillet, 2014; Bower et al., 2019; Katyal et al., 2019; Ortenzi et al., 2020; Graham & Pierrehumbert, 2020; Lichtenberg et al., 2021).

In this work, we aim to better understand the chemical diversity of possible cloud material compositions under the varying element abundances in the atmospheres of rocky exoplanets. We want to establish a link between the planetary surface and the cloud material composition in the atmosphere above. Although this relation will be degenerate (see discussion in Sect. 4.7), it will be a step towards constraining the surface conditions with future observations of atmospheric and cloud composition. We focus on the lower atmosphere, the troposphere, where the atmospheric gas interacts with the planet surface chemically, and is then mixed upwards by convection to form the clouds.

First, we introduce our atmospheric model in Sect. 4.2, before we show the results of one example model in Sect. 4.3.1. We describe how the resulting cloud materials depend on the assumed crust element abundances in Sect. 4.3.2 and what that implies for the atmospheric gas composition in Sect. 4.3.3. The link between water clouds and water as a stable condensate on the planet surface is discussed in Sect. 4.3.4. The impact of surface pressure on the results is shown in Sect. 4.3.5. In Sect. 4.4, we discuss the implications of this model to planets that will become observable in the near future. We conclude with a summary of our findings in Sect. 4.5.

4.2 Method: Atmospheric model

In the work presented here, we develop a model for the lower atmosphere (troposphere) linked to the surface of a rocky planet. That is, a planet with an overall density consistent with a rocky body ($\rho \approx 5\,\mathrm{g/cm^3}$) and a surface which can be either solid or molten. The atmosphere and surface are considered to be in chemical and phase equilibrium and the atmosphere is built from bottom to top based on the surface-atmosphere interaction.

4.2.1 Polytropic atmosphere

The atmosphere is considered to be in hydrostatic equilibrium,

$$\frac{\mathrm{d}p}{\mathrm{d}z} = -\rho g \tag{4.1}$$

with the atmospheric pressure p, atmospheric height z, gas mass density ρ and gravitational acceleration g. The latter is deduced from the assumed planetary mass M_P and radius R_P by

$$g = \frac{GM_\mathrm{P}}{R_\mathrm{P}^2}, \tag{4.2}$$

where G is the gravitational constant. The extent of the atmosphere is small compared to the planetary radius and thus we treat g as constant. Temperature T and pressure p are assumed to be related by the barotropic equation of state,

$$T = \mathrm{const} \cdot p^\kappa. \tag{4.3}$$

We note that κ is related to the change of temperature with increasing height in the troposphere, the lapse rate $\mathrm{d}T/\mathrm{d}z$. This assumption is motivated by observations of the lapse rate in atmospheres of solar system bodies (Table 4.1). Using Eq. 4.3 and the ideal gas law

$$p = \frac{\rho}{\mu} k_\mathrm{B} T, \tag{4.4}$$

where μ is the mean molecular weight and k_B is the Boltzmann constant, we get

$$\frac{\mathrm{d}T}{\mathrm{d}z} = \frac{\mathrm{d}T}{\mathrm{d}p}\frac{\mathrm{d}p}{\mathrm{d}z} = \mathrm{const} \cdot (-\rho g)\kappa p^{\kappa-1} = (-\rho g)\,\kappa\,\frac{T}{p} = -\kappa g \frac{\mu}{k_\mathrm{B}}. \tag{4.5}$$

Rearranging for κ,

$$\kappa = \frac{k_\mathrm{B}}{\mu g}\frac{\mathrm{d}T}{\mathrm{d}z}. \tag{4.6}$$

The polytropic index γ is given by

$$\gamma = \frac{1}{1-\kappa}. \tag{4.7}$$

For an adiabatic atmosphere, the polytropic index is given by

$$\gamma_{\text{adiabat}} = \frac{c_p}{c_v} \overset{\text{ideal gas}}{\approx} \frac{f+2}{f}\,, \tag{4.8}$$

with f being the number of degrees of freedom of the gas species. For a cold gas consisting of linear molecules such as H_2, CO_2, or N_2, the number of degrees of freedom is $f = 5$ and thus $\gamma_{\text{adiabat}} \approx 1.4$. However, the latter part of Eq. (4.8) only holds true, if the gas is an ideal gas and thus energy is only stored in its translational and rotational degrees of freedom. In real atmospheres the species can react with each other, which releases chemical binding energy as function of height, for example due to condensation, in which case the atmospheric structure will be flatter than an adiabat. Table 4.1 provides an overview of multiple atmospheres of planets and moons in our solar system. Although the rocky bodies in our solar system show a large range in $\mathrm{d}T/\mathrm{d}z$, the polytropic indices are only ranging from $\gamma = 1.114$ to $\gamma = 1.282$ for the rocky bodies. The gas giant Jupiter on the other hand shows a higher polytropic index with $\gamma = 1.441$. Therefore, we assume $\gamma = 1.25$ in all our models for rocky exoplanets instead of its adiabatic value. The resulting atmospheric profiles can be seen in Fig. 4.1. Furthermore, the difference in mean molecular weight for the different atmospheres can be seen in Table 4.1, underlining it's potential for atmospheric characterisation.

The effect of deviations from adiabatic profiles due to condensation is sometimes referred to as moist convection, opposed to dry convection, when considering the condensation of water clouds. However, similar physics is at work for different condensates. Under dry conditions no condensates form, and the lapse rate is large, close to its adiabatic value. Phase transitions result in the release of latent heat (enthalpy of vaporisation), which heats up the surrounding gas, resulting in a smaller lapse rate. Calculations show that the release of latent heat is negligible for mineral material condensation in a H_2-rich gas of solar composition (Woitke & Helling, 2003), because the number of condensible molecules per gas particle is $< 10^{-4}$, as is true in Jupiter's atmosphere. However, if substantial amounts of the atmosphere can condense, the difference may become significant. In the Earth atmosphere, the condensible fraction is about 10^{-2}, which results in lapse rates of (10-30) K/km and (3.5-6.5) K/km, for dry and moist convection, respectively (see e.g. Peirce et al., 1998; Muralikrishna & Manickam, 2017).

Table 4.1: Comparison of the lower atmospheres of multiple bodies in the solar system.

	Earth	Venus	Mars	Titan	Jupiter
T_{surf} [K]	288	740*	210$^{\cap}$	94†	
p_{surf} [bar]	1	93*	0.006$^{\cup}$	1.5†	
g [m/s^2]	9.81	8.87*	3.72	1.35	24.8
μ [amu]	29	43.5	43.5	27.4	2.3
$\frac{\mathrm{d}T}{\mathrm{d}z}$ [K/km]	6.5$^{\diamond}$	7.8^{+}	2$^{\triangle}$	1.0$^{\natural}$	2.1
Valid to [bar]	0.2	0.23^{+}	$3 \cdot 10^{-4}\nabla$	0.3$^{\forall}$	0.3§
κ	0.197	0.166	0.102	0.220	0.306
γ	1.245	1.199	1.114	1.282	1.441

References: ($\diamond$) Muralikrishna & Manickam (2017); ($*$) Basilevsky & Head (2003); ($\dagger$) Fulchignoni et al. (2005); ($\cup$) Haberle (2015); ($\cap$) Smith (2008); ($+$) Limaye et al. (2017); (∇) Holstein-Rathlou et al. (2016); ($\forall$) Schinder et al. (2012); ($\S$) Seiff et al. (1998)

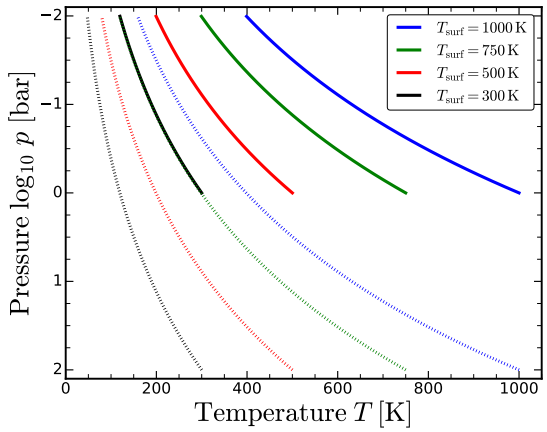

Figure 4.1: Pressure-temperature diagrams for various models investigated in this work. Models for surface pressure of 1 bar and 100 bar are shown with solid and dotted lines, respectively. The line colour corresponds to the surface temperature. All models are calculated up to 10 mbar.

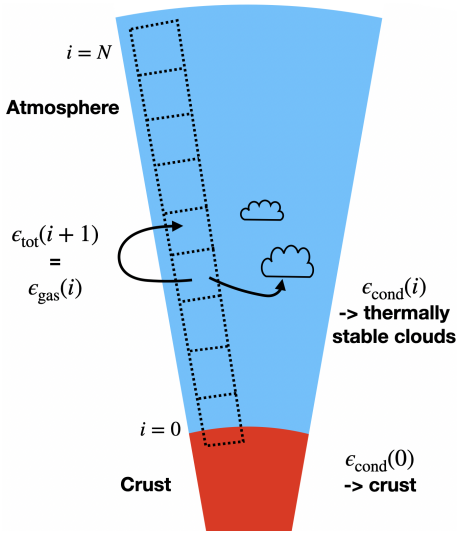

Figure 4.2: Sketch of the bottom-to-top GGchem model for an atmosphere with cloud condensation. Chemical and phase equilibrium is solved in each atmospheric layer, and the condensates are interpreted as clouds. The condensed element abundances ϵ_{cond} are removed, and the remaining gas phase element abundances in layer i are used for the total element abundances ϵ_{tot} in the next atmospheric layer $i + 1$.

Table 4.2: Comparison of different element abundances given in % mass fractions used in this work.

	BSE	BSE12	BSE15	CC	MORB	CI	PWD	Earth	Archean	solar
	1	1∗	1∗	2	3	4	5†	1∇	1∗	6
H	0.006	1.198	1.457	0.045	0.023	1.992		0.3341	2.309	98.4
C	0.006	0.0054	0.005	0.199	0.019	3.520	1.2	1.957	0.0052	0.316
N	8.8E-05	7.9E-05	7.7E-05	0.006	5.5E-05	0.298		0.02533	7.6E-05	0.092
O	44.42	49.280	50.320	47.20	44.5	46.420	41.0	50.100	49.880	0.765
F	0.002	0.0018	0.0017	0.053	0.017	0.0059		0.04816	0.0017	0.000067
Na	0.29	0.260	0.253	2.36	2.012	0.505		2.145	0.251	0.0039
Mg	22.01	19.69	19.180	2.20	4.735	9.790	18.0	1.999	19.010	0.094
Al	2.12	1.897	1.847	7.96	8.199	0.860	0.27	7.234	1.831	0.0074
Si	21.61	19.33	18.830	28.80	23.62	10.820	18.0	26.17	18.670	0.089
P	0.008	0.0072	0.0070	0.076	0.057	0.098	0.22	0.06906	0.0069	0.00078
S	0.027	0.024	0.024	0.070	0.110	5.411	3.3	0.06361	0.023	0.041
Cl	0.004	0.0036	0.0035	0.047	0.014	0.071		0.04271	0.0035	0.0011
K	0.02	0.018	0.017	2.14	0.152	0.055		1.945	0.017	0.00041
Ca	2.46	2.201	2.143	3.85	8.239	0.933	6.9	3.499	2.125	0.0086
Ti	0.12	0.107	0.105	0.401	0.851	0.046		0.3644	0.104	0.00042
Cr	0.29	0.260	0.253	0.013	0.033	0.268		0.01181	0.251	0.00222
Mn	0.11	0.098	0.096	0.072	0.132	0.195		0.06543	0.095	0.0014
Fe	6.27	5.610	5.463	4.32	7.278	18.710	10	3.926	5.416	0.172
sum	99.77	99.99	100.00	99.81	99.99	100.00	99.73	100.00	100.00	100.00

Notes: ∗: Element abundances based on BSE abundances, but altered by the addition of H_2O, see Sect. 4.2.3

†: The PWD data is completed by taking the missing element abundances from BSE, MORB, or CI as indicated.

∇: The element abundances are created by a fit to Earth atmospheric concentrations, see Sect. 4.6.

(1) Bulk Silicate Earth: Schaefer et al. (2012); (2) Continental Crust: Schaefer et al. (2012); (3) Mid Oceanic Ridge Basalt: Arevalo & McDonough (2010); (4) CI chondrite: Lodders et al. (2009); (5) Polluted White Dwarf: Melis & Dufour (2016); (6) solar: Asplund et al. (2009)

4.2.2 Modelling approach

In order to model the atmosphere of a rocky exoplanet, we assume a polytropic atmosphere in hydrostatic equilibrium, as described in Eq.(4.5) with the polytropic index $\gamma = 1.25$ (Sect. 4.2.1), and calculate the abundances of gas and condensed species in chemical and phase equilibrium at each point in the atmosphere.

In each atmospheric layer, we use the chemical and phase equilibrium solver GGchem (Woitke et al., 2018) to determine the abundances of the thermally-stable condensates. These condensates j are then removed from the model, until the supersaturation ratio S_j for each thermally-stable condensate is unity (see also Sect. 1.4). This way, we determine the depletion of elements by condensation with increasing height, following a parcel of gas which is moving upwards in the atmosphere. We assume that the condensation and removal by precipitation is fast enough to ensure that all supersaturation ratios obey $S \leq 1$ at any point in the atmosphere. The element depletion from this approach reduces the abundance of affected elements until $S_j = 1$ is reached. Therefore the depletion does not reduce the affected elements completely, but some remnant parts determined by the vapour pressure remain in the gas phase.

This approach is similar in nature to those in previous works by for example Lewis (1969), Lewis & Prinn (1970), and Weidenschilling & Lewis (1973). These works have used a similar approach of atmospheric equilibrium calculation with removal of thermally-stable condensates to investigate cloud condensates and gas compositions. They especially focused on gas giants as well as ice giants and included the major volatile elements (esp. H, He, C, N, and O). In the model presented here, we include further elements (see Sec. 4.2.3) into our model to also investigate the stability of metal-bearing condensates. The inclusion of the most common rock-forming elements also allows the investigation of the planetary crust in contact with the atmosphere. This allows us to use this approach for rocky exoplanets.

A further difference to the previous studies is the assumed atmospheric structure. The older models (e.g. Lewis, 1969) include a feedback from the cloud condensation to the atmospheric $(p_{\rm gas}, T_{\rm gas})$ structure. In order to keep our model as quick and simple as possible, we do not include any of these feedbacks and keep the polytropic index constant throughout the atmosphere.

The base of our atmospheric model for rocky planets is at the bottom of the atmosphere, where we calculate the chemical composition of the crust and the gas above it in chemical and

phase equilibrium (similar to Herbort et al., 2020). These results only depend on the total element abundances $\epsilon_{\rm tot}$, the surface pressure $p_{\rm surf}$, and the surface temperature $T_{\rm surf}$. The gas phase composition of the boundary layer ($i = 0$) is a by-product of this computation. The resulting element composition of the crust is denoted by $\epsilon_{\rm cond}(0)$ and the element composition of the gas in contact with the crust as $\epsilon_{\rm gas}(0)$, see Herbort et al. (2020). We then continue to model the atmosphere layer by layer, from bottom to top. The gas phase element abundances in one atmospheric layer i are used for the total element abundances of the layer above it $\epsilon_{\rm tot}(i+1) = \epsilon_{\rm gas}(i)$, where $i = \{1, ..., N-1\}$ is a layer index and N the total number of atmospheric layers. We use $N = 300$ throughout the models presented in this work. Figure 4.2 provides a sketch of our modelling approach.

With this simple approach we provide a fast atmospheric model to identify potential cloud condensates and to discuss at which heights these condensates might occur. We do not include kinetic cloud formation, nucleation rates, photochemistry, release of latent heat, nor kinetic chemistry in this model. Also geological effects (volcanism, subduction etc.) and biological rates are not included.

An important result of this modelling procedure are the number densities of the condensed species $n_{\rm cond}(z)$. These number densities reflect the amount of condensates that fall out as we lift the gas parcel by Δz. According to our approximation of an instant and complete removal of all condensates, $n_{\rm cond}$ is expected to be an estimate and upper limit for the actual cloud densities, where that removal is slower and incomplete. The calculation of the actual cloud densities would require a proper kinetic cloud model, including nucleation, mixing, growth, and gravitational settling rates, which goes beyond the scope of this chapter. Instead, we use the normalised number density ($n_{\rm cond}/n_{\rm tot}$) of the condensed species ($n_{\rm cond}$) with respect to the total gas density ($n_{\rm tot}$) as an indicator for a cloud species to be relevant or not. We have experimented with different threshold concentrations and use 10^{-10} for the investigation of dominating cloud condensates (esp. Sect. 4.3.2.1) and 10^{-20} for trace condensates that allow an investigation of chemical connections of different condensates (esp. Sect. 4.3.2.2). Regions in $(p_{\rm gas}, T_{\rm gas})$ where these thresholds are overcome indicate the positions of the cloudy regions. Our results are hence presented in Sect. 4.3 for these choices of the threshold value.

One intrinsic result of this model is that for a given cloud condensate, the highest number density of condensates is found when a condensate becomes thermally stable (cloud base). For the atmosphere above, the number density decreases subsequently, resulting in a characteristic

shark-fin-like cloud distribution. This can also be seen in works such as Atreya et al. (1999). Ackerman & Marley (2001) introduced a factor $f_{\rm rain}$ to their models to reproduce a more realistic cloud formation model by allowing replenishment to the lower atmospheric layers and different supersaturation levels. We do not include a similar factor to our model, as the scope of this work is to investigate which condensate can be thermally stable in general. The information on which condensates are thermally stable can subsequently be used for future kinetic cloud formation models.

All our atmospheres are calculated up to $p_{\rm gas} = 10\,\mathrm{mbar}$. A continuation of the model to lower pressures with an isothermal or inversed temperature profile would produce no further clouds in our model. The potential condensates would be undersaturated in such regions, because the thermodynamic conditions for condensation would become less and less favourable with constant or increasing temperature.

4.2.3 Input parameters

We use the equilibrium condensation code GGchem (Woitke et al., 2018) and include 18 different elements (H, C, N, O, F, Na, Mg, Al, Si, P, S, Cl, K, Ca, Ti, Cr, Mn, and Fe). In total 471 gas species and 208 condensed species are included in our models. The molecular equilibrium constants $k_p(T)$ are based on Stock (2008), Barklem & Collet (2016), and the NIST/JANAF database (Chase et al., 1982; Chase, 1986, 1998). The $\Delta G^0_{\rm f}(T)$ for the condensed phase are taken from SUPCRTBL (Zimmer et al., 2016) and the NIST/JANAF database. The thermochemical data included in GGchem is tested down to temperatures of 100 K.

In order to investigate a large variety of different planets, various total element abundances $\epsilon_{\rm tot}$ are used at the base of the atmosphere. These are Bulk Silicate Earth (BSE, Schaefer et al., 2012), Continental Crust (CC, Schaefer et al., 2012), Mid Oceanic Ridge Basalt (MORB, Arevalo & McDonough, 2010), and CI chondrite (CI, Lodders et al., 2009). We add elemental compositions deduced from the polluted white dwarf SDSS J104341.53+085558.2 (Melis & Dufour, 2016). The contamination of such white dwarfs is interpreted as the accretion of planets and planetary bodies falling into the white dwarf and is the only current method to constrain the overall element abundances of planets in other stellar systems (see e.g. Farihi et al., 2016; Harrison et al., 2018; Wilson et al., 2019; Bonsor et al., 2020). However, not all elements can be measured in the polluted white dwarf, so we complete the dataset with element ratios from BSE, MORB, and CI to create the element abundances PWD BSE, PWD MORB, and PWD CI, respectively.

As in Herbort et al. (2020), we also include element abundances based on BSE, where the H and O abundances are increased to allow liquid water to be stable at the surface. Therefore, models with 12 % mass fraction and 15 % mass fraction added water are included and referred to as BSE12 and BSE15, respectively. We furthermore include an Archean model, inspired by an early Earth atmosphere, which might have been dominated in reducing species such as H_2 and CH_4 (Catling & Zahnle, 2020), before life emerged and ultimately caused the accumulation of atmospheric molecular oxygen during the Great Oxidation Event (Holland, 2002). Experiments by (Miller, 1953) and Miller & Urey (1959) used a similar atmospheric composition to study the origin of life. More recent research suggests that the early Earth had signifiantly smaller amounts of CH_4 in the atmosphere (see e.g. Kasting, 2014; Catling & Zahnle, 2020). In the exoplanetary context, similar atmospheres could exist, especially for high mass planets, which can sustain their hydrogen envelope and thus host a reducing atmosphere rich in hydrogen (Owen et al., 2020). In order to investigate an atmosphere similar to the current day Earth, we created a model to represent these conditions. In Sect. 4.6 we describe this model in detail. A model with solar abundances from Asplund et al. (2009) is also included.

4.3 Results

The resulting properties of our models are presented in this section. We aim to establish which cloud materials are likely to form over what kind of planetary surface. In our model, the planetary surface is characterised by the surface pressure (p_{surf}) the surface temperature (T_{surf}) and the set of total element abundances (ϵ_{tot}). For the atmospheric part of the model, we have introduced two more parameters, the polytropic index γ, and the surface gravity g. The composition of the near-crust atmospheric gas (i.e. the lowest point in our model) is determined by chemical and phase equilibrium with the planet surface.

First, we study the results for one specific set of element abundances (Sect. 4.3.1). Subsequently, we compare the results for different element abundances and investigate the cloud material (Sect. 4.3.2) and gas composition (Sect. 4.3.3). The link between water clouds and water on the surface is studied in Sect. 4.3.4. In Sect. 4.3.5 we focus on the influence of surface pressure to the cloud layers.

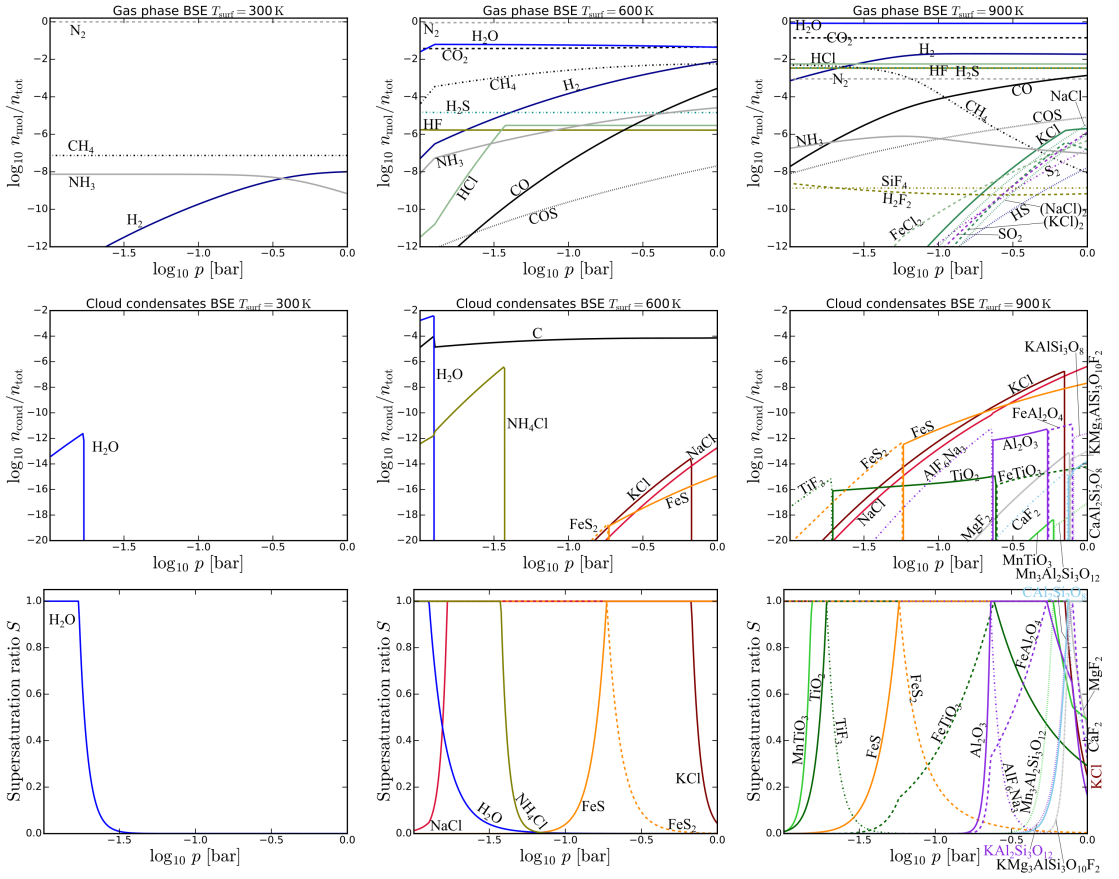

Figure 4.3: Atmospheric models for BSE total element abundances at different surface temperatures. **Upper panels:** gas composition, **middle panels:** cloud composition, **lower panels:** saturation levels. **Left panels:** T_{surf} = 300 K, **middle panels:** T_{surf} = 600 K, **right panels:** T_{surf} = 900 K. All gas species that reach a concentration of at least 1 ppb somewhere in the atmosphere are shown. All cloud species down to a concentration of 10^{-20} are shown. The supersaturation ratios of all condensates in the middle panels are visualised in the respective lower panel. Condensates belonging to one condensate chain are depicted in one colour.

4.3.1 Bulk Silicate Earth model

The principle behaviour of our model is studied for one example set of element abundances chosen to be Bulk Silicate Earth (BSE, Schaefer et al., 2012), considering different surface temperatures (T_{surf} = 300 K, 600 K, 900 K). These three surface temperatures represent some of the observed rocky exoplanets, namely Trappist-1 c,d (Delrez et al., 2018), LHS 1478 b (Soto et al., 2021), and K2-228 b (Livingston et al., 2018), respectively. Section. 4.4 provides a link to further known planets and the implications of our models with regard to cloud and surface compositions. Figure 4.3 shows the atmospheric composition (upper panels), cloud-condensate composition (middle panels) and saturation levels (lower panels) for these three models.

The composition of the gas phase as seen in the upper panels of Fig. 4.3 is determined by a) the

changing local thermodynamic condition ($p_{\rm gas}, T_{\rm gas}$), resulting in a smooth change in gas phase abundance, and b) the local element abundances. The local element abundance will be affected by the amount of material condensing ($n_{\rm cond}$). The onset of condensation results in a knee in the gas phase abundances.

For $T_{\rm surf} = 300\,{\rm K}$ (left side of Fig. 4.3, representative of Trappist-1 c,d), the atmosphere is almost a pure N_2 atmosphere with trace amounts of CH_4, NH_3, and H_2 with gas phase abundances of $10^{-6} > n_{\rm mol}/n_{\rm tot} > 10^{-9}$. H_2O[s] is the only condensate that is more abundant than $n_{\rm cond}/n_{\rm tot} > 10^{-20}$ and is thermally stable in the upper atmosphere.

The $T_{\rm surf} = 600\,{\rm K}$ model (middle column in Fig. 4.3, representative of LHS 1378 b) is also dominated by N_2, with H_2O, CO_2, H_2, and CH_4 reaching gas phase abundances of $10^{-1} > n_{\rm mol}/n_{\rm tot} > 10^{-3}$. Further 6 molecules reach gas phase abundances with $n_{\rm mol}/n_{\rm tot} > 10^{-9}$. The main condensates are H_2O[s], C[s], and NH_4Cl[s]. H_2O[s] is thermally stable higher in the atmosphere with respect to the $T_{\rm surf} = 300\,{\rm K}$ model. C[s] is the only condensate stable throughout the atmosphere with roughly constant normalised number density. Furthermore KCl[s], NaCl[s], FeS[s], and FeS_2[s] are present at lower normalised number densities ($n_{\rm con}/n_{\rm tot} < 10^{-12}$).

The most abundant gas species in the atmosphere of the $T_{\rm surf} = 900\,{\rm K}$ model (right side of Fig. 4.3, representative of K2-228 b) is H_2O, followed by CO_2 at $n_{\rm mol}/n_{\rm tot} \approx 10^{-1}$. Further species with $n_{\rm mol}/n_{\rm tot} > 10^{-3}$ are H_2, HCl, H_2S, HF, and N_2. The gas phase abundance of CO decreases with height, while CH_4 becomes more abundant. They are equally abundant at a pressure of $p_{\rm gas} \approx 0.1$ bar at abundances of $n_{\rm mol}/n_{\rm tot} \approx 10^{-4}$. This change from CO to CH_4 as carbon bearing molecules is an example for temperature dependent change of gas phase compositions independent of a change in element abundance. Further 12 molecules show gas phase abundances of $n_{\rm mol}/n_{\rm tot} > 10^{-9}$ in the $T_{\rm surf} = 900\,{\rm K}$ model, underlining the larger diversity in the gas composition for higher $T_{\rm gas}$. The most abundant condensates are NaCl[s], KCl[s], and FeS[s], which are most abundant in the near-crust atmosphere. Further 14 condensates reach normalised number densities of $n_{\rm cond}/n_{\rm tot} > 10^{-20}$.

As described in Woitke et al. (2018) two kinds of condensation occur in the atmosphere. Type 1: condensation from the gas phase. A new condensate becomes stable and removes elements from the gas phase. These condensations result in a knee in the gas phase abundances. Type 2: a transition from one to another condensate without a change in the gas phase, which is characterised by one condensate becoming unstable ($S < 1$) while another one becomes stable ($S = 1$). A type

2 transition links the two affected condensates to a condensate chain, a condensation sequence.

The occurring cloud condensate species can be grouped into three different groups.

- Group 1: Materials that are stable in the lowest atmospheric layer directly above the surface.
  T_{surf} = 300 K: none;
  T_{surf} = 600 K: C[s], NaCl[s], and FeS[s];
  T_{surf} = 900 K: NaCl[s], FeS[s], $KAlSi_3O_8$[s], $FeTiO_3$[s], $KMg_3AlSi_3O_{10}F_2$[s], $CaAl_2Si_2O_8$[s], and $Mn_3Al_2Si_3O_{12}$[s].

- Group 2: Materials that form by type 1 condensation.
  T_{surf} = 300 K: H_2O[s];
  T_{surf} = 600 K:H_2O[s], NH_4Cl[s], and KCl[s];
  T_{surf} = 900 K: KCl[s].

- Group 3: Materials that form by type 2 condensation.
  T_{surf} = 300 K: none;
  T_{surf} = 600 K: FeS_2[s];
  T_{surf} = 900 K: FeS_2[s], Al_2O_3[s], $FeAl_2O_4$ [s], AlF_6Na_3[s], MgF_2, CaF_2[s], TiO_2[s], TiF_3[s], and $MnTiO_3$[s].

Based on these groups, the condensates can be linked to condensate chains, which are listed in the following:

gas → H_2O[s]

gas → NH_4Cl[s]

gas → KCl[s]

crust → C[s]

crust → NaCl[s]

crust → FeS[s] → FeS_2[s]

crust → $KAlSi_3O_8$[s] → Al_2O_3[s] → $FeAl_2O_4$[s]→ AlF_6Na_3[s]

crust → $KMg_3AlSi_3O_{10}F_2$[s] → MgF_2[s]

crust → $CaAl_2Si_2O_8$[s] → CaF_2[s]

crust → $FeTiO_3$[s] → TiO_2[s]→ TiF_3[s]

crust → $Mn_3Al_2Si_3O_{12}$[s] → $MnTiO_3$[s].

4.3.2 Cloud diversity over diverse rocky surfaces

In this section we study the influence of the surface composition to the thermal stability of cloud species. The surface composition is determined by the total element abundance ($\epsilon_{\rm tot}$, see Table 4.2 and Sect.4.2.3), surface pressure ($p_{\rm surf}$) and surface temperature ($T_{\rm surf}$). In this section we keep $p_{\rm surf} = 1$ bar for all models. We cover the range of $T_{\rm surf} = 300\,{\rm K}$ to $T_{\rm surf} = 1000\,{\rm K}$.

4.3.2.1 Dominating cloud materials for varying crust composition

In Fig. 4.4 the most abundant thermally stable cloud condensates are represented as the normalised number density ($n_{\rm cond}/n_{\rm tot}$) of the number density of composite units ($n_{\rm cond}$, see Sec. 4.2.2) with respect to the total gas density ($n_{\rm tot}$) for the different sets of element abundances. For each thermally stable cloud condensate, the regions, in the ($p_{\rm gas}, T_{\rm surf}$) parameter space where the normalised number density exceeds a given threshold ($n_{\rm cond}/n_{\rm tot} > 10^{-10}$ for Fig. 4.4) is considered as that condensate being stable and sufficiently abundant. This region forms an individual cloud layer for each condensate. The high-pressure border of a condensate cloud layer (cloud base) is coinciding with the highest abundance of the specific condensate. For the low-pressure boundary of the cloud layer (cloud top) two regimes exist: 1) The normalised number density of the cloud condensate drops below the threshold, or 2) the condensate undergoes a type 2 transition such that another condensate becomes stable (condensate chain). Examples for these two regimes are NH_4Cl[s], NaCl[s], and KCl[s] for the drop below the threshold and H_2O[l] to H_2O[s] or FeS[s] to FeS_2[s] for the type 2 transitions for the atmosphere above a MORB like planetary surface.

Throughout the considered crust compositions, the cloud condensates which reach the overall highest normalised number densities ($n_{\rm cond}/n_{\rm tot} \approx 10^{-2}$) are H_2O[l,s], C[s], and NH_3[s]. Overall, the individual cloud layers can be separated into two categories, separated by $T_{\rm gas}$ into high and low temperature cloud condensates. For $T_{\rm gas} \lesssim 400\,{\rm K}$ we find H_2O[l,s], C[s], S_2[s] and nitrogen containing condensates (NH_3[s], NH_4Cl[s], NH_4SH[s]) thermally stable. For $T_{\rm gas} \gtrsim 600\,{\rm K}$ halides (NaCl[s], KCl[s]), iron sulphides (FeS[s], FeS_2[s]), iron oxides (FeO[s], Fe_2O_3[s], Fe_3O_4[s]), and aluminium containing condensates (Al_2O_3[s], $Al_6F_6Na_3$[s], AlF_3[s], $KAlSi_3O_8$[s]) are thermally stable and more abundant than $n_{\rm cond}/n_{\rm tot} > 10^{-10}$. The only cloud species to break this separation of high and low temperature clouds at normalised number densities of $n_{\rm cond}/n_{\rm tot} > 10^{-20}$ is C[s] which can be stable at any ($p_{\rm gas}, T_{\rm gas}$) point investigated in this chapter. Furthermore, C[s] shows the unique behaviour of almost vertical cloud base rise with decreasing or increasing surface tem-

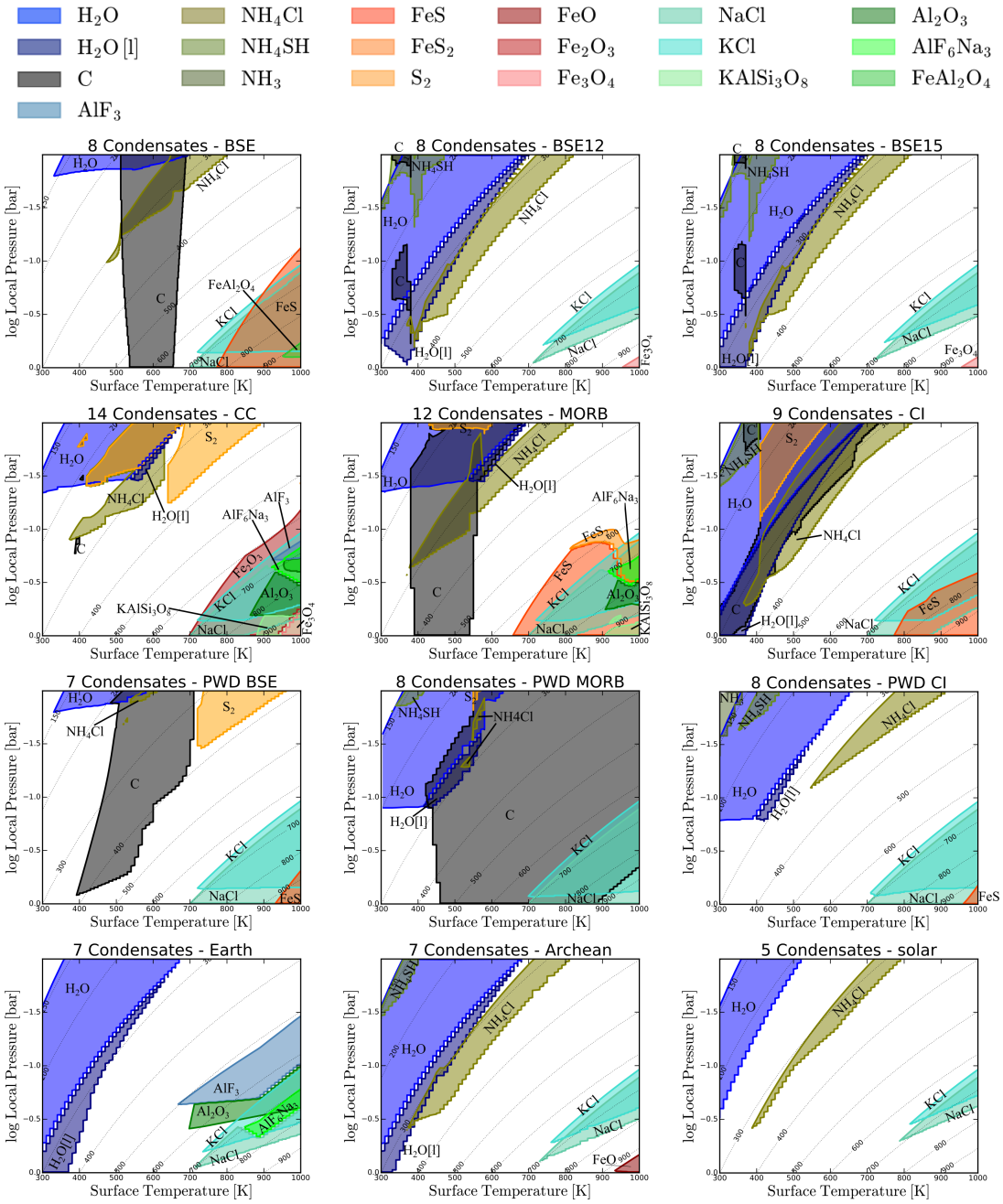

Figure 4.4: All thermally stable condensates with normalised number densities of $n_{\mathrm{cond}}/n_{\mathrm{tot}} > 10^{-10}$ locally for various elemental abundances are shown. The liquid phase of condensates is indicated by [l], while all other condensates are solids. Each column in every subplot is one bottom-to-top atmospheric model with the corresponding surface temperature on the x axis. Models have been calculated by steps of 10 K in T_{surf}. The dotted lines refer to the local gas temperature of the atmosphere in Kelvin. All models are calculated for $p_{\mathrm{surf}} = 1$ bar and $\gamma = 1.25$. The colour scheme for the cloud species is consistent for all element abundances and given in legend above.

peratures (530 K and 660 K for BSE, 380 K and 550 K for MORB, respectively), confining the C[s] condensation in a specific range of surface temperatures for these models. However, in the CI model, C[s] shows characteristics of the other cold temperature condensates and the cloud base follows the temperature curve. The cloud base for all other cloud condensates is dependent on the

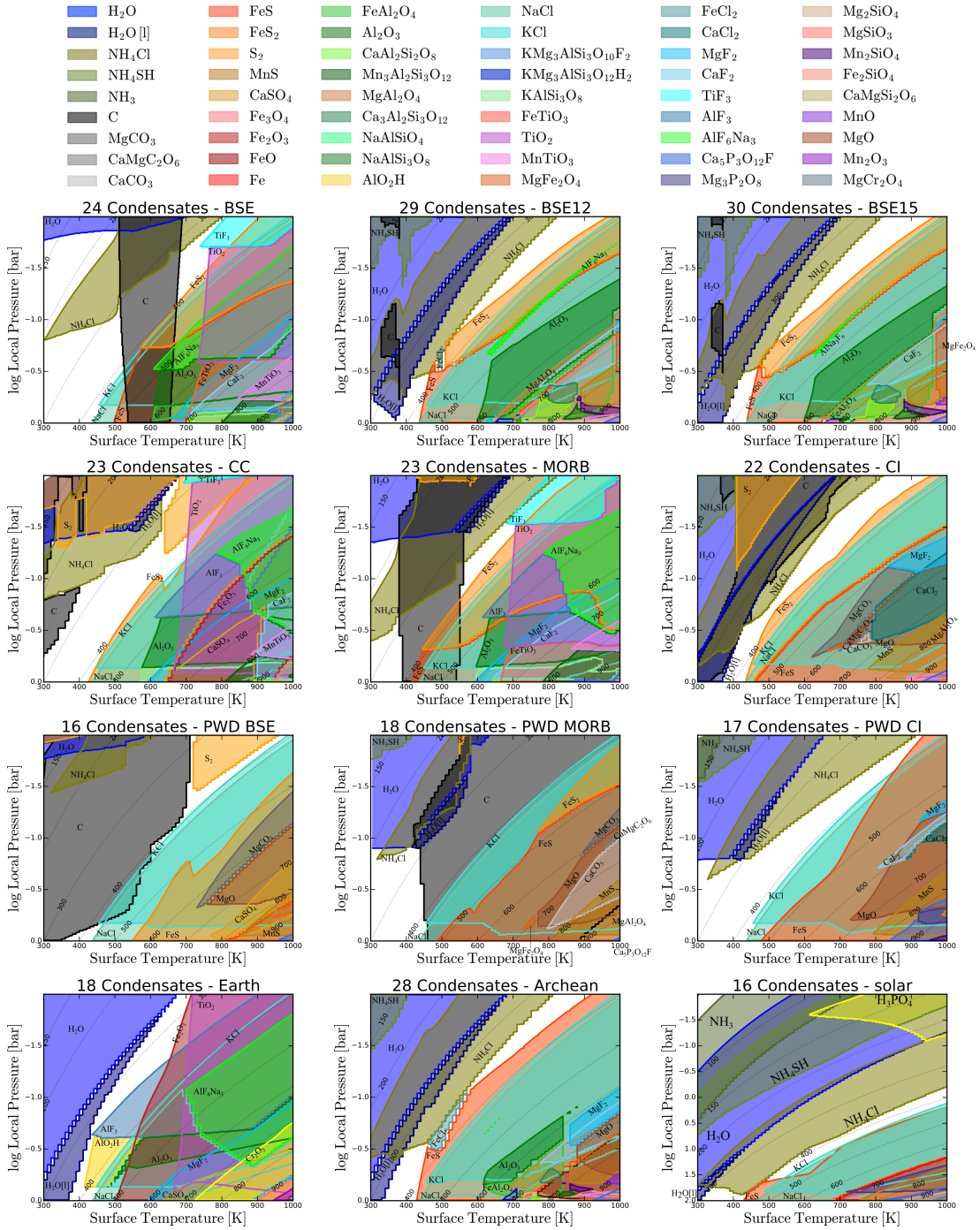

Figure 4.5: As Fig. 4.4, but with all condensates with normalised number densities higher than $n_{\mathrm{cond}}/n_{\mathrm{tot}} > 10^{-20}$. The colour scheme is consistent with Fig. 4.4, but extended to include the further condensates. All models are calculated for $p_{\mathrm{surf}} = 100\,\mathrm{bar}$ and $\gamma = 1.25$.

local temperature and therefore diagonal in the $(p_{\mathrm{gas}}, T_{\mathrm{surf}})$ space (see Fig. 4.4), if not constrained by condensate chains.

Towards lower surface temperature the cloud condensates tend to remain stable, but decrease in normalised number density (comparison of Figs.4.4 and 4.5). Again, a counterexample is C[s],

Table 4.3: A list of all cloud condensates according to their highest normalised number density over all element abundances considered in this work and 300 K ≥ T_{surf} ≥ 1000 K. All models with p_{surf} = 1 bar are included. All low temperature ($T \lesssim 400$ K) cloud condensate materials are indicated in bold.

Peak normalised number density	$n_{cond}/n_{tot} > 10^{-10}$	$10^{-10} > n_{cond}/n_{tot} > 10^{-15}$	$10^{-15} > n_{cond}/n_{tot} > 10^{-20}$
Water	**H_2O, H_2O[l]**		
Phlogopite		$KMg_3AlSi_3O_{10}F_2$	$KMg_3AlSi_3O_{12}H_2$
Carbon	**C**	$CaCO_3$	$MgCO_3$, $CaMgC_2O_6$
Nitrogen	**NH_4Cl, NH_4SH, NH_3**		
Sulphur	**S_2**, FeS, FeS_2	$CaSO_4$, MnS	
Phosphorus			$Mg_3P_2O_8$
Apatite			$Ca_5P_3O_{12}F$
Chlorine	NaCl, KCl	$CaCl_2$	$FeCl_2$
Fluorine	AlF_3, AlF_6Na_3	MgF_2, CaF_2, TiF_3	
Metals		Fe	
Hydroxide		AlO_2H	
Metaloxides	FeO, Fe_2O_3, Fe_3O_4 $FeAl_2O_4$, Al_2O_3	MgO, TiO_2 , Cr_2O_3 $MgFe_2O_4$, $FeTiO_3$, $MgAl_2O_4$	MnO, Mn_2O_3 $MgCr_2O_4$, $MnTiO_3$
Silicates	$KAlSi_3O_8$	Mg_2SiO_4, $MgSiO_3$ $CaAl_2Si_2O_8$, $Mn_3Al_2Si_3O_{12}$	$NaAlSiO_4$, $NaAlSi_3O_8$ $CaMgSi_2O_6$, $Ca_3Al_2Si_3O_{12}$ Mn_2SiO_4, Fe_2SiO_4

which becomes unstable with colder surface temperatures (BSE, MORB, PWD MORB).

For the low temperature cloud materials, H_2O[l,s] is the dominant cloud constituent, with cloud bases at various pressure levels, depending on the total H and O abundances. See Sect. 4.3.4 for an in depth investigation of the pressure level of the H_2O[l,s] cloud base.

Independent of the total element abundance, NaCl[s] is always thermally stable at slightly higher pressure levels than KCl[s]. For all investigated crust compositions, both are stable condensates in the respective atmospheres. The maximum normalised number density for both halides decreases with decreasing planetary surface temperature. For $T_{surf} \approx 700$ K the maximum normalised number density for these halide cloud species drops below $n_{cond}/n_{tot} = 10^{-10}$ in all of the models.

4.3.2.2 Cloud material diversity and transitions

In addition to the most abundant cloud species discussed in Sect. 4.3.2.1 many more cloud condensates are thermally stable for the (p_{gas}, T_{gas}) range studied here, but do not reach normalised number densities of $n_{cond}/n_{tot} > 10^{-10}$. In order to understand the diversity and chemical connection of potential cloud condensates in exoplanet atmospheres and also potential links of cloud species to the surface conditions (p_{surf}, T_{surf}, composition), we further investigate thermally-stable cloud condensates with lower normalised number densities. Although these cloud condensates are less likely to be detected, they can help the further understanding of cloud formation, diversity and stability in general. The thermally-stable cloud condensates with $n_{cond}/n_{tot} > 10^{-20}$ for the different surface compositions can be seen in Fig. 4.5. This reveals more condensates that are thermally

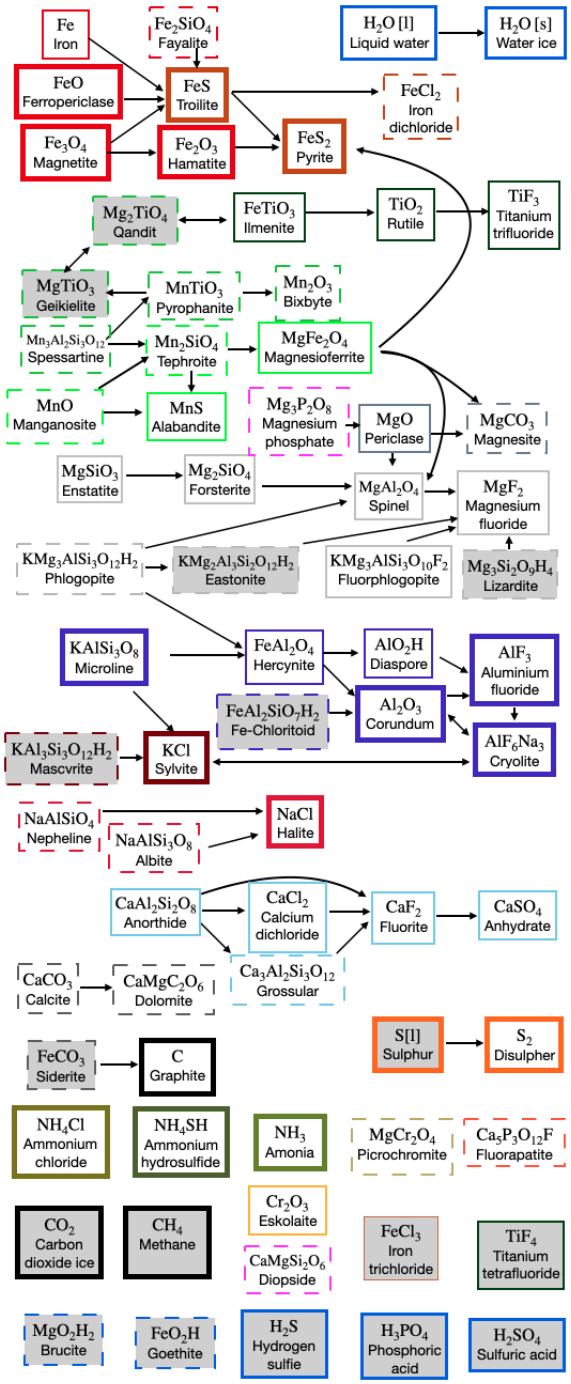

Figure 4.6: Overview of cloud material transitions in all of the models for materials with $n_{\rm cond}/n_{\rm tot} > 10^{-20}$. Different box styles correspond to the peak abundance of the condensates as in Table 4.3 ($n_{\rm cond}/n_{\rm tot} > 10^{-10}$ (thick), $n_{\rm cond}/n_{\rm tot} > 10^{-15}$ (thin), and $n_{\rm cond}/n_{\rm tot} > 10^{-20}$ (dashed)). The colours represent the different condensate chains. Along the arrows, the atmospheric pressure is decreasing and the condensates undergo a phase 2 transition (Woitke et al., 2018). Multiple arrows away from a specific condensate indicates that different transitions are found over the various models. For example FeS transitions to FeS_2 in most models, but for BSE12 and Archean it also shows a transition to $FeCl_2$. However, only one of them exists in any one model. Condensates without an arrow are not part of any condensate chain and do not undergo any phase 2 transition. Boxes with grey background refer to condensates that have only been found thermally stable in the high pressure models.

stable for the high-temperature condensate species, while no further low-temperature condensates become stable. However, the gap between the low and high-temperature cloud condensates is being filled from the high-temperature condensates at relatively low normalised number densities. The general separation into the two temperatures regimes at a local temperature of $T_{\mathrm{gas}} \approx 400\,\mathrm{K}$ remains.

In Table 4.3 all 55 cloud materials that are thermally stable in at least one atmosphere above a rocky surface with surface temperatures $300\,K \leq T_{\mathrm{surf}} \leq 1000\,\mathrm{K}$ and $p_{\mathrm{surf}} = 1\,\mathrm{bar}$ are listed and sorted with respect to their maximum normalised number density $n_{\mathrm{cond}}/n_{\mathrm{tot}}$. As described in Sect. 4.3.1, most of these condensates can be arranged in cloud chains by type 2 transitions. Only 7 condensates (S_2[s], C[s], NH_4Cl[s], NH_4SH[s], NH_3[s], $MgCr_2O_4$[s], and $Ca_5P_2O_{12}F$[s]) show no apparent type 2 transition to another condensate and therefore do not belong to any cloud chain. In Fig. 4.6 these condensate chains are visualised. Not all of these transitions occur in all models for different element abundances.

4.3.3 Atmospheric gas composition

The formation of clouds in an atmosphere removes the affected elements partially from the gas phase and therefore changes the composition of the atmosphere with respect to the atmosphere without condensation. This results in a depleted atmospheric compositions above the cloud layer. In this section we investigate the changes in the atmospheric composition with atmospheric height.

Woitke et al. (2021) introduced an atmospheric classification based on the gas phase abundances of atmospheres only consisting of H, C, N, and O, resulting in three distinctive atmospheric types (see also Chapter 3).

- Type A atmospheres are hydrogen-rich; they contain H_2O, CH_4, NH_3 and either H_2 or N_2, but no CO_2 and no O_2.
- Type B atmospheres are oxygen-rich; they contain O_2, H_2O, CO_2 and N_2, but no CH_4, no NH_3 and no H_2.
- Type C atmospheres show the coexistence of CH_4, CO_2, H_2O and N_2, with traces of H_2, but no O_2 and no CO.

In Fig. 4.7, we show how the gas phase element abundances change with height for rocky planets differing in their surface rock composition and their surface temperatures. As in Woitke

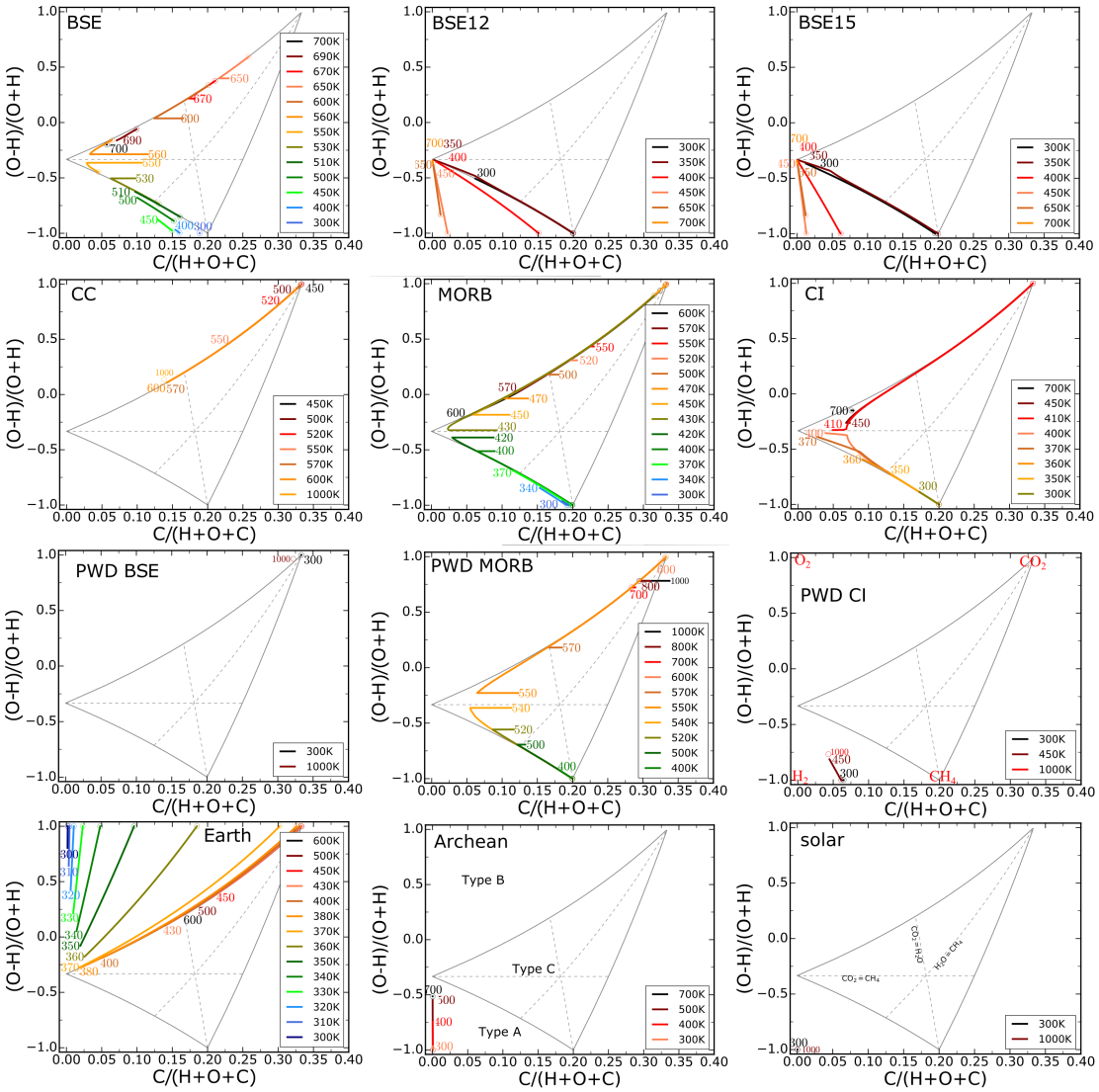

Figure 4.7: Atmospheric compositions with decreasing pressure and various surface temperatures. The base of each atmospheric profile is indicated by the corresponding T_{surf} and the top by open circles. The axis of overall redox state measured from O and H abundances as (O-H)/(O+H) and C content relative to H, O, and C are the same as in Woitke et al. (2021). The atmospheric types, atmospheric end members of certain points as well as lines of equal abundances of certain molecules are indicated in the bottom right plots.

et al. (2021), the atmospheric composition is shown in the (O-H)/(O+H) over C/(H+O+C) plane, where H, C, and O stand for the respective element abundances. (O-H)/(O+H) ranges from 1 (only oxygen, no hydrogen, fully oxidising) to -1 (only hydrogen, no oxygen, fully reducing) and therefore is a measure of the overall redox potential of the atmosphere, that is how likely oxidising and reducing reactions are. The C/(H+O+C) value is a measure of the carbon fraction in the system, with respect to H, O, and C. The solid grey lines in Fig. 4.7 show the separation of the different atmospheric types (type A below the triangle, type B above and type C inside). The dashed lines reflect equal abundances of H_2O and CO_2, H_2O and CH_4, as well as CH_4 and CO_2 (see lower right

panel in Fig. 4.7). Each coloured line in Fig. 4.7 corresponds to one of our hydrostatic, polyropic atmospheric models. The composition at the bottom of the atmosphere is marked by the surface temperature in Fig. 4.7, whereas the top of our atmospheric model at 10 mbar is marked with an open circle. This allows to see the changes in the atmospheric composition of the atmosphere. The cloud condensates that are thermally stable in each of the models can be seen in the respective subplot in Figs. 4.4 and 4.5.

Models with surface temperature $T_{\rm surf} \gtrsim 600\,\mathrm{K}$ show very little change in the parameter space in Fig. 4.7 with increasing height, as condensation of for example KCl[s] or NaCl[s] does not affect the abundances of C, H, and O. On the other hand cloud condensates such as Al_2O_3[s] or TiO_2[s] do affect the oxygen element abundance. However, these condensates are limited by the much less abundant elements Al and Ti and therefore the overall oxygen abundance, and thus (O-H)/(O+H), does not change significantly.

For surface temperatures $T_{\rm surf} \lesssim 600\,\mathrm{K}$, the atmospheric elemental abundances drastically change with atmospheric height. Especially C[s] and H_2O[l,s] become thermally stable and therefore cause the atmospheres to evolve towards either oxygen or hydrogen rich atmospheres. For oxygen rich atmospheres, the carbon content can reach up to 1/3 (pure CO_2), while hydrogen rich atmospheres can only reach up to a carbon content of 1/5 (pure CH_4). These regions for (O-H)/(O+H) are the only regions in Fig. 4.7 that are not affected by condensation of H_2O[l,s] and C[s] for lower temperatures (see also Woitke et al., 2021). In which of these two states an atmosphere evolves, is determined by whether the near-crust atmosphere is over-abundant in O or H with respect to H_2O, that is whether the atmospheric composition lies above or below (O-H)/(O+H)=-0.33. This is equivalent to whether CO_2 or CH_4 are more abundant than the other. This motivates the subtypes of C1 and C2 for type C atmospheres above and below the (O-H)/(O+H)=-0.33 threshold, respectively. By condensation, the atmosphere cannot change from one to another type C atmosphere. Thus measurements, that infer a specific atmospheric type in the high atmosphere can constrain the possible atmospheric conditions at the surface.

The removal of condensate results in the atmosphere becoming either CO_2 dominated (e.g. rocky planets with MORB or CI composition and high $T_{\rm surf}$) or CH_4 dominated atmospheres (e.g. rocky planet with CI like composition and low $T_{\rm surf}$). Furthermore, the atmospheres can reach any point with $(\mathrm{O}-\mathrm{H})/(\mathrm{O}+\mathrm{H}) = -1.0$ and varying carbon content, thus ranging from H_2 atmospheres (eg. solar composition, any $T_{\rm surf}$) to CH_4 dominated atmospheres (e.g. CI composition,

low T_{surf}). The intermediate states are also occurring (e.g. PWD CI or BSE12).

Only models for a CC like surface composition with $T_{\mathrm{surf}} > 600\,\mathrm{K}$ and Earth abundances with $T_{\mathrm{surf}} < 380\,\mathrm{K}$ fall into the atmospheric type B. From calculations by Woitke et al. (2021) this results in O_2 being present. However, the models also show the presence of SO_2, indicating the emergence of subtypes for the type B atmospheres when further elements than H, C, O, and N become of significant importance. The further investigation of these subtypes will be addressed in a future paper. However, as Fig. 4.7 shows, the impurities by further elements are small enough, so that the atmospheres still fall into the three types shown in Woitke et al. (2021).

In general, the atmospheric type does not change with atmospheric height, neither by condensation nor changes in $(p_{\mathrm{gas}}, T_{\mathrm{gas}})$ in our polytropic atmosphere model. Contrasting this, the O/H and C/O ratios, which have been used by previous studies to characterise atmospheres of planets (see e.g. Madhusudhan, 2012; Moses et al., 2013; Brewer et al., 2017) can change drastically throughout the atmospheres (Figs. 4.11 and 4.12 in Sect. 4.8). This suggests, that the atmospheric types are a good indicator for atmospheres of rocky exoplanets.

In Fig. 4.7 it can be seen that the atmospheric composition with increasing height evolves towards (O-H)/(O+H) $\rightarrow \pm 1$. Type C atmospheres evolve towards either CO_2 or CH_4 dominated atmospheres. Also type A and B atmospheres with a high C content will evolve towards similar compositions. Distinguishing these endpoints will need precise measurements of the C, H, and O abundances together with the detection of the specific trace molecules which define the atmospheric type.

Although the atmospheric type does not change throughout one atmosphere for a given (p_{surf}, T_{surf}) and rocky surface composition, changing these parameters can cause the entire atmosphere to change the atmospheric type. For example the BSE, MORB, and CI rocky surface compositions, show that the atmospheric type of the entire atmosphere changes with surface temperature. This suggests, that planetary atmospheres can change the atmospheric type of the entire atmosphere over time, for example by cooling down.

A further indicator for the atmospheric conditions can be some specific cloud types, which are indicative of reducing or oxidising conditions. For the low temperature cloud condensates our models show that S_2[s] is only stable under oxidising circumstances, while NH_4SH[s] is the sulphur condensate under reducing conditions. NH_4Cl[s] can exist under both conditions but is constrained by the stability of NH_4SH[s] in our models.

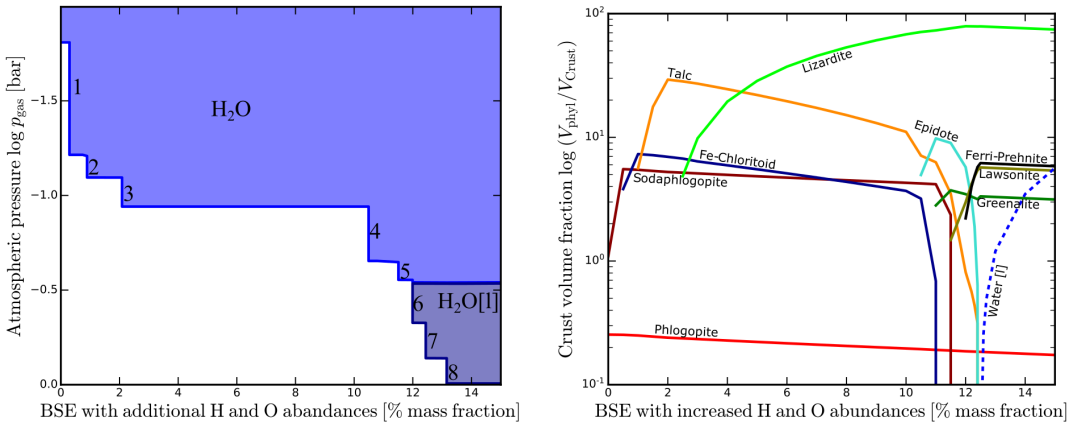

Figure 4.8: Influence of crust hydration on the water cloud base. The model is based on the BSE model, with increasing additional H and O abundances. The models are calculated for T_{surf} = 350 K and p_{surf} = 1 bar. **Left panel:** pressure level of the water cloud base. **Right panel:** crust volume fraction of different phyllosilicates. The sum formulas of the different condensate can be seen in Table 4.4.

4.3.4 The link between planetary surface hydration and water clouds

Herbort et al. (2020) have shown that H_2O[l,s] will only be thermally stable in the presence of silicate material, if after the formation of phyllosilicates, that is the hydration of the silicates, an excess of H and O prevails. If this is the case, we call these phyllosilicates 'saturated'. Hence, only if all phylosilicates are saturated, water can appear in condensed form which we have shown to be the case for the near-crust atmosphere. In the following we demonstrate that even if the phyllosilicates that form in the crust of a rocky planet for a given (p_{surf}, T_{surf}) are not saturated in the above sense, H_2O[l,s] can become thermally stable in the atmosphere stratification that develops above such a crust because of its different thermodynamic conditions where $p_{gas} < p_{surf}$ and $T_{gas} < T_{surf}$. If H_2O[l,s] is a stable condensate at the crust, the H_2O[l,s] cloud base is in the atmosphere crust interaction layer (BSE15, CI, Earth, Archean). For all other models the cloud base of H_2O[l,s] is at lower pressures.

Figure 4.8 shows the dependence of the local gas pressure level at the cloud base for the water cloud on the hydration of the crust. We test this dependence by increasing the H and O abundances of the BSE total element abundances in a 2:1 ratio. The number of added elements is given in percent mass fraction relative to the unaltered BSE abundance. The local pressure level of the H_2O[l,s] cloud base does not continuously decrease with increased element abundances, but changes if a given phyllosilicate is saturated. Coinciding with this, a further phyllosilicate becomes stable. With further additional H and O added to the total element abundance, the stable unsaturated phyllosilicates incorporate the additional H and O. In Fig. 4.8 these changes are indicated

Table 4.4: Limitation and stability of phyllosilicates in the crust of models with BSE total element abundances and increased H and O abundances. The numbers refer to the cloud base pressure changes in Fig. 4.8.

	limited	stable
1	$NaMg_3AlSi_3O_{12}H_2$[s]	$FeAl_2SiO_7H_2$[s]
	Sodaphlogopite	Fe-Chloritoid
2	$FeAl_2SiO_7H_2$[s]	$Mg_3Si_4O_{12}H_2$[s]
	Fe-Chloritoid	Talc
3	$Mg_3Si_4O_{12}H_2$[s]	$Mg_3Si_2O_9H_4$[s]
	Talc	Lizardite
4		$Ca_2FeAl_2Si_3O_{13}H$[s]
		Epidote
5	$Ca_2FeAl_2Si_3O_{13}H$[s]	$Fe_3Si_2O_9H_4$[s]
	Epidote	Greenalite
6	$Fe_3Si_2O_9H_4$[s]	$CaAl_2Si_2O_{10}H_4$[s]
	Greenalite	Lawsonite
7	$Mg_3Si_2O_9H_4$[s]	$Mg_3Si_2O_9H_4$[s]
	Lizardite	Ferri-Prehnite
8	$CaAl_2Si_2O_{10}H_4$[s]	H_2O[l]
	Lawsonite	Water
	$Ca_2FeAlSi_3O_{12}H_2$[s]	
	Ferri-Prehnite	

with numbers, and listed in Table 4.4. For change 4, no phyllosilicate reaches its maximum, but Epidote becomes stable. For change 8, two different condensates reach their limit, while H_2O[l] (water) becomes a stable condensate and the water cloud is in contact with the surface.

This investigation underlines the importance of phyllosilicates on the stability of H_2O[l,s] at the surface of rocky exoplanets. We have shown that, under the assumption of a hydrostatic equilibrium atmosphere in chemical phase equilibrium with the crust, it is possible to have H_2O[l,s] thermally stable in the atmosphere but not at the crust, although the planetary surface conditions of $(p_{\rm surf}, T_{\rm surf})$ are consistent with water condensates.

4.3.5 The effect of surface pressure on cloud composition

The planetary surface pressure can currently not be measured directly and therefore leaves a degeneracy for the surface conditions if only the conditions of the upper atmosphere of a planet are known. For atmospheres with a polytropic index of $\gamma = 1.25$, the $(p_{\rm gas}, T_{\rm gas})$ profile of an atmosphere with $T_{\rm surf} = 300\,{\rm K}$ and $p_{\rm surf} = 1\,{\rm bar}$ and an atmosphere with $T_{\rm surf} = 750\,{\rm K}$ and $p_{\rm surf} = 100\,{\rm bar}$ are indistinguishable for $P_{\rm gas} < 1\,{\rm bar}$. In our solar system this can be seen in the comparison of Earth and Venus. Both show clouds at comparable $(p_{\rm gas}, T_{\rm gas})$, but Venus has a high pressure atmosphere. The atmospheric height, and therefore the surface pressure, can only

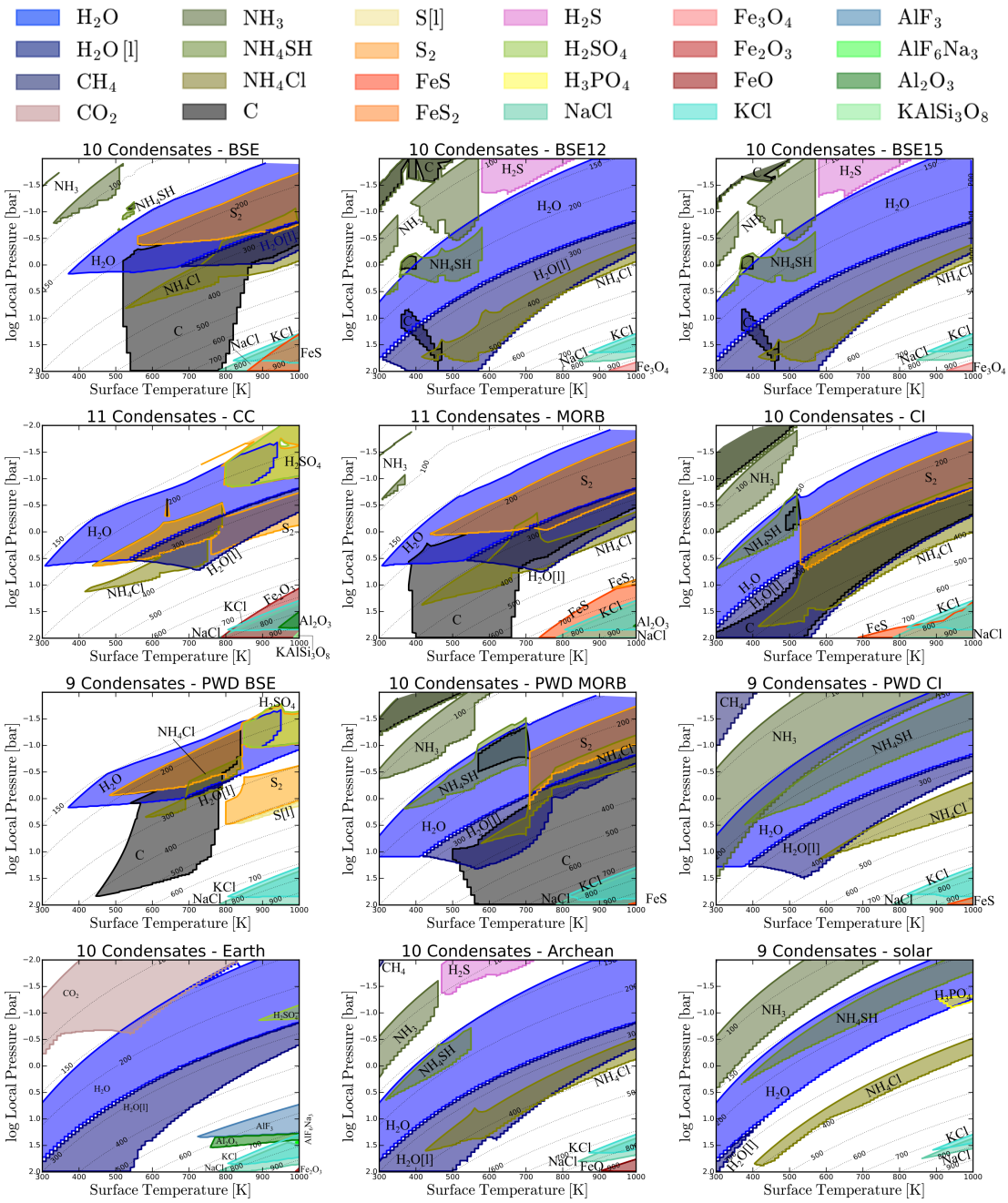

Figure 4.9: As Fig. 4.4, but for $p_{\mathrm{surf}} = 100\,\mathrm{bar}$. All models are calculated for $\gamma = 1.25$. All thermally stable condensates with normalised number densities of $n_{\mathrm{cond}}/n_{\mathrm{tot}} > 10^{-10}$ locally are shown.

be determined at wavelengths where the atmosphere is optically thin. This means that optical wavelengths are limiting us to the upper atmosphere of Venus while radio wavelengths enable us to investigate the surface of Venus. In this section we investigate in how far an increased surface pressure of $p_{\rm surf} = 100$ bar affects the thermal stability of cloud condensates.

In Fig. 4.9 all thermally stable cloud condensates with $n_{\rm cond}/n_{\rm tot} > 10^{-10}$ are shown for 12 different element abundances for a rocky planetary surface with $p_{\rm surf} = 100$ bar. Overall, Fig. 4.9 demonstrates that, similarly to the $p_{\rm surf} = 1$ bar models (Sect. 4.3.2), the thermally stable cloud materials can be separated into high and low local temperature regimes. Whereas the temperature for the lowest cloud base of the low temperature clouds is located at $T_{\rm gas} \approx 400$ K for all models with $p_{\rm surf} = 1$ bar, the corresponding temperature for the $p_{\rm surf} = 100$ bar models changes with different $T_{\rm surf}$ from $T_{\rm gas} \approx 550$ K at $p_{\rm gas} = 100$ bar for atmospheric models with $T_{\rm surf} = 550$ K to $T_{\rm gas} \approx 450$ K at $p_{\rm gas} \approx 2$ bar for atmospheric models with $T_{\rm surf} = 1000$ K.

In comparison to the $p_{\rm surf} = 1$ bar models, a total of 17 further condensates are thermally stable with $n_{\rm cond}/n_{\rm tot} > 10^{-20}$. All of the condensates that reach normalised number densities of $n_{\rm cond}/n_{\rm tot} > 10^{-10}$ (H_2S[s], H_2SO_4[s], S[l], CO_2[s], CH_4[s], and H_3PO_4[s]) are part of the low temperature cloud condensates. H_2S[s], CO_2[s], and CH_4[s] form only for very low temperatures of $T_{\rm gas} \lesssim 150$ K, which is not in the parameter space for the $p_{\rm surf} = 1$ bar atmospheres. Of these low temperature cloud condensates, only S[l] has a type 2 transition to anther condensate (S[l] to S_2[s]) and therefore forms a condensate chain.

Our models show that some cloud condensates only form under specific atmospheric compositions and therefore these condensates can be used as indicators for these atmospheric types. For the low temperature cloud condensates we find sets of mutually exclusive cloud condensates that do not coexist with each other. One mutually exclusive sets is NH_3[s], H_2S[s], and H_2SO_4[s]. NH_3[s] only forms in N-rich type A atmospheres, while H_2SO_4[s] only forms in type B atmospheres. H_2S[s] can form in type A and type B atmospheres. Another pair of mutually exclusive condensates is S_2[s] and NH_4SH[s], with the latter only forming in H-rich environments.

The investigation of the cloud condensates with $n_{\rm cond}/n_{\rm tot} > 10^{-20}$ shows that the gap between the high and low temperature cloud layers is filled with thermally stable condensates. Further 2 condensates ($FeCl_3$[s], TiF_4[s]) reach $n_{\rm cond}/n_{\rm tot} > 10^{-15}$, while 9 condensates reach $n_{\rm cond}/n_{\rm tot} > 10^{-20}$. These can be divided into the different groups of pyhllosilicates ($KAl_3Si_3O_{12}H_2$[s], $FeAl_2SiO_9H_2$[s], $Mg_3Si_2O_0H_4$[s], $KMg_2Al_3Si_2O_{12}H_2$[s]), hydroxides (MgO_2H_2[s], FeO_2H[s]),

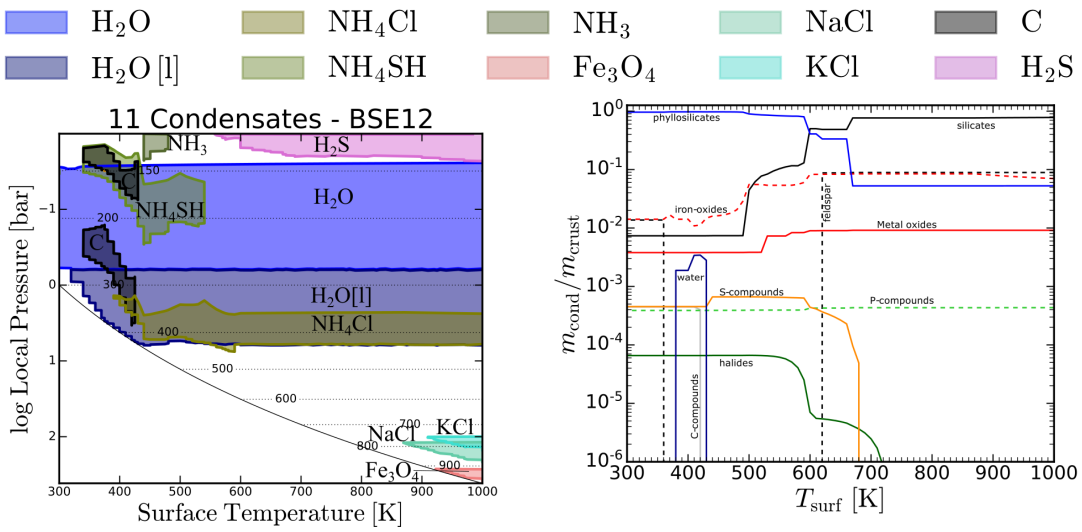

Figure 4.10: Left panel: Thermally stable cloud condensates with $n_{cond}/n_{tot} > 10^{-10}$ for overlapping atmospheric (p_{gas}, T_{gas}) profiles with varying surface conditions (p_{surf}, T_{surf}). All atmospheric profiles go through $(p_{gas} = 1\,\text{bar}, T_{gas} = 300\,\text{K})$ and have a BSE12 like crust composition. $(p_{surf}$ and $T_{surf})$ for each model are indicated by the solid black line. The polytropic index is kept at $\gamma = 1.25$ for all models. **Right panel:** Crust composition for the atmospheric models in the left panel. The condensates belonging to each group are listed in Table 4.5.

carbonates ($FeCO_3$[s]), and metal oxides ($MgTiO_3$[s], Mg_2TiO_4[s]). Only FeO_2H[s], $FeCl_3$[s], and TiF_4[s] are stable in the low temperature cloud regime, while all other cloud condensates are thermally stable relatively close to the surface.

The lesser abundant cloud condensates enhance the condensate chains discussed in Sect. 4.3.2.2. Every condensate that is only found in the high $p_{surf} = 100\,\text{bar}$ models is shaded in grey in Fig. 4.6.

With the increased surface pressure, the boiling point of water also increases, allowing liquid water as a stable condensate for higher temperatures as well. This becomes especially noticeable for the model with a BSE12 surface composition, where there is no water stable at the surface with $p_{surf} = 1\,\text{bar}$. But for $p_{surf} = 100\,\text{bar}$, H_2O[l] is stable for $T_{surf} \geq 370\,\text{K}$ and $T_{surf} \leq 570\,\text{K}$. This shows that liquid water could be found on planets with high pressure although their element abundances do not allow water condensates at (p_{surf}, T_{surf}) conditions similar to Earth.

Only reflected light observations from rocky exoplanets can provide direct information on surface properties (e.g. Madden & Kaltenegger, 2018; Asensio Ramos & Pallé, 2021). Transmission spectroscopy on the other hand is limited to the higher atmosphere and potentially a higher cloud deck (Komacek et al., 2020), but can provide estimates about the (p_{gas}, T_{gas}) conditions. However, these high atmosphere conditions are ambiguous with regard to the surface pressure and therefore, assuming a surface temperature. One (p_{gas}, T_{gas}) point can be used with Eq. 4.3 to find (p_{surf}, T_{surf}). The resulting polytropic atmosphere shows the exact same atmospheric structure in

Table 4.5: Explanation of the crust condensate grouping from Fig. 4.10 for the BSE12 like crust composition.

Group	Included condensates	Condensate name
Silicates	Mg_2SiO_4[s]	Fosterite
	Fe_2SiO_4[s]	Fayalite
	$MgSiO_3$[s]	Enstatite
	$CaTiSiO_5$[s]	Sphene
	$CaMgSi_2O_6$[s]	Diopside
	$Mn_3Al_2Si_3O_{12}$[s]	Spessartine
Feldspar	$NaAlSi_3O_8$[s]	Albite
	$CaAl_2Si_2O_8$[s]	Anorthide
Metal oxides	$MgCr_2O_4$[s]	Picrochromite
	$FeTiO_3$[s]	Ilmenite
	Cr_2O_3[s]	Eskolaite
Iron Oxides	Fe_3O_4[s]	Magnetide
Phyllosilicates	$CaAl_2Si_2O_{10}H_4$[s]	Lawsonite
	$Fe_3Si_2O_9H_4$[s]	Greenalite
	$CaAl_4Si_2O_{12}H_2$[s]	Margarite
	$Ca_2FeAlSi_3O_{12}H_2$[s]	Ferri-Prehnite
	$Mg_3Si_2O_9H_4$[s]	Lizardite
	$Ca_2Al_3Si_3O_{13}H$[s]	Clinozoisite
	$FeAl_2SiO_7H_2$[s]	Fe-Chloritoid
	$Ca_2FeAl_2Si_3O_{13}H$[s]	Epidote
	$Mg_3Si_4O_{12}H_2$[s]	Talc
	$KMg_3AlSi_3O_{12}H_2$[s]	Phlogopite
	$NaMg_3AlSi_3O_{12}H_2$[s]	Sodaphlogopite
Water	H_2O[l]	Liquid water
Halides	$CaCl_2$[s]	Ca-Dichloride
	MgF_2[s]	Mg-Flouride
	CaF_2[s]	Flourite
	NaCl[s]	Halite
P-compounds	$Ca_5P_3O_{12}F$[s]	Flourapatite
S-compounds	FeS_2[s]	Pyrite
	FeS[s]	Troilite
C-compounds	$CaCO_3$[s]	Calcite

the higher atmosphere, but can be calculated to different surface conditions.

All models in Fig. 4.10 follow atmospheric profiles of $T = 300\,\mathrm{Kbar}^{-0.2} \cdot p^{0.2}$ with different $(p_{\mathrm{surf}}, T_{\mathrm{surf}})$. In the upper panel of Fig. 4.10, all thermally stable cloud condensates that reach normalised number densities of $n_{\mathrm{cond}}/n_{\mathrm{tot}} > 10^{-10}$ for these atmospheric profiles are shown. The crust composition is BSE12 like. Although the $(p_{\mathrm{gas}}, T_{\mathrm{gas}})$ in the higher atmosphere are by construction the exact same for the different models, the changes in the surface pressure level result in different cloud condensates becoming thermally stable. NH_4Cl[s] and H_2O[l,s] are thermally stable at similar temperatures, independent of the surface conditions. However, for models with higher

($p_{\rm surf}, T_{\rm surf}$) H_2S[s] becomes thermally stable, while for the lower ($p_{\rm surf}, T_{\rm surf}$) C[s], NH_4SH[s], and NH_3[s] are thermally stable condensates in the higher atmosphere. This is a result of different condensate makeup of the crust (lower panel of Fig. 4.10). The different crust forming condensates are grouped according to their nature (see Table 4.5). H_2S[s] is only a cloud condensate, if enough sulphur and hydrogen are available in the near-crust atmosphere. This can also be seen by sulphur compounds only becoming stable in the crust for $T_{\rm surf} \leq 650\,\mathrm{K}$. For lower surface pressures, the sulphur remaining in the atmosphere is condensing and becomes a stable condensate in form of NH_4SH[s]. Furthermore, the phyllosilicates become more important as well. A similar effect can be seen for the condensation of C[s], which - in the case of BSE12 crust composition - only occurs once carbon is a stable crust condensate ($T_{\rm surf} \leq 400\,\mathrm{K}$).

The results from Fig. 4.10 underline that assuming the right surface conditions is crucial for understanding the atmosphere. Although elements that undergo high temperature condensation are depleted during the atmospheric build-up, the resulting upper atmosphere is affected by the removal of different condensates in the atmosphere with respect to the formation in the crust for a lower surface pressure. This is a result of the full availability of elements at the crust, and not the depleted element abundances in the gas phase. Especially Si is forming crust condensates and is thus very depleted in the near crust atmosphere. This in turn results in Silicate clouds only being stable close to the crust, if at all.

4.4 Implications for observable planets

In this section we use the material presented in Sect. 4.3 to discuss the possible implications of observations by future space missions and ground based instruments. The observations of a specific exoplanet can in principle provide three different types of information. First, the molecular composition of the gas above a cloud layer, which can be observed via absorption lines, probing the optically thin part of the atmosphere (e.g. Benneke & Seager, 2012; Helling et al., 2019; Samra et al., 2020; Young et al., 2020). Second, information about the chemical composition of the cloud layer can be obtained by absorption bands of solid materials (e.g. Wakeford & Sing, 2015; Pinhas & Madhusudhan, 2017; Barstow, 2020; Gao et al., 2020), and third, potentially, the temperature and pressure at the cloud deck (e.g. Line & Parmentier, 2016; Mai & Line, 2019; Fossati et al., 2020).

The detection of certain atmospheric gases (H_2O, CO_2, CH_4, H_2, and O_2) can be used to iden-

tify the atmospheric type of atmospheres (see Woitke et al., 2021). This atmospheric type of the optically thin atmosphere is the same as the atmospheric type at the near-crust atmosphere, as the atmospheric type does not change with height, despite the condensation of clouds. Additionally, the detection of certain cloud condensates can constrain the element abundance ratio between O and H. For example, S_2[s] can only be thermally stable, when O>H. Whereas NH_4SH[s] is only thermally stable for H>O.

Table 4.6: Connection between different cloud condensates in the high atmosphere and the crust composition for $T_{surf} \leq 700\,K$. Corresponding confirmed planets with equilibrium temperatures $250\,K < T_{eq} < 700\,K$ are listed as well.

T_{surf} [K]	Planet	$M_P[M_\oplus]$	$R_P[R_\oplus]$	T_{eq}[K]	Ref.	H_2O[l,s]	C[s]	NH_4Cl[s]	NH_4SH[s]	NH_3[s]	S_2[s]
<350	TRAPPIST-1 e	0.6 ± 0.6	0.92 ± 0.04	251 ± 5	(1)	all			BSE12	PWD CI	
	K2-3 d	2.8	1.6 ± 0.3	282.0	(2)				BSE15		
	TRAPPIST-1 d	0.4 ± 0.3	0.77 ± 0.04	288 ± 6	(1)				CI		
	TOI-700 d	2.3 ± 0.7	1.19 ± 0.11	300 ± 60	(3)				Archean		
	TRAPPIST-1 c	1.4 ± 0.7	1.056 ± 0.004	341 ± 7	(1)						
	K2-3 c	2.1 ± 1.1	1.9 ± 0.3	344.0	(2)						
350-400	TOI-237 b	2.9 ± 1.5	1.44 ± 0.12	355.0	(4)	all	BSE12		BSE12		
	K2-155 d	4.9 ± 1.2	1.9 ± 0.5	381 ± 40	(5)		BSE15		BSE15		
	K2-240 c	4.7 ± 0.5	1.8 ± 0.3	389 ± 18	(6)		CI		CI		
	K2-239 d	1.4 ± 0.5	1.10 ± 0.11	399 ± 1	(6)				PWD MORB		
	TRAPPIST-1 b	0.9 ± 0.8	1.086 ± 0.004	400 ± 8	(1)				PWD CI		
400-450	K2-239 c	0.9 ± 0.3	1.00 ± 0.11	427 ± 22	(6)	all	CI		BSE12		CC, CI
									BSE15		
									PWD CI		
450-500	K2 42 d	< 0.9	0.57 ± 0.18	450 ± 45	(7)	all	MORB		BSE12		CC, CI
							CI		BSE15		MORB
500-550	K2-239 b	1.4 ± 0.5	1.10 ± 0.11	502.0	(6)	all	BSE	solar			CC, CI
	TOI-776 b	4.7 ± 1.0	1.83 ± 0.11	513 ± 12	(8)		MORB				MORB
	GJ 357 b	2.1 ± 0.4	1.17 ± 0.04	525 ± 10	(9)		CI				
	TOI-270 b	1.9 ± 1.1	1.25 ± 0.09	528 ± 50	(10)		PWD BSE				
	Kepler-167 d	1.9 ± 1.0	1.20 ± 0.05	536.0	(11)						
550-600	Kepler-62 c	4.131	0.54 ± 0.04	578 ± 40	(12)	all	BSE	PWD MORB			CC, CI
	LHS 1478 b	2.3 ± 0.20	1.24 ± 0.06	595 ± 10	(13)	but solar	MORB, CI	solar			PWD MORB
							PWD BSE				
							PWD MORB				
600-650	GJ 9827 d	3.4 ± 0.7	1.96 ± 0.08	605 ± 20	(14)	all, but	BSE	BSE			CC
	LHS 1815 b	4.2 ± 1.5	1.09 ± 0.07	617 ± 90	(15)	solar	MORB, CI	solar			
	Kepler-114 c	2.9 ± 0.7	1.60 ± 0.19	623.0	(16)	PWD BSE	PWD BSE				
	K2 244 b	5.7 ± 2.4	1.75 ± 0.13	638 ± 7	(17)		PWD MORB				
	K2 252 b	5.6 ± 2.4	1.74 ± 0.17	639 ± 7	(17)						
650-700	GJ 486 b	2.8 ± 0.13	1.31 ± 0.07	700 ± 13	(18)	BSE, BSE12	BSE	BSE, BSE12			CC
						BSE15, CC	MORB, CI	BSE15, MORB			
						MORB, CI	PWD BSE	PWD CI			
						Earth, Archean	PWD MORB	Archean			
								solar			

Notes: The listed confirmed planets are all transiting and have planetary masses of $M_P < 8\,M_\oplus$, planetary radii of $R_P < 2\,R_\oplus$ and equilibrium temperatures of $250\,K < T_{eq} < 700\,K$. For these planets, we assume $T_{eq} = T_{surf}$ and a surface pressure of $p_{surf} = 1\,bar$. The temperature ranges are determined by comparable cloud condensate composition in the upper atmosphere as shown in Fig. 4.4.

References: (1) Gillon et al. (2017); (2) Sinukoff et al. (2016); (3) Suissa et al. (2020); (4)Waalkes et al. (2020); (5) Hirano et al. (2018); (6) Díez Alonso et al. (2018); (7) Muirhead et al. (2012); (8) Luque et al. (2021); (9) Luque et al. (2019); (10) Günther et al. (2019); (11) Kipping et al. (2016); (12) Borucki et al. (2013); (13) Soto et al. (2021) ; (14)Niraula et al. (2017); (15) Gan et al. (2020); (16) Batalha et al. (2013); (17) Livingston et al. (2018); (18) Trifonov et al. (2021)

Table 4.7: Connection between cloud condensates in the upper atmosphere and the crust composition as in Table 4.6, but for $700 < T_{surf} < 1000$ K.

T_{surf} [K]	Planet	M_P[$M_\oplus$]	R_P[$R_\oplus$]	T_{eq}[K]	Ref.	C[s]	NH_4Cl[s]	S_2[s]	FeS[s]	FeS_2[s]	KCl[s] NaCl[s]	AlF_3[s]	Fe_2O_3[s]
700-750	GJ 143 c	3.69919	0.89 ± 0.07	703 ± 24	(19)	CI	BSE	CC				Earth	
	K2 155 b	4.7 ± 0.4	1.81 ± 0.16	708 ± 40	(5)	PWD MORB	BSE12	PWD BSE					
	K2 154 b	6.8 ± 2.5	1.99 ± 0.21	715 ± 9	(17)		BSE15						
	GJ 9827 c	1.9 ± 0.5	1.20 ± 0.05	722 ± 25	(20)		MORB						
	Kepler-114 b	7 ± 4	1.26 ± 0.14	722.0	(15)		PWD CI						
							Archean						
							solar						
750-800	KOI-1599.01	4.6 ± 0.3	1.9 ± 0.4	755.0	(21)	PWD MORB	BSE	CC				Earth	
	GJ 3473 b	1.9 ± 0.3	1.264 ± 0.006	773 ± 16	(22)		BSE12	PWD BSE					
	TOI-1235 b	5.9 ± 0.7	1.69 ± 0.08	775 ± 13	(23)		BSE15						
	K2 257 b	0.7 ± 0.5	0.83 ± 0.06	789 ± 14	(17)		MORB						
	K2 254 b	5.2 ± 2.6	1.63 ± 0.28	791 ± 26	(16)		PWD CI						
							Archean						
							solar						
800-900	L 168-9 b	4.6 ± 0.6	1.390 ± 0.09	820 ± 160	(24)	PWD MORB	PWD CI	CC	BSE	MORB	BSE	Earth	
	TOI-178 c	4.8 ± 0.7	1.67 ± 0.11	873 ± 18	(25)			PWD BSE			BSE12		
	LTT 3780 b	3.1 ± 0.6	1.33 ± 0.08	892.0	(26)						BSE15		
											Archean		
											solar		
900-1000	HD 136352 b	4.6 ± 0.5	1.48 ± 0.06	911 ± 18	(27)	PWD MORB		PWD BSE	BSE	MORB	BSE	Earth	CC
	K2 228 b	3.2 ± 1.7	1.21 ± 0.10	914 ± 14	(17)						BSE12		
	TOI-1634 b	4.9 ± 0.7	1.79 ± 0.09	924 ± 22	(28)						BSE15		
	K2 158 c	3.6 ± 2.0	1.28 ± 0.13	948 ± 13	(17)						PWD BSE		
	K2 224 b	4.9 ± 2.4	1.56 ± 0.16	1002 ± 11	(17)						PWD CI		
	Kepler-93 b	4.5 ± 0.9	1.57 ± 0.11	1037.0	(29)						Archean		
	K2-233 b	3 ± 3	1.40 ± 0.07	1040 ± 27	(30)						solar		
	TOI-178 b	1.5 ± 0.5	1.15 ± 0.08	1040 ± 22	(25)								
	GJ 9827 b	4.9 ± 0.4	1.53 ± 0.06	1040 ± 40	(20)								

Notes: The listed confirmed planets are all transiting and have planetary masses of $M_P < 8\,M_\oplus$, planetary radii of $R_P < 2\,R_\oplus$ and equilibrium temperatures of $750\,K < T_{eq} < 1050\,K$. For these planets, we assume $T_{eq} = T_{surf}$ and a surface pressure of $p_{surf} = 1$ bar. The temperature ranges are determined by comparable cloud condensate composition in the upper atmosphere as shown in Fig. 4.4.

References: (5) Hirano et al. (2018); (16) Batalha et al. (2013); (17) Livingston et al. (2018); (19) Dragomir et al. (2019); (20) Niraula et al. (2017); (21)Panichi et al. (2019); (22) Kemmer et al. (2020); (23) Bluhm et al. (2020); (24) Astudillo-Defru et al. (2020); (25) Leleu et al. (2021); (26) Cloutier et al. (2020); (27) Kane et al. (2020); (28) Cloutier et al. (2021); (29) Ballard et al. (2014); (30) Lillo-Box et al. (2020)

Furthermore, the chemical composition of the clouds at a given ($p_{\rm gas}, T_{\rm gas}$) is related to the crust composition, although conclusions can be ambiguous (see Tables 4.6 and 4.7). For example, the detection of S_2[s] at ($p_{\rm gas} \approx 30\,$mbar, $T_{\rm gas} \approx 200\,$K) constrains the surface conditions to $T_{\rm surf} \approx 400\,$K and $T_{\rm surf} \approx 1000\,$K, under the assumption of a polytropic atmosphere with surface pressures of 1 bar. Our study shows, that under these conditions, the cloud condensate S_2[s] constrains the crust composition to be CC or CI like for the 1 bar atmosphere. For $p_{\rm surf} = 100\,$bar, the crust compositions is more ambiguous, and could be similar to BSE, CC, MORB, CI, PWD BSE, or PWD MORB. However, additionally ruling out the presence of water clouds can further constrain the crust composition to only CC or PWD BSE.

In order to use cloud condensates to constrain crust compositions of already known planets, we created a list of known transiting planets with planetary masses $M_{\rm P} < 8\,M_\oplus$, planetary radius $R_{\rm P} < 2\,R_\oplus$ and equilibrium temperature $250\,{\rm K} < T_{\rm eq} < 1050\,{\rm K}$. In Tables 4.6 and 4.7 we provide an overview of which cloud condensates suggest a certain crust composition. For this classification, we assume a polytropic atmosphere with $p_{\rm surf} = 1\,$bar and $T_{\rm surf} = T_{\rm eq}$. Where $T_{\rm eq}$ is the reported equilibrium temperature of the respective planets.

One of the fundamental assumptions for the determination of the crust composition is the surface pressure, which cannot directly be determined, leaving a degeneracy if only the upper atmosphere is constrained (see also Keles et al., 2018; Yu et al., 2021). Our study showed that the detection of H_2S[s] or H_2SO_4[s] condensates would suggest a high surface pressure.

Although our study does show the thermal stability of H_2O[l,s] clouds high in the atmosphere for all crust compositions, water as a stable condensate on the surface of the respective rocky exoplanets is rare (see Sect. 4.3.4). Only if the water cloud base is close to the surface, water can be stable at the planetary surface. Therefore, a detection of water clouds alone, without further constraints on the height and extent of those clouds, does not necessarily imply that liquid water is also present on the surface. This is underlined by the thermal stability of water cloud condensates in the solar abundance model. Such an atmospheric composition can be representative of primordial atmospheres of rocky planets but also more massive planets such as mini-Neptunes.

Our work shows that multiple cloud condensates can be thermally stable in one atmosphere. Some of which are connected via condensate chains (Fig. 4.6). Although not always all condensates of a condensate chain appear as thermally stable condensates in a given atmosphere, the condensate chains itself are robust against changes in crust composition as well as ($p_{\rm surf}, T_{\rm surf}$).

Based on this, the detection of a condensate in a planetary atmosphere can suggest further condensates in lower atmospheric layers. An example would be the detection of FeS_2[s], which suggests the presence of FeS[s] in lower atmospheric layers. As these clouds would most likely be situated in the optically thick part of the atmosphere, their detection will be a great challenge.

4.5 Summary

The work presented in this Chapter investigated the stability of a large collection of cloud species in the troposphere of rocky planets made of various elemental compositions. We considered a solid planetary surface in chemical and phase equilibrium with the near-crust atmosphere, where the deposition and the outgassing rates balance each other for every condensed species. Other geological (e.g. tectonics and volcanism) or biological fluxes are disregarded. Our cloud condensate models are then based on a hydrostatic, polytropic ($p_{\rm gas}, T_{\rm gas}$) profile in the lower (tropospheric) part of the atmosphere, where we assumed the polytropic index to be $\gamma = 1.25$ in all models. The model uses a bottom-up algorithm where we determine, in each new layer, which condensates become thermally stable and successively remove the elements contained in these condensates, until chemical and phase equilibrium is again established.

This fast and simple model provides first insights into the sequence of cloud layers to be expected in the atmospheres of rocky exoplanets, depending on surface temperature, surface pressure, and crust composition. These equilibrium cloud condensation sequences should be regarded as a starting point for further investigations in kinetic cloud formation models. However, models that include boundary fluxes, both at the bottom and the top of the atmosphere, for example geological and biological fluxes from below, or atmospheric escape rates at the top, as well as non-equilibrium processes such as photochemistry are beyond the scope of this thesis.

The thermally stable cloud condensates in our model can be divided into low and high temperature cloud condensates, with a dividing temperature of about $T \approx 400\,\mathrm{K}$. Below that dividing temperature, the overall most abundant condensates are H_2O[l,s], C[s], and NH_3[s]. Further condensates at low temperatures are S_2[s] or contain ammonia, in particular NH_4Cl[s] and NH_4SH[s]. Only in models with high surface pressures, we find H_2SO_4[s] to become another stable condensate in high atmospheric layers. For very low temperatures ($T \lesssim 150\,\mathrm{K}$) CO_2[s], CH_4[s], NH_3[s], and H_2S[s] clouds can be present. H_2S[s] is also only thermally stable for higher surface pressures.

In our Solar System some of these cloud condensate are present in various planets. For exam-

ple H_2O[s,l] on Earth, while on Mars clouds of CO_2[s] (Montmessin et al., 2007) and H_2O[s] ice (Curran et al., 1973) are present. For the clouds on Venus, H_2SO_4[s] is discussed as the main cloud constituent (e.g. Knollenberg & Hunten, 1980; Rimmer et al., 2021a). The four giant planets in our solar system are thought to have multiple cloud layers consisting of H_2O[s], NH_4SH[s], and NH_3[s] (e.g. Atreya et al., 1999; Wong et al., 2015). Furthermore, CH_4[s] clouds are found in the atmospheres of Uranus, Neptune, and Saturn's moon Titan (e.g. Brown et al., 2002; Sromovsky et al., 2011; Lellouch et al., 2014). For clouds on Neptune's moon Triton, N_2[s] has been been suggested (Tokano, 2017).

At higher temperatures $T \gtrsim 500\,\mathrm{K}$, the most relevant cloud species are found to be halides (KCl[s], NaCl[s]), iron sulphides (FeS[s], FeS_2[s]) and iron oxides (FeO[s], Fe_2O_3[s], Fe_3O_4[s]). Contrasting to previous research focusing on giant planets, which are hydrogen rich, we do not find any Na_2S[s] in our models (Visscher et al., 2006; Parmentier et al., 2016; Gao et al., 2020) but rather NaCl[s] instead. For temperatures higher than investigated in this Chapter ($T_{\mathrm{surf}} \gtrsim 1250\,\mathrm{K}$), when S is more abundant than Cl, we find Na_2S[s] as a stable cloud condensate (see also Woitke et al., 2020).

The only condensate that is thermally stable in the temperature range $400\,\mathrm{K} \lesssim T_{\mathrm{gas}} \lesssim 500\,\mathrm{K}$ and also high in abundance is C[s] (i.e. graphite clouds). It is the only condensate which can be stable throughout the atmospheric parameter range investigated in this work. In agreement to this, previous studies have shown that carbon is thermally stable in the form of graphite for carbon-rich stars, but also giant planets with C/O$\geq$ 0.85 (e.g. Sharp, 1988; Lodders & Fegley, 1997, 2002; Moses et al., 2013; Mbarek & Kempton, 2016).

Looking at all condensed species, including those with trace abundances, we show that for the various different element abundances and surface temperatures from 300 K to 1000 K considered in this Chapter, a total of 55 condensates are found to be thermally stable in models with 1 bar surface pressure, plus additional 17 condensates for the 100 bar models. The gap between the low and high-temperature cloud condensates is filled by the high-temperature condensates at lower abundances.

The different cloud condensates are not independent of each other but follow a sequence of mostly type 2 phase transitions as explained in Woitke et al. (2018), characterised by sudden changes of the stable condensates. Since we are only considering models with $T < 1000\,K$ in this Chapter, type 1 phase transitions, where condensates are slowly building up from the gas phase,

are relatively rare. It is remarkable that these condensation sequences, or condensation chains as shown in Fig. 4.6, are relatively robust against changes of the surface element abundances, even for the hydrogen-rich models considered in this Chapter (Archean and solar element abundances). These models can be seen as a chemical composition of atmospheres either of very young or very massive planets, which are able to keep the light elements in the atmosphere over longer times.

All atmosphere models in this Chapter can be classified as being either a member of a type A (H-rich), type B (O-rich), or type C atmosphere (coexistence of CO_2 and CH_4), according to Woitke et al. (2021). An important conclusion from this investigation is that the atmospheric type does not change as function of height, despite the changing element abundances due to condensation, whereas other characteristics such as the carbon to oxygen ratio (C/O) or the metallicity (O/H) can change significantly. This finding emphasises the robustness of the classification scheme presented in Woitke et al. (2021) and Chapter 3.

The results of this bottom-to-top atmospheric model are a step towards solving the inverse problem of inferring surface conditions based on cloud condensates and the higher atmospheric composition. In general, the inferred crust composition, based on cloud condensates, is degenerate (see Tables 4.6 and 4.7). This shows again how challenging and ambiguous the task of inferring surface conditions from the high atmosphere conditions can be. However, certain condensates, such as the sulphur-containing clouds at the low-temperature regime, do constrain the surface conditions. For a further discussion on the degeneracies see Sect. 4.7. For example, NH_4SH[s] and S_2[s] are only thermally stable in reducing and oxidising environments, respectively, whereas H_2SO_4[s] and H_2S[s] have only been found for our polytropic atmospheres with higher surface pressure. This increased $p_{\rm surf}$ results in an increased $T_{\rm surf}$, which is incompatible with liquid water at the planetary surface. Loftus et al. (2019) found that thick H_2SO_4[s] clouds and hazes are incompatible with a substantial water ocean, as the sulphur compound will dissolve in the ocean. It has been suggested that under oxygen rich conditions sulphur will condense in the form of S_8[s] (e.g. Hu et al., 2013). We on the other hand find the allotrope S_2[s] to form instead.

We note that H_2O[l,s] is a thermally stable cloud condensate for every crust composition investigated in this Chapter. However, the pressure level of the H_2O[l,s] cloud base is varying substantially among the models and is a consequence of the hydration level of the surface rocks. Only for a fully hydrated crust where all hydrated minerals have formed, water clouds extend down to the atmosphere-crust interaction layer, which is equivalent to H_2O[l,s] as a stable part of

the planetary crust. This underlines, that the detection of water vapour in a planetary atmosphere or even water condensates do not necessarily imply the presence of surface water.

Although the crust compositions without H_2O[l] are not habitable for water-based life, we show that H_2O[l] can be stable in parts of these planetary atmospheres. These conditions can be used for thoughts on aerial biospheres (Seager et al., 2021b). With our model, we can show, that not only liquid water is stable in some atmospheres, but other condensates, which can provide some nutrients for biological processes (e.g. NH_4SH[s] or $Mg_3P_2O_8$[s]). Additionally some gas phase molecules such as CH_4 or NH_3 could provide energy sources for life to thrive.

4.6 The Earth model

The composition of the surface of the Earth and its atmosphere are strongly affected by geological processes such as plate tectonics and volcanism, as well as biological activity (see e.g. Claire et al., 2006; Mills et al., 2014; Lammer et al., 2018). It is nevertheless an interesting question whether or not a simple model can be constructed, in which crust and atmosphere are in chemical and phase equilibrium with each other, to better discuss and quantify the influence of the non-equilibrium processes. In this Section, we demonstrate that it is indeed possible to find a set of total (condensed + gas) element abundances which simultaneously fit the measured molecular abundances in the Earth atmosphere and the condensed mass fractions in the Earth's crust when assuming chemical and phase equilibrium.

Our starting point of this model are the mass fractions f_k of the 18 elements H, C, N, O, F, Na, Mg, Al, Si, P, S, Cl, K, Ca, Ti, Cr, Mn, and Fe as measured in the Earth's continental crust (Schaefer et al., 2012), see also column 'CC Schaefer' in Table A.2 in Herbort et al. (2020). These are the abundances which represent the condensed matter in the model.

Next, we (i) convert these mass fractions f_k to nuclei particle ratios, (ii) multiply with a large, arbitrary factor $\Delta = 1000$ to account for the dominance of condensed over gaseous matter, and (iii) add the observed gas abundances in the Earth atmosphere. Resulting in

$$\epsilon_k^{\mathrm{tot}} = \Delta \frac{f_k}{m_k} + \sum_i s_{i,k} \, (c_i^{\mathrm{gas}} + \delta_i), \tag{4.9}$$

where m_k is the mass of element k, $s_{i,k}$ is the stoichiometric factor of element k in molecule i, c_i^{gas} is the particle concentration of molecule i in the Earth atmosphere, and δ_i are corrections as

Table 4.8: Comparison of Earth atmospheric data (Muralikrishna & Manickam, 2017) with a GGchem phase-equilibrium model at $p = 1.013$ bar and $T = 288.15$ K based on total element abundances adjusted to fit the data, see text.

	N_2	O_2	H_2O	Ar	CO_2	Ne	He	CH_4	H_2	SO_2	HNO_3
observed (c_i)	77%	20.5%	10 ppm – 5%	0.93%	400 ppm	18 ppm	5.2 ppm	1.8 ppm	550 ppb	75 ppb	?
GGchem model	77%	20.5%	1.7%	0.93%	400 ppm	18 ppm	5.2 ppm	≪	≪	≪	2 ppb

The measured concentrations of H_2O depend on latitude, height, and weather conditions. The value of 1.7% corresponds to saturated liquid water (100% humidity) at 288.15 K in the model. Molecules marked with '≪' and all other molecules not listed have concentrations $< 10^{-10}$ in the model.

discussed below.

Based on these total element abundances $\epsilon_k^{\rm tot}$ we ran a GGchem model for the mean conditions at the surface of Earth $p = 1.013$ bar and $T = 288.15$ K. The results include an identification of the stable condensates, the condensed mass fractions (which are very close to f_k because of the large factor Δ), and the molecular concentrations in the atmosphere.

Without corrections δ_i, this experiment results in an almost pure N_2 atmosphere ($\sim 99\%$) with traces of noble gases, but all other molecules are incorporated in the condensed species. For example, the gaseous H_2O disappears in phyllosilicates and the CO_2 is incorporated in form of carbonates. In order to arrive at a better fit, we add

- more O_2 to make the crust extremely oxidised, until a small leftover of O_2 is contained in the atmosphere,
- more H_2O to completely saturate the phyllosilicates, and then even more to achieve an atmosphere that is saturated with liquid water,
- more CO_2 to completely saturate the carbonates in the crust, until we have some leftover CO_2 in the atmosphere.

After some trial and error, we determined the correction terms of $\delta_{\rm O2} \approx 4.92$, $\delta_{\rm H2O} = 160$, and $\delta_{\rm CO2} \approx 162.8$ for Eq. 4.9. With this, we arrived at a model that roughly fits the composition of the Earth atmosphere (Table 4.8) and makes interesting predictions about the Earth crust composition in phase equilibrium (Table 4.9).

The resulting mass fractions of the elements included in this chapter are given in Table 2.2. The noble gases show no condensate phase in the parameter space investigated and are therefore not included in this work. The resulting mass fractions $m_{\rm f,i}$ necessary to match the Earth atmosphere are $m_{\rm f,He} = 2.462 \cdot 10^{-10}$, $m_{\rm f,Ne} = 4.306 \cdot 10^{-9}$, and $m_{\rm f,Ar} = 4.379 \cdot 10^{-6}$.

Table 4.9: Composition of the Earth crust as predicted from the GGchem phase equilibrium model described in Table4.8.

formula	name	mass fraction
$NaAlSi_3O_8$[s]	*albite*	24.2%
SiO_2[s]	*quartz*	22.8%
$Al_2Si_2O_9H_4$[s]	*kaolinite*	16.3%
$CaMgC_2O_6$[s]	*dolomite*	15.0%
$KAlSi_3O_8$[s]	*microcline*	13.8%
FeO_2H[s]	*goethite*	6.25%
TiO_2[s]	*rutile*	0.61%
$Ca_5P_3O_{12}F$[s]	*fluorapatite*	0.38%
$CaSO_4$[s]	*anhydrite*	0.27%
Mn_2O_3[s]	*bixbyite*	0.094%
H_2O[l]	*liquid water*	0.077%
NaCl[s]	*halite*	0.070%
MgF_2[s]	*Mg-fluoride*	0.048%
Cr_2O_3[s]	*eskolaite*	0.017%
CaF_2[s]	*fluorite*	0.009%

It is noteworthy that, when we choose a ten times larger value for Δ, that is 10000 instead of 1000, we arrive at results that are very close to those listed in Tables 4.8 and 4.9, when the corrections δ_i are also increased by a factor of 10. Hence, given an initial set of condensed element fractions (here f_k) and the necessity to fit the abundances of the main molecules in the atmosphere (here c_i) leads to unique conclusions.

The results in Table 4.8 show that it is indeed possible to fit the concentrations of the main molecules N_2, O_2, H_2O and CO_2 (type B atmosphere), and the noble gases, but it is entirely impossible to fit other molecules with ppb-concentrations, in particular CH_4, which is a well-known non-equilibrium indicator for biological activity (see e.g. Cicerone & Oremland, 1988; Sterzik et al., 2012; Guzmán-Marmolejo et al., 2013). Sulphur is found to be practically absent from the gas phase. The most relevant sulphur molecule is H_2SO_4 with a concentration of $\sim 10^{-15}$ in this model.

Table 4.9 shows a number of well-known minerals that are indeed found in large quantities on the Earth surface. Remarkably, we find *goethite* which is a weathering product of iron that is abundantly found in soil and other low-temperature environments such as sediment. *Kaolinite* is a common clay mineral with chemical composition $Al_2Si_2O_5(OH)_4$. It is a soft, earthy mineral produced by the chemical weathering of aluminium silicate minerals such as feldspar. Sulphur is found to be completely locked up in *anhydrite* in the model. However, more abundantly found

on Earth is *gypsum* with chemical formula $CaSO_4 \cdot 2\,H_2O$, the weathering product of *anhydrite*, but unfortunately, *gypsum* is not included in GGchem's data collection. We therefore consider the results of our simple GGchem model as continental crust after complete weathering, that is after bringing the material in intensive contact with atmosphere and water, in the limiting case $t \to \infty$. All other condensates not listed in Table 4.9 have exactly zero mass fractions in the model, because they are transformed into thermodynamically even more stable condensates in equilibrium.

4.7 Degeneracies in obtaining the surface composition

The model presented in this chapter works towards understanding the link between the surface and the atmospheric composition as well as potential cloud condensates in these atmospheres. One application for this model is the reverse problem of inferring the surface composition and conditions from measurements of high atmospheric composition and cloud condensates. This inverse problem is becoming highly important for future missions such as JWST, but especially ARIEL, LUVOIR, and HabEx, which are especially designed to detect and characterise atmospheres of rocky exoplanets. Our model helps towards identifying and understanding some of the degeneracies implied by the concept.

The approach of an atmosphere and crust in chemical and phase equilibrium yields a unique composition of the gas and condensate phase under the assumption of a known total element abundance of the entire system. However, even the best future measurement will not provide the entire mass element abundance, but rather the gas composition, which is only a result of the constraints of the supersaturation ratio $S_j \leq 1$ for all condensates j. From the gas phase abundances, a list of thermally stable condensates can be inferred.

Any given set of element abundances ($\epsilon_{\rm tot}$) results in solutions for the gas composition ($\epsilon_{\rm gas}$) and crust condensates ($\epsilon_{\rm crust}$) for all elements k. That is

$$\epsilon^k_{\rm tot} = \epsilon^k_{\rm gas} + \epsilon^k_{\rm crust}. \tag{4.10}$$

However, for one given set of gas phase abundances $\epsilon_{\rm gas}$, the total element abundances are not unambiguously defined. Only the list $\{c_j | j = 1, ..., N\}$ of N stable condensates c_j with supersaturation ratios $S_j = 1$ is well defined. If we add an amount of elements to $\epsilon^k_{\rm tot}$ that corresponds to the stoichiometry ($s_{j,k}$) of a chosen stable condensate, that condensate will simply fall out again. This does not change the supersaturation ratio and therefore has no influence on the resulting gas

abundances. The modified total element abundances $\tilde{\epsilon}^k_{\rm tot}$ can be obtained by

$$\tilde{\epsilon}^k_{\rm tot} = \epsilon^k_{\rm tot} + X_j s_{j,k}, \tag{4.11}$$

where X_j can be any number for a stable condensate, as long as the abundance of the corresponding condensate remains positive. The gas phase results are the same for both $\epsilon^k_{\rm tot}$ and $\tilde{\epsilon}^k_{\rm tot}$, resulting in an N-dimensional manifold for the crust composition, if the gas phase is known. Thus, we can predict the mixture of stable condensates, and determine for example whether or not water is stable on the surface of an exoplanet. However, we cannot predict how much of any of these stable condensates is present, when only the gas properties are known.

4.8 Gas phase composition plots

Here we show the gas phase composition plots for the lower temperature models (Fig. 4.11 and 4.12).

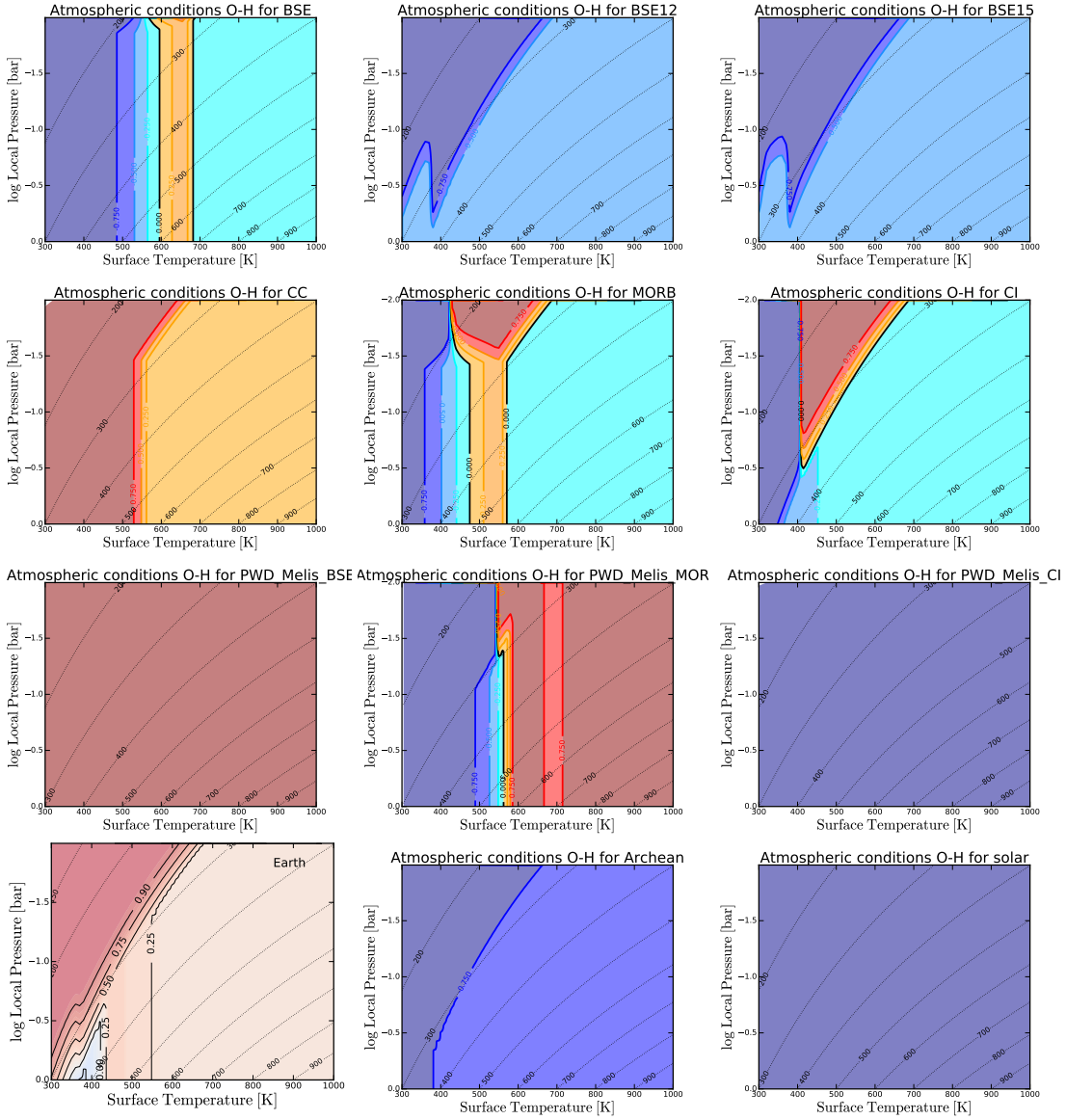

Figure 4.11: Comparison of the gas phase O and H abundances, expressed as the (O-H)/(O+H) ratio. Oxygen is dominant in the red regions, whereas carbon dominance is indicated in blue regions. As in Fig. 4.4 the dotted lines indicate the local gas temperatures.

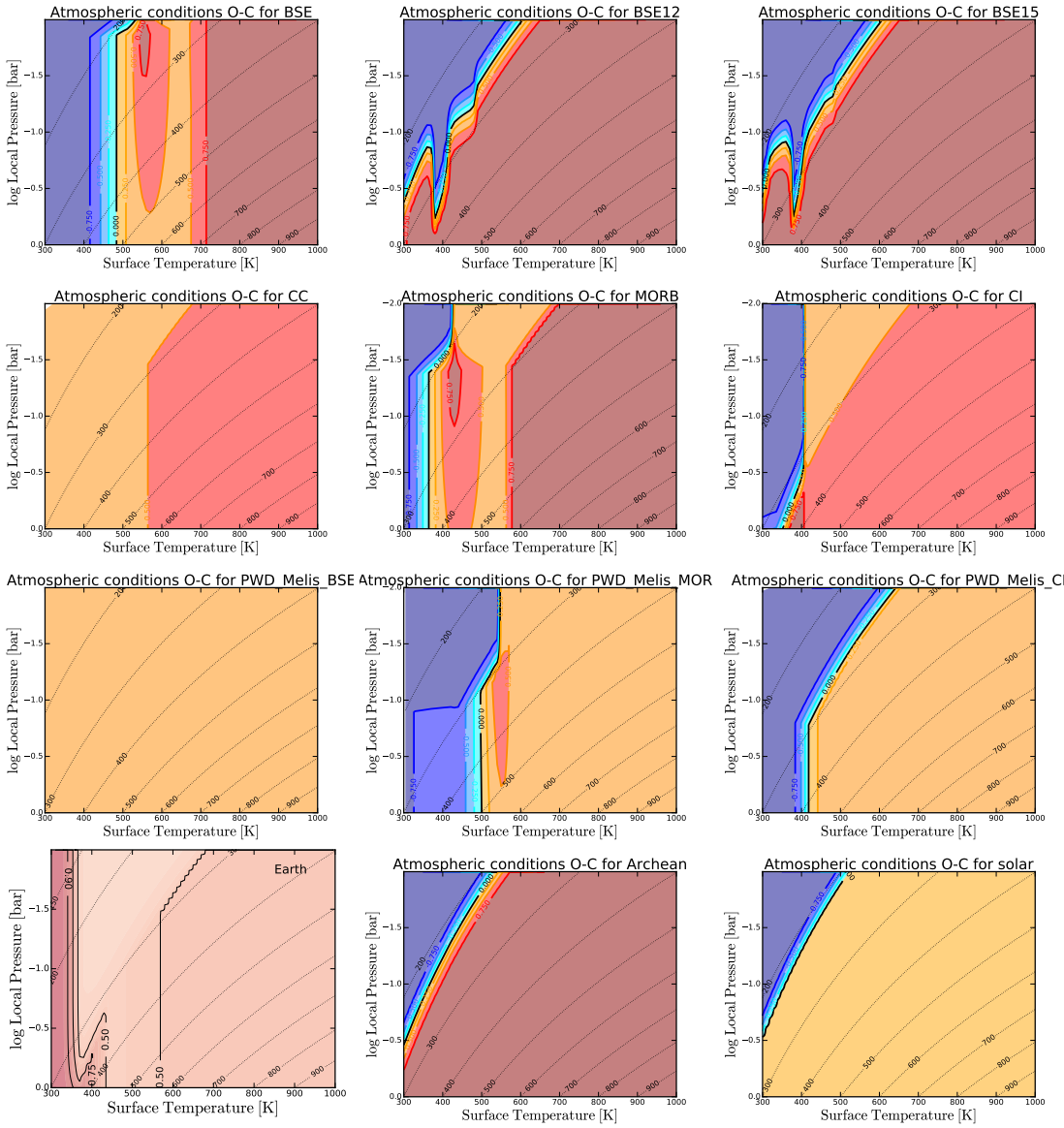

Figure 4.12: Comparison of the gas phase O and C abundances, expressed as the (O-C)/(O+C) ratio. Oxygen is dominant in the red regions, whereas carbon dominance is indicated in blue regions. The colour scheme is consistent for all panels. As in Fig. 4.4 the dotted lines indicate the local gas temperatures.

"Of course life can pop up in many a place
Exotic locations abound out in space
Like subsurface oceans on wild icy moons
Or Venus' clouds, drifting in balloons"

- Sean Raymond, *Black Holes. Stars, Earth & Mars*

5

Chemical state of CHNOPS elements and implications on habitability

In this chapter the atmospheric conditions of regions, where liquid water is a thermally stable condensate, are explored. We especially focus on the chemical state of the present elements. Based on the availability of the nutrient elements (carbon, hydrogen, nitrogen, oxygen, and sulphur) we introduce a scheme of different habitability levels and apply it to models based on those presented in Chapter 4 and Herbort et al. (2022).

This section is currently unpublished, but will be submitted as 'The atmospheres of rocky exoplanets III. Chemical state of CHNOPS elements and implications on habitability' by O. Herbort, P. Woitke, A. L. Zerkle, Ch. Helling to Astronomy & Astrophysics.

5.1 Introduction

Some of the key questions for humankind are what the thermo-chemical conditions favourable for the creation, evolution and persistence of life on Earth and other planets are. In recent times, many exoplanets have been detected and the question of the potential for biological and chemical processes to exist on these planets arose. These worlds show a vast diversity, some without analogue in our own solar system. Especially for the rocky planets, a large diversity of different atmospheric compositions is expected (e.g. Leconte et al., 2015; Grenfell et al., 2020). While the extent of these atmospheres can range from a large envelope of primordial gas to almost no atmosphere at all, the composition can be very diverse, covering reducing and oxidizing atmospheres. With the upcoming next generation ground and space based telescopes (e.g. ELT (Gilmozzi & Spyromilio, 2007), ARIEL (Tinetti et al., 2018), LUVOIR (Bolcar et al., 2016), and HabEx (Stahl et al., 2020)) observations of atmospheres of smaller planets will becomes feasible (see e.g. Lopez-Morales et al., 2019; Wunderlich et al., 2021; Ito et al., 2021). The detailed understanding of the planets itself becomes important for interpreting observations, especially for the detection of biosignatures (Catling et al., 2018; Meadows et al., 2018; Lisse et al., 2020; Lyons et al., 2021). These signatures of life are mostly confined to water based life, as it is the only known form of life on our planet. However, other solvents could potentially replace the liquid water for the formation of life (e.g. Ballesteros et al., 2019).

Water is a commonly-present molecule throughout the universe. Besides the oceans and troposphere of Earth, liquid water is present in the Solar System in sub-glacial oceans on Europa and Enceladus (Tjoa et al., 2020), was present on young Mars (Lammer et al., 2018), and in clouds of sub-Neptunes (Charnay et al., 2021) and gas giants (Mang et al., 2022). A similar diversity of water environments is to be expected for exoplanets, providing many planets with liquid water to study. Whereas the liquid and frozen surface oceans provide the potential for surface biospheres on rocky planets, water clouds can be present for larger planets as well as rocky planets (Benneke et al., 2019; Charnay et al., 2021). As the origin of life in water droplets in an atmosphere has been discussed (e.g. Woese, 1979), this provides the potential for aerial biospheres not only for rocky planets, but also for mini-Neptunes (Seager et al., 2021b). Furthermore, planets with extended hydrogen envelopes could also have surface water oceans at high atmospheric pressures, if the temperatures are temperate and could also host habitable environments (Madhusudhan et al., 2021).

Similar aerial biospheres have been proposed for Venus, as the temperatures in Venus' clouds at a pressure level of around 1 bar are similar to those on Earth's surface and allow in principle for the presence of liquid water droplets and therefore potential biological activity in the clouds (e.g. Morowitz & Sagan, 1967; Dartnell et al., 2015; Kotsyurbenko et al., 2021; Rimmer et al., 2021a; Patel et al., 2022). The recent detection of PH_3 (phosphine) in Venus' atmosphere by (Greaves et al., 2021) has sparked many discussions on the detection itself (e.g. Snellen et al., 2020; Lincowski et al., 2021; Krissansen-Totton et al., 2021), but also about the origin of PH_3 under the assumption of its actual presence. (Bains et al., 2021, 2022) discussed that there is no known process available to abiotically produce a PH_3 feature in the Venus atmosphere. Omran et al. (2021) further discuss phosphine production on rocky exoplanets in more general terms. Assuming the production by some kind of living organism, this would introduce the necessity of a biosphere which is only present in a cloud layer. Individual organisms would need to remain afloat for long enough to metabolize and reproduce, before eventually falling towards the surface of Venus (Seager et al., 2021b,a; Patel et al., 2022). This concept of aerial biospheres enlarges the possibilities of potential habitability form the presence of liquid water on the surface to all planets with liquid water clouds. See Seager et al. (2021b) for a discussion on the potential of aerial biospheres on mini-Neptunes. The water clouds of such planets could provide the chemical potential for the formation of life (Hallsworth et al., 2021).

For the formation of life, the presence of liquid water is not the only hurdle to overcome, but also further elements need to be present. Simple life as we know it is based on the presence of carbon, hydrogen, nitrogen, oxygen, phosphorus, and sulphur, in the following referred to as CHNOPS elements (Horneck et al., 2016). Chemical reactions triggered by stellar radiation, lightning, high energetic particles, and cosmic rays can form amino acids and other pre-biotic molecules from which life can eventually form (see e.g. Bailey et al., 2014; Ferus et al., 2017; Ranjan et al., 2021; Barth et al., 2021). For these reactions, the molecular state in which the elements are present is of particular importance, because elemental speciation dictates bioavailability.

In order to constrain the pre-biotic atmospheres from which life might evolve, we investigate and characterise the chemical state of the elements present in the atmosphere, where liquid water is thermally stable. We use a chemical equilibrium model for the lower parts of atmospheres of rocky exoplanets with various surface compositions, which allow the study of all elements present in the gas phase, especially focussing on the different nutrients which are necessary for the formation of pre-biotic molecules in exoplanetary atmospheres.

In Sect. 5.2, we describe the atmospheric model in use and introduce our concept of habitability levels in Sect. 5.3). The resulting habitability levels and chemical states of the different elements are discussed in Sect. 5.4. We finish with a discussion and implications for potential biospheres in Sect. 5.5.

5.2 Atmospheric model

In order to investigate the availability of nutrients in exoplanet atmospheres, we use the atmospheric model presented in Herbort et al. (2022) which uses the chemical equilibrium solver GGchem (Woitke et al., 2018). The bottom-to-top atmosphere model describes the lower atmosphere with a polytropic hydrostatic equilibrium atmosphere which takes element depletion by cloud formation into account (see Fig. 5.1). The base of the atmosphere is in chemical phase equilibrium with the crust as described in Herbort et al. (2020). In every atmospheric layer, the chemical equilibrium is solved and all thermally stable condensates are removed while the gas phase is the total element abundance of the atmospheric layer above. This depletes the element abundances of all elements affected by cloud formation. Each bottom-to-top atmosphere is fully defined by the surface pressure ($p_{\rm surf}$), surface temperature ($T_{\rm surf}$), set of total element abundances ($\epsilon_{\rm tot}$) and the polytropic index (γ).

For the (p, T) profiles investigated in this work a constant polytropic index $\gamma = 1.25$ (see Sect. 4.2.1) is assumed and the surface conditions are defined such that the atmosphere reaches the reference temperature of $T_{\rm ref} = 300\,{\rm K}$ in the atmosphere at $p_{\rm ref} = 1\,{\rm bar}$. As shown in Herbort et al. (2022) this is guaranteed for a $(p_{\rm gas}, T_{\rm gas})$ profile defined by

$$T_{\rm gas} = \frac{T_{\rm ref}}{p_{\rm ref}^{1-1/\gamma}} p_{\rm gas}^{1-1/\gamma}. \tag{5.1}$$

We investigate a surface temperature range from 300 K to 1000 K. The surface pressures for the different surface temperatures are given by Eq. 5.1 to ensure that all atmospheric profiles reach the reference point.

In our calculations, the included 18 elements (H, C, N, O, F, Na, Mg, Al, Si, P, S, Cl, K, Ca, Ti, Cr, Mn, and Fe) can form 471 gas species and 208 condensates. The total element abundances $\epsilon_{\rm tot}$ in this work are the same as in Herbort et al. (2022) (see Table 2 therein). These are based on Bulk Silicate Earth (BSE, Schaefer et al., 2012), Continental Crust (CC, Schaefer et al., 2012), Mid Oceanic Ridge Basalt (MORB, Arevalo & McDonough, 2010), CI chondrite (CI, Lodders

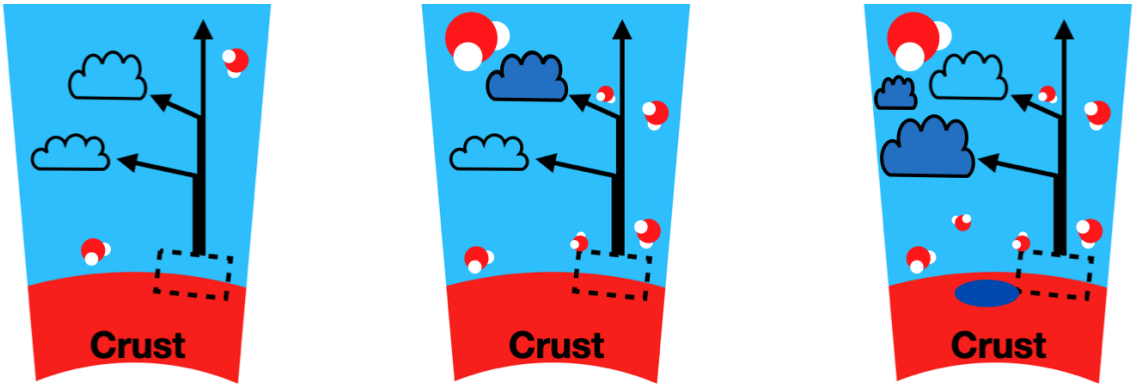

Figure 5.1: The sketch summarises the atmospheric model and motivates different regimes for the presence of water. The crust and near-crust atmosphere are in chemical equilibrium and indicated by the dashed box. On this, the bottom-to-top atmospheric model is based. All thermally stable cloud condensates are removed from the gas composition (arrows to the side), while the gas-phase element abundances are transported to the atmospheric layer above. The uncoloured clouds indicate an arbitrary cloud condensate, while the blue clouds indicate water clouds. The different panels indicate different regimes of water stability and therefore different potentials of habitable environments. **Left panel:** Water is only present in the gas phase and therefore this planet cannot be habitable. **Middle panel:** Water clouds are present high in the atmosphere, but there is no water condensate present at the surface, indicating a potential for an aerial biosphere. **Right panel:** Water is stable at the surface (blue pond) and in form of thermally stable water clouds throughout the atmosphere. This allows for surface and aerial habitability.

et al., 2009), and solar abundances (Asplund et al., 2009). Furthermore, we use sets of element abundances based on BSE with increased abundances of H and O (BSE12, BSE15). The Earth set of total element abundances is fitted to the current day atmospheric composition of Earth (see Appendix A Herbort et al., 2022). The Archean model represents a strongly reducing atmosphere above a water ocean. These four models are described in further detail in Herbort et al. (2022).

5.3 Habitability levels

The characterisation of the habitability potential of different atmospheric compositions should take not only the presence of liquid water, but also the availability of essential elements into account. Therefore we introduce a concept of habitability levels in the following.

The first important substance for any discussion of any biology as we know it is liquid water. This lead to the postulation of the habitable zone, where water can exist on the surface of a planet (e.g. Huang, 1959; Kasting et al., 1993). Based on the presence of water and some further assumptions on the needs for the evolution of life different habitable zones have been postulated (e.g. Hoehler, 2007; Ramirez, 2020). However, these approaches do not take into account the presence and chemical state of elements necessary for the formation of pre-biotic molecules, of special importance are the CHNOPS elements (Horneck et al., 2016). Therefore, we formulate

Table 5.1: Definition of the different nutrient availability levels.

Habitability levels	H_2O[l]	C	N	S	P
Level 0	✘	-	-	-	-
Level 1C	✔	✔	✘	✘	-
Level 1N	✔	✘	✔	✘	-
Level 1S	✔	✘	✘	✔	-
Level 2CN	✔	✔	✔	✘	-
Level 2CS	✔	✔	✘	✔	-
Level 2SN	✔	✘	✔	✔	-
Level 3	✔	✔	✔	✔	-
Level 3red	✔	red	red	red	-
Level 3ox	✔	ox	ox	ox	-
P	✔	-	-	-	✔

Notes: Tick marks refer to the presence of the respective molecule or molecules incorporating the respective element at abundance levels above ppb in the gas phase. The cross marks indicate, that no molecules carrying this element are present at abundances $> 10^{-9}$. The state of the elements indicated with '-' do not matter for the definition of the respective habitability level. 'red': indicates that the reduced form of the respective element (CH_4, NH_3, H_2S) is present at abundances higher than ppb. 'ox': indicates the presence of the oxidised state (CO_2, NO_x, SO_2) at abundances higher than ppb.
different habitability levels based on the presence and chemical state of these elements.

All habitability levels discussed in this chapter require the stability of water condensates and, therefore, points in the atmosphere where no water is thermally stable are defined as Level 0, independent of the presence of other elements. The further habitability levels have the stability of water as a precondition and are based on the presence of the elements C, N, and S, as H and O are by definition already present in the form of H_2O. We define an element i as present, if the concentration of an i bearing molecule is greater than one part per billion (10^{-9}, ppb). If one or two of these are present, this classifies as Level 1 and Level 2, respectively. In order to distinguish the different kinds of Level 1 and 2, the present elements are added to the notation. For example, if C is present, but not N and S, the atmospheric composition classifies as Level 1C. Following on this, the habitability level 3 requires the presence of all three elements.

For the habitability level 3 we further distinguish between the chemical redox state of the CNS elements. If all three elements are present in a reduced form (CH_4 for C, NH_3 for N, and H_2S for S), the habitability level is classified as Level 3red. The need for this additional distinction is motivated as it is known that under such reducing conditions processes such as lightning can result in the formation of pre-biotic molecules, such as HCN, amino acids, and nucleobasis (e.g. Miller, 1953; Miller & Urey, 1959; Toupance et al., 1975; Ferris et al., 1978; Parker et al., 2011; Ferus

Table 5.2: gas-phase molecules according to their highest abundance in the models in the pressure-temperature range discussed in the text.

Element	10%	0.1%	10^{-6}	10^{-9}
C	CO_2, CH_4		CO, COS	
N	N_2	NH_3		HNO_3, NO_2 (Earth $T_{surf} < 400$ K)
P				P_4O_6(solar $T_{surf} > 920$ K)
S		H_2S, SO_2	COS, $[S]_x$	S_2O(PWD BSE), H_2SO_4(Earth $T_{surf} > 920$ K)
Cl		HCl Cl_2(Earth)		OHCl(Earth $T_{gas} > 425$ K)
F		HF		SiF_4($T_{surf} > 900$ K)
others	O_2, H_2, H_2O			

Notes: Some of the present molecules are only present in few atmospheric models. For these, the defining character of these models is added in brackets. Examples are a specific temperature range or a given total element abundance.

et al., 2017; Pearce et al., 2022). Similarly to the reduced case, we define the oxidised regime as Level 3ox with the presence of CO_2, NO_2, and SO_2. It is also possible, that different redox states of an element coexist in an atmosphere. If for carbon, nitrogen, and sulphur the oxidised and reduced from coexist, with all species present at abundances more than 10^{-9}, the atmosphere is categorised as habitability level 3redox. In Chapter 3 we have shown that the coexistence of CO_2 and CH_4 is a fundamental result of chemical equilibrium for specific element abundances.

In addition to the habitability levels based on CNS, the presence of phosphorus is a further constraint for the formation of life. As it is a limiting factor for the biosphere on Earth (Syverson et al., 2021), we use it as a category on its own. All habitability levels are summarised in Table 5.1.

Molecular nitrogen shows a very strong triple bond, which makes it much less accessible for life than other nitrogen sources such ans NH_3 or NO_2. Although natural processes (e.g. UV, cosmic rays, lightning) and some microbes can produce the easier accessible forms of nitrogen (a process known as nitrogen fixation (see e.g. Burris & Wilson, 1945; Stüeken, 2016)) exist, we further specify between the presence of accessible nitrogen forms and N_2.

We apply our definition of habitability levels for the atmospheric (p_{gas}, T_{gas}) points for a temperature range that allows the formation of liquid water at the corresponding pressures. Additionally, we extend the area of interest by ~50 K in both directions, as this allows the investigation of the surrounding parameter space, providing insights to the influences on the atmospheric conditions directly above and below a potential aerial biosphere.

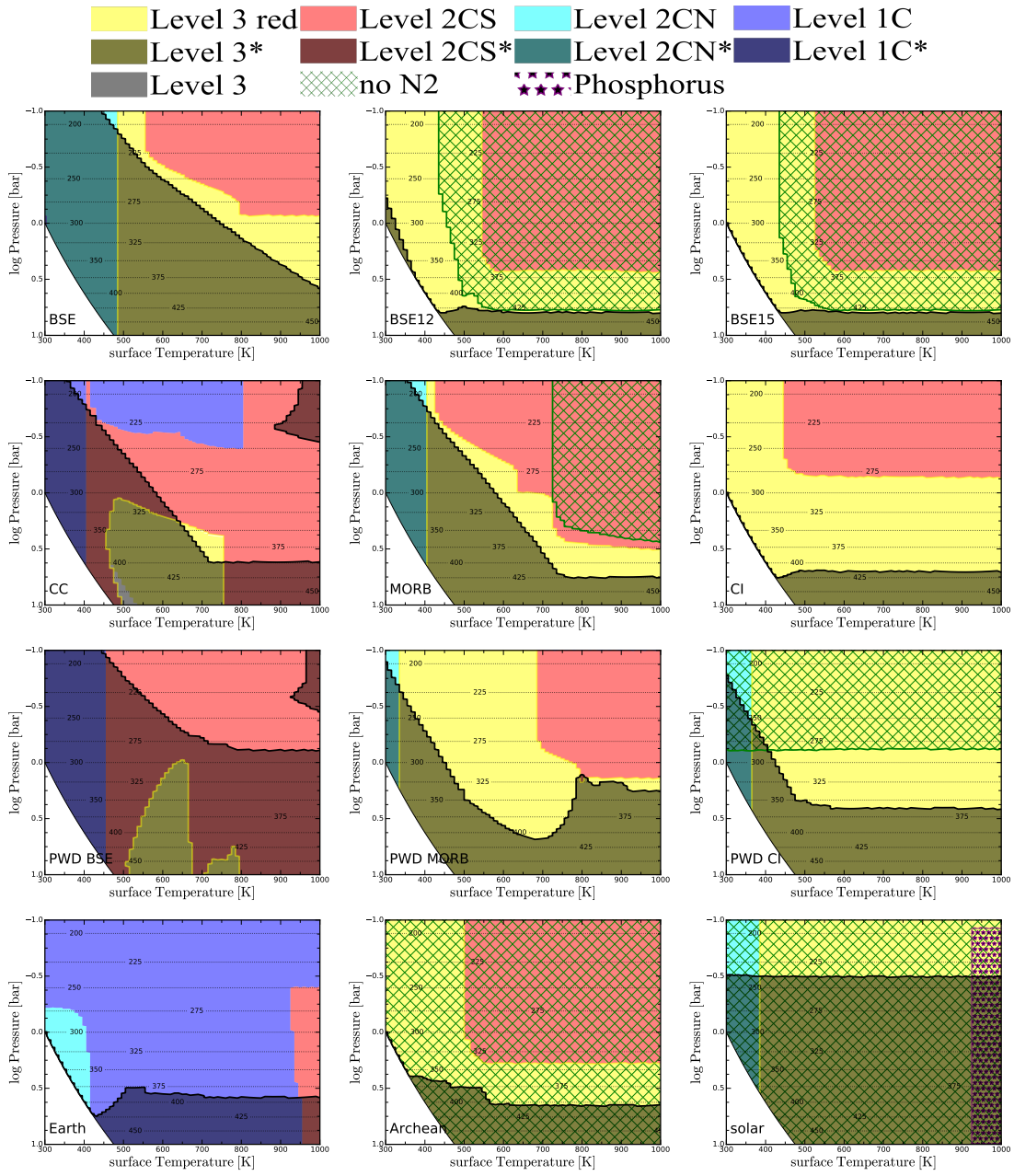

Figure 5.2: Habitability levels as defined in Table 5.1. The colouring of all present habitability levels are given in the legend above. The solid black line provides the pressure level of the H_2O[l,s] cloud base in the respective models. The darker shade of the habitability levels (indicated with * in the legend), are showing the corresponding habitability level of gas-phase composition although the primary assumption of the presence of H_2O[l,s] is not fulfilled. The green cross hatched region indicates $N_2/N_{tot} < 10^{-9}$.

5.4 Results

In this section we investigate the habitability levels in our bottom-to-top atmospheric models with different sets of total element abundances. The atmospheric model provides insights to the crust condensate composition, atmospheric gas composition, and possible cloud condensates. These vary with the different sets of total element abundances and surface conditions ($p_{\rm surf}, T_{\rm surf}$). First we investigate the presence of different habitability levels (Sect. 5.4.1) before the individual abundant elements are discussed in further detail individually (Sects. 5.4.2 to 5.4.7).

5.4.1 Habitability levels

The habitability levels (defined in Sect 5.3) for the twelve sets of total element abundances with varying surface conditions are shown in Fig. 5.2. Although the habitability levels all need the presence of water condensates, the regions without water condensates are indicated similarly to the habitability levels, but shaded in black. Of the 18 elements included in this model, only the elements C, H, N, O, P, S, Cl, F, and Si are present in the investigated atmospheric ($p_{\rm gas}, T_{\rm gas}$) space in form of a gas-phase molecule with abundances higher than $n_i/n_{\rm tot} > 10^{-9}$, where n_i is the number density of the the molecule i and $n_{\rm tot}$ is the total number density. All 23 molecules, that reach abundances above 1 ppb in the investigated part of the atmosphere are listed in Table 5.2 and sorted according to their peak abundance in any of the models.

Most atmospheres for the different sets of total element abundances show the presence of Level 3red at the water cloud base. However, for $T_{\rm surf} \lesssim 400\,{\rm K}$, the abundances of the sulphur bearing molecules are lower than 10^{-9} and the habitability level drops to Level 2CN or Level 1C with additional N_2 being present. For these lower temperatures, the S abundance in the atmosphere is significantly lower, as more sulphur is incorporated into the crust (see Fig. 5.3). In order to simplify the understanding of the crust composition, we group similar condensates together (Table 5.3). For a further discussion on the surface composition, see Sect. 5.6.

The most dominant transition in the habitability levels is the change from Level 3red to Level 2 CS, which occurs in most of the models, This depletion in available nitrogen is a result of the condensation of NH_4Cl[l], which reduces the N element abundances. Especially for the BSE12, BSE15, MORB sets of total element abundances, the condensation of NH_4Cl[s] depletes the N abundances such that also the N_2 abundance drops below 10^{-9}.

Besides H_2O[l,s] and NH_4Cl[s] a total of further 16 thermally stable condensates with normalised number densities of $n_{\mathrm{cond}}/n_{\mathrm{tot}} > 10^{-10}$ are present. This threshold is consistent with the high abundance threshold in Chapter 4 These thermally stable cloud condensates can be seen in Fig. A.2 in Appendix A. For all sets of total element abundances NaCl[s] and KCl[s] are stable condensates for $T_{\mathrm{gas}} > 700\,\mathrm{K}$. Furthermore, every set of element abundances shows a $(p_{\mathrm{gas}}, T_{\mathrm{gas}})$ region, where H_2O[s] condenses. Only for the solar abundances there is no regime with H_2O[l] as a condensate. Another cloud condensate that is thermally stable in atmosphere of all element abundances, except solar, is the N bearing condensate NH_4Cl[s].

A more strict definition of the habitability levels would include an abundance threshold of 10^{-6} instead of 10^{-9} for the relevant elements. The resulting habitability levels for this are shown in Fig. A.1. The parameter space that the Level 3red habitability regions are covering are significantly shrunken and mostly replaced by Level 2 CS, showing that especially the presence of N can be a limiting factor, if abundances of the order of 10^{-8} for nitrogen bearing species is not sufficient.

In all models that reach habitability level 3, the molecules are present in the reduced form. This is also true for the majority of the parts of the atmosphere, where water is not a stable condensate. The only model, where this is not the case is for the CC total element abundances with $T_{\mathrm{surf}} \approx 500\,\mathrm{K}$ and $T_{\mathrm{gas}} > 425\,\mathrm{K}$.

5.4.2 Hydrogen, oxygen and water

Water gas is a fundamental molecule in planetary atmospheres and can be a dominant gas-phase molecule in many atmospheres, especially for higher temperatures. The condensate form is of vital importance for the discussion its condensate form is of vital The most fundamental molecule for the discussion of habitability is water, which is not only present as a condensate, but also as a dominant gas-phase molecule in many planetary atmosphere. Figure A.8 in the Appendix A shows all gas-phase molecules consisting of only H and O.

The BSE and PWD BSE models are the models with the lowest H_2O abundance, due to the low hydrogen mass fraction in the total element abundances. H_2O does not reach abundances above 10^{-6} for $T_{\mathrm{surf}} \lesssim 430\,\mathrm{K}$ and for $T_{\mathrm{surf}} \lesssim 340\,\mathrm{K}$ the H_2O abundance stays below 10^{-9}. The only other models, for which the H_2O abundances drops below 10^{-9} are the sets of total element abundances of MORB and CC with $T_{\mathrm{surf}} \lesssim 340\,\mathrm{K}$. For all other models, the H_2O abundances are significantly higher and can become the most abundant gas-phase species, especially for high

surface temperature models.

As noted above, for all sets of total element abundances, there exist atmospheric models, where H_2O[l,s] cloud condensates are stable and abundant. The H_2O gas-phase abundance above the cloud base is a result of the assumption of unity for the supersaturation, $S(H_2O[l,s]) = 1$. Therefore every two models at the same (p_{gas}, T_{gas}) above the water cloud base show the same gas-phase abundance of H_2O. This confines the maximum H_2O abundance for the atmosphere above.

In Fig. A.8, the gas-phase molecules of H_2 and O_2 are also shown. The only model which shows presence of gaseous O_2 is the Earth model, as it is created to have an atmospheric composition similar to modern day Earth's atmosphere for $T_{surf} = 288\,K$ at the surface, see Appendix A of Herbort et al. (2022). For higher surface temperatures, the O_2 abundance reduces as the CO_2 abundance increases to become the most abundant gas-phase molecule, surpassing N_2. As the Earth model is the only model with a type B atmosphere (see Woitke et al., 2021; Herbort et al., 2022), it is the only model to show O_2 as a gas species. For H_2 on the other hand, the picture is different, as especially the models with total element abundances of solar, Archean, and CI total element abundances result in atmospheres rich in H_2 for all surface temperatures. For BSE12 and BSE15 total element abundances, H_2 is present for all T_{surf} where water is not condensing. For all other models H_2 is only a trace gas.

5.4.3 Carbon

Of the CNS elements, carbon is the only element, for which there is always a molecule present at abundances higher than 10^{-9} for the entire parameter space of all sets of total element abundances studied in this chapter. Carbon is bound in different oxidisation states, ranging from CH_4 to CO_2, with some additional traces of CO and COS at ppm abundances (see Fig. A.3). As shown in Woitke et al. (2021), the coexistence of CH_4 and CO_2 is a fundamental result of chemical equilibrium for all atmospheres of atmospheric type C (see definition of atmospheric types therein). For $T_{gas} \lesssim 350\,K$, both redox end-members of carbon are present at abundances higher than 0.1% in multiple models, while only PWD CI, Earth, Archean, and Solar total element abundances show no coexistence of these redox states throughout the parameter space. The trace forms of carbon COS and CO are only present at abundances up to a few ppm, if CO_2 is present at more than 0.1%.

Throughout the atmospheres in this chapter, the only form of carbon which is thermally stable

as a condensate in the atmosphere is C[s] (graphite). It is only thermally stable in atmospheres where CH_4 and CO_2 coexist. In these cases, the atmospheric composition in the upper parts of the atmosphere evolves towards the dominance of the more abundant one of the two carbon molecules. The abundance of the respective other molecule decreases significantly as a result due to the ongoing depletion of carbon in the atmosphere. As discussed in Herbort et al. (2022) (see also Chapter 2), graphite is the only condensate, which can be thermally stable for the entire investigated T_{gas} parameter space. The models based on CC total element abundances are the only ones, for which CH_4 and CO_2 coexist in the atmosphere and C[s] does not condense.

For the carbon condensation, the different element abundances fall into three different regimes. For the element abundance without carbon condensation in the atmosphere and a hydrogen-rich atmosphere, also no carbon bearing condensate is stable as part of the crust. However, for the Earth model, where also no graphite condenses in the atmosphere, all non-gaseous carbon is bound in $CaCO_3$ and $CaMgC_2O_6$. The other element abundances have either one or a multitude of carbon-bearing condensates stable at the crust.

For PWD BSE ($T_{\mathrm{surf}} < 700\,\mathrm{K}$ and PWD MORB the carbon condensates are $CaCO_3$[s], C[s], and $CaMgC_2O_6$[s]. These condensates are also stable for the model with the highest C abundance (3.5% mfrac for the CI), but the further condensates of $MgCO_3$[s], NCO_3[s], $FeCO_3$[s], and $CaFeC_2O_6$ are also stable. The carbon abundance in BSE, BSE12, BSE15, and MORB is more than two orders of magnitude lower than for CI or the PWD models. This results in a much simpler carbon condensate phase, with either C[s] or $CaCO_3$[s] being stable for the corresponding models. Similarly for the CC element abundance, carbon is bound in the crust in form of $CaMgC_2O_6$[s] for $T_{\mathrm{surf}} < 680\,\mathrm{K}$.

5.4.4 Nitrogen

The nitrogen in the gas phase can be found in forms of N_2, NH_3, HNO_3, and NO_2 and their distribution is shown in Fig. A.4. While there are no N bearing condensates in the crust for any model, NH_4Cl[s] and NH_4SH[s] are thermally stable condensates in the atmospheres (see Fig. A.2).

For many sets of element abundances, N_2 is a main N carrier at abundances over $1‰$ for the entire investigated parameter space (BSE, CC, CI, Earth) or up to a certain threshold surface temperature ($T_{\mathrm{surf}} < 450\,\mathrm{K}$: BSE12, BSE15; $T_{\mathrm{surf}} < 650\,\mathrm{K}$: MORB, PWD BSE; $T_{\mathrm{surf}} < 775\,\mathrm{K}$:

PWD MORB). Otherwise, for H-rich atmospheres, NH_3 becomes the main N carrier for the entire parameter space of PWD CI, Archean, and Solar, but also for $T_{\rm surf} > 450\,{\rm K}$ BSE12, BSE15. For the latter two, the dominance of N_2 over NH_3 is only present, when H_2O[l] is a stable crust condensate.

Although N is considered as an omnipresent gas species, we find the high atmosphere can be depleted in nitrogen for $T_{\rm surf} \gtrsim 550\,{\rm K}$ and therefore higher surface pressures. The depletion of N, is caused by the condensation of NH_4Cl[s], which removes a considerable amount of N from the gas phase. This is the case for the the sets of total element abundances of BSE12, BSE15, and Archean. For MORB abundances, this temperature threshold is $T_{\rm surf} > 725\,{\rm K}$. The condensation of NH_4Cl[s] is present in most models and coincides with the condensation of H_2O[l]. Therefore the NH_4Cl[s] condensates are of additional interest for the discussion of habitability.

A further N condensate is NH_4SH[s], which is only thermally stable higher up in the atmosphere, where $T_{\rm gas} < 250\,{\rm K}$. This is the case for BSE12, BSE15, PWD MORB, and PWD CI and further depletes the available nitrogen.

5.4.5 Sulphur

The gas phase of sulphur is mainly formed by H_2S and SO_2, with further traces of COS, S_X, S_2O, and H_2SO_4. The distribution of these molecules is visualised in Fig. A.5. Showing, that for higher $T_{\rm surf}$ a higher abundance of sulphur can be expected in the planetary atmospheres. most models show the presence of H_2S as the major S bearing species. Only for models with a moderately high ($\epsilon_{\rm O}/\epsilon_{\rm tot}$), SO_2 becomes more significant (high $T_{\rm gas}$ of CC and PWD BSE total element abundances). Even for these atmospheres H_2S is present in the gas phase at levels up to ppm abundances. The only models where no S bearing molecule is present at abundances greater than ppb for $T_{\rm surf} > 450\,{\rm K}$ are the Earth model, which shows only H_2SO_4 present for $T_{\rm surf} > 900\,{\rm K}$ This significantly depleted S abundance with respect to all of the other models is a result of the thermal stability of S condensates in oxydised environments. The investigation of S in CHNO+S atmospheres are further discussed in detail in Janssen et al (in prep.). For the CC model and $400\,{\rm K} < T_{\rm surf} < 800\,{\rm K}$, the condensation of S_2[s] is sufficient enough to reduce the S abundance for $T_{\rm gas} \lesssim 240\,{\rm K}$ to below ppb levels. For all models, with $T_{\rm surf} \gtrsim 450\,{\rm K}$ H_2S is present with more than ppb abundances in the region of the H_2O[l] cloud base.

For most of the element abundances, the majority of the sulphur is kept in the crust as con-

densates. This explains the higher abundance of sulphur bearing molecules with higher temperatures, as the vapour pressure of the condensates increases with increasing temperature. Only for BSE12, BSE15, and Archean total element abundances and $T_{\rm surf} > 700\,{\rm K}$ no S condensate is stable at the crust. For most abundances and $T_{\rm surf}$ only one S condensate is thermally stable. These stable condensates are FeS for BSE, MORB, PWD MORB, PWD CI (all $T_{\rm surf}$), BSE12, BSE15 ($680\,{\rm K} < T_{\rm surf} < 440\,{\rm K}$), CI ($T_{\rm surf} > 510\,{\rm K}$), Archean ($T_{\rm surf} < 690\,{\rm K}$), solar ($T_{\rm surf} < 670\,{\rm K}$); FeS_2 for BSE12, BSE15 ($T_{\rm surf} < 430\,{\rm K}$), CC ($T_{\rm surf} < 640\,{\rm K}$), CI ($T_{\rm surf} < 500\,{\rm K}$), PWD BSE ($T_{\rm surf} < 350\,{\rm K}$); $CaSO_4$[s] for CC ($T_{\rm surf} > 650\,{\rm K}$), Earth (all $T_{\rm surf}$), and MnS for solar ($T_{\rm surf} > 680\,{\rm K}$). The PWD BSE total element abundance is the only model, where multiple S condensates are stable for the same surface condition. These stable condensates are FeS[s] and one of $CaSO_4$[s] and FeS_2[s] for $T_{\rm surf} > 800\,{\rm K}$ and $350\,{\rm K} < T_{\rm surf} < 800\,{\rm K}$, repetitively.

The sulphur-containing cloud condensates fall into three categories. First, at the highest temperatures, pure sulphur condensates of S2[s] and S[l] dominate. These can be present over a large range of surface conditions. In general, the S_2[s] cloud base lies at lower pressures than the H_2O[l] cloud bases. Second, H_2SO_4[s], which is only stable for models with high pressures at the surface and cold local temperatures of $T_{\rm gas} \lesssim 300\,{\rm K}$. The H_2SO_4[s] and S_2[s] condensates can coexist in the one atmospheric model. Third, the NH_4SH[s] condensate is only stable for $T_{\rm gas} \lesssim 250\,{\rm K}$. As NH_4SH[s] does not coexist in an atmosphere with either S_2[l], S[l], and H_2SO_4[s], these condensates could be used for the characterisation of the atmospheric conditions.

5.4.6 Phosphorus

The rarest of the CHNOPS elements is phosphorus, which is for all non-solar total element abundances almost completely bound in the crust, in the form of hydroxyapatite and fluorapatite, $Ca_5P_3O_{13}H$[s] and $Ca_5P_3O_{12}F$[s], repsectively. Apatite has been found to be the main phosphorus carrier for example on the Chelyabinsk meteorite (Walton et al., 2021). This shows that P will be a limiting element for the formation and evolution of life in the atmospheres of almost all rocky exoplanets.

Only models for solar element abundances and $T_{\rm surf} > 900\,{\rm K}$ show any phosphorus-bearing molecule at abundances higher than 10^{-9} in the atmosphere. At the crust-atmosphere interaction layer of these models, PH_3 is the dominant P carrier, with about 3 orders of magnitude higher abundance than P_4O_6. However, as virtually no Ca is present in the atmosphere, the remaining P cannot condense in form of apatite and only condenses much higher in the atmosphere, when

H_3PO_4[s] becomes thermally stable at around $p = 10^{-0.5}$ bar and $T_{gas} = 250$ K. Despite the overall reducing atmospheric conditions in the H_2 dominated atmosphere, the most important P carrier changes close to the surface at $T_{gas} \approx 900$ K from PH_3 to P_4O_6.

5.4.7 Chlorine and fluorine

Besides the CHNOPS elements, the two halides fluorine and chlorine are present in atmospheric models of all total element abundances. The gas phases in the relevant temperature regime are visualised in the Appendix A in Fig. A.6 and Fig. A.7, respectively. They behave very similar to each other and are therefore discussed together in this section.

Most of the halides are condensed in the crust in form of NaCl[s] and $Ca_5P_3O_{12}F$[s]. Additionally MgF_2[s] tends to be stable towards higher temperatures, whereas CaF_2[s] is stable towards lower temperatures. Only for the CC total element abundances, the additional condensate of $KMg_2AlSi_3O_{10}F_2$[s] is thermally stable at the crust for $T_{surf} > 370$ K. The further condensate of $CaCl_2$[s] is only found stable in the model of BSE12 total element abundances for $T_{surf} \approx 590$ K.

The halides show increasing gas-phase abundances for high surface temperatures, where residual Cl and F atoms remain in the gas phase. The most important species being HCl and HF for all atmospheres. In the atmospheres at $T_{gas} \gtrsim 700$ K, the condensation of KCl and NaCl occurs for every total element abundance. However, this condensation is limited by the abundance of K and Na, respectively. As a result, the abundance of HCl and HF reaches up to a few ‰in the atmospheres based on a high surface temperature. The presence of these hydrogen halides in coexistence with H_2O[l] can result in acidic environments, if they dissolve in the water droplets. Whether this acidity benefits or limits the formation of pre-biotic molecules is beyond the scope of this thesis and is therefore not included in the habitability levels as either helpful or harmful.

In addition to the abundant HF, SiF_4 is also present with abundances higher than 1ppb in atmospheres of models for the CC and Earth total element abundances and $T_{surf} \gtrsim 900$ K. These are the only cases in this study, where Si is present.

5.5 Summary and discussion

Liquid water is considered one of the fundamental necessities for the formation of life as we know it. It can be a stable condensate on the surface of rocky exoplanets and as a cloud condensate in atmospheres of many different exoplanets. In this chapter we investigated the gas-phase molecules

and thermally stable condensates in the surrounding of liquid water condensates by using the bottom-to-top equilibrium chemistry atmosphere models presented in Herbort et al. (2022) for various elemental compositions.

As the conditions for the formation of life are not fully understood, the concept of the habitable zone where liquid water can exist is used to investigate whether a planet could be habitable (e.g. Huang, 1959; Kasting et al., 1993). However, liquid water itself alone is not sufficient to form life, as many more elements are necessary for the formation of pre-biotic molecules and for the following evolution of biology. While complex life uses a vast range of elements, simple life forms and especially pre-biotic molecules are built from the CHNOPS elements. Therefore we define habitability levels not only on the presence of water condensates, but also by including the abundances of the CHNOPS elements.

We find that for most atmospheres at $(p_{\rm gas}, T_{\rm gas})$ points, where liquid water is stable, CNS bearing molecules are present at abundances above 10^{-9}. Carbon is in general present in every atmosphere, while the sulphur availability in the gas phase increases with increasing $T_{\rm surf}$. For lower $T_{\rm surf}$ nitrogen in the form of either NH_3 or N_2 is in present as a major contributor to the atmospheric composition for most atmospheres. However, for models with higher $T_{\rm surf}$, the presence of gaseous nitrogen can be significantly depleted by the condensation of NH_4Cl[s], which leaves an upper atmosphere devoid of nitrogen. The limiting element of the CHNOPS elements is phosphorus, which is mostly bound in the planetary crust. This is consistent with the scarcity of phosphorus limiting the biosphere on Earth (Syverson et al., 2021).

5.5.1 Implications for surface biospheres

The limiting factor for habitability at the surface of a planet based on the model investigated in this work, is the presence of liquid water. If water is present at the surface, CNS are available in the gas phase of the near-crust atmosphere. The only exception is the present day Earth model, which lacks the presence of gaseous S by construction.

The available elements for the equilibration of crust and atmosphere are dependent on the overall planetary composition and therefore formation history, as well as the tectonic regimes present (e.g. Tosi et al., 2017; Dorn et al., 2018; Kruijver et al., 2021; Meier et al., 2021; Höning et al., 2021), determining the available 'equilibrated crust'. Also the evolution of the planet as well as star play a crucial role, as this determines the long-term temperature of the planet (Turbet

et al., 2021; Seales & Lenardic, 2021). The formation of hydrated minerals can also play a crucial role in the long-term stability of water condensates (Herbort et al., 2020; Beck et al., 2021). An example for this is the surface of Mars, which previously hosted liquid water, which is now bound in hydrated rocks (see e.g. Ehlmann et al., 2010; Wernicke & Jakosky, 2021).

Even if $(p_{\mathrm{surf}}, T_{\mathrm{surf}})$ of a planet allow the formation of liquid water and water is present in the atmosphere, even in the form of clouds, our models show that no water ocean is to be implied from these (compare also Ding & Wordsworth, 2022). Especially if the surface pressure is not well constrained, the presence of water clouds is not conclusive for the presence of water at the surface of the respective planet. Therefore additional detection methods of a surface ocean are necessary to confirm the existence of one (e.g. Williams & Gaidos, 2008; Lustig-Yaeger et al., 2018; Ryan & Robinson, 2022)

Given that water is available at the surface, all other elements should be present in some form. Metals which are important for charge balances in many biological processes can be made available by chemical weathering or by dissolution of condensates into water. Similarly, the lack of phosphorus in the atmosphere can be overcome for surface biospheres. However, there can be the difficulty of the accumulation of pre-biotic molecules, if the water reservoir is too large and no exposed land is available (Noack et al., 2016). This leads to Darwin's idea of the warm little pond with some dry-wet cycles (Darwin, 1871; Follmann & Brownson, 2009; Pearce et al., 2017). This hurdle also needs to be overcome for potential life on the icy moons in our solar system (see e.g. Vance et al., 2007; Tjoa et al., 2020; Taubner et al., 2020). If indeed it can be shown that life can form in a water ocean without any exposed land, this constraint becomes weaker and the potential for the surface habitability becomes mainly a question of water stability.

5.5.2 Implications for aerial biospheres

Many of the models show the presence of a liquid water zone in the atmospheres, which is detached from the surface. These regions could be of interest for the formation of life in forms of aerial biospheres.

As described in previous work by e.g. Seager et al. (2021b), focussing on sub Neptunes – which have thicker atmospheres than planets investigated in this work – aerial biospheres are a region of various scarcities of nutrients. We show that it is likely to have regions in planets where the fundamental elements (CHNOS) are all present. The chemical state of these elements in the

environment of liquid water condensates is mostly reduced, which is favourable for the formation of pre-biotic molecules. However, we also show that the presence of phosphorus is unlikely in our models, as it is bound in the crust in form of apatite. A further hurdle for more complex life is the ability to use ions for charge balancing. Life on Earth uses metal ions for this, these however, are not present in the atmospheric phase, as they are bound in the crust. Further cloud condensates to H_2O[l,s] like NH_4Cl[s] could play this role for life in such environments (see Seager et al., 2021b). Our models show that these two cloud condensates coexist for most atmospheric models.

The lacking atoms of phosphorus and metals could in principle be provided by atmospheric updrafts induced by storms on the planet. The closer the liquid water zone is to the surface, the more likely an updraft of surface material would be. However, further cloud layers are expected at higher temperatures on planets with higher surface pressure (e.g. NaCl[s], KCl[s],FeS[s], or FeS_2[s]). These condensates could be delivered to the higher atmospheres by storms and accumulated by life in the higher atmosphere.

5.5.3 Further discussion

The atmospheric composition in this chapter focussed on the pre-biotic atmospheric composition The atmospheric composition after the emergence of life on a planet can deviate drastically from the pre-biotic atmospheric composition caused by biological activity itself (e.g. Holland, 2002; Gregory et al., 2021). Our approach does not directly aim for the understanding of biosignatures and atmospheres of planets, which are inhabited, but for the conditions in which pre-biotic chemistry can occur.

The results of our approach of a large variety of different atmospheric compositions in chemical equilibrium atmospheres can provide insights to which signatures of biology could also be produces by a simple chemical equilibrium atmosphere. We for example, show that N_2 is a major atmospheric component for planets with $T_{\rm surf} < 400\,{\rm K}$, whereas N in general can be lacking in atmospheres based on higher $T_{\rm surf}$. Lammer et al. (2019) state that N_2 itself can be a sign of a biosignature or effective tectonic regimes. Our models of an equilibrated crust with the atmosphere can be seen as representative of active tectonic regimes. as otherwise only a small portion of the crust is able to equilibratewith the atmosphere. Following up on this, Sproß et al. (2021) state that the coexistence of N_2 and O_2 is only a result of biology. We find that this coexistence - as well as the presence of O_2 in general - is only possible in a model with element abundances adopted to produce this exact atmospheric feature.

Another pair of atmospheric gas species that is discussed as a biosignature is CO_2 and CH_4 (e.g. Krissansen-Totton et al., 2019; Wogan et al., 2020; Mikal-Evans, 2021). However, as discussed in Woitke et al. (2021), it is possible to have these two molecules coexists in chemical equilibrium. In our atmospheres, we find this element pair coexisting at abundances above ppm abundances for many atmospheres with $T_{\rm gas} > 275\,{\rm K}$. For a concentration greater than ‰ of both, CO_2 and CH_4, $T_{\rm gas} > 350\,{\rm K}$ is necessary. Therefore, high abundances of both molecules at cool temperatures could be explained by some out-of-equilibrium process such at biology. In the early Earth atmosphere during the Archean, the methane has been a product of biology (methanogenesis Ueno et al., 2006). Similarly it has been discussed that the presence of CH_4 in plumes of Enceladus is potentially a result of methanogenesis (Affholder et al., 2021).

HCN has been found for example on the surface of Titan Lellouch et al. (2017) and the comet Hale-Bopp (Jewitt et al., 1997). Its production in planetary atmosphere is possible by lightning, especially if CH_4 and N_2 are present (Hodosan et al., 2017; Pearce et al., 2022). However, we do not find the presence of HCN in any of our models, underlining their non-equilibrium origin. With the presence of HCN, Rimmer et al. (2021b) found that the production of HC_3N should occur on super-Earths rich in nitrogen and an overall reduced atmospheric composition by photochemistry.

Further molecules that we do not find to be present in any of our models are more complex hydrocarbons than CH_4. However, these have been found in various environments ranging from interstellar matter (e.g. Henning & Salama, 1998) to places in our solar system. Examples are the C_2H_4 haze on Triton (Ohno et al., 2021) or various different molecules on comets such at 67P (Müller et al., 2022).

Huang et al. (2021) found that the detection of NH_3 can be a biosignature on planets, where a deep atmosphere is excluded. We however find, that NH_3 can be present throughout the atmosphere of uninhabited planets with low pressure atmospheres. However, only if no water condensate is stable at the surface, we find that the NH_3 abundance actually exceeds 1‰.

By construction of the model, the influence of stellar irradiation to the planetary atmosphere is not discussed. A proper understanding of the influence of the host star to the atmosphere requires the upper atmosphere and is therefore beyond the work in this chapter. This can have a major factor for the atmospheric evolution Chen et al. (2020); Turbet & Selsis (2021); Chebly et al. (2021); Locci et al. (2022); Teal et al. (2022). The triggered photochemistry can not only destroy pre-biotic molecules, but also enhance the formation of these as many reactions need the input of

some sort of energy, this can for example be provided by the stellar irradiation (in form of UV radiation) or lightning discharges. Whether the strong UV radiation during flares of M dwarfs is harmful for the evolution of life has been a matter of discussion (Shields et al., 2016; O'Malley-James & Kaltenegger, 2019). This leads to the hypothesis, that potentially orange dwarfs may be best candidates for habitability (Arney et al., 2016).

5.6 Surface composition

The composition of the crust in contact with the atmosphere above have to be understood within the context of the model. Under the assumption of a known total element abundance, as it is done in this work, the atmospheric composition and the crust composition are precisely defined for each set of element abundances, surface temperature and surface pressure. However, for one given atmosphere the crust composition itself is constrained to the thermally stable condensates, but not their respective abundance in the crust itself. Therefore the crust composition for one given atmosphere is an N-dimensional manifold , where N is the number of thermally stable condensates (see also Appendix A of Herbort et al., 2022). In this work we use a fixed set of total element abundances to obtain the atmospheric composition and corresponding surface composition.

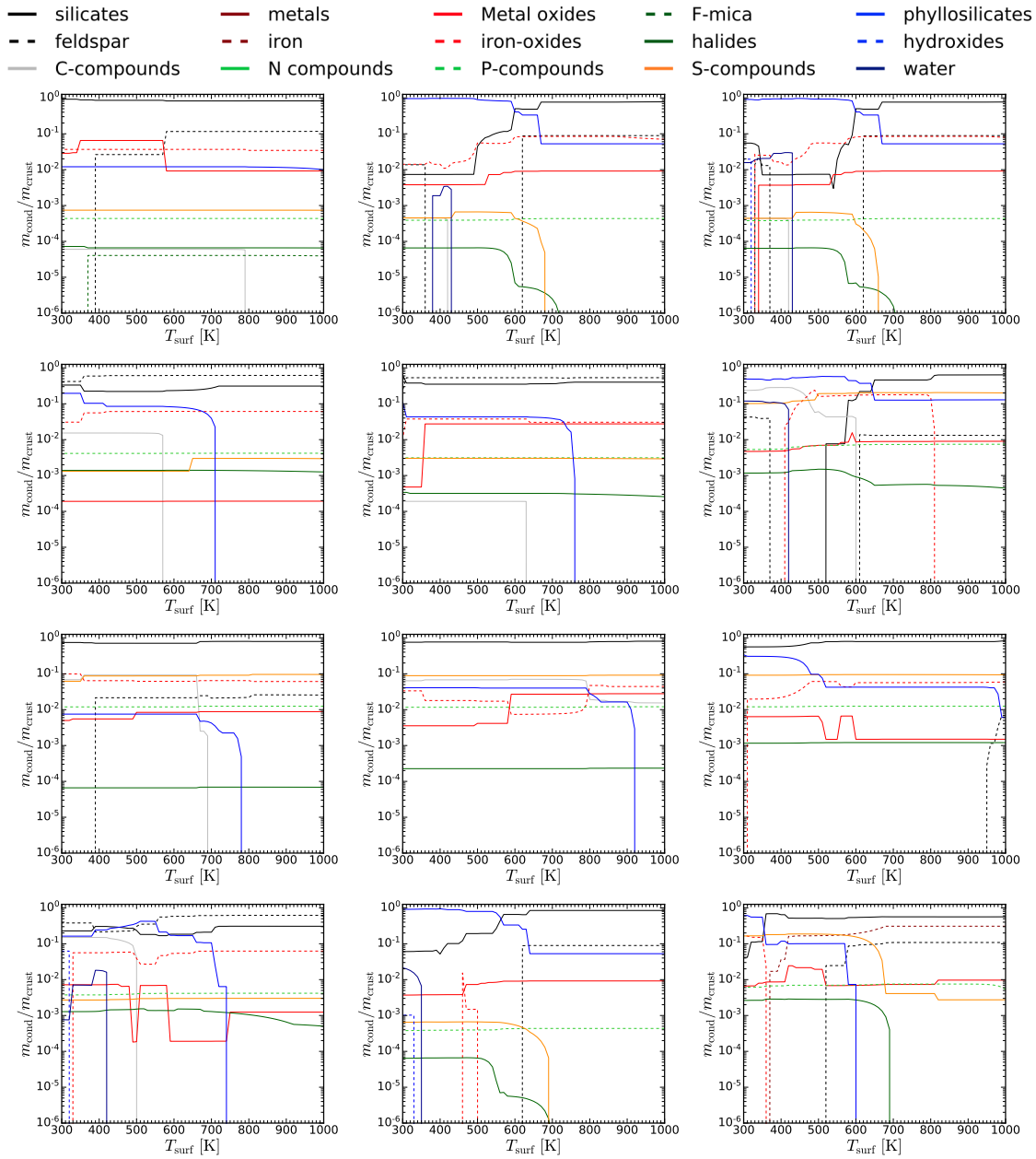

Figure 5.3: Crust composition of the different models with the different element abundances. The condensates included in the different condensate groups are explained in Table 5.3.

Table 5.3: Condensates present in the surfaces of the different models according to their grouping.

Group	Condensate	Name	Group	Condensate	Name
Silicates	Al_2SiO_5	Kyanite	Nitrogen	NH_3	Amonia
	$Ca_2Al_2Si_3O_{12}$	Prehnite		P_3N_5	P-nitride
	$Ca_2Al_2SiO_7$	Gehlenite		TiN	Ti-nitride
	$Ca_2MgSi_2O_7$	Åkermanite	Phosphorus	$Ca_5P_3O_{13}H$	Hydroxyapatite
	$Ca_3Fe_2Si_3O_{12}$	Andradite		$Ca_5P_3O_{12}F$	Fluorapatite
	$CaMgSi_2O_6$	Diopside		P	Phosphorus
	$CaMgSiO_4$	Monticellite		P [l]	Liquid phosphorus
	$CaSiO_3$	Wollastonite	F- Mica	$KMg_3AlSi_3O_{10}F_2$	Fluorphlogopite
	$CaTiSiO_5$	Sphene	Halides	NaCl	halite
	Fe_2SiO_4	Fayalite		KCl	Sylvite
	$KAlSiO_4$	Kalsilite		MgF_2	Mg-fluoride
	Mg_2SiO_4	Fosterite		CaF_2	Fluorite
	$MgSiO_3$	Enstatite		KF	K-fluoride
	$Mn_3Al_2Si_3O_{12}$	Spessartine		AlF_6Na_3	Cryolite
	Mn_2SiO_4	Tephroite	Sulphur	$CaCl_2$	Ca-dichloride
	Na_2SiO_3	Na-metasilicate		CaS	Ca-sulfide
	$NaCrSi_2O_6$	Kosmochlor		$CaSO_4$	Anhydrite
	$NaFeSi_2O_6$	Acmite		FeS	Troilite
	$NaAlSiO_4$	Nepheline		FeS_2	Pyrite
	SiO_2	Quarz		MgS	Mg-sulphide
Feldspar	$CaAl_2Si_2O_8$	Anorthite		MnS	Alabandite
	$KAlSi_3O_8$	Microcline	Phyllosilicates	$Al_2Si_2O_9H_4$	Kaolinite
	$NaAlSi_3O_8$	Albite		$Ca_2Al_2Si_3O_{12}H_2$	Prehnite
Carbon	C	Graphite		$Ca_2Al_3Si_3O_{13}H$	Clinozoisite
	$CaCo_3$	Calcite		$Ca_2FeAl_2Si_3O_{13}H$	Epidote
	$CaFeC_2O_6$	Ankerite		$Ca_2FeAlSi_3O_{12}H_2$	Ferri prehnite
	$CaMgC_2O_6$	Dolomite		$Ca_2MnAl_2Si_3O_{13}H$	Piemontite
	$FeCO_3$	Siderite		$CaAl_2Si_2O_{10}H_4$	Lawsonite
	$MgCO_3$	Magnesite		$CaAl_2Si_4O_{16}H_8$	Laumonite
	$MnCO_3$	Rhodochrosite		$CaAl_4Si_2O_{12}H_2$	Margarite
	SiC	Silicon carbide		$Fe_3Si_2O_9H_4$	Greenalite
Metals	Mn	Manganese		$FeAl_2SiO_7H_2$	Fe-chloritoid
	Na	Sodium		$KFe_3AlSi_3O_{12}H_2$	Annite
	Na [l]	Liquid sodium		$KMg_3AlSi_3O_{12}H_2$	Phlogopite
Iron	Fe	Iron		$Mg_3Si_2O_9H_4$	Lizardite
Metal oxides	Al_2O_3	Chorundum		$Mg_3Si_4O_{12}H_2$	Talc
	$CaTiO_3$	Perovsike		$MgAl_2SiO_7H_2$	Mg-chloritoid
	Cr_2O_3	Eskolaite		$MnAl_2SiO_7H_2$	Mn-chloritoid
	$FeAl_2O_4$	Hercynite		$NaAl_3Si_3O_{12}H_2$	Paragonite
	$FeTiO_3$	Ilmenite		$NaMg_3AlSi_3O_{12}H_2$	Sodaphlogopite
	$MgAl_2O_4$	Spinel	Hydroxides	FeO_2H	Goethide
	$MgCr_2O_4$	Picrochromite		AlO_2H	Diaspore
	Mn_2O_3	Bibyxbite		MgO_2H_2	Brucite
	$MnTiO_3$	Pyrophanite	Water	H_2O	Water
	Ti_4O_7	Titanium oxide		H_2O [l]	Liquid water
	TiO_2	Rutile			
Iron oxides	Fe_3O_4	Magnetite			
	Fe_2O_3	Hematite			
	FeO	Ferropericlase			

"On ne doit rien craindre dans la vie - il suffit de comprendre"
Nothing in life is to be feared, it is only to be understood.

- Marie Salomea Skłodowska Curie

6 Summary

The work presented in this thesis focussed on the investigation of atmospheres of rocky exoplanets and worked towards understanding their diversity and the link between the surface and atmospheric composition. The use of diverse sets of total element abundances allowed the analysis of different surface and atmospheric compositions. The presented atmospheric model allows the link for surfaces to thermally stable condensates in the atmosphere.

In this chapter, the overarching results from the individual parts of this thesis are summarised and set into context of each other.

6.1 Crust composition, surface water, and near-crust atmosphere

All of the atmospheric models presented in this thesis are based on chemical and phase equilibrium. The inclusion of rock inspired total element abundances allowed the investigation of the atmospheric and crustal compositions of a rocky exoplanet at a given pressure and temperature.

For $T_{\rm surf} \gtrsim 3500\,{\rm K}$, the atmospheric gas is composed of vaporised rock, resulting in atmo-

spheres dominated by atoms (O, Na, Mg, and Fe), metal oxides (SiO, NaO, MgO, CaO, AlO, and FeO), and some metal hydroxides (KOH and NaOH). For lower temperatures, the metals are mostly incorporated in the solid crust, while the atmosphere is rich in oxygen, where O_2 can be the most abundant gas species. Other dominant gas species in the surface temperature range from $\sim$ 500 K to $\sim$ 3500 K are H_2O, CO_2, and SO_2. For particularly hydrogen rich sets of element abundances, H_2 remains the dominant gas species. For $T_{\rm surf} \lesssim 500$ K the dominant gas species becomes either N_2 or CH_4.

We have shown that the stability of water condensates at the surface is suppressed by the formation of phyllosilicates. These hydrated minerals incorporate OH or H_2O groups into their lattice structure and are thermally favourable with respect to silicates plus water condensates. This makes the inclusion of phyllosilicates, as potential condensates, crucial for lower temperatures, as they bind a large amount of hydrogen in the condensate phase for $T_{\rm surf} \lesssim 700$ K. Only if all minerals that can be hydrated are hydrated, water can become a thermally stable condensate in liquid or solid phase, depending on temperature.

6.2 Cloud condensates in the bottom-to-top atmosphere

In Chapter 4 we presented a bottom-to-top atmospheric model which is based on the chemical phase equilibrium model of the atmosphere-crust interaction layer. The atmosphere is assumed to be in hydrostatic equilibrium and the pressure-temperature profile is given by a constant polytropic index. Solving the chemical phase equilibrium in every atmospheric layer allows the investigation of the gas phase and the thermally stable cloud condensates. The removal of all thermally stable condensates from the element abundance for the atmospheric layer above depletes the atmospheric composition in the affected elements. Although the link in not unambiguous, the cloud condensates can be used to constrain the overall surface composition (see Tables 4.6 and 4.7).

Overall, we find a separation between different cloud condensates, which are stable for high and low temperatures. While the main condensates for $T_{\rm gas} \gtrsim 400$ K are halides and iron compounds (KCl[s], NaCl[s], FeS[s], FeS_2[s], FeO[s], Fe_2O_3[s], and Fe_3O_4[s]), for $T_{\rm gas} \lesssim 400$ K the condensates are hydrogen rich and include H_2O[l,s], NH_3[s], NH_4Cl[s], and NH_4SH[s]. For even colder temperatures of $T_{\rm gas} \lesssim 150$ K we find further condensates of CO_2[s], CH_4[s], NH_3[s], and H_2S[s] to become thermally stable. While all of these condensates are constrained to a certain temperature regime, we find that C[s] (graphite) is the only condensate, which can be thermally

stable for all ($p_{\mathrm{gas}}, T_{\mathrm{gas}}$) points investigated in this thesis. This underlines the importance of further investigations on graphite as a cloud condensate.

6.3 Atmospheric types

Investigations of equilibrium gas compositions of elemental mixtures containing only C, H, N, and O result in the formulation of three distinct atmospheric types. These are given by

- Type A: hydrogen rich atmospheres with H_2O, CH_4, NH_3, and either H_2 or N_2.

- Type B: oxygen rich atmospheres with O_2, H_2O, CO_2, and N_2. The addition of further elements to the gas composition will especially change the O_2 abundance. For example the addition of sulphur can favour the formation of SO_2.

- Type C: carbon rich atmospheres with CH_4, CO_2, H_2O, and N_2. Especially the coexistence of CH_4 and CO_2 are important to be noted here.

These atmospheric types are especially of interest for lower temperatures, as for higher temperatures ($T \gtrsim 600\,\mathrm{K}$), other trace gasses become importance. The most important trace gases emerging being H_2 and CO. The condensate phase of these atmospheres is less complex and only consists of two condensates. While H_2O[l,s] is a potential thermally stable condensate for all atmospheric types, the thermal stability of C[s] can only be archived in type C atmospheres.

Although no planet in our solar system shows a type C atmosphere, especially slightly warmer exoplanets could very well have such atmospheres. These would provide a potential false positive for the postulated biosignature of the coexistence of CH_4 and CO_2 without the presence of CO.

The investigation of the different atmospheres based on the bottom-to-top atmospheric model presented in Chapter. 4 shows that the atmospheric type is intrinsic to the atmosphere as a whole and does not change with the removal of thermally stable condensates in the atmosphere. This indicates, that the atmospheric types could be used for the characterisation of atmospheres with upcoming space missions and ground based instruments.

6.4 The surrounding gas of water clouds and implications on habitability

Water is one of the fundamental needs for the formation of life and therefore used as one of the indicators for potential habitability. In our models, we have water at the surface of only a few sets of total element abundances, as the hydrated minerals incorporate the majority of hydrogen. As the rock forming elements are overwhelmingly incorporated in the condensate phase, there is no possibility for hydrated minerals to form in the atmosphere as cloud condensates to outcompete water formation. For all sets of total element abundances, there are surface conditions ($p_{\rm surf}, T_{\rm surf}$, for which water condensates become thermally stable in the polytropic atmosphere .

In order to quantify how habitable the given atmospheres are, we introduced habitability levels based on the presence and chemical state of carbon, nitrogen, and sulphur. The investigations of our atmospheric models for different surface compositions have shown that it is common to have reduced forms of carbon, nitrogen, and sulphur present at the water cloud base, providing the essential molecules for the formation of pre-biotic molecules. Atmospheres with high surface temperatures also show the presence of HCl and HF at significant abundances. Whether this acidic environment is beneficial for the formation of life is beyond the scope of this thesis. The only models which show the presence of any phosphorus bearing species present in the atmosphere are for solar abundances and $T_{\rm surf} \gtrsim 900\,{\rm K}$. For all other models phosphorus is not present and can therefore be assumed to be a limiting factor for life. Similarly, no metals are present in the surrounding of the water clouds, which could limit the possibilities for complex life. Another condensate, which is commonly present at similar points in the atmosphere to water, is NH_4Cl[s]. For some atmospheres, this condensate is prominent enough to effectively deplete the nitrogen abundance, resulting in the absence of N bearing molecules in the atmospheric layers above.

"Aber das ist eine andere Geschichte und soll ein andermal erzählt werden."
But that is another story and should be told at another time.

- Michael Ende, *Die Unendliche Geschichte*

7 Outlook

The work during this thesis provides a great insight to the composition of the lower atmospheres for a range of different rocky exoplanets. The presented work leaves many undiscovered pathways, which could not be followed in the scope of the thesis. However, in the following three ideas of potential future work, based on the results presented in this theses, are discussed.

7.1 Include thermally stable cloud condensates in kinetic cloud formation models

The investigation of the bottom-to-top atmospheres provided an extended list of thermally stable cloud condensates present in our hydrostatic, polytropic, chemical equilibrium atmospheres. A logical next step is to investigate the differences of the thermally stable cloud condensates models presented here with kinetic cloud formation models like DiffuDrift (Woitke et al., 2020). This will allow a further understanding in how far results from fast and simple atmospheric models can be used for further investigations without the need for more complex models.

Besides the validation and constraining of our results, the list of thermally stable condensates provided in this work can be used to inform the more in depth models in their choice of potential cloud condensation nuclei and cloud growth species. This could for example be accomplished by applying our model for a specific planetary (p, T) profile and a fixed element abundance. The resulting thermally stable cloud condensates can be used as a shortlist for the potential cloud species in the more complex models.

A further aspects that such a comparison can investigate is the separation of cloud condensates in high and low temperature condensates which is shown in our model. Special focus can lie on the investigation of graphite clouds. Their thermal stability is only possible for type C atmospheres which show the coexistence of CO_2 and CH_4 in chemical equilibrium. This coexistence has been discussed as a promising and potentially detectable biosignature candidate (e.g. Krissansen-Totton et al., 2019; Wogan et al., 2020; Krissansen-Totton et al., 2022). Therefore understanding whether this atmospheric type is possible is of great interest.

7.2 Stellar influence and atmospheric loss

The atmospheric model presented in this thesis is based on the assumption that equilibrium is reached at every point in the atmosphere. However, there are various different phenomenon which drive the atmosphere away from this assumption. Especially the influence of stellar irradiation can have large effects, as it drives photochemistry in the atmosphere as well as the atmospheric loss. Therefore investigating which of the resulting atmospheric compositions from our models are actually stable requires photochemical modelling and linking the models for the low atmosphere with high atmosphere models.

A model from the surface of a rocky planet to the high atmosphere, which includes photochemistry and atmospheric loss would allow the investigation of atmospheric evolution around various different stars. One important question, which can be addressed with this model is the presence of atmospheres on rocky planets orbiting M dwarfs. This is particularly important as rocky planets around M dwarfs are relatively easy to detect, and M dwarfs are the most abundant stellar type in our galaxy. However, the interplay of the atmosphere with the intense radiation, especially during stellar flares, is a process that needs to be studied in more detail. As mentioned above, the existence of atmospheres where CH_4 and CO_2 are both abundant would have significant implications for the search for biosignatures. Differentiating an atmospheric composition which is

influences by biological processes from an uninhabited atmosphere is only possible, if the natural atmospheres without the influence of biological processes are understood to rule out false positives of biosignatures.

7.3 Observability of atmospheric features

Our models have shown the potential to constrain the surface composition and conditions by the presence of some atmospheric gas species and cloud condensates. However, it is beyond the scope of this thesis to investigate the observability of these atmospheres in general and the surface constraining species specifically.

Future missions such as ARIEL and instruments at the 30 m telescopes, will bring the capability for investigations of atmospheres of rocky exoplanets. In order to prepare for these observations, it becomes important to understand which atmospheric features of the presented atmospheric compositions can be observed. Therefore, the investigation of theoretical transmission spectra for the resulting atmospheres of this thesis with for example ARCiS (Min et al., 2020) is an essential future step which can help in understanding which surface constraining features will become observable. This will substantially help for the characterisation of rocky exoplanets.

A

Supplementary figures

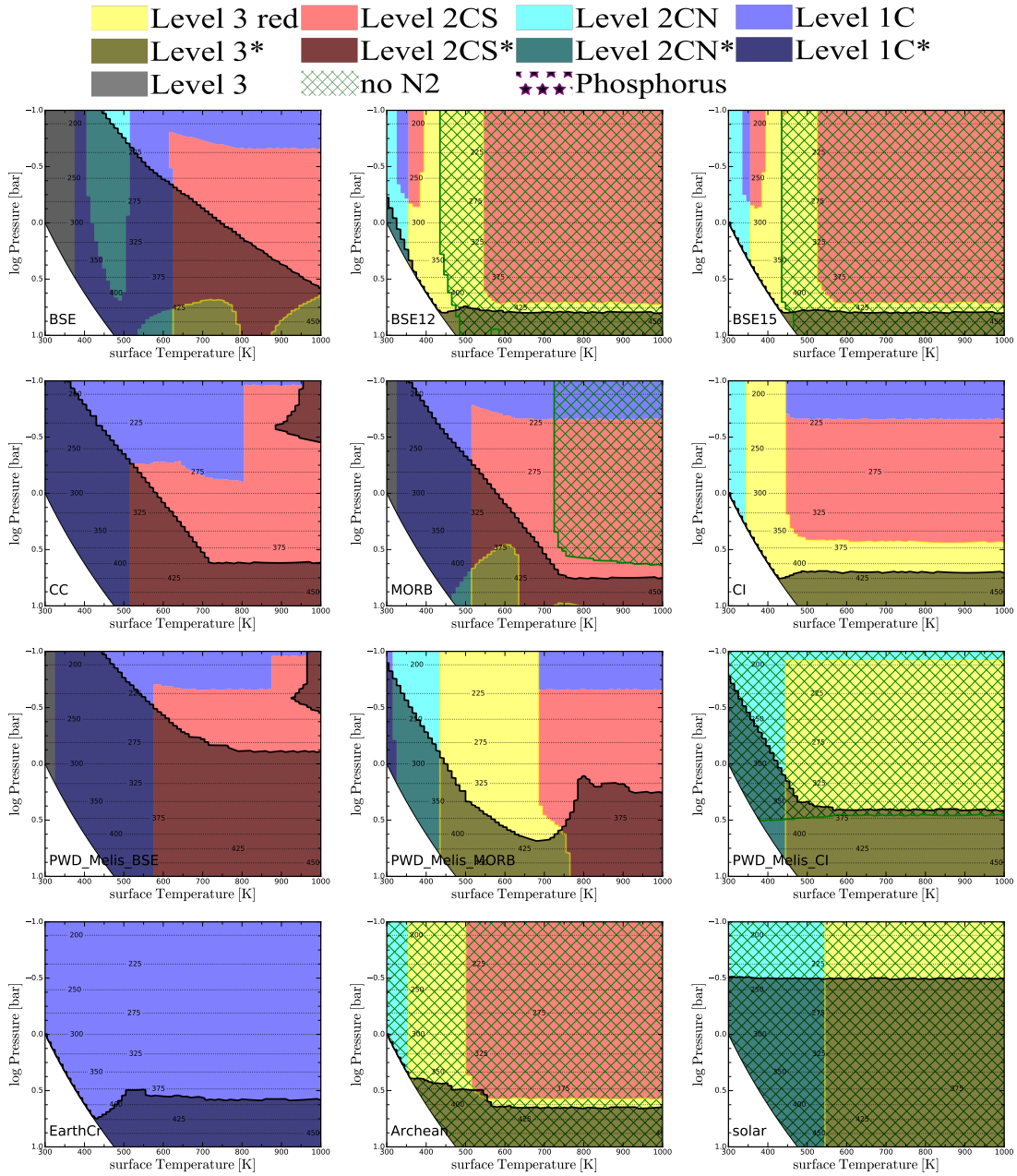

Figure A.1: Habitability levels as defined in Table 5.1 and shown in Fig. 5.2, but with abundance thresholds of 10^{-6}.

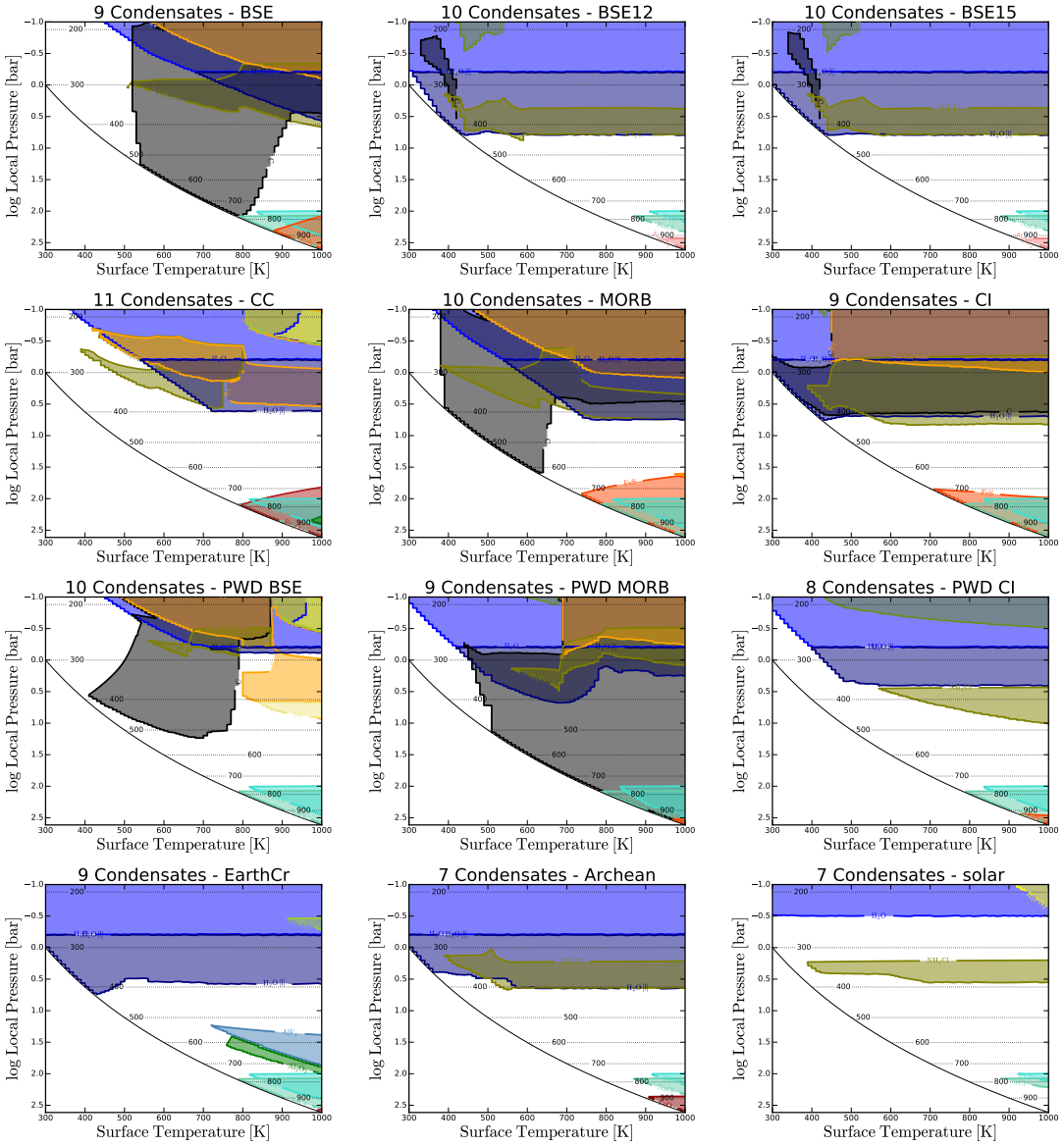

Figure A.2: Thermally stable cloud condensates with $\log_{10}(n_{\rm cond}/n_{\rm cond}) > -10$ for different element abundances and surface conditions. Each panel shows one total element abundance. The thin solid black line shows the surface conditions that are used as the starting point for the respective atmospheric models. The dotted lines show the local gas phase temperature.

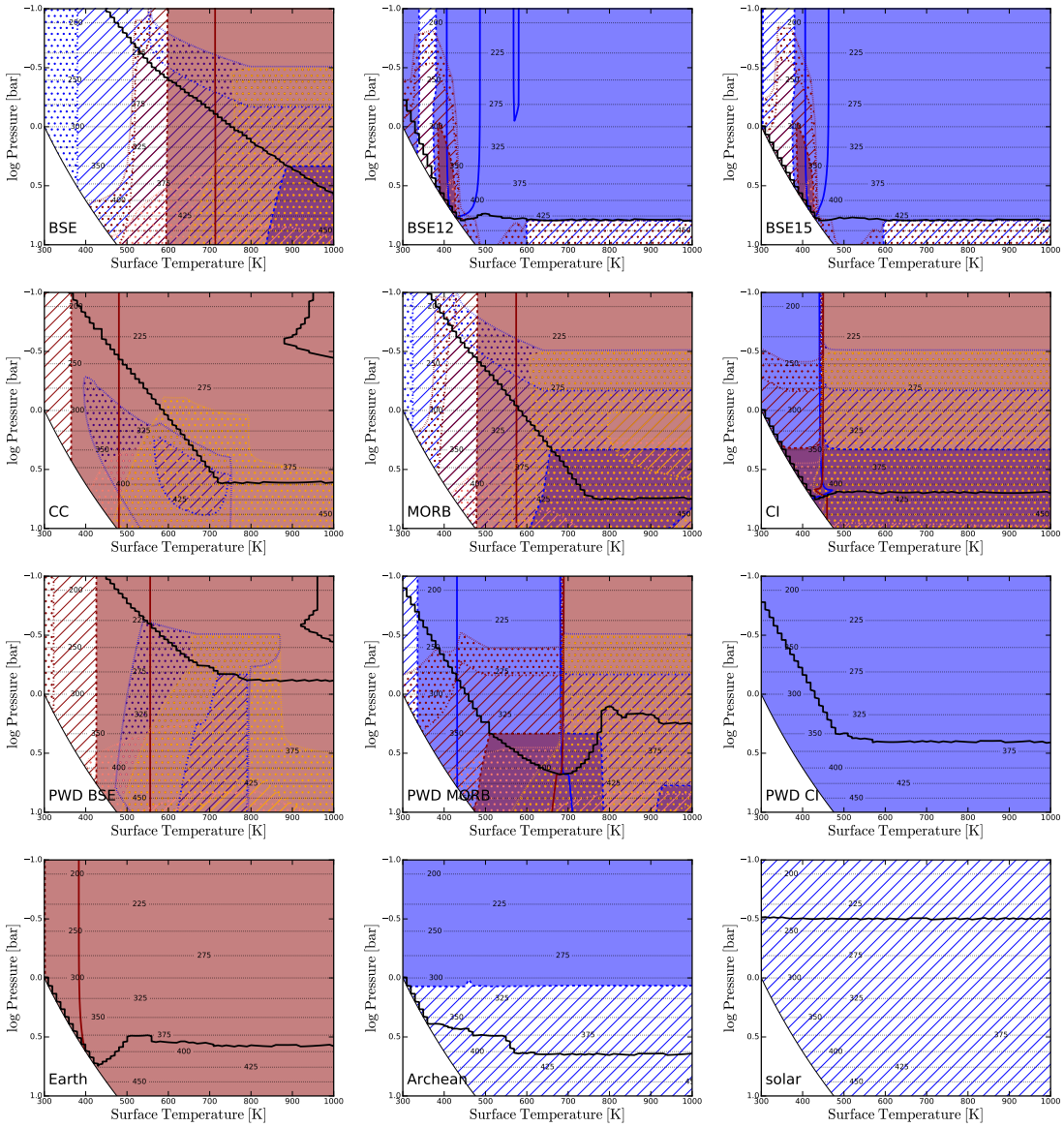

Figure A.3: The abundance of all carbon bearing species with higher abundance than ppb. The different lines indicate abundance levels of 10% (solid), 0.1% (dashed), 10^{-6} (dash dotted), and 10^{-9} (dotted). Abundances higher than 0.1% are filled, higher than ppm is hatched with lines, and abundances above ppb are indicated by dots. The molecules shown are CH_4 in blue, CO_2 in darkred, CO in salmon, and COS in orange.

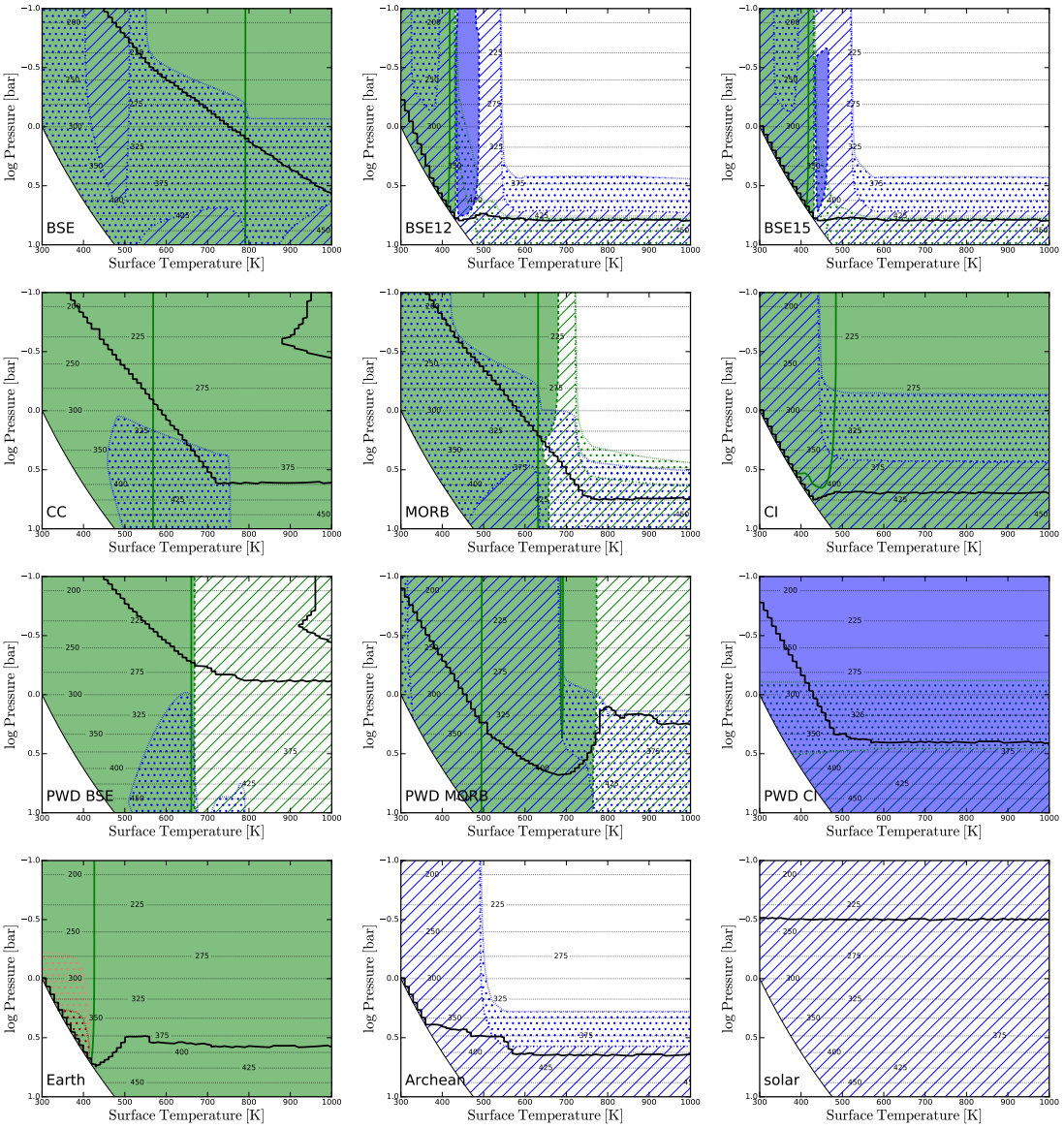

Figure A.4: As in Fig. A.3, but for all N bearing molecules. The colours refer to N_2 in green, NH_3 in blue, HNO_3 in salmon, and NO_2 in darkred.

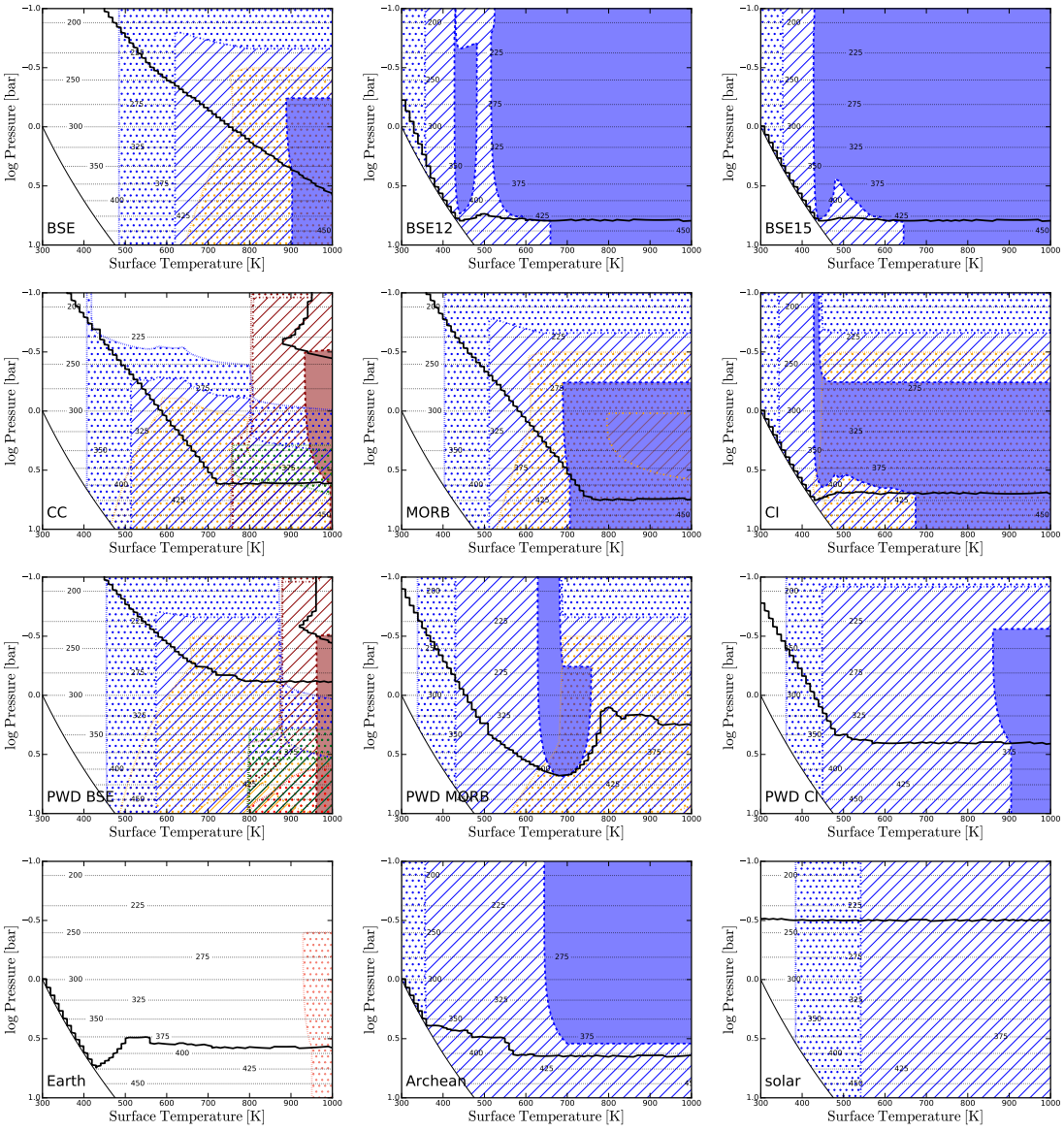

Figure A.5: As in Fig. A.3, but for all S bearing molecules. The colours refer to COS (orange); SO_2 (darkred); S_2O (red); H_2S (blue); Sx (green); H_2SO_4 (salmon)

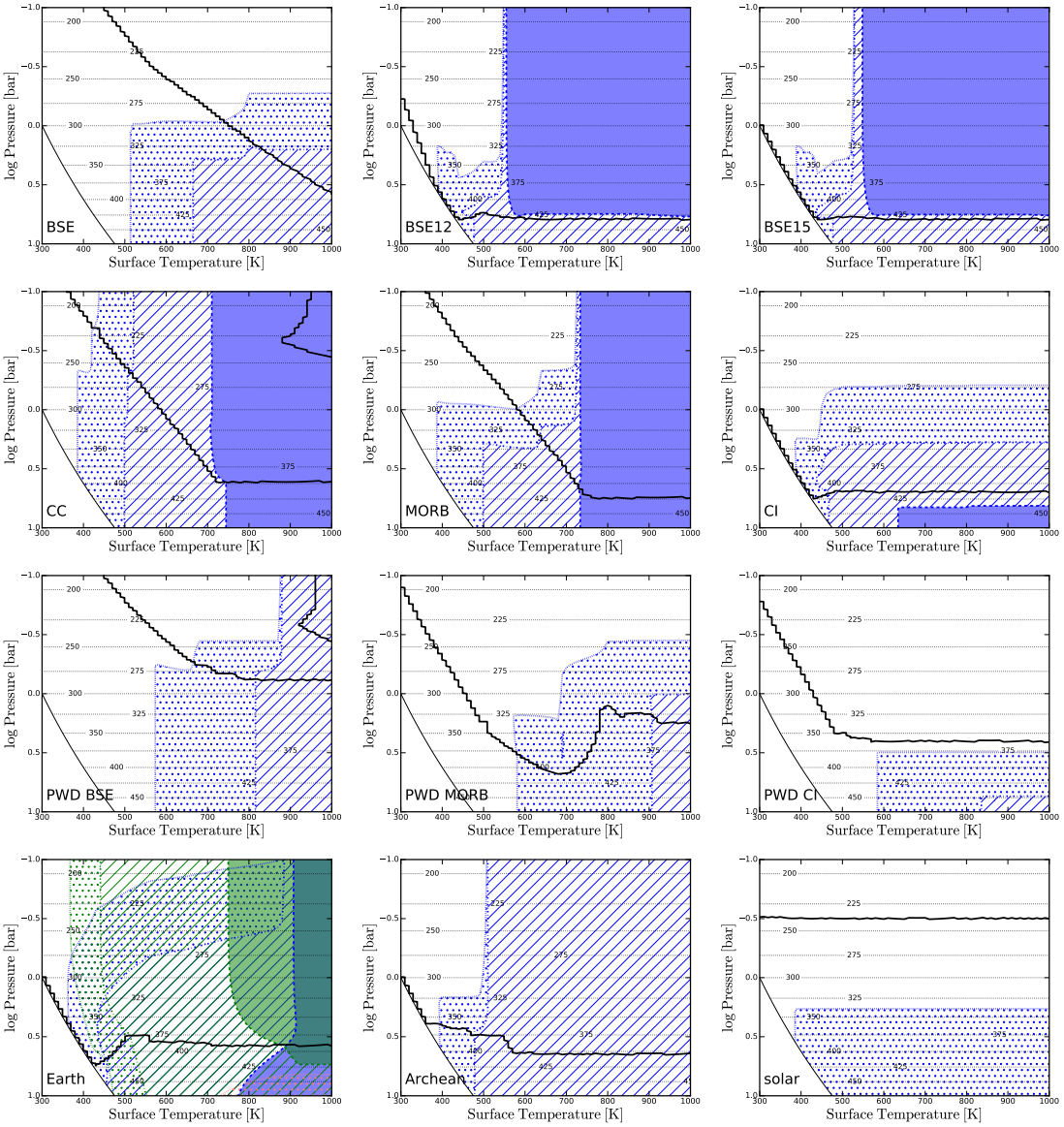

Figure A.6: As in Fig. A.3, but for all Cl bearing molecules. The colours refer to HCl (blue), Cl_2 (green), OHCl (red).

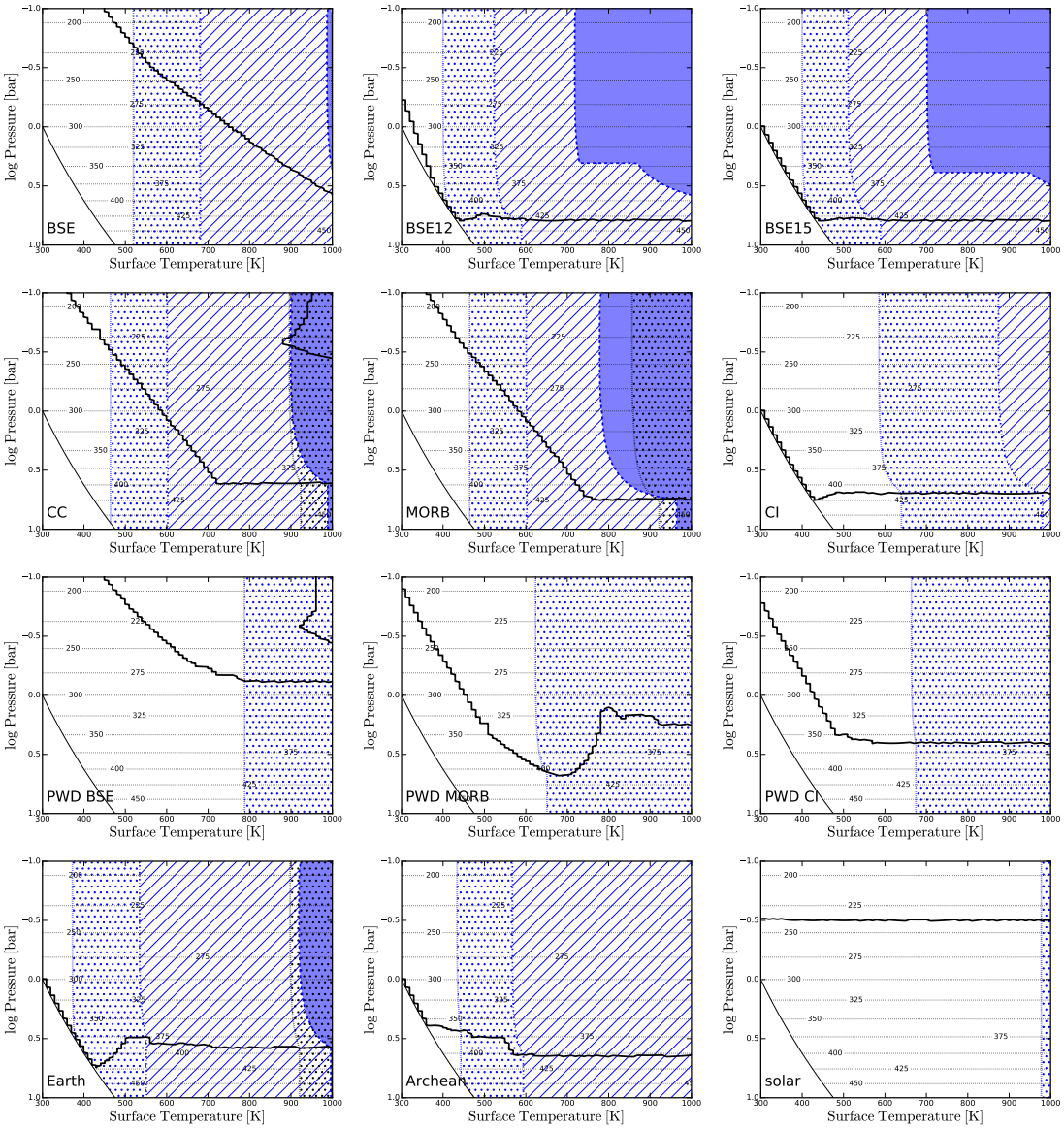

Figure A.7: As in Fig. A.3, but for all F bearing molecules. The colours refer to HFx (blue) and SiF_4 (black)

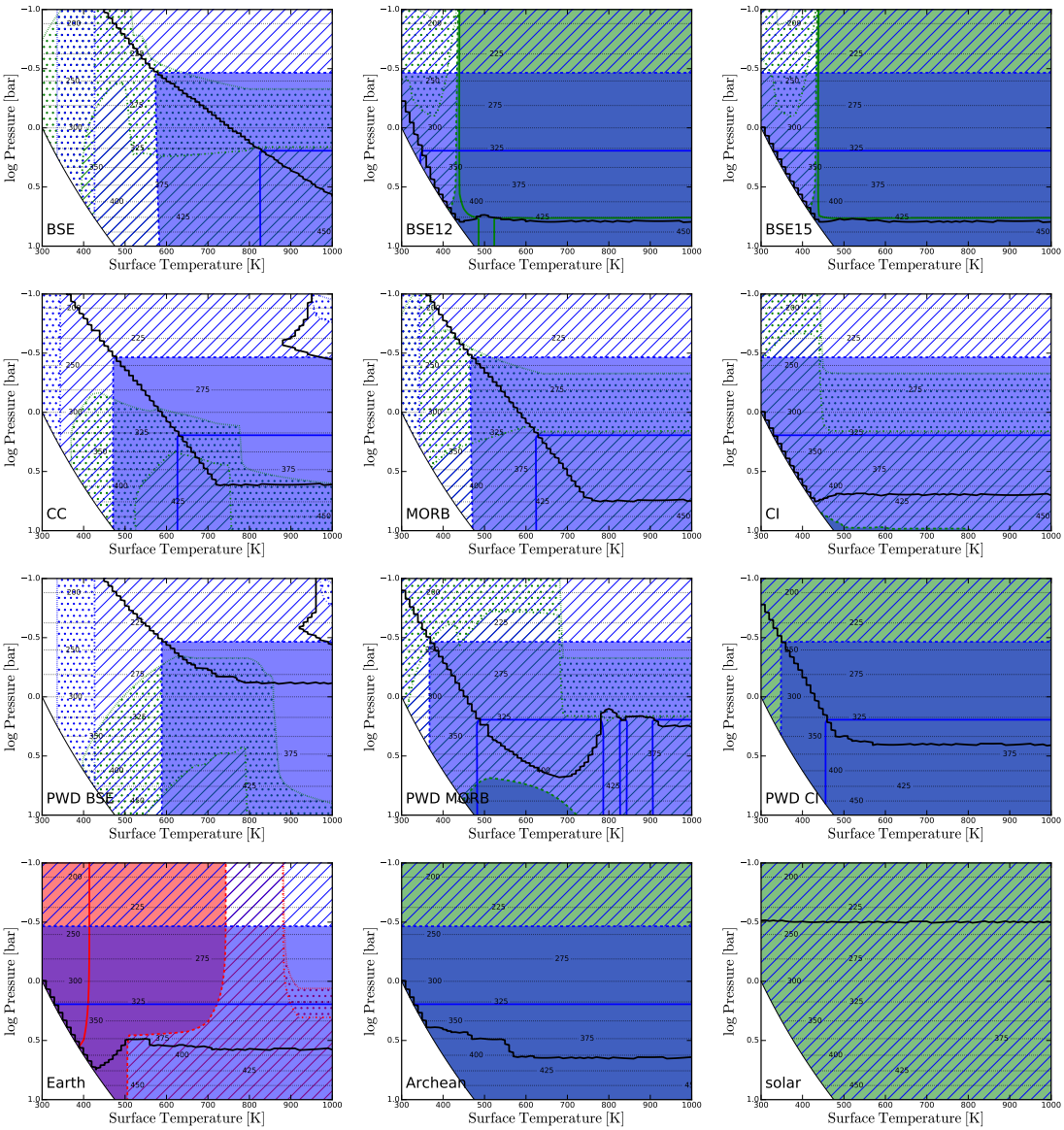

Figure A.8: As in Fig. A.3, but only for H_2 (green), O_2 (red), and H_2O (blue).

Bibliography

Ackerman, A. S., & Marley, M. S. 2001, ApJ, 556, 872, astro-ph/0103423

Affholder, A., Guyot, F., Sauterey, B., Ferrière, R., & Mazevet, S. 2021, Nat. Astron., 5, 805

Alonso-Floriano, F. J. et al. 2019, Astron. Astrophys., 621, 1811.08901

Anglada-Escudé, G. et al. 2016, Nature, 536, 437, 1609.03449

Arcangeli, J. et al. 2018, Astrophys. J., 855, L30, 1801.02489

Ardaseva, A., Rimmer, P. B., Waldmann, I., Rocchetto, M., Yurchenko, S. N., Helling, C., & Tennyson, J. 2017, Mon. Not. R. Astron. Soc., 470, 187, 1704.07917

Arevalo, R., & McDonough, W. F. 2010, Chem. Geol., 271, 70

Arney, G. et al. 2016, Astrobiology, 16, 873, 1610.04515

Asensio Ramos, A., & Pallé, E. 2021, A&A, 646, A4, 2012.04460

Asplund, M., Grevesse, N., Sauval, A. J., & Scott, P. 2009, Annu. Rev. Astron. Astrophys., 47, 481, 0909.0948

Astudillo-Defru, N. et al. 2020, Astron. Astrophys., 636, A58

Atreya, S., Wong, M., Owen, T., Mahaffy, P., Niemann, H., de Pater, I., Drossart, P., & Encrenaz, T. 1999, Planet. Space Sci., 47, 1243

Baglin, A. et al. 2006, in 36th COSPAR Sci. Assem., Vol. 36, 3749

Bailey, R., Helling, C., Hodosán, G., Bilger, C., & Stark, C. 2014, ApJ, 784, 43, 1312.6789

Bains, W. 2014, Int. J. Astrobiol., 13, 101

Bains, W. et al. 2021, Astrobiology, 21, 1277, 2009.06499

Bains, W., Shorttle, O., Ranjan, S., Rimmer, P. B., Petkowski, J. J., Greaves, J. S., & Seager, S. 2022, Universe, 8, 54, 2112.00140

Ballard, S. et al. 2014, ApJ, 790, 12, 1405.3659

Ballesteros, F., Fernandez-Soto, A., & Martínez, V. 2019, Astrobiology, 19, 642

Barker, E. 1972, Nature, 238, 447

Barklem, P., & Collet, R. 2016, A&A, 588, A96, 1602.03304

Barman, T. S., Konopacky, Q. M., Macintosh, B., & Marois, C. 2015, Astrophys. J., 804, 1503.03539

Barstow, J. K. 2020, Mon. Not. R. Astron. Soc., 497, 4183

Barth, P. et al. 2021, MNRAS, 502, 6201, 2012.12132

Basilevsky, A. T., & Head, J. W. 2003, Reports Prog. Phys., 66, 1699

Batalha, N. M. et al. 2013, ApJS, 204, 24, 1202.5852

Beatty, T. G. 2022, Mon. Not. R. Astron. Soc., 2105.09990

Beck, P., Eschrig, J., Potin, S., Prestgard, T., Bonal, L., Quirico, E., & Schmitt, B. 2021, Icarus, 357, 2011.00279

Belov, G. V., Iorish, V. S., & Yungman, V. S. 1999, Calphad, 23, 173

Benneke, B., & Seager, S. 2012, ApJ, 753, 100, 1203.4018

——. 2013, ApJ, 778, 153, 1306.6325

Benneke, B. et al. 2019, Astrophys. J., 887, L14, 1909.04642

Benz, W. et al. 2021, Exp. Astron., 51, 109, 2009.11633

Berline, S., & Bricker, C. 1969, J. Chem. Educ., 46, 499

Bilger, C., Rimmer, P., & Helling, C. 2013, MNRAS, 435, 1888, 1307.2565

Bischoff, A. 1998, Meteorit. Planet. Sci., 33, 1113

Blecic, J., Harrington, J., & Bowman, M. O. 2016, Astrophys. J. Suppl. Ser., 225, 4, 1505.06392

Bluhm, P. et al. 2020, Astron. Astrophys., 639, 2004.06218

Bolcar, M. R., Feinberg, L., France, K., Rauscher, B. J., Redding, D., & Schiminovich, D. 2016, in Society of Photo-Optical Instrumentation Engineers (SPIE) Conference Series, Vol. 9904, Sp. Telesc. Instrum. 2016 Opt. Infrared, Millim. Wave, ed. H. A. MacEwen, G. G. Fazio, M. Lystrup, N. Batalha, N. Siegler, & E. C. Tong, 99040J

Bonfanti, A., Fossati, L., Kubyshkina, D., & Cubillos, P. 2021, A&A, 656, A157, 2110.09106

Bonsor, A., Carter, P. J., Hollands, M., Gänsicke, B. T., Leinhardt, Z., & Harrison, J. H. 2020, Mon. Not. R. Astron. Soc., 492, 2683, 2001.04499

Borucki, W. J. et al. 2013, Science (80-.)., 340, 587

——. 2010, Science (80-.)., 327, 977

Bowens, R. et al. 2021, A&A, 653, 2107.06375

Bower, D. J., Kitzmann, D., Wolf, A. S., Sanan, P., Dorn, C., & Oza, A. V. 2019, Astron. Astrophys., 631, A103, 1904.08300

Brandl, B. R. et al. 2014, in Society of Photo-Optical Instrumentation Engineers (SPIE) Conference Series, Vol. 9147, Ground-based Airborne Instrum. Astron. V, ed. S. K. Ramsay, I. S. McLean, & H. Takami, 914721, 1409.3087

Brewer, J. M., Fischer, D. A., & Madhusudhan, N. 2017, AJ, 153, 83, 1612.04372

Brown, M. E., Bouchez, A. H., & Griffith, C. A. 2002, Nature, 420, 795

Burris, R. H., & Wilson, P. W. 1945, Annu. Rev. Biochem., 14, 685

Cafferty, B. J., Fialho, D. M., Khanam, J., Krishnamurthy, R., & Hud, N. V. 2016, Nat. Commun., 7, 11328

Catling, D. C., & Claire, M. W. 2005, Earth Planet. Sci. Lett., 237, 1

Catling, D. C. et al. 2018, Astrobiology, 18, 709, 1705.06381

Catling, D. C., & Zahnle, K. J. 2020, Sci. Adv., 6

Charnay, B., Blain, D., Bézard, B., Leconte, J., Turbet, M., & Falco, A. 2021, Astron. Astrophys., 646, 2011.11553

Chase, M. 1986, JANAF thermochemical tables

——. 1998, J. Phys. Chem. Ref. Data, Monograph

Chase, M., Curnutt, J., Downey, J., McDonald, R., Syverud, A., & Valenzuela, E. 1982, in J. Phys. Conf. Ser., Vol. 11, 695–940

Chebly, J. J., AlvaradoGómez, J. D., & Poppenhaeger, K. 2021, Astron. Nachrichten, Nov., 2111.09707

Chen, G., Pallé, E., Parviainen, H., Murgas, F., & Yan, F. 2021, Astrophys. J. Lett., 913, L16, 2104.13058

Chen, G. et al. 2018, The GTC exoplanet transit spectroscopy survey IX. Detection of haze, Na, K, and Li in the super-Neptune WASP-127b, 1805.11744

Chen, H., Zhan, Z., Youngblood, A., Wolf, E. T., Feinstein, A. D., & Horton, D. E. 2020, Nat. Astron., 5, 298

Cicerone, R. J., & Oremland, R. S. 1988, Global Biogeochem. Cycles, 2, 299

Claire, M., Catling, D., & Zahnle, K. 2006, Geobiology, 4, 239

Cloutier, R. et al. 2021, TOI-1634 b: An Ultra-short-period Keystone Planet Sitting inside the M-dwarf Radius Valley, 2103.12790

——. 2020, Astron. J., 160, 3

Cousin, A. et al. 2017, Icarus, 288, 265

Curran, R. J., Conrath, B. J., Hanel, R. A., Kunde, V. G., & Pearl, J. C. 1973, Science (80-.)., 182, 381

D'Angelo, M., Cazaux, S., Kamp, I., Thi, W. F., & Woitke, P. 2019, Astron. Astrophys., 622, A208, 1808.06183

Dartnell, L. R., Nordheim, T. A., Patel, M. R., Mason, J. P., Coates, A. J., & Jones, G. H. 2015, Icarus, 257, 396

Darwin, C. 1871, Letter to Joseph Hooker (Darwin1871)

De Wit, J. et al. 2016, Nature, 537, 69, 1606.01103

Del Genio, A. D., Way, M., Kiang, N. Y., Aleinov, I., Puma, M. J., & Cook, B. 2019, ApJ, 887, 197, 1910.03479

Delrez, L. et al. 2018, Mon. Not. R. Astron. Soc., 475, 3577, 1801.02554

Demory, B.-O. et al. 2016a, Nature, 532, 207

Demory, B. O., Gillon, M., Madhusudhan, N., & Queloz, D. 2016b, Mon. Not. R. Astron. Soc., 455, 2018, 1505.00269

Désert, J.-M., Vidal-Madjar, A., Lecavelier Des Etangs, A., Sing, D., Ehrenreich, D., Hébrard, G., & Ferlet, R. 2008, A&A, 492, 585, 0809.1865

Dhaliwal, J. K., Day, J. M. D., & Moynier, F. 2018, Icarus, 300, 249

Díez Alonso, E. et al. 2018, Mon. Not. R. Astron. Soc. Lett., 480, L1, 1806.01181

Ding, F., & Wordsworth, R. D. 2022, arXiv e-prints, arXiv:2201.08423, 2201.08423

Dittmann, J. A. et al. 2017, Nature, 544, 333, 1704.05556

Domagal-Goldman, S. D., Meadows, V. S., Claire, M. W., & Kasting, J. F. 2011, Astrobiology, 11, 419

Domagal-Goldman, S. D., Segura, A., Claire, M. W., Robinson, T. D., & Meadows, V. S. 2014, Astrophys. J., 792, 90, 1407.2622

Dorn, C., Harrison, J. H., Bonsor, A., & Hands, T. O. 2019, Mon. Not. R. Astron. Soc., 484, 712, 1812.07222

Dorn, C., Noack, L., & Rozel, A. 2018, A&A, 614, A18, 1802.09264

Dragomir, D. et al. 2019, Astrophys. J., 875, L7

Drake, M. J., & Righter, K. 2002, Determining the composition of the Earth

Duschl, W., Gail, H. P., & Tscharnuter, W. 1996, A&A, 312, 624

Edwards, B. et al. 2020, Astron. J., 161, 44, 2011.08815

Ehlmann, B., Mustard, J., & Murchie, S. 2010, Geophys. Res. Lett., 37, L06201

Elkins-Tanton, L. 2012, Annu. Rev. Earth Planet. Sci., 40, 113

Farihi, J., Koester, D., Zuckerman, B., Vican, L., Gansicke, B. T., Smith, N., Waith, G., & Breedt, E. 2016, Mon. Not. R. Astron. Soc., 463, 3186, 1608.07278

Ferris, J. P., Joshi, P. C., Edelson, E. H., & Lawless, J. G. 1978, J. Mol. Evol., 11, 293

Ferus, M., Kubelík, P., Kníek, A., Pastorek, A., Sutherland, J., & Civis, S. 2017, Sci. Rep., 7, 6275

Follert, R. et al. 2014, in Ground-based Airborne Instrum. Astron. V, Vol. 9147, 914719

Follmann, H., & Brownson, C. 2009, Naturwissenschaften, 96, 1265

Fossati, L. et al. 2020, Astron. Astrophys., 643, A131

Fujii, Y. et al. 2018, Astrobiology, 18, 739, 1705.07098

Fulchignoni, M. et al. 2005, Nature, 438, 785

Gail, H. P., & Sedlmayr, E. 1999, A&A, 347, 594

Gaillard, F., & Scaillet, B. 2014, Earth Planet. Sci. Lett., 403, 307

Gale, A., Dalton, C., Langmuir, C., Su, Y., & Schilling, J.-G. 2013, Geochemistry, Geophys. Geosystems, 14, 489

Gan, T. et al. 2020, Astron. J., 159, 160

Gao, P. et al. 2020, Nat. Astron., 4, 951, 2005.11939

Gardner, J. P. et al. 2006, Space Sci. Rev., 123, 485, 0606175

Gaudi, B. S. et al. 2018, arXiv e-prints, arXiv:1809.09674, 1809.09674

Giacobbe, P. et al. 2021, Nature, 592, 205

Gillon, M. et al. 2017, Nature, 542, 456, 1703.01424

Gilmore, M., Treiman, A., Helbert, J., & Smrekar, S. 2017, Venus Surface Composition Constrained by Observation and Experiment

Gilmozzi, R., & Spyromilio, J. 2007, The Messenger, 127, 11

Graham, R. J., & Pierrehumbert, R. 2020, Astrophys. J., 896, 115, 2004.14058

Grasset, O. et al. 2013, Planet. Space Sci., 78, 1

Greaves, J. S. et al. 2021, Nat. Astron., 5, 655, 2009.06593

Greber, N. D., Dauphas, N., Bekker, A., Ptáček, M. P., Bindeman, I. N., & Hofmann, A. 2017, Science (80-.)., 357, 1271

Gregory, B. S., Claire, M. W., & Rugheimer, S. 2021, Earth Planet. Sci. Lett., 561, 116818

Grenfell, J. L. et al. 2020, Space Sci. Rev., 216, 98

Grotzinger, J. P. 2013, Science (80-.)., 341, 1475

Günther, M. N. et al. 2019, Nat. Astron., 3, 1099

Guzmán-Marmolejo, A., Segura, A., & Escobar-Briones, E. 2013, Astrobiology, 13, 550

Haberle, R. M. 2015, in Encycl. Atmos. Sci. (Second Ed., second edi edn., ed. G. R. North, J. Pyle, & F. Zhang (Oxford: Academic Press), 168–177

Hallsworth, J. E. et al. 2021, Nat. Astron., 5, 665

Hammond, M., & T. Pierrehumbert, R. 2017, Astrophys. J., 849, 152

Haqq-Misra, J. D., Domagal-Goldman, S. D., Kasting, P. J., & Kasting, J. F. 2008, Astrobiology, 8, 1127

Harman, C. E., Felton, R., Hu, R., Domagal-Goldman, S. D., Segura, A., Tian, F., & Kasting, J. F. 2018, Astrophys. J., 866, 56

Harman, C. E., Schwieterman, E. W., Schottelkotte, J. C., & Kasting, J. F. 2015, Astrophys. J., 812, 137, 1509.07863

Harrison, J. H., Bonsor, A., & Madhusudhan, N. 2018, Mon. Not. R. Astron. Soc., 479, 3814, 1806.09917

Hashimoto, G. L., Roos-Serote, M., Sugita, S., Gilmore, M. S., Kamp, L. W., Carlson, R. W., & Baines, K. H. 2008, J. Geophys. Res., 113, E00B24

Heller, R., & Armstrong, J. 2014, Astrobiology, 14, 50, 1401.2392

Heller, R., & Barnes, R. 2013, Astrobiology, 13, 18, 1209.5323

Helling, C. 2019, Annu. Rev. Earth Planet. Sci., 47, 583, 1812.03793

Helling, C. et al. 2008, MNRAS, 391, 1854, 0809.3657

——. 2019, Astron. Astrophys., 631, 1906.08127

Helling, C., Kawashima, Y., Graham, V., Samra, D., Chubb, K., Min, M., Waters, L., & Parmentier, V. 2020, A&A, 641, A178, 2005.14595

Henning, T., & Salama, F. 1998, Science (80-.)., 282, 2204

Herbort, O., Woitke, P., Helling, C., & Zerkle, A. 2020, Astron. Astrophys., 636, A71

Herbort, O., Woitke, P., Helling, C., & Zerkle, A. L. 2022, A&A, 658, A180

Hinkel, N. R., Timmes, F. X., Young, P. A., Pagano, M. D., & Turnbull, M. C. 2014, Astron. J., 148, 1405.6719

Hirano, T. et al. 2018, Astron. J., 155, 124

Hirschmann, M. M. 2012, Earth Planet. Sci. Lett., 341, 48

Hodosan, G., Helling, C., & Rimmer, P. 2017, in Planet. Radio Emiss. VIII, ed. G. Fischer, G. Mann, M. Panchenko, & P. Zarka, 345–356, 1711.08053

Hoehler, T. M. 2007, Astrobiology, 7, 824

Hoeijmakers, H. J. et al. 2018, Nature, 560, 453, 1808.05653

Holland, H. D. 2002, Geochim. Cosmochim. Acta, 66, 3811

Holland, T. J. B., & Powell, R. 2011, J. Metamorph. Geol., 29, 333

Holstein-Rathlou, C., Maue, A., & Withers, P. 2016, Planet. Space Sci., 120, 15

Höning, D., Baumeister, P., Grenfell, J. L., Tosi, N., & Way, M. J. 2021, J. Geophys. Res. Planets, 126, 2109.08756

Horneck, G. et al. 2016, Astrobiology, 16, 201

Hu, R., Ehlmann, B. L., & Seager, S. 2012, Astrophys. J., 752, 1204.1544

Hu, R., Seager, S., & Bains, W. 2013, Astrophys. J., 769, 1302.6603

Huang, J., Seager, S., Petkowski, J. J., Ranjan, S., & Zhan, Z. 2021, arXiv e-prints, arXiv:2107.12424, 2107.12424

Huang, S.-S. 1959, Am. Sci., 47, 397

Ito, Y., Changeat, Q., Edwards, B., Al-Refaie, A., Tinetti, G., & Ikoma, M. 2021, Exp. Astron.

Jewitt, D., Matthews, H., Owen, T., & Meier, R. 1997, Science (80-.)., 278, 90

Johnstone, C. P. 2020, Astrophys. J., 890, 79, 1912.07027

Johnstone, C. P., Khodachenko, M. L., Lüftinger, T., Kislyakova, K. G., Lammer, H., & Güdel, M. 2019, Astron. Astrophys., 624, 1904.01063

Kaltenegger, L. 2017, ARA&A, 55, 433

Kane, S. R. et al. 2020, Astron. J., 160, 129

Kargel, J., & Lewis, J. 1993, Icarus, 105, 1

Kasting, J. F. 2014, in Earth's Early Atmos. Surf. Environ., ed. G. H. Shaw, Vol. 504 (Geological Society of America), 0

Kasting, J. F., Whitmire, D. P., & Reynolds, R. T. 1993, Icarus, 101, 108

Katyal, N., Nikolaou, A., Godolt, M., Grenfell, J. L., Tosi, N., Schreier, F., & Rauer, H. 2019, Astrophys. J., 875, 31, 1903.04623

Katyal, N. et al. 2020, Astron. Astrophys., 643, 2009.14599

Keles, E., Grenfell, J. L., Godolt, M., Stracke, B., & Rauer, H. 2018, Astrobiology, 18, 116

Kemmer, J. et al. 2020, Astron. Astrophys., 642, A236

Kipping, D., Bakos, G. Á., Buchhave, L., Nesvorný, D., & Schmitt, A. 2012, ApJ, 750, 115, 1201.0752

Kipping, D. M. et al. 2016, Astrophys. J., 820, 112

Kislyakova, K. et al. 2017, Nat. Astron., 1, 878, 1710.08761

Kite, E. S., & Barnett, M. N. 2020, Proc. Natl. Acad. Sci. U. S. A., 117, 18264, 2006.02589

Kite, E. S., Bruce Fegley Jr., Schaefer, L., & Gaidos, E. 2016, Astrophys. J., 828, 80, 1606.06740

Kite, E. S., & Ford, E. B. 2018, ApJ, 864, 75, 1801.00748

Knollenberg, R., & Hunten, D. 1980, J. Geophys. Res., 85, 8039

Koester, D. 2009, Astron. Astrophys., 498, 517, 0903.1499

Komacek, T. D., Fauchez, T. J., Wolf, E. T., & Abbot, D. S. 2020, Astrophys. J., 888, L20

Konacki, M., & Wolszczan, A. 2003, ApJ, 591, L147, astro-ph/0305536

Kotsyurbenko, O. R. et al. 2021, Astrobiology, 21, 1186

Kreidberg, L. et al. 2014, Nature, 505, 69, 1401.0022

——. 2019, Nature, 573, 87, 1908.06834

Krissansen-Totton, J. et al. 2019, BAAS, 51, 158

Krissansen-Totton, J., Fortney, J. J., & Nimmo, F. 2021, Planet. Sci. J., 2, 2111.00033

Krissansen-Totton, J., Thompson, M., Galloway, M. L., & Fortney, J. J. 2022, Nat. Astron., 6, 189, 2202.10333

Kruijver, A., Höning, D., & van Westrenen, W. 2021, Planet. Sci. J., 2, 208, 2110.03295

Lammer, H., Sproß, L., Grenfell, J. L., Scherf, M., Fossati, L., Lendl, M., & Cubillos, P. E. 2019, Astrobiology, 19, 927, 1904.11716

Lammer, H. et al. 2014, Mon. Not. R. Astron. Soc., 439, 3225, 1401.2765

——. 2018, A&A Rev., 26, 2

Leconte, J., Forget, F., & Lammer, H. 2015, Exp. Astron., 40, 449

Léger, A. et al. 2011, Icarus, 213, 1, 1102.1629

——. 2009, Astron. Astrophys., 506, 287, 0908.0241

Leleu, A. et al. 2021, Astron. Astrophys., 649, A26

Lellouch, E., Bézard, B., Flasar, F., Vinatier, S., Achterberg, R., Nixon, C., Bjoraker, G., & Gorius, N. 2014, Icarus, 231, 323

Lellouch, E. et al. 2017, Icarus, 286, 289, 1606.03293

Lewis, J. S. 1969, Icarus, 10, 365

Lewis, J. S., & Prinn, R. G. 1970, Science (80-.)., 169, 472

Lichtenberg, T., Bower, D. J., Hammond, M., Boukrouche, R., Sanan, P., Tsai, S.-M., & Pierrehumbert, R. T. 2021, J. Geophys. Res. Planets, 126, 2101.10991

Liggins, P., Shorttle, O., & Rimmer, P. B. 2020, Earth Planet. Sci. Lett., 550, 2007.12037

Lillo-Box, J. et al. 2020, Astron. Astrophys., 640, A48

Limaye, S. S. et al. 2017, Icarus, 294, 124

Lincowski, A. P. et al. 2021, Astrophys. J. Lett., 908, L44, 2101.09837

Line, M. R., & Parmentier, V. 2016, Astrophys. J., 820, 78

Lisse, C. M. et al. 2020, Astrophys. J., 898, L17, 2006.07403

Livingston, J. H. et al. 2018, AJ, 156, 78, 1806.11504

Locci, D., Petralia, A., Micela, G., Maggio, A., Ciaravella, A., & Cecchi-Pestellini, C. 2022, The Planetary Science Journal, 3, 1, 2112.02942

Lodders, K., & Fegley, B. 1997, in American Institute of Physics Conference Series, Vol. 402, Astrophys. Implic. Lab. study presolar Mater., ed. T. J. Bernatowicz & E. Zinner, 391–423

Lodders, K., & Fegley, B. 2002, Icarus, 155, 393

Lodders, K., Palme, H., & Gail, H. P. 2009, Landolt Börnstein, 4B, 712, 0901.1149

Loftus, K., Wordsworth, R. D., & Morley, C. V. 2019, Astrophys. J., 887, 231, 1908.02769

Lopez-Morales, M. et al. 2019, BAAS, 51, 162, 1903.09523

Lowell, P. 1908, Mars as the Abode of Life

Luger, R., & Barnes, R. 2015, Astrobiology, 15, 119

Luque, R. et al. 2019, Astron. Astrophys., 628, A39

——. 2021, Astron. Astrophys., 645, A41

Lustig-Yaeger, J., Meadows, V. S., Tovar Mendoza, G., Schwieterman, E. W., Fujii, Y., Luger, R., & Robinson, T. D. 2018, AJ, 156, 301, 1901.05011

Lyons, T. et al. 2021, Bull. AAS, 53, 2008.04803

Madden, J., & Kaltenegger, L. 2018, Astrobiology, 18, 1559, 1807.11442

Madhusudhan, N. 2012, ApJ, 758, 36, 1209.2412

Madhusudhan, N., Piette, A. A., & Constantinou, S. 2021, ApJ, 918, 1, 2108.10888

Mahapatra, G., Helling, C., & Miguel, Y. 2017, Mon. Not. R. Astron. Soc., 472, 447, 1706.07219

Mai, C., & Line, M. R. 2019, Astrophys. J., 883, 144

Mang, J., Gao, P., Hood, C. E., Fortney, J. J., Batalha, N., Yu, X., & de Pater, I. 2022, arXiv e-prints, arXiv:2202.01355, 2202.01355

Mansfield, M., Kite, E. S., Hu, R., Koll, D. D. B., Malik, M., Bean, J. L., & Kempton, E. M.-R. 2019, Astrophys. J., 886, 141, 1907.13150

Marconi, A. et al. 2016, in Society of Photo-Optical Instrumentation Engineers (SPIE) Conference Series, Vol. 9908, Ground-based Airborne Instrum. Astron. VI, ed. C. J. Evans, L. Simard, & H. Takami, 990823, 1609.00497

Martínez-Rodríguez, H., Caballero, J. A., Cifuentes, C., Piro, A. L., & Barnes, R. 2019, ApJ, 887, 261, 1910.12054

Marusiak, A. G. et al. 2021, The Planetary Science Journal, 2, 150

Mayor, M., & Queloz, D. 1995, Nature, 378, 355

Mbarek, R., & Kempton, E. M.-R. 2016, Astrophys. J., 827, 121, 1602.02759

McArthur, B. E. et al. 2004, Astrophys. J., 614, L81, 0408585

Meadows, V. S. 2017, Astrobiology, 17, 1022

Meadows, V. S. et al. 2018, Astrobiology, 18, 630, 1705.07560

Meier, T. G., Bower, D. J., Lichtenberg, T., Tackley, P. J., & Demory, B.-O. 2021, ApJ, 908, L48, 2103.02374

Melis, C., & Dufour, P. 2016, Astrophys. J., 834, 1, 1610.08016

Miguel, Y. 2018, Mon. Not. R. Astron. Soc., 482, 2893, 1809.08230

Miguel, Y., Kaltenegger, L., Fegley, B., & Schaefer, L. 2011, Astrophys. J. Lett., 742, L19, 1110.2426

Mikal-Evans, T. 2021, Mon. Not. R. Astron. Soc., 510, 980, 2111.09685

Miller, S. L. 1953, Science (80-.)., 117, 528

Miller, S. L., & Urey, H. C. 1959, Science (80-.)., 130, 245

Miller-Ricci, E., Seager, S., & Sasselov, D. 2009, ApJ, 690, 1056, 0808.1902

Mills, B., Lenton, T. M., & Watson, A. J. 2014, Proc. Natl. Acad. Sci., 111, 9073

Min, M., Ormel, C. W., Chubb, K., Helling, C., & Kawashima, Y. 2020, A&A, 642, A28, 2006.12821

Montmessin, F., Gondet, B., Bibring, J. P., Langevin, Y., Drossart, P., Forget, F., & Fouchet, T. 2007, J. Geophys. Res., 112, E11S90

Moreras-Marti, A., Fox-Powell, M., Stueeken, E., Di Rocco, T., Galloway, T., Osinski, G. R., Cousins, C. R., & Zerkle, A. L. 2021, Geochim. Cosmochim. Acta, 308, 157

Morowitz, H., & Sagan, C. 1967, Nature, 215, 1259

Moses, J. I. et al. 2013, Astrophys. J., 777, 1306.5178

Muirhead, P. S. et al. 2012, Astrophys. J., 747, 144

Müller, D. R. et al. 2022, arXiv e-prints, arXiv:2202.03521, 2202.03521

Muralikrishna, I. V., & Manickam, V. 2017, in Environ. Manage., ed. I. V. Muralikrishna & V. Manickam (Butterworth-Heinemann), 337–397

Niemann, H. et al. 2005, Nature, 438, 779

Nikolaou, A., Katyal, N., Tosi, N., Godolt, M., Grenfell, J. L., & Rauer, H. 2019, Astrophys. J., 875, 11

Nikolov, N. et al. 2018, Nature, 557, 526, 1806.06089

Niraula, P. et al. 2017, Astron. J., 154, 266

Noack, L. et al. 2016, Icarus, 277, 215

Nortmann, L. et al. 2018, Science (80-.)., 362, 1388, 1812.03119

Nuth, J. A., & Donn, B. 1982, J. Chem. Phys., 77, 2639

Ohno, K., Zhang, X., Tazaki, R., & Okuzumi, S. 2021, Astrophys. J., 912, 37

Okumura, S., & Nakashima, S. 2004, Phys. Chem. Miner., 31, 183

Olson, P., & Sharp, Z. D. 2018, Earth Planet. Sci. Lett., 498, 418

O'Malley-James, J. T., & Kaltenegger, L. 2019, Mon. Not. R. Astron. Soc., 485, 5598, 1904.03956

Omran, A., Oze, C., Jackson, B., Mehta, C., Barge, L. M., Bada, J., & Pasek, M. A. 2021, Astrobiology, 21, 1264

Ortenzi, G. et al. 2020, Sci. Rep., 10, 10907

Owen, J. E., Shaikhislamov, I. F., Lammer, H., Fossati, L., & Khodachenko, M. L. 2020, Space Sci. Rev., 216, 129

Owen, J. E., & Wu, Y. 2016, ApJ, 817, 107, 1506.02049

Panichi, F., Migaszewski, C., & Goździewski, K. 2019, Mon. Not. R. Astron. Soc., 485, 4601

Paquette, C., Pelletier, C., Fontaine, G., & Michaud, G. 1986, Astrophys. J. Suppl. Ser., 61, 197

Parker, E. T., Cleaves, H. J., Callahan, M. P., Dworkin, J. P., Glavin, D. P., Lazcano, A., & Bada, J. L. 2011, Orig. Life Evol. Biosph., 41, 569

Parmentier, V., Fortney, J. J., Showman, A. P., Morley, C., & Marley, M. S. 2016, ApJ, 828, 22, 1602.03088

Patel, B. H., Percivalle, C., Ritson, D. J., Duffy, C. D., & Sutherland, J. D. 2015, Nat. Chem., 7, 301

Patel, M., Mason, J., Nordheim, T., & Dartnell, L. 2022, Icarus, 373, 114796

Pearce, B. K., Pudritz, R. E., Semenov, D. A., & Henning, T. K. 2017, Proc. Natl. Acad. Sci., 114, 11327, 1710.00434

Pearce, B. K. D., Molaverdikhani, K., Pudritz, R. E., Henning, T., & Cerrillo, K. E. 2022, 2201.00829

Peirce, J. J., Weiner, R. F., & Vesilind, P. A. 1998, in Environ. Pollut. Control (Fourth Ed., fourth edi edn., ed. J. J. Peirce, R. F. Weiner, & P. A. Vesilind (Woburn: Butterworth-Heinemann), 271–286

Pepe, F. et al. 2021, A&A, 645, A96, 2010.00316

Phillips, C. B., & Pappalardo, R. T. 2014, EOS Trans., 95, 165

Pinchuk, P. et al. 2019, AJ, 157, 122, 1901.04057

Pinhas, A., & Madhusudhan, N. 2017, Mon. Not. R. Astron. Soc., 471, 4355

Poulet, F. et al. 2005, Nature, 438, 623

Quanz, S. et al. 2021, arXiv e-prints, arXiv:2101.07500, 2101.07500

Quirrenbach, A. et al. 2012, in Ground-based Airborne Instrum. Astron. IV, Vol. 8446, 84460R

Ramirez, R. M. 2020, Sci. Rep., 10, 7432

Ranjan, S., Kufner, C. L., Lozano, G. G., Todd, Z. R., Haseki, A., & Sasselov, D. D. 2021, arXiv e-prints, arXiv:2110.00432, 2110.00432

Reynolds, R., Squyres, S., Colburn, D., & McKay, C. 1983, Icarus, 56, 246

Ribas, I., Guinan, E. F., Güdel, M., & Audard, M. 2005, ApJ, 622, 680, astro-ph/0412253

Ribas, I. et al. 2018, Nature, 563, 365, 1811.05955

Rice, K. et al. 2019, Mon. Not. R. Astron. Soc., 484, 3731, 1812.07302

Ricker, G. R. et al. 2015, J. Astron. Telesc. Instruments, Syst., 1, 14003

Rimmer, P. B., Jordan, S., Constantinou, T., Woitke, P., Shorttle, O., Hobbs, R., & Paschodimas, A. 2021a, Planet. Sci. J., 2, 2101.08582

Rimmer, P. B., Majumdar, L., Priyadarshi, A., Wright, S., & Yurchenko, S. 2021b, ApJ, 921, L28, 2107.13097

Robie, R., & Hemingway, B. 1995, U.S. Geol. Surv. Bull, 2131, 461

Rossi, L., & Stam, D. M. 2017, Astron. Astrophys., 607, 1708.07009

——. 2018, Astron. Astrophys., 616, 1805.08686

Rudnick, R., & Gao, S. 2003, Treatise on Geochemistry, 3, 659

Ryan, D. J., & Robinson, T. D. 2022, The Planetary Science Journal, 3, 33, 2109.11062

Sagan, C., Thompson, W. R., Carlson, R., Gurnett, D., & Hord, C. 1993, Nature, 365, 715

Salz, M. et al. 2018, A&A, 620, A97, 1812.02453

Samra, D., Helling, C., & Min, M. 2020, Astron. Astrophys., 639, 2004.13502

Sandora, M., & Silk, J. 2020, Mon. Not. R. Astron. Soc., 495, 1000, 2005.04005

Schaefer, L., & Elkins-Tanton, L. T. 2018, Philos. Trans. R. Soc. London Ser. A, 376, 20180109, 1809.01629

Schaefer, L., & Fegley, B. 2007, Icarus, 186, 462, astro-ph/0606671

Schaefer, L., Lodders, K., & Fegley, B. 2012, Astrophys. J., 755, 41, 1108.4660

Schiaparelli, G. 1882, L'Astronomie, 1, 216

Schinder, P. J. et al. 2012, Icarus, 221, 1020

Schulze-Makuch, D., Heller, R., & Guinan, E. 2020, Astrobiology, 20, 1394

Schwieterman, E. W. et al. 2018, Astrobiology, 18, 663, 1705.05791

Seager, S. 2010, Exoplanet Atmospheres: Physical Processes

Seager, S., Bains, W., & Hu, R. 2013a, Astrophys. J., 775, 1309.6014

——. 2013b, Astrophys. J., 777, 1309.6016

Seager, S., Bains, W., & Petkowski, J. 2016, Astrobiology, 16, 465

Seager, S., Petkowski, J. J., Gao, P., Bains, W., Bryan, N. C., Ranjan, S., & Greaves, J. 2021a, Astrobiology, 21, 1206, 2009.06474

Seager, S., Petkowski, J. J., Günther, M. N., Bains, W., Mikal-Evans, T., & Deming, D. 2021b, Universe, 7, 172

Seager, S., Turner, E., Schafer, J., & Ford, E. 2005, Astrobiology, 5, 372, astro-ph/0503302

Seales, J., & Lenardic, A. 2021, Icarus, 367, 114560, 2102.01077

Seidel, J. V. et al. 2019, Astron. Astrophys., 623, 1902.00001

Seiff, A. et al. 1998, J. Geophys. Res., 103, 22857

Sekiya, M., Nakazawa, K., & Hayashi, C. 1980, Prog. Theor. Phys., 64, 1968

Sharp, C. 1988, Irish Astron. J., 18, 205

Sharp, C., & Huebner, W. 1990, ApJS, 72, 417

Shen, J., Zerkle, A. L., & Claire, M. W. 2021, Astrobiology, ahead of p

Sheppard, K. B., Mandell, A. M., Tamburo, P., Gandhi, S., Pinhas, A., Madhusudhan, N., & Deming, D. 2017, ApJ, 850, L32, 1711.10491

Shields, A. L., Ballard, S., & Johnson, J. A. 2016, Phys. Rep., 663, 1, 1610.05765

Sinukoff, E. et al. 2016, ApJ, 827, 78, 1511.09213

Smith, M. D. 2008, Annu. Rev. Earth Planet. Sci., 36, 191

Snellen, I., Guzman-Ramirez, L., Hogerheijde, M., Hygate, A., & van der Tak, F. 2020, A&A, 644, L2, 2010.09761

Snellen, I. A., De Kok, R. J., De Mooij, E. J., & Albrecht, S. 2010, Nature, 465, 1049, 1006.4364

Soto, M. G. et al. 2021, A&A Accept., 2102.11640

Sousa-Silva, C., Seager, S., Ranjan, S., Petkowski, J. J., Zhan, Z., Hu, R., & Bains, W. 2020, Astrobiology, 20, 235, 1910.05224

Spaargaren, R. J., Ballmer, M. D., Bower, D. J., Dorn, C., & Tackley, P. J. 2020, Astron. Astrophys., 643, 2007.09021

Sproß, L., Scherf, M., Shematovich, V. I., Bisikalo, D. V., & Lammer, H. 2021, Astron. Reports, 65, 275

Sromovsky, L., Fry, P., & Kim, J. 2011, Icarus, 215, 292, 1503.02476

Stahl, H. P., Kuan, G., Arnold, W., Baysinger, M., Brooks, T., Garcia, J., & Knight, J. B. 2020, in Society of Photo-Optical Instrumentation Engineers (SPIE) Conference Series, Vol. 11443, Soc. Photo-Optical Instrum. Eng. Conf. Ser., 114433C

Stern, R. J., Gerya, T., & Tackley, P. J. 2018, Geosci. Front., 9, 103

Sterzik, M. F., Bagnulo, S., & Palle, E. 2012, Nature, 483, 64

Stock, J. 2008, PhD thesis, Technische Universität Berlin

Stock, S. et al. 2020, arXiv e-prints, 2010.00474

Stökl, A., Dorfi, E., & Lammer, H. 2015, A&A, 576, A87, 1505.06859

Struve, O. 1952, Obs., 72, 199

Stüeken, E., Kipp, M., Koehler, M., Schwieterman, E., Johnson, B., & Buick, R. 2016, Astrobiology, 16, 949, 1612.02865

Stüeken, E. E. 2016, Astrobiology, 16, 730

Suissa, G. et al. 2020, Astron. J., 160, 118

Syverson, D. et al. 2021, Geophys. Res. Lett., 48, e94442, 2002.07667

Taubner, R.-S. et al. 2020, Space Sci. Rev., 216, 9

Taylor, S. R., & McLennan, S. M. 1995, Rev. Geophys., 33, 241

Teal, D., Kempton, E. M. R., Bastelberger, S., Youngblood, A., & Arney, G. 2022, arXiv e-prints, arXiv:2201.08805, 2201.08805

Teinturier, L., Vieira, N., Jacquet, E., Geoffrion, J., Bestavros, Y., Keating, D., & Cowan, N. B. 2022, 2201.00825

Thi, W. F., Hocuk, S., Kamp, I., Woitke, P., Rab, C., Cazaux, S., Caselli, P., & D'Angelo, M. 2020, Astron. Astrophys., 635, arXiv:1812.04357, 1812.04357

Thompson, M. A., Telus, M., Schaefer, L., Fortney, J. J., Joshi, T., & Lederman, D. 2021, Nat. Astron., 5, 575, 2104.08360

Tinetti, G. et al. 2018, Exp. Astron., 46, 135

Tinetti, G., Rashby, S., & Yung, Y. L. 2006, ApJ, 644, L129

Tjoa, J. N., Mueller, M., & Van Der Tak, F. F. 2020, Astron. Astrophys., 636, 2003.09231

Tokano, T. 2017, Icarus, 289, 120

Tosi, N. et al. 2017, Astron. Astrophys., 605, 1707.06051

Toupance, G., Raulin, F., & Buvet, R. 1975, Orig. Life, 6, 83

Trainer, M., Pavlov, A., Dewitt, H., Jimenez, J., McKay, C., Toon, O., & Tolbert, M. 2006, Proc. Natl. Acad. Sci., 103, 18035

Trifonov, T. et al. 2021, Science (80-.)., 371, 1038

Tsiaras, A. et al. 2016, Astrophys. J., 820, 99, 1511.08901

Tsuji, T. 1973, A&A, 23, 411

Turbet, M., Bolmont, E., Chaverot, G., Ehrenreich, D., Leconte, J., & Marcq, E. 2021, Nature, 598, 276

Turbet, M., Leconte, J., Selsis, F., Bolmont, E., Forget, F., Ribas, I., Raymond, S., & Anglada-Escudé, G. 2016, A&A, 596, A112, 1608.06827

Turbet, M., & Selsis, F. 2021, arXiv e-prints, arXiv:2104.06391, 2104.06391

Ueno, Y., Yamada, K., Yoshida, N., Maruyama, S., & Isozaki, Y. 2006, Nature, 440, 516

Vago, J. L. et al. 2017, Astrobiology, 17, 471

Vance, S., Harnmeijer, J., Kimura, J., Hussmann, H., DeMartin, B., & Brown, J. M. 2007, Astrobiology, 7, 987

Vance, S., & Melwani Daswani, M. 2020, Philos. Trans. R. Soc. London Ser. A, 378, 20180421

Velde, B. 1995, Orig. Mineral. clays clays Environ.

Visscher, C., Lodders, K., & Fegley Bruce, J. 2006, ApJ, 648, 1181, astro-ph/0511136

Waalkes, W. C. et al. 2020, Astron. J., 161, 13

Wakeford, H., & Sing, D. 2015, A&A, 573, A122, 1409.7594

Walton, C. R. et al. 2021, arXiv e-prints, arXiv:2112.06038, 2112.06038

Wang, Y., Pavlis, G. L., & Li, M. 2019a, Earth Planet. Sci. Lett., 505, 42

Wang, Z.-C., Wu, Y.-Z., Zhang, X.-M., & Lu, Y. 2019b, Res. Astron. Astrophys., 19, 52, 1810.00338

Way, M. J., Del Genio, A. D., Kiang, N. Y., Sohl, L. E., Grinspoon, D. H., Aleinov, I., Kelley, M., & Clune, T. 2016, Geophys. Res. Lett., 43, 8376

Wedepohl, K. H. 1995, Geochim. Cosmochim. Acta, 59, 1217

Weidenschilling, S., & Lewis, J. 1973, Icarus, 20, 465

Weiss, L. M., & Marcy, G. W. 2014, Astrophys. J. Lett., 783, L6, 1312.0936

Wernicke, L. J., & Jakosky, B. M. 2021, J. Geophys. Res., 126, e06351

Westall, F., & Brack, A. 2018, Space Sci. Rev., 214, 50

Williams, D. M., & Gaidos, E. 2008, Icarus, 195, 927, 0801.1852

Wilson, D. J., Gänsicke, B. T., Farihi, J., & Koester, D. 2016, Mon. Not. R. Astron. Soc., 459, 3282, 1604.03104

Wilson, T. G., Farihi, J., Gänsicke, B. T., & Swan, A. 2019, Mon. Not. R. Astron. Soc., 487, 133, 1904.05891

Winn, J. N. 2010, arXiv e-prints, 1001.2010

Woese, C. R. 1979, J. Mol. Evol., 13, 95

Wogan, N., Krissansen-Totton, J., & Catling, D. C. 2020, Planet. Sci. J., 1, 58, 2009.07761

Woitke, P., & Helling, C. 2003, A&A, 399, 297

Woitke, P., Helling, C., & Gunn, O. 2020, Astron. Astrophys., 634, A23, 1911.03777

Woitke, P., Helling, C., Hunter, G., Millard, J., Turner, G., Worters, M., Blecic, J., & Stock, J. 2018, Astron. Astrophys., 614, A1, 1712.01010

Woitke, P., Herbort, O., Helling, C., Stüeken, E., Dominik, M., Barth, P., & Samra, D. 2021, Astron. Astrophys., 646, A43, 2010.12241

Wolszczan, A. 1994, Science (80-.)., 264, 538

Wolszczan, A., & Frail, D. 1992, Nature, 355, 145

Wong, M. H., Atreya, S. K., Kuhn, W. R., Romani, P. N., & Mihalka, K. M. 2015, Icarus, 245, 273

Wordsworth, R., & Kreidberg, L. 2021, arXiv e-prints, arXiv:2112.04663, 2112.04663

Wunderlich, F. et al. 2020, ApJ, 901, 126, 2006.11349

Wunderlich, F., Scheucher, M., Grenfell, J. L., Schreier, F., Sousa-Silva, C., Godolt, M., & Rauer, H. 2021, Astron. Astrophys., 647, 2012.11426

Yoshizaki, T., Ash, R. D., Yokoyama, T., Lipella, M. D., & McDonough, W. F. 2018, 1812.11717

Young, M. E., Fossati, L., Johnstone, C., Salz, M., Lichtenegger, H., France, K., Lammer, H., & Cubillos, P. E. 2020, Astron. Nachrichten, 341, 879

Yu, X., Moses, J. I., Fortney, J. J., & Zhang, X. 2021, How to Identify Exoplanet Surfaces Using Atmospheric Trace Species in Hydrogen-dominated Atmospheres, 2104.09843

Zahnle, K., Marley, M. S., Morley, C. V., & Moses, J. I. 2016, Astrophys. J., 824, 137, 1604.07388

Zahnle, K. J., Gacesa, M., & Catling, D. C. 2019, Geochim. Cosmochim. Acta, 244, 56, 1809.06960

Zerkle, A. L., Claire, M. W., Domagal-Goldman, S. D., Farquhar, J., & Poulton, S. W. 2012, Nat. Geosci., 5, 359

Zimmer, K., Zhang, Y., Lu, P., Chen, Y., Zhang, G., Dalkilic, M., & Zhu, C. 2016, Comput. Geosci., 90, 97

Zollinger, R. R., Armstrong, J. C., & Heller, R. 2017, MNRAS, 472, 8, 1707.07040

Zuckerman, B., Koester, D., Melis, C., Hansen, B. M., & Jura, M. 2007, Astrophys. J., 671, 872, 0708.0198

"I wish it need not have happened in my time," said Frodo.
"So do I," said Gandalf, "and so do all who live to see such times. But that is not for them to decide. All we have to decide is what to do with the time that is given us."

- J.R.R. Tolkien, *The Fellowship of the Ring*